Mathematical models for the glass sheet redraw process

Doireann O'Kiely

Christ Church

University of Oxford

Submitted for the degree of
Doctor of Philosophy

Hilary 2017

Acknowledgements

I would like to thank my supervisors Ian Griffiths, Peter Howell, Chris Breward and Ulrich Lange for their help and guidance throughout my PhD studies. Their enthusiasm, insight and patience have made this experience enjoyable and rewarding. I am also grateful to colleagues in the Mathematical Institute for comments and advice, and to Schott AG for sharing their data and knowledge, and welcoming me to their research group and pilot plant during visits.

Thank you also to my friends and family for their support, especially my parents Fearga and Pádraig and my partner Pete.

Abstract

In this thesis we derive mathematical models for the glass sheet redraw process for the production of very thin glass sheets. In the redraw process, a prefabricated glass block is fed into a furnace, where it is heated and stretched by the application of draw rollers to reduce its thickness. Redrawn sheets may be used in various applications including smartphone and battery technology. Our aims are to investigate the factors determining the final thickness profile of a glass sheet produced by this process, as well as the growth of out-of-plane deformations in the sheet during redraw. Our method is to model the glass sheet using Navier–Stokes equations and free-surface conditions, and exploit small aspect ratios in the sheet to simplify and solve these equations using asymptotic expansions.

We first consider a simple two-dimensional sheet to determine which physical effects should be taken into account in modelling the redraw process. Next, we derive a mathematical model for redraw of a thin three-dimensional sheet. We consider the limits in which the heater zone is either short or long compared with the sheet half-width. The resulting reduced models predict the thickness profile of the redrawn sheet and the initial shape required to redraw a product of uniform thickness. We then derive mathematical models for buckling of thin viscous sheets during redraw. For buckling of a two-dimensional glass sheet due to gravity-induced compression, we predict the evolution of the centreline and investigate the early- and late-time behaviour of the system. For a three-dimensional glass sheet undergoing redraw, we use numerical solutions to investigate the behaviour of the sheet mid-surface.

Contents

List of Figures

Chapter 1

Introduction

1.1 Overview

Thin glass sheets are becoming more and more prevalent in everyday technology, with current applications including substrates in thin-film batteries and thumbprint sensors in smartphones, and futuristic applications such as bendable televisions and tablets on the horizon (Horvatitsch, 2016; Burke, 2016). Drawing is a technique widely used in the manufacture of these thin glass sheets, as well as glass fibres. The most common drawing techniques require hot molten glass to be extruded and stretched as it cools. However, this method requires glass to be heated to very high temperatures, and so may be unsuitable when using specialist glasses which are prone to devitrification or which contain components that will evaporate or react with the atmosphere. This method is also inefficient if only a small quantity of product is required. In such situations, an alternative two-step approach to drawing can be used. A sheet known as a preform is first cast in a mould or by the float-glass process (Howell, 1994), and later fed vertically into a furnace where it is reheated and stretched by the application of a tensile force at a fixed distance downstream. As the glass stretches, it thins and contracts laterally. A schematic of this *redrawing* process is shown in figure 1.1.

Glass is characterized by a viscosity that decreases rapidly with increasing temperature; for a typical glass used in the redraw process the required temperature change of approximately 250K corresponds to a viscosity change of three orders of magnitude. For this reason most of the stretching takes place in the region where the glass temperature is maximal. Redraw is a batch process, but each process runs for a long time so that it typically operates in a steady state. In an ideal scenario, this process would produce long ($\sim$ 10–100m), very thin ($\sim$ 100μm) glass sheets of close to uniform thickness, or more generally with a particular desired thickness profile.

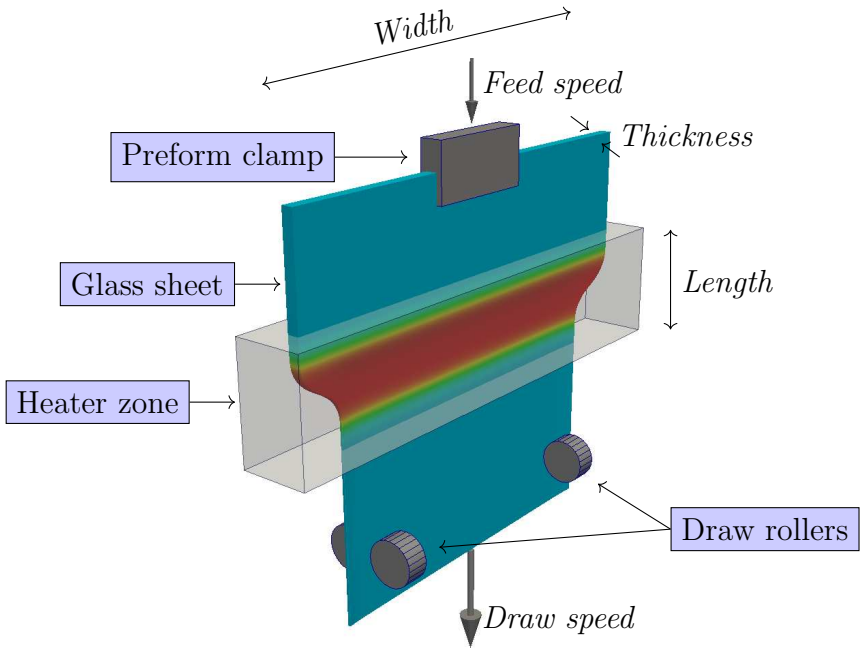

Figure 1.1: Schematic of the glass redraw process.

Schott AG are a supplier of specialist glasses and glass products, and use the redraw process in the manufacture of thin glass sheets. They are interested in understanding two key phenomena that occur during redraw:

- necking-in and thinning of the sheet, and the resulting thickness profile, and
- development of out-of-plane deformations such as ripples.

The thickness profile of the sheet exiting the furnace depends on the length of the heater zone compared with the width of the preform. Experimental observations at Schott AG indicate that when minimal reduction in width is desired, a short heater zone is preferable. The redrawn sheet then has a uniform thickness profile except for in small regions near the edges, where it is thicker (see figure 1.2). Ideally, redrawn sheets are cooled and rolled onto large spools for post-processing, but sheets with non-uniform thickness are likely to break when rolled, and thick edges must be removed before the product is sold. Meanwhile, in scenarios where the desired final product has the same aspect ratio as the preform, a very long heater zone is required (Lange, 2016), but in reality the finite length of the heater zone and the effect of surface tension both act to change the shape of the sheet.

Out-of-plane deformations of the glass sheet sometimes develop in the redraw process at Schott AG. A very drastic example are the ripples shown in figure 1.3.

Figure 1.2: Thick edge in a glass sheet redrawn at Schott AG. Photo by Dominic Vella.

These out-of-plane ripples persist downstream of the heater zone and draw rollers, and render the product unusable. The source of these ripples is not immediately obvious, and the extreme temperatures required for the manufacturing process make in situ imaging of ripple formation very difficult. During the redraw process, glass is stretched under tension, but may experience compression in the lateral direction in some parts of the sheet, rendering it unstable to out-of-plane deformations, and this instability may give rise to the observed ripples.

Figure 1.3: Ripples in a glass sheet redrawn at Schott AG. Photo from Schott pilot plant.

Schott AG currently undertake a number of experiments on the redraw process in

a pilot plant and use these, along with fully three-dimensional CFD calculations, to learn about how the process operates and to suggest ways to reduce defects. Simplified mathematical models provide a means to gain further insight into the process. Thus, our overarching aim is to derive a collection of mathematical models to describe various aspects of the redraw process and provide insight into a range of phenomena observed during manufacture.

1.2 Typical parameter values

The material parameters used for one particular glass type and redraw process are shown in Table 1.1. These parameters may vary significantly between glass types and manufacturing processes.

Parameter	Symbol	Approximate Value	Units
Density	ρ	2100	$\mathrm{kg\,m^{-3}}$
Feed speed	U	8.33×10^{-4}	$\mathrm{m\,s^{-1}}$
Heater zone length	d	0.12	m
Preform half-thickness	h_{in}	10^{-3}	m
Preform half-width	b_{in}	0.2	m
Maximum temperature	T_s	1300	K
Minimum viscosity	μ_s	3.16×10^4	Pa s
Surface tension coefficient	γ	0.3	$\mathrm{N\,m^{-1}}$
Specific heat	c_p	1300	$\mathrm{J\,kg^{-1}\,K^{-1}}$
Thermal conductivity	k_c	2.0	$\mathrm{W\,m^{-1}\,K^{-1}}$
Refractive index	n_0	1.47	–
Stefan-Boltzmann constant	σ_{SB}	5.67×10^{-8}	$\mathrm{W\,m^{-2}\,K^{-4}}$
Absorption coefficient	χ	200	$\mathrm{m^{-1}}$
Specific emissivity	ϵ_r	0.9	–
Heat transfer coefficient	m_h	100	$\mathrm{W\,m^{-2}}$

Table 1.1: Typical parameter values for redraw of a borosilicate glass sheet through a short heater zone (Griffiths and Howell, 2008; Taroni et al., 2012; Lange, 2014; Buellesfeld et al., 2014).

1.3 Literature review

Redraw is an example of an extensional flow problem, in which the longitudinal and transverse velocities do not vary significantly across the sheet thickness. Models developed for other extensional flow problems, such as downdraw (Matovich and

Pearson, 1969) and the float glass process (Howell, 1994, 1996) may be adapted for the redraw process. These processes share a number of key features and are characterized by small ratios of thickness to other lengthscales which may be exploited to simplify corresponding mathematical models. We give an overview of existing studies of these processes here, and we will provide a more comprehensive review of the literature relevant to the problem at hand at the beginning of each chapter.

Studies of extensional flow date back to the experimental work of Trouton (1906), who developed an empirical formula for the extension of a fibre subject to a tensile force. The Trouton model, which governs the velocity and thickness (radius) profiles of a sheet (fibre) under tension, has since been derived, generalized and analysed by various authors. Solutions for steady-state isothermal drawing of a fibre are obtained by Matovich and Pearson (1969), who consider the effects of viscosity, inertia, surface tension and gravity. Studies typically focus on the leading-order behaviour in the limit of a thin sheet or slender fibre, although Schultz and Davis (1982) propose an asymptotic expansion in powers of ϵ^2, where ϵ is the ratio of fibre radius to its length. Beyond leading order, the boundary conditions at the top and bottom of the fibre cannot be applied directly to the bulk solution, so the authors instead apply a cross-averaged version and thus calculate the proposed $O(\epsilon^2)$ correction terms. Dewynne et al. (1989) consider the tapering of a cylindrical glass fibre in which the central region is heated and the ends are pulled apart, and track the evolution of imperfections in the initial radius when viscous stretching dominates the stress balance. Griffiths and Howell (2008) model drawing of a non-axisymmetric tube, solving an inverse problem to obtain the die shape required to produce a desired final shape.

The temperature profile of fibres and sheets undergoing drawing has received significant attention due to its role in the dynamics and stability of drawing processes. Matovich and Pearson (1969) extend their model for isothermal fibre drawing to a fibre that is being cooled due to heat transfer with the surrounding atmosphere. Myers (1989) investigates the role of radiation in determining the temperature during drawing of a cylindrical preform, and determines that radiation dominates heat transfer in the particular process of interest. Taroni et al. (2012) study the interplay between extensional flow and heat transport in a glass fibre where both radiation and diffusion play a role in heat transport in the bulk, and both radiation and Newton cooling contribute to heat transfer with the surroundings. They determine a hierarchy of problems for the temperature profile in the fibre in various heat-transfer regimes.

A model for the viscous flow of a three-dimensional sheet characterized by its small aspect ratio of thickness to other lengthscales is derived by Howell (1994, 1996),

who used this as a model for the float glass process. This thin-sheet model has also been used by Filippov and Zheng (2010) to study the redraw process. They calculated numerical solutions for the thickness and stress profile in the sheet for different temperature profiles. Meanwhile, drawn sheets with thick edges have also been studied in the related problem of casting of polymer films. For example, Dobroth and Erwin (1986) propose formulas for the bulk and edge thickness in terms of the ratio of the draw to the feed speed, and d'Halewyu et al. (1990) and Silagy et al. (1999) use a thin-sheet model for casting of a polymer film.

An early study of buckling of a viscous material is presented by Taylor (1969), whose experiments include a viscous thread floating on mercury, which buckles when its ends are pushed together. This inspired the development of a mathematical model by Buckmaster et al. (1975), who investigate the timescale for buckling compared with the timescale for thickness changes and derive solutions for the buckling of a viscous thread whose ends are pushed together. Howell (1994) derives governing equations for a thin-sheet model undergoing out-of-plane motion, applying the resulting model to the examples of windscreen sagging and glass blowing. Filippov and Zheng (2010) suggest that the stability of a stretched thin viscous sheet is linked to the existence of so-called hyperbolic zones in which the principal stresses have opposite signs. They calculate these zones for a glass sheet undergoing redraw, and observe qualitatively different hyperbolic zones for different temperature profiles. More recently, Srinivasan et al. (2017) solve the linear-stability problem for small out-of-plane deformations, determining the fastest-growing eigenmodes and corresponding growth rates for early-time growth of ripples in sheets, and investigate the dependence of the buckling behaviour on the length of the heater zone through which the sheet is drawn. They determine that compressive buckling zones are always present upstream of the stretching region, and that short heater zones give rise to a second buckling region downstream of the stretching region.

1.4 Thesis outline

In this thesis, a collection of mathematical models is derived to describe aspects of the redraw process and provide insight into various phenomena observed during manufacture. In Chapter 2 we discuss the role of heat flow and stability in models of glass sheet redraw. We consider stretching of a two-dimensional thin glass sheet and determine the temperature profile in the sheet in different parameter regimes. We discuss the coupling between heat and fluid flow in industrially relevant regimes,

and assess the stability of the sheet to thickness perturbations. In Chapters 3–4 we develop mathematical models for three-dimensional thin sheets undergoing redraw to determine the dependence of the product thickness on process parameters. In Chapter 3, we consider the scenario in which the furnace is short compared with the sheet width. In this case the redrawn sheet has almost uniform thickness, but is thicker in small regions near the sheet edges. We quantify the size and extent of these thick edges and their dependence on process parameters, as well as investigating how thick edges may be avoided. In Chapter 4 we consider the alternative scenario, in which the furnace is long compared with the sheet width. In this limit, the aspect ratio of the sheet is preserved at leading order, but correction terms are significant in reality, and we quantify these. In Chapters 5 and 6 we turn our attention to buckling of thin viscous sheets. The gravity-driven buckling of a two-dimensional sheet provides a starting point for the study of a sheet in which regions of both tension and compression are present, and we develop a model for this process in the thin-sheet limit in Chapter 5. We investigate the interplay between the growth of out-of-plane deformations and the evolution of the stress profile in the sheet through numerical solutions as well as an asymptotic analysis of the late-time behaviour. In Chapter 6 we extend our model to buckling of a three-dimensional thin glass sheet undergoing redraw, taking particular care to derive the free-boundary conditions at a curved edge. We determine the fastest-growing buckling modes and corresponding growth rates, and propose a simple model to quantify the dependence of the growth rate on the sheet properties. Finally, in Chapter 7 we draw conclusions and discuss related work that should be carried out in the future.

1.5 Publications

At the time of submission, one paper (O'Kiely et al., 2015) has been publised from this thesis, containing the work in Chapter 3 and co-authored by D. O'Kiely, C. J. W. Breward, I. M. Griffiths, P. D. Howell and U. Lange (supervisors). In this paper, a model is developed for redraw of a three-dimensional thin sheet through a short heater zone, the model is analysed and solutions are compared to i) numerical simulations carried out in Polyflow, and ii) experimental data. The model analysis and numerical solution of this model were carried out by DOK under the supervision of CJWB, IMG, PDH and UL, while the numerical simulations in Polyflow and experiments were carried out by UL and colleagues at Schott AG; this is acknowledged in Chapter 3. UL also

carried out the numerical simulations in Polyflow presented in Chapter 4, and this is acknowledged.

Chapter 2

Modelling of two-dimensional glass sheets: heat flow and stability

2.1 Introduction

In this chapter we study the behaviour of a two-dimensional thin glass sheet undergoing redraw. Since the viscosity of the glass is a strong function of temperature, the temperature and flow of the glass may be coupled, and we investigate this here. We also investigate the stability of the sheet to thickness perturbations. Draw resonance is a phenomenon observed in fibre and sheet drawing in which oscillatory perturbations propagate along the fibre or sheet and grow in amplitude, resulting in a product with a varicose variation in thickness. Typically, the drawing process becomes unstable when the speed of the draw rollers relative to the input speed is too large. The aim of this chapter is to examine heat flow and draw resonance in a two-dimensional sheet to determine the extent to which they should be taken into account in modelling the glass sheet redraw process. For the most part, this is a direct application of existing models of float glass, downdraw or fibre drawing from the literature to the case of two-dimensional redraw. However, this chapter will form a basis for modelling more complicated systems, and the results obtained here will be used to justify simplifications made elsewhere in the thesis.

During the redraw process, glass is heated and cooled by feeding it through a furnace, and this temperature change leads to a spatial variation in the viscosity. The flow of glass in the sheet is affected by the temperature-dependent viscosity, and flow of heat is affected by the glass motion, so there is a two-way coupling between heat and fluid flow. Equations governing extensional flow in a fibre in the slender limit have been previously derived by Matovich and Pearson (1969), while equations governing extensional flow in a thin sheet were derived by Howell (1994). Matovich

and Pearson (1969) also present a model for the temperature in a fibre, where the temperature inside the fibre is governed by an advection–diffusion equation and heat is exchanged with the surroundings by Newton cooling. Myers (1989) presents a model for the temperature during drawing of a cylindrical preform through a furnace, in the particular case where radiation dominates the transport of heat inside the fibre as well as heat transfer with the surroundings. Taroni et al. (2012) also consider the problem of drawing of a cylindrical glass fibre. They track the temperature and fluid flow and investigate the asymptotic behaviour of the steady-state solution in two different distinguished limits of the aspect ratio

$$\epsilon = \frac{h_{in}}{L}, \tag{2.1}$$

(where h_{in} is the preform half-thickness and L the sheet length) and the Péclet number

$$\mathrm{Pe} = \frac{\rho c_p U L}{k_c}. \tag{2.2}$$

Here ρ, c_p and k_c are the density, specific heat capacity and thermal conductivity of the glass respectively, and U is a characteristic velocity, so that Pe is the ratio between the rates of advection and diffusion of heat. Taroni et al. (2012) find that, when $\epsilon\,\mathrm{Pe} = O(1)$, the temperature profile is approximately uniform across the cylinder radius, while for $\epsilon^2\,\mathrm{Pe} = O(1)$ significant temperature variations are expected across the cylinder radius due to competition between convection and transverse diffusion. In both cases, the flow affects the temperature profile at leading order and *vice versa*. Meanwhile, Scheid et al. (2009) model coupled heat and fluid flow in downdraw of a two-dimensional thin sheet. They consider regimes in which temperature variations across the sheet thickness are significant, and make the *ad hoc* simplifying assumption that the temperature profile is parabolic across the sheet thickness. After this assumption is made it is only necessary to solve for the average temperature, which is coupled to the thickness and velocity of the sheet.

Redraw is a batch process, but each batch is very long and we assume that the process operates in a steady state most of the time. The stability of fibre and sheet drawing to thickness perturbations has received a great deal of attention due to the restrictions that such instabilities place on industrial operating regimes. Comprehensive reviews of the vast literature on draw resonance may be found in Petrie and Denn (1976) and Hyun (1999); we limit our discussion to the literature of most relevance here. The study of draw resonance has focused mainly on (i) isothermal drawing, and (ii) downdraw, in which a sheet or fibre of molten glass is extruded vertically and undergoes stretching as it cools. Pearson and Matovich (1969) investigate the stability of

steady-state isothermal fibre drawing, and predict that this process becomes unstable when the "draw ratio" D between the speed at the draw rollers and the input speed exceeds a critical value of approximately 20.2. The effect of temperature variation on stability has been studied for fibres by authors such as Shah and Pearson (1972) and Myers (1989), and more recently by Scheid et al. (2009) for sheets. Shah and Pearson (1972) show that cooling of a fibre during redraw increases the critical draw ratio above which the sheet is unstable to draw resonance, while Myers (1989) finds that radiative heat transfer with a furnace during drawing of a cylindrical preform also increases the critical draw ratio. Scheid et al. (2009) carry out stability analysis of a sheet with coupled heat and fluid flow undergoing downdraw in regimes where the temperature varies across the sheet thickness at leading order. Their analysis shows cooling to be stabilizing over a range of values of the heat transfer coefficient, which measures the importance of heat transfer with the surrounding air. However, their analysis also shows that, in the limit when heat transfer with the air dominates, cooling is destabilizing. These results demonstrate that, except under extreme conditions, significantly larger draw speeds can be achieved for non-isothermal drawing without encountering resonance than can be achieved for isothermal drawing. Draw resonance is typically not observed in industrial redraw processes (Lange, 2014), which suggests that the sheet is stable to thickness perturbations for typical process parameters.

In §2.2 we outline the equations governing the thickness and velocity of a two-dimensional sheet in the limit where the sheet is very thin compared with its length. In §2.3 we derive equations governing the temperature in a thin sheet during redraw in two asymptotic limits, (i) where diffusion in the transverse direction dominates over advection in the direction of drawing, and (ii) where diffusion and advection both enter the governing equations at leading order. In each case we present numerical solutions for the temperature profile in the sheet and discuss the role of fluid flow in determining the temperature. In §2.4 we analyse the stability of a two-dimensional sheet undergoing redraw to thickness perturbations, and determine the critical draw ratio above which the sheet becomes unstable. Finally, in §2.5 we discuss the implications of our results for modelling redraw of a three-dimensional thin glass sheet.

2.2 Fluid flow

We use two-dimensional Cartesian coordinates (x, z), with x pointing in the direction of drawing and z in the transverse direction. We consider a sheet of thickness $2h(x, t)$ with velocity (u, w) undergoing redraw through a furnace of length L with furnace

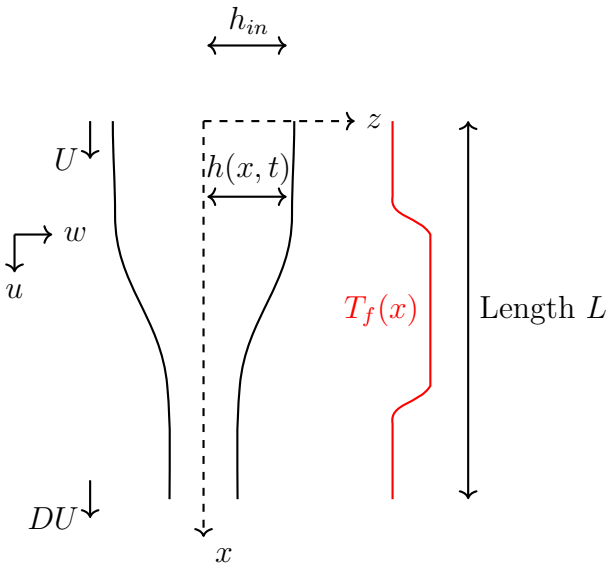

Figure 2.1: Two-dimensional glass sheet with thickness $2h(x,t)$ and velocity vector $\boldsymbol{u} = (u, w)$ subject to a furnace profile $T_f(x)$ undergoing redraw in the x-direction with inlet speed U and increased draw speed DU.

profile $T_f(x)$ as shown in figure 2.1. The equations governing redraw of a thin sheet can be adapted directly from models for float glass (Howell, 1994) or the downdraw process (Scheid et al., 2009). The Reynolds number $\mathrm{Re} = \rho LU/\mu_s$ (where ρ is density, U characteristic velocity and μ_s characteristic viscosity) is typically small in industrial processes, so we neglect inertia, and the flow in the sheet is governed by the two-dimensional Stokes equations

$$\nabla \cdot \boldsymbol{u} = 0, \quad \nabla \cdot \boldsymbol{\sigma} = \mathbf{0}, \tag{2.3}$$

where $\boldsymbol{u} = (u, w)$ is the velocity vector, $\nabla = (\partial/\partial x, \partial/\partial z)$, and

$$\boldsymbol{\sigma} = -p\mathbb{I} + \mu\left(\nabla\boldsymbol{u} + (\nabla\boldsymbol{u})^T\right) \tag{2.4}$$

is the stress tensor, with p denoting pressure, μ the viscosity and $\mathbb{I}$ the identity matrix. We emphasize that the viscosity $\mu(x, z, t)$ can vary due to local temperature changes. A typical expression for the viscosity is (Filippov and Zheng, 2010)

$$\mu = \exp\left[-A + \frac{B}{T - \hat{T}_c}\right], \tag{2.5}$$

where T is the temperature, and A, B and $\hat{T}_c$ are experimentally determined parameters.

In principle, we should also include gravitational effects in our model. Indeed, the Stokes number

$$\mathrm{St} = \frac{\text{gravity effects}}{\text{viscous effects}} = \frac{\rho g L^2}{\mu U} \approx 10 \tag{2.6}$$

using the parameters in Table 1.1. However, this value overestimates the effect of gravity as we have used the *smallest* value of viscosity μ (which typically varies over three or more orders of magnitude, cf. §2.3) and the *smallest* value of U, which increases by a factor of the draw ratio D, typically between 20 and 100 - so in reality the lengthscale over which μU takes the value obtained from Table 1.1 is shorter than the length of the furnace, and the ratio of gravity to viscous effects is smaller. In this thesis we will typically neglect gravity, assuming that its effect is small compared with the viscous stresses imposed by the draw rollers. The exception to this assumption is in Chapter 5, where we will consider scenarios in which the effect of gravity contributes significantly to the acceleration of the glass sheet.

There is no fluid flux across the free surfaces $z = \pm h(x,t)$ of the sheet, and we neglect surface tension so that there is no surface traction, i.e.

$$\frac{\mathrm{D}}{\mathrm{D}t}\left(z \mp h\right) = 0, \quad \boldsymbol{\sigma}\cdot\hat{\boldsymbol{n}} = \mathbf{0}, \tag{2.7}$$

where $\mathrm{D}/\mathrm{D}t = \partial/\partial t + \boldsymbol{u}\cdot\nabla$ is the convective derivative and $\hat{\boldsymbol{n}}$ is the outward-pointing normal to the sheet. A sheet with initial thickness $2h_{in}$ is fed into the furnace at a characteristic velocity U, and drawn out of the furnace at a velocity which is increased by a factor D known as the draw ratio, so we write

$$u = U, \quad h = h_{in} \quad \text{on} \quad x = 0, \tag{2.8a}$$

$$u = DU \quad \text{on} \quad x = L. \tag{2.8b}$$

In principle, we should also impose boundary conditions on the transverse velocity w, but this is not necessary in the thin sheet limit (we discuss this in more detail in Chapter 4).

We introduce dimensionless variables

$$(x', z') = \left(\frac{x}{L}, \frac{z}{\epsilon L}\right), \quad h' = \frac{h}{\epsilon L}, \quad t' = \frac{t}{L/U}, \tag{2.9a}$$

$$(u', w') = \left(\frac{u}{U}, \frac{w}{\epsilon U}\right), \quad \mu' = \frac{\mu}{\mu_s}, \quad p' = \frac{p}{\mu_s U/L}, \quad T' = \frac{T}{T_s}, \tag{2.9b}$$

where $\epsilon = h_{in}/L \ll 1$ is the aspect ratio of the sheet, and $\mu_s = \mu(T_s)$ is the viscosity at some characteristic temperature T_s which we will choose in §2.3. Substituting our

dimensionless variables into the governing equations (2.3)–(2.8) and dropping primes from the notation, we find that the Stokes equations (2.3) are transformed to

$$u_x + w_z = 0, \tag{2.10a}$$

$$\left(-p + 2\mu u_x\right)_x + \left(\epsilon^{-2}\mu u_z + \mu w_x\right)_z = 0, \tag{2.10b}$$

$$\left(\mu u_z + \epsilon^2 \mu w_x\right)_x + \left(-p + 2\mu w_z\right)_z = 0, \tag{2.10c}$$

where subscripts are used to denote differentiation. The no-flux and no-stress conditions (2.7) become

$$w = \pm\left(h_t + u h_x\right), \tag{2.11a}$$

$$\pm h_x\left(-p + 2\mu u_x\right) = \left(\epsilon^{-2}\mu u_z + \mu w_x\right), \tag{2.11b}$$

$$\pm h_x\left(\mu u_z + \epsilon^2 \mu w_x\right) = \left(-p + 2\mu w_z\right), \tag{2.11c}$$

on $z = \pm h(x,t)$, and the boundary conditions (2.8) at either end of the sheet can be written as

$$u = h = 1 \quad \text{on} \quad x = 0, \tag{2.12a}$$

$$u = D \quad \text{on} \quad x = 1. \tag{2.12b}$$

Here and in later chapters we will exploit small aspect ratios in glass sheets undergoing redraw to derive simplified models. The result for the leading-order velocity and thickness of a flat two-dimensional sheet is well-known (see, for example Howell, 1994), but we give a brief overview of the derivation here because it will be useful for reference in later chapters. Our procedure is to expand variables in powers of ϵ^2, for example

$$u = u_0 + \epsilon^2 u_1 + \cdots \tag{2.13}$$

and so on. Evaluating the in-plane momentum equation (2.10b) at leading order and applying no-stress boundary condition (2.11b), we find that

$$u_0 = u_0(x,t), \tag{2.14}$$

i.e. the leading-order flow is extensional. We then determine an expression for the leading-order pressure by evaluating the transverse momentum equation (2.10c) at leading order and applying no-stress condition (2.11c) to find

$$p_0 = 2\mu w_{0z} = -2\mu u_{0x}, \tag{2.15}$$

where the second equality is obtained by applying conservation of mass (2.10a). We now integrate the mass-conservation equation (2.10a) and in-plane momentum equation (2.10b) across the sheet thickness and apply the free-boundary conditions (2.11)

to obtain equations governing the average flux and tension in the sheet. Evaluating at leading order, we find

$$h_{0t} + (u_0 h_0)_x = 0, \tag{2.16a}$$

$$4\bar{\mu} h_0 u_{0x} = F(t), \tag{2.16b}$$

where $F(t)$ is the uniform tension in the sheet, and

$$\bar{\mu}(x,t) = \frac{1}{2h_0} \int_{-h_0}^{h_0} \mu(x,z,t)\ \mathrm{d}z \tag{2.17}$$

is the viscosity averaged across the sheet thickness. The feed and draw conditions (2.12) evaluated at leading order are

$$u_0 = h_0 = 1 \quad \text{on} \quad x = 0, \tag{2.18a}$$

$$u_0 = D \quad \text{on} \quad x = 1. \tag{2.18b}$$

We solve the equations (2.16)–(2.18) governing the leading-order velocity and thickness in conjunction with equations governing the temperature and hence viscosity of the glass.

2.3 Heat flow

2.3.1 Full dimensional problem

In this section we derive equations governing the leading-order temperature in a thin two-dimensional sheet undergoing redraw by adapting the model of Taroni et al. (2012) for fibre drawing. At very high temperatures, radiative heat transport may be comparable to heat transport via diffusion. We assume that the sheet is optically thick, i.e. that the thickness is large compared with the typical lengthscale for absorption of photons. In this limit, the transport of heat in the glass by radiation may be taken into account by modifying the diffusion coefficient in the advection–diffusion equation using the Rosseland approximation (Myers, 1989), so the flow of heat in the sheet is governed by

$$\rho c_p \left(T_t + \mathbf{u} \cdot \nabla T\right) = \nabla \cdot \left[\left(k_c + \frac{16 n_0^2 \sigma_{SB}}{3\chi} T^3 \right) \nabla T \right], \tag{2.19}$$

where n_0 is the refractive index, χ is the glass absorption coefficient and σ_{SB} is the Stefan–Boltzmann constant. The validity of the optically-thin assumption can be checked by comparing the sheet thickness $2h_{in} = 2 \times 10^{-3}$m with $1/\chi$, where χ is the

estimated absorption coefficient $\chi = 200\text{m}^{-1}$ (Paek and Runk, 1978; Taroni et al., 2012). These values suggest that our assumption may not be physical, but we note that χ depends on both temperature and wavelength (Taroni et al., 2012) and make the assumption that the sheet is optically thick so that we can write down a relatively simple model for heat transport in the sheet.

The flux of heat across the free surfaces $z = \pm h(x,t)$ is balanced by heat exchange with the atmosphere. In the absence of radiative heat transfer, this exchange is modelled using Newton's law of cooling, so the heat flux is proportional to the temperature change across the surface. We assume that the heat absorbed by the air from the glass is redistributed by convection, so that the ambient air temperature T_a in the furnace does not change in time. We modify Newton's law of cooling by including black-body radiation emitted from the sheet surface and absorbed from the furnace to give

$$\mp\left(k_c + \frac{16n_0^2\sigma_{SB}}{3\chi}T^3\right)\frac{\partial T}{\partial z} = \sigma_{SB}\epsilon_r(T^4 - T_f^4) + m_h(T - T_a) \quad \text{on} \quad z = \pm h, \quad (2.20)$$

where $T_f(x)$ and $T_a(x)$ denote furnace temperature and ambient air temperature respectively, ϵ_r is the specific emissivity of the glass and m_h is the heat transfer coefficient. The heat transfer coefficient m_h can be calculated by dividing the thermal conductivity of the air by the lengthscale across which the heat transfer occurs, i.e. the thickness of the thermal boundary layer in the air (which depends on the air flow in the furnace). We also assume the inlet temperature is given by

$$T(0,t) = T_a(0). \quad (2.21)$$

We note that this is similar to the model used by Scheid et al. (2009) for heat flow in a sheet undergoing downdraw, but includes terms describing the flow of heat inside the sheet due to radiation, as well as heat transfer between the sheet and the furnace due to radiation.

2.3.2 Non-dimensionalization

We use the dimensionless variables introduced in (2.9), choosing the maximum furnace temperature as the characteristic temperature T_s. Substituting the dimensionless variables (2.9) into the governing equations and dropping primes from the notation, we find that the heat equation (2.19) is transformed to

$$\epsilon^2\,\text{Pe}\left(\frac{\partial T}{\partial t} + u\frac{\partial T}{\partial x} + w\frac{\partial T}{\partial z}\right) = \epsilon^2\frac{\partial^2}{\partial x^2}\left(T + \gamma_r T^4\right) + \frac{\partial^2}{\partial z^2}\left(T + \gamma_r T^4\right), \quad (2.22)$$

and the boundary condition (2.20) becomes

$$\mp \left(1 + 4\gamma_r T^3\right) \frac{\partial T}{\partial z} = \epsilon\alpha \left(T^4 - T_f^4\right) + \epsilon\beta(T - T_a) \quad \text{on} \quad z = \pm h, \tag{2.23}$$

where T_f and T_a are now the dimensionless furnace temperature and ambient air temperature profiles, and

$$\gamma_r = \frac{4n_0^2\sigma_{SB}T_s^3}{3\chi k_c}, \quad \alpha = \frac{\sigma_{SB}\epsilon_r T_s^3 L}{k_c}, \quad \text{and} \quad \beta = \frac{m_h L}{k_c} \tag{2.24}$$

are dimensionless parameters which may be interpreted as follows. In the glass, the transport of heat is characterized by the Péclet number Pe defined by (2.2) and γ_r, which quantifies the importance of radiative heat transport. At the glass surface, parameters α and β measure heat transfer from/to the sheet due to radiation and air convection respectively. Estimates for these dimensionless parameters are listed in Table 2.1.

Parameter	Symbol	Approximate Value
Péclet number	Pe	140
Bulk radiation coefficient	γ_r	0.9
Surface radiation coefficient	α	6.7
Air transfer coefficient	β	6.0

Table 2.1: Estimates for dimensionless parameters relating to heat flow in glass sheets during redraw (Taroni et al., 2012; Lange, 2013).

We consider a dimensionless temperature profile of the form (Lange, 2013)

$$T_f(x) = \theta_0 + (1 - \theta_0)\left(\frac{1}{1 + \exp[-k(x - x_L)]} + \frac{1}{1 + \exp[k(x - x_R)]} - 1\right), \tag{2.25}$$

and assume $T_a(x) = 0.75T_f(x)$ (Taroni et al., 2012). The coefficient k characterizes the shape of the furnace profile, and in particular how steep the temperature gradients are, while x_L and x_R are the inflection points. A schematic is shown in figure 2.2 illustrating the significance of these values. The dimensionless viscosity is governed by

$$\mu = \exp\left[\frac{1}{\nu}\left(\frac{1}{T - T_c} - \frac{1}{1 - T_c}\right)\right], \tag{2.26}$$

where $\nu = T_s/B$ and $T_c = \hat{T}_c/T_s$. We expect the glass viscosity to vary strongly in the temperature ranges of interest, and hence typically $\nu \ll 1$.

Finally, we specify the inlet temperature $T(0, t)$ and the initial temperature profile $T(x, 0)$. In principle, we should also impose a downstream condition on T at $x = 1$,

but, as we will see below, this is no longer required when our specific thin-sheet approximations are made. Our procedure now is to exploit the small aspect ratio and perform an asymptotic expansion of T. In §2.3.3 we address regimes in which transverse diffusion in the bulk dominates over advection in the direction of drawing, and in §2.3.4 we consider the limit where heat transfer with the surroundings dominates the behaviour at the sheet surface. In §2.3.5 we consider regimes in which transverse diffusion in the bulk is balanced by advection.

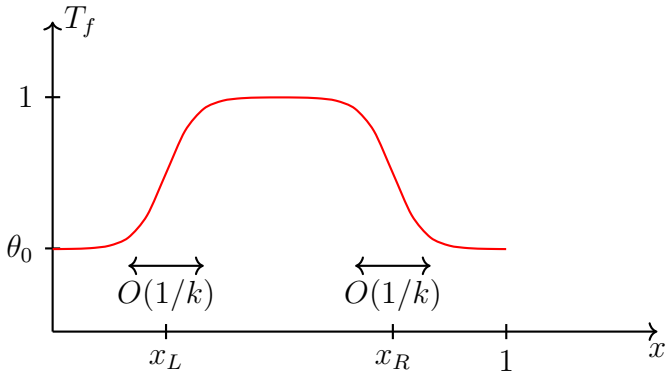

Figure 2.2: Schematic of the furnace profile and the role played by the coefficients θ_0, k, x_L and x_R. The dimensionless temperature profile increase from θ_0 to 1 over a distance of $O(1/k)$ around $x = x_L$, and then decreases from 1 to θ_0 over a distance of $O(1/k)$ around $x = x_R$.

2.3.3 Diffusion-dominated regime

We first consider the asymptotic regime where $\epsilon^2 \ll \epsilon^2\,\mathrm{Pe} \ll 1$ as $\epsilon \to 0$, which corresponds physically to a system in which transverse diffusion and radiation dominate the transport of heat in the bulk of the sheet. We assume $\alpha/(\epsilon\,\mathrm{Pe})$ and $\beta/(\epsilon\,\mathrm{Pe})$ are $O(1)$, so that heat exchange with the surroundings balances advection. We also treat γ_r as $O(1)$ so that radiation contributes to the transport of heat in the bulk, although we will find that γ_r does not enter the problem at leading order in this limit. We expand T in powers of $\epsilon^2\,\mathrm{Pe}$. Solving the heat equation (2.22) at leading order together with the surface heat balance (2.23), we find

$$T_0 = T_0(x,t), \tag{2.27}$$

so that the temperature is uniform across the sheet thickness. Evaluating (2.22) at $O(\epsilon^2\,\mathrm{Pe})$, integrating across the sheet thickness and applying boundary conditions (2.23), we arrive at

$$h_0\left(T_{0t} + u_0 T_{0x}\right) = -\left[a\left(T_0^4 - T_f^4\right) + b\left(T_0 - T_a\right)\right], \tag{2.28}$$

where the dimensionless parameter

$$a = \frac{\alpha}{\epsilon \,\mathrm{Pe}} = \frac{1}{\epsilon} \frac{\sigma_{SB} \epsilon_r T_s^3}{\rho c_p U} \tag{2.29}$$

measures radiative heat transfer from the surface relative to the heat capacity of the sheet, and the reduced Stanton number

$$b = \frac{\beta}{\epsilon \,\mathrm{Pe}} = \frac{1}{\epsilon} \frac{m_h}{\rho c_p U} \tag{2.30}$$

measures heat transfer with the atmosphere relative to heat capacity. The terms on the left-hand side of (2.28) correspond to advection of heat by the glass, and the terms on the right-hand side correspond to heat exchange with the surroundings.

The full model describing fluid and heat flow in the glass sheet in this regime is then given by

$$h_{0t} + (u_0 h_0)_x = 0, \tag{2.31a}$$

$$4\mu(T_0) h_0 u_{0x} = F(t), \tag{2.31b}$$

$$h_0 \left(T_{0t} + u_0 T_{0x}\right) = -\left[a\left(T_0^4 - T_f^4\right) + b\left(T_0 - T_a\right)\right], \tag{2.31c}$$

with boundary conditions

$$h_0 = u_0 = 1, \quad T_0 = T_a(0) \quad \text{on} \quad x = 0, \tag{2.32a}$$

$$u_0 = D \quad \text{on} \quad x = 1. \tag{2.32b}$$

We study the steady-state behaviour by letting $T_{0t} = h_{0t} = 0$. We integrate mass equation (2.31a) and use boundary conditions (2.32a) to find $u_0 h_0 = 1$. Substituting into (2.31c) then yields

$$T_{0x} = -[a(T_0^4 - T_f^4) + b(T_0 - T_a)]. \tag{2.33}$$

This immediately yields the key result that, in a steady state, the leading-order temperature profile in this limit is independent of the thickness and velocity profiles in the sheet. This is in contrast to the case of a fibre (Taroni et al., 2012), in which a square root of the axial velocity is retained in front of the convection term. In this regime, one can first determine the temperature profile in the sheet and then later prescribe the viscosity profile while modelling the flow.

We solve (2.33) numerically using MATLAB's built-in ode solver `ode45`, for two different (a, b) pairs with $T_c = 0.34$ and $\nu = 0.1$ in the viscosity–temperature relation (2.26). In all cases the furnace profile is given by (2.25), with $\theta_0 = 0.8$, $k = 20$,

$x_L = 0.25$ and $x_R = 0.75$, the ambient air temperature is given by $T_a = 0.75T_f(x)$ and the inlet temperature is chosen to be $T_a(0)$. These parameters are chosen for their relevance in industrial processes of interest (Lange, 2013). For heat transfer parameters $a = b = 1$, heat transfer with the atmosphere and furnace are balanced by the advection of the sheet, so that the temperature in the sheet increases and then decreases due to heat exchange with both the atmosphere and the furnace (see figure 2.3). The sheet does not heat up as much as the furnace due to advection of the glass and heat transfer with the atmosphere. In the case $a = 50$, $b = 1$, radiative heat transfer with the furnace dominates, and the temperature profile in the sheet is close to that of the furnace except in a boundary layer near $x = 0$ (cf. §2.3.4). In both cases, the varying temperature profile of the sheet causes the glass viscosity to change by many orders of magnitude as it moves through the furnace. In particular, a dimensionless temperature change of 0.2 corresponds to a typical dimensional temperature change of 260K, which gives rise to a viscosity change of about three orders of magnitude.

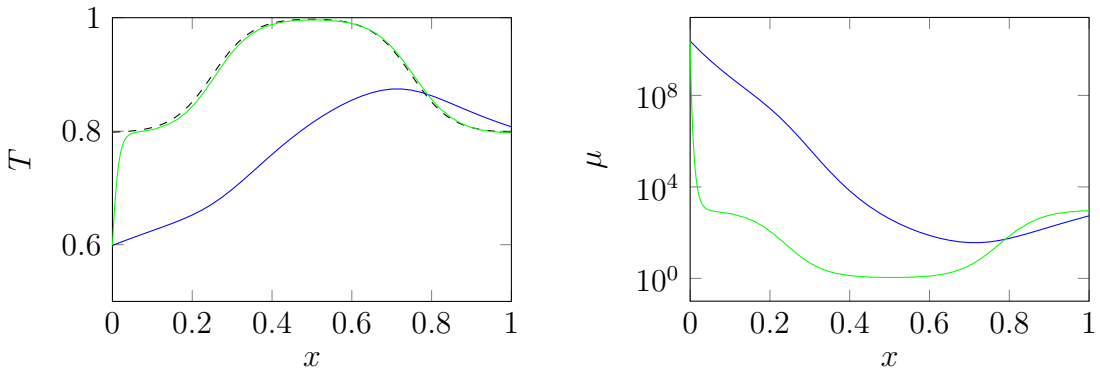

(a) Temperature of glass sheet.

(b) Viscosity of glass sheet

Figure 2.3: (a) Steady-state temperature (2.33) and (b) viscosity (2.26) profiles for the diffusion-dominated limit $\epsilon^2\,\mathrm{Pe} \ll 1$, for furnace profile (2.25) with $\theta_0 = 0.8$, $k = 20$, $x_L = 0.25$ and $x_R = 0.75$, and with viscosity parameters $\nu = 0.1$, $T_c = 0.34$. The blue solid curves correspond to $a = b = 1$, and the green solid curves are for $a = 50$, $b = 1$. The furnace profile (2.25) is shown for comparison as a black dashed curve in (a).

2.3.4 Heat-transfer-dominated limit

We now consider scenarios in which at least one of a or b is large. Physically, this corresponds to a regime in which heat transfer with the surroundings dominates heat flow at the glass–air interface, so that the temperature of the glass is close to that of

the furnace or the atmosphere throughout the process. Formally, we set $b/a = O(1)$ and take the limit $a \to \infty$. At leading order in the small parameter a^{-1}, (2.28) imposes that

$$T_0(x) = \tau(x), \tag{2.34}$$

where $\tau(x)$ is the unique positive solution to the algebraic equation

$$\left(\tau(x)^4 - T_f(x)^4\right) + \frac{b}{a}\left(\tau(x) - T_a(x)\right) = 0. \tag{2.35}$$

We make two key observations about this solution. Firstly, $\tau(x)$ does not depend on u and h, which implies that the temperature profile is not coupled to the flow at leading order, even in the time-dependent case, as expected when heat transfer with the surroundings dominates over convection. Secondly, the solution cannot satisfy a general inlet condition $T_0(0) = T_a(0)$, indicating that this solution is not valid in a boundary layer of $O(a^{-1})$ near $x = 0$ where T_{0x} is large and the temperature of the sheet adjusts rapidly (see figure 2.3).

2.3.5 Advection balances diffusion regime

We now consider the regime $\epsilon^2 \operatorname{Pe} = O(1)$, which corresponds to a situation in which heat transport across the sheet is balanced with convection in the heat equation (2.22) so that temperature gradients across the sheet thickness exist at leading order. The leading-order thickness, velocity and temperature are then governed by

$$h_{0t} + \left(u_0 h_0\right)_x, \tag{2.36a}$$

$$4\bar{\mu}(T_0) h_0 u_{0x} = F(t), \tag{2.36b}$$

$$\overline{\operatorname{Pe}}\left(T_{0t} + u_0 T_{0x} - z u_{0x} T_{0z}\right) = \left[T_0 + \gamma_r T_0^4\right]_{zz}, \tag{2.36c}$$

where $\overline{\operatorname{Pe}} := \epsilon^2 \operatorname{Pe} = O(1)$ and $w_0 = -z u_{0x}$ is obtained from the mass equation (2.10a). The free-surface boundary conditions (2.23) become

$$\mp\left(1 + 4\gamma_r T_0^3\right) T_{0z} = \bar{\alpha}\left(T_0^4 - T_f^4\right) + \bar{\beta}\left(T_0 - T_a\right) \quad \text{on} \quad z = \pm h_0, \tag{2.37}$$

where $\bar{\alpha} = \epsilon\alpha$ and $\bar{\beta} = \epsilon\beta$ are treated as $O(1)$ constants to give a dominant balance, and the feed and draw conditions at leading order are given by

$$h_0 = u_0 = 1, \quad T_0 = T_a(0) \quad \text{at} \quad x = 0, \tag{2.38a}$$

$$u_0 = D \quad \text{at} \quad x = 1. \tag{2.38b}$$

In the time-dependent case an initial condition $T(x, z, 0)$ is also required.

The leading-order temperature T_0 is now a function of two spatial variables, and is coupled to the leading-order velocity u_0 and thickness h_0 on a domain whose shape is not known *a priori*. We seek a steady-state solution and map the governing equations (2.36)–(2.38) to a fixed domain $(x/\overline{\mathrm{Pe}}, z/h_0) \in [0, 1/\overline{\mathrm{Pe}}] \times [0, 1]$. We then use second-order finite differencing in $\eta = z/h_0$ to obtain a series of ODEs in $\xi = x/\overline{\mathrm{Pe}}$. We use `ode15s` in MATLAB to determine the solution for a given value of the tension F, and use `fsolve` to find the correct F for a given draw ratio D.

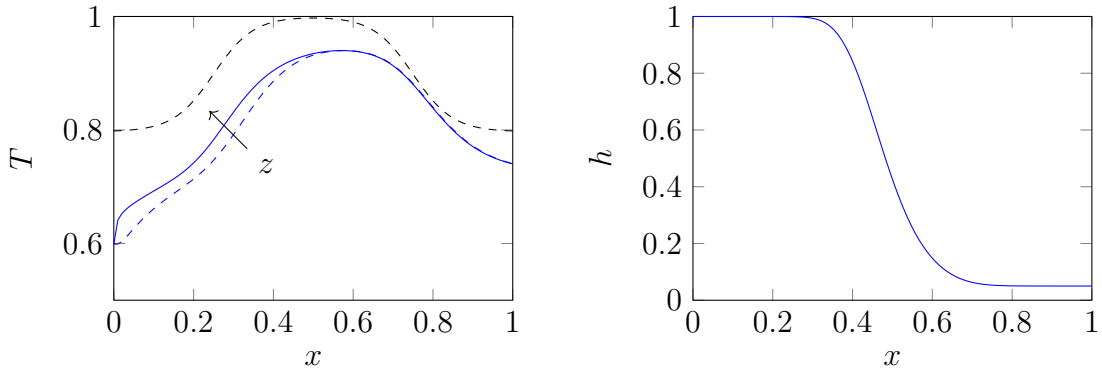

(a) Temperature of glass sheet.

(b) Thickness of glass sheet

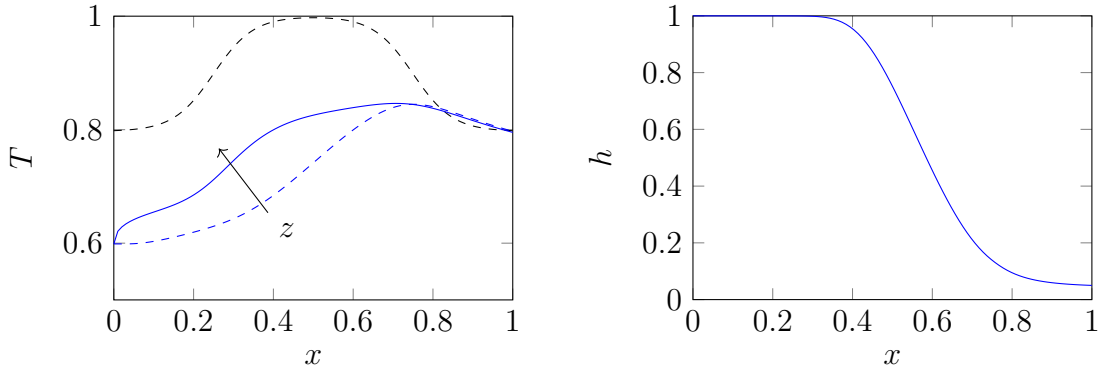

(c) Temperature of glass sheet.

(d) Thickness of glass sheet

Figure 2.4: Temperature and thickness profiles (2.16)–(2.18) and (2.36)–(2.38) of glass sheets for (a), (b) $\overline{\mathrm{Pe}} = 1$ and (c), (d) $\overline{\mathrm{Pe}} = 5$, with $\bar{\alpha} = \bar{\beta} = 5$, $\gamma_r = 1$, $T_c = 0.34$, $\nu = 0.1$ and $D = 20$. The temperature at the sheet edge is shown as a blue solid line and the temperature at the sheet centre as a dashed blue line. The furnace profile (2.25) with $\theta_0 = 0.8$, $k = 20$, $x_L = 0.25$ and $x_R = 0.75$ is shown for comparison as a black dashed line in (a) & (c).

We calculate temperature and flow profiles for two different values of $\overline{\mathrm{Pe}}$ with $\bar{\alpha} = \bar{\beta} = 5$ (see figure 2.4). We observe a temperature difference between the centre

and surface of the sheet. This temperature variation is larger for the $\overline{\mathrm{Pe}} = 5$ case than the $\overline{\mathrm{Pe}} = 1$ case due to the increased role of advection relative to transverse diffusion. In both cases the temperature is approximately uniform across the sheet thickness near the bottom of the furnace, where the sheet is very thin. When $\overline{\mathrm{Pe}} = 1$, the temperature profile experiences only a small delay relative to the furnace profile due to the strong heat transfer between the sheet and the atmosphere and furnace (see figure 2.4a). When the reduced Péclet number $\overline{\mathrm{Pe}}$ is increased to 5 so that advection is increased relative to diffusion, the sheet heats up less and there is a larger spatial delay in the temperature profile relative to the furnace profile (see figure 2.4c). We also observe that the thickness change is localized in the portion of the sheet where temperature is maximized and hence viscosity is minimized (see figure 2.4b and d).

2.3.6 Radiative heat transfer

Redraw is undertaken at sufficiently high temperatures that radiative heat transfer is significant. In this chapter we have assumed the sheet is optically thick, meaning the mean free path of photons is very small compared with the sheet thickness, and radiative heat transfer may be treated as a diffusion-like process. If the glass sheet is so thin that its thickness is comparable with the mean free path, this assumption breaks down, and a new model for radiative heat transfer is required. Modest (2013) determines the fraction of incident radiation absorbed, transmitted and reflected by a window pane using ray tracing. In the limit where the sheet is optically thin, and temperature variations across the sheet thickness can be neglected, we could in principle derive a simplified model for the radiative heat transfer between the semi-transparent glass and its environment by extending the ray-tracing approach of Modest (2013).

Comparing the typical values of glass thickness and absorption coefficient shown in Table 1.1 suggests that a sheet undergoing redraw might be more accurately modelled using an optically-thin assumption. However, in this thesis we use established models for optically thick sheets, and we leave the development of a model for optically thin sheets as future work.

2.3.7 Summary

We consider two regimes for the Péclet number Pe, the first in which transverse heat flow across the sheet dominates over advection, i.e. $\epsilon^2 \ll \epsilon^2 \,\mathrm{Pe} \ll 1$, and the second in which the two effects are balanced, i.e. $\epsilon^2 \,\mathrm{Pe} = O(1)$, and derive a model

for the leading-order temperature profile in each case. These models demonstrate the role that the material parameters and the temperature profile play in determining the thickness and velocity profiles of the sheet. In the case $\epsilon^2 \ll \epsilon^2 \operatorname{Pe} \ll 1$, the steady-state temperature is uniform across the sheet and independent of the flow. The temperature profile follows loosely that of either the furnace or ambient air temperature depending on the relative importance of radiative and conductive heat transfer at the surface. The temperature profile of the sheet exhibits a delay relative to that of the furnace and atmosphere; this is due to advection. If heat transfer with the surroundings dominates and $\epsilon^2 \ll \epsilon^2 \operatorname{Pe} \ll 1$, then there is no delay; the temperature is controlled by the furnace and ambient air temperatures and does not depend on the velocity or thickness of the sheet. This means that by imposing a particular furnace profile we effectively impose a corresponding temperature profile in the sheet. In the case $\epsilon^2 \operatorname{Pe} = O(1)$ the behaviour of the sheet is more complicated, with temperature variations across the sheet observed even at leading order and the temperature and flow profiles fully coupled. The two-dimensional system of equations governing temperature, velocity and thickness are mapped to a rectangular domain and then solved numerically using the method of lines. As in the case when $\epsilon^2 \operatorname{Pe} \ll 1$, the temperature profile in the sheet differs from that of the furnace due to advection, with the size of the delay increasing as the Péclet number increases. The temperature also varies across the sheet thickness, and this variation increases as the Péclet number increases.

For the parameter estimates given in Table 2.1 and the aspect ratio $\epsilon = 8.3 \times 10^{-3}$ given in Table 1.1, we observe that $\epsilon^2 \operatorname{Pe} \ll 1$, and we assume this is the case in the processes modelled in Chapters 3–6. Under this assumption (and assuming the sheet is optically thick), the temperature is approximately uniform across the sheet thickness and, in steady-state conditions, the temperature and hence viscosity profile can be calculated before the thickness and velocity profiles are known, so we can impose a prescribed viscosity profile in the equations governing fluid flow in the sheet. However, the $\epsilon^2 \operatorname{Pe} = O(1)$ case and the optically thin case may be important for other processes and/or material parameters.

2.4 Draw resonance

2.4.1 Background

Pearson and Matovich (1969) propose that cooling stabilizes fibre drawing to thickness perturbations because parts of the fibre that are thinner will cool more and resist

further thinning compared with parts of the fibre that are thicker. In redraw, the sheet undergoes both heating and cooling, so we might expect a combination of stabilizing and destabilizing effects. Myers (1989) finds that the critical draw ratio above which drawing of a cylindrical preform (which is heated and then cooled) becomes unstable to draw resonance is larger than that for isothermal drawing, and that this stabilizing effect increases as the dependence of viscosity on temperature increases. Scheid et al. (2009) find that, during drawing of a thin sheet, the effect of cooling is typically stabilizing, but can actually destabilize the process if heat transfer with the surroundings is very strong. These conflicting results make it difficult to predict how the critical draw ratio will behave for redraw of a thin sheet.

2.4.2 Linear-stability analysis

We determine the stability of a sheet undergoing redraw to thickness perturbations by performing a linear-stability analysis in the industrially relevant limit $\epsilon^2 \ll \epsilon^2\,\mathrm{Pe} \ll 1$. For brevity of notation we drop subscripts denoting expansion in powers of $\epsilon^2\,\mathrm{Pe}$. The steady-state temperature $T^{(0)}$ is governed by (2.33) subject to $T^{(0)}(0) = T_a(0)$, and the steady-state velocity $u^{(0)}$ and thickness $h^{(0)}$ are then given by

$$u^{(0)} = \exp\left(\log(D)\frac{\int_0^x \frac{\mathrm{d}x'}{\mu\left(T^{(0)}\right)}}{\int_0^1 \frac{\mathrm{d}x}{\mu\left(T^{(0)}\right)}}\right), \tag{2.39a}$$

$$h^{(0)} = \exp\left(-\log(D)\frac{\int_0^x \frac{\mathrm{d}x'}{\mu\left(T^{(0)}\right)}}{\int_0^1 \frac{\mathrm{d}x}{\mu\left(T^{(0)}\right)}}\right), \tag{2.39b}$$

while the steady-state tension $F^{(0)}$ in the sheet is

$$F^{(0)} = \frac{4\log(D)}{\int_0^1 \frac{\mathrm{d}x}{\mu\left(T^{(0)}\right)}}. \tag{2.40}$$

We consider a small perturbation to the steady-state solution using the notation

$$F(t) = F^{(0)}[1 + \phi], \tag{2.41a}$$

$$h(x,t) = h^{(0)}(x)[1 + \phi\tilde{h}], \tag{2.41b}$$

$$u(x,t) = u^{(0)}(x)[1 + \phi\tilde{u}], \tag{2.41c}$$

$$T(x,t) = T^{(0)}(x)[1 + \phi\tilde{T}], \tag{2.41d}$$

where the perturbation to the tension $\phi(t) \ll 1$, and all other perturbations are measured relative to this. Taylor-expanding the viscosity (2.26) about the steady-state temperature, we find the perturbed viscosity is given by

$$\mu = \exp\left[\frac{1}{\nu}\left(\frac{1}{T^{(0)}-T_c} - \frac{1}{1-T_c}\right)\right]\left[1 - \phi\tilde{T}\frac{T^{(0)}}{\nu\left(T^{(0)}-T_c\right)^2} + O\left(\phi^2\right)\right]. \tag{2.41e}$$

We substitute (2.41) into (2.31)–(2.32) and neglect terms that are quadratic or higher in ϕ. The resulting equations are thus linear in the perturbation variables, and we consider a single Fourier mode $\phi = e^{\lambda t}$, where λ is the growth rate of the perturbation and the spatial variation is given by $\tilde{h}(x)$, $\tilde{u}(x)$ and $\tilde{T}(x)$. The perturbation variables are governed by

$$\tilde{u}_x = -\frac{u_x^{(0)}}{u^{(0)}}\left(\tilde{h} + \tilde{u} - \tilde{T}\frac{T^{(0)}}{\nu\left(T^{(0)}-T_c\right)^2} - 1\right), \tag{2.42a}$$

$$\tilde{h}_x = -\tilde{u}_x - \lambda h^{(0)}\tilde{h}, \tag{2.42b}$$

$$\tilde{T}_x = -\frac{T_x^{(0)}}{T^{(0)}}\tilde{T} - \left[4a(T^{(0)})^3 + b\right]\tilde{T} - \frac{T_x^{(0)}}{T^{(0)}}(\tilde{u}+\tilde{h}) - \lambda h^{(0)}\tilde{T}, \tag{2.42c}$$

with boundary conditions

$$\tilde{u}(0) = \tilde{h}(0) = \tilde{T}(0) = 0, \tag{2.43a}$$

$$\tilde{u}(1) = 0. \tag{2.43b}$$

This is analogous to the linear-stability analysis carried out by Scheid et al. (2009) for downdraw (taking the limit $\epsilon^2\,\mathrm{Pe} \to 0$ in their analysis), but with an extra term describing radiative heat transfer between the sheet and furnace, and a modified viscosity-temperature relation (2.26). We note that, even though the leading-order steady-state temperature does not depend on the thickness and velocity profiles, the time-dependent temperature is altered by a perturbation to the flow.

After calculating the steady-state temperature, velocity and thickness for a given value of the draw ratio D (following the procedure outlined in §2.3.3 and integrating for u_0 using Chebfun, Driscoll et al., 2014), we solve (2.42) with initial conditions (2.43a) for a given value of λ using MATLAB's built-in solver `ode45`. We use `fsolve` to find the (largest) growth rate λ for which $\tilde{u}(1) = 0$. We then search for the critical draw ratio D_{crit} for which the appropriate eigenvalue λ has zero real part, again using `fsolve`. Beyond this value of D_{crit}, λ has positive real part and the system becomes unstable. We use continuation to provide suitable initial guesses to the nonlinear solver, starting from the result of Renardy (2006) that for $a = b = 0$ the critical draw ratio $D_{crit} \approx 20.2$ with $\lambda \approx 14\mathrm{i}$.

2.4.3 Results

We determine the critical draw ratio above which the sheet is unstable to draw resonance for a range of different heat exchange and viscosity parameters. Since heat exchange with the atmosphere and radiative heat exchange with the furnace are comparable (see table 2.1), we set $a = b$ and vary the Stanton number b for a range of different values of ν, which determines how strongly the viscosity (2.26) depends on the temperature. Neutral stability curves are plotted in figure 2.5 for a redraw process with furnace temperature profile

$$T_f(x) = \theta_0 + (1 - \theta_0)\left(\frac{1}{1 + \exp[-k(x - x_L)]} + \frac{1}{1 + \exp[k(x - x_R)]} - 1\right), \quad (2.44)$$

with $\theta_0 = 0.8$, $k = 20$, $x_L = 0.25$ and $x_R = 0.75$, and $T(0, t) = T_a(0) = 0.75\theta_0$, and $T_c = 0.34$ in (2.26).

In the limit where the heat transfer coefficients satisfy a, $b \ll 1$, the response of the glass temperature to the surroundings is weak and it is almost isothermal, so the critical draw ratio is close to the isothermal result of 20.2 (see figure 2.5). For a, $b \ll 1$, we observe that the critical draw ratio above which the sheet is unstable is *smaller* than in the isothermal case. For moderate values of a and b we observe that the critical draw ratio increases, i.e. the sheet is stabilized during redraw compared with isothermal drawing. When a, $b \gg 1$, heat transfer with the surroundings dominates the heat balance in the sheet and the temperature is only very weakly affected by perturbations to the flow, so the stabilizing effect is decreased. As a, $b \to \infty$, the temperature profile in the sheet does not change and the critical draw ratio approaches a constant value for a given ν.

As ν is decreased the viscosity gradients in the sheet increase (2.26), and the stabilization effect is amplified, as expected (Myers, 1989). We note in particular that for $\nu = 0.5$ and a, $b \in [1, 10]$, the critical draw ratio beyond which the sheet becomes unstable is always in excess of 10^6. For smaller values of ν the solver encounters difficulties with the very large values of D_{crit}, but we expect that the critical draw ratio will be even larger for the industrial value of $\nu = 0.1$. These critical draw ratios are much larger than typical industrial draw ratios of $D = 10^1$–10^2, which explains why draw resonance is not observed in reality in the redraw process (Lange, 2014).

2.4.4 Summary

In this section we investigate the stability of the redraw process for a glass sheet by performing a linear-stability analysis about the steady-state. We derive an eigen-

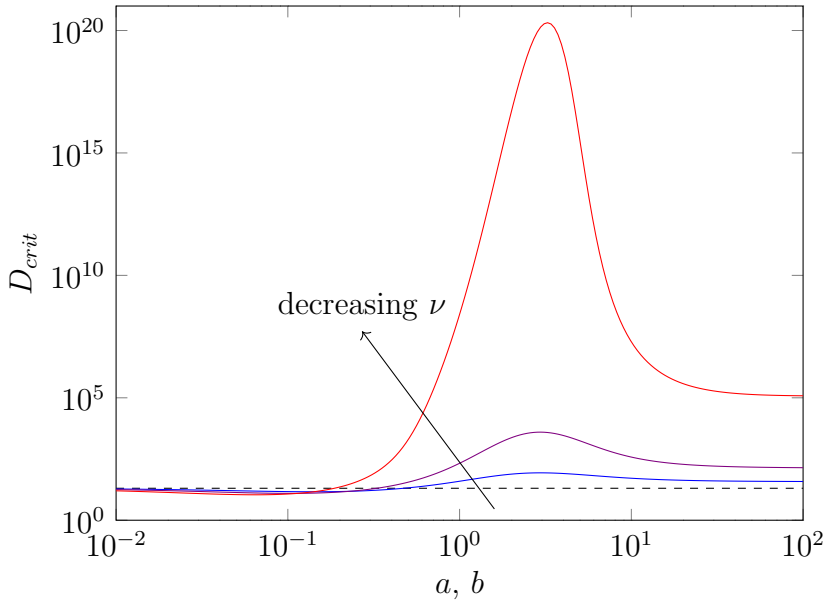

Figure 2.5: Neutral stability curves for the redraw process governed by (2.31)–(2.32) with T_f given by (2.44) for $\nu = 2.0$ (blue), $\nu = 1.0$ (purple) and $\nu = 0.5$ (red).

value problem for perturbations to the steady state, which we solve numerically to determine the critical draw ratio beyond which the sheet is unstable. We present neutral stability curves for typical industrial parameters, and observe that typical critical draw ratios are much larger than typical industrial draw ratios, so that draw resonance is not a concern in the glass sheet redraw process.

2.5 Discussion

In this chapter we investigate the coupling between heat and fluid flow in a two-dimensional thin sheet undergoing redraw, and examine the stability of the sheet to draw resonance. We categorize the heat transfer problem into one of two regimes:

- The aspect ratio ϵ and Péclet number Pe satisfy $\epsilon^2 \ll \epsilon^2\,\mathrm{Pe} \ll 1$, so transverse flow of heat dominates in the bulk, and the heat transfer coefficients α and β satisfy $\alpha/(\epsilon\,\mathrm{Pe})$, $\beta/(\epsilon\,\mathrm{Pe}) = O(1)$ so that advection is balanced by heat exchange with the surroundings. Under steady-state conditions, the leading-order temperature profile does not depend on the velocity or thickness of the sheet.

- $\epsilon^2\,\mathrm{Pe} = O(1)$ so advection of heat by the moving glass balances transverse diffusion, and $\epsilon\alpha$, $\epsilon\beta = O(1)$ so these effects are balanced by heat transfer with the surroundings at the surface. The leading-order temperature varies across

the sheet thickness, and the temperature, velocity and thickness of the sheet are fully coupled.

In industrial processes of interest in this thesis, $\epsilon^2 \ll \epsilon^2 \operatorname{Pe} \ll 1$, so that the temperature profile is independent of the flow. Furthermore, the representative parameters given in Tables 1.1 and 2.1 imply that $\alpha/\epsilon \operatorname{Pe} = 5.7$ and $\beta/\epsilon \operatorname{Pe} = 5.1$, which suggests that heat transfer with the surroundings is more important than advection. Based on these results, in Chapters 3–6 we do not study the flow of heat inside the glass sheets considered, and instead supplement the equations governing the motion with a prescribed viscosity profile.

For an industrial furnace profile in the limit $\epsilon^2 \ll \epsilon^2 \operatorname{Pe} \ll 1$, we determine the critical draw ratio above which a sheet undergoing redraw becomes unstable to draw resonance. For the viscosity profile and heat transfer coefficients relevant in this thesis, the critical draw ratios are much larger than draw ratios typically used. Furthermore, draw resonance has not been observed in any of the numerous numerical and laboratory experiments carried out into the redraw process, so we can safely assume that that draw resonance is not a concern in the redraw processes we consider in the remainder of this thesis.

Chapter 3

Redraw through a short heater zone

3.1 Introduction

One method used by Schott AG to manufacture very thin glass sheets (thickness $\sim$ 100μm) is to redraw prefabricated glass blocks through very short heater zones (Buellesfeld et al., 2014). This method allows sheets to be redrawn without substantial loss of width, and with essentially uniform final thickness except for in small regions near the edges. Near the edge, the sheet thickness is typically larger than in the bulk; we refer to this phenomenon as *edge thickening*. A sample measured thickness profile is plotted in figure 3.1(a). It is evident that after redraw the cross-section is far from uniform, with the edges thicker than the centre by a factor of around six. The presence of such thick edges may result in breakage when the sheet is rolled up for storage and transportation, and it is therefore desirable to understand and eliminate this behaviour. Figure 3.1(b) shows the results of simulation experiments (Lange, 2013, details may be found in §3.5). Again the edges are much thicker than the centre, and, apart from the case where the heater zone is longer than the sheet half-width, there is a large region in the centre of the sheet with approximately uniform thickness.

A model for the viscous flow of a three-dimensional sheet characterized by its small aspect ratio of thickness to typical in-plane lengthscales is derived by Howell (1994, 1996), who used this as a model for the float glass process. This thin-sheet model has also been used by Filippov and Zheng (2010) to study the redraw process. Studies of the redraw process, for example by Filippov and Zheng (2010), as well as experimental results such as those shown in figure 3.1, show that both the width and the thickness of the sheet are affected by stretching and that the final thickness of the sheet is typically non-uniform. Furthermore, numerical simulations using Polyflow (Lange, 2013)

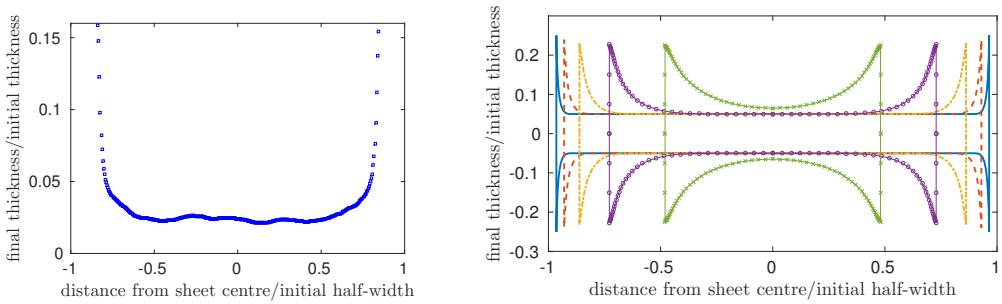

(a) (b)

Figure 3.1: (a) Thickness profile of a glass sheet drawn with draw ratio draw speed/feed speed = 38 at Schott AG plant, (b) Numerical solutions calculated at Schott AG of final sheet cross-section for draw ratio 20 and various heater zone lengths: the ratios of heater zone length to initial sheet half-width are 0.1 (blue line), 0.2 (red dashed), 0.4 (yellow dot-dashed), 0.8 (purple circles) and 1.6 (green crosses).

show that when the heater zone is very short, these non-uniformities are confined to neighbourhoods of the sheet edges, as shown in figure 3.1(b).

The same edge-thickening phenomenon has been observed in the related problem of casting of polymer films, for example by Dobroth and Erwin (1986) and Silagy et al. (1999). Dobroth and Erwin (1986) investigate the relative importance of die swell, surface tension and edge stress effects in the edge-thickening phenomenon. They determine that edge stress effects dominate the behaviour and, by assuming that the centre of the sheet is subject to plane strain while the edge experiences uniaxial stress, propose the relationships

$$\frac{\text{final bulk thickness}}{\text{initial bulk thickness}} = \frac{1}{\text{draw ratio}}, \tag{3.1a}$$

and

$$\frac{\text{final edge thickness}}{\text{initial edge thickness}} = \frac{1}{\sqrt{\text{draw ratio}}}, \tag{3.1b}$$

where the draw ratio is the ratio of the sheet speed at the draw rollers to the preform speed. D'Halewyu et al. (1990) and Silagy et al. (1999) use the thin-sheet model to describe casting of a polymer film of uniform temperature, and show numerically that this model does indeed predict the experimentally observed non-uniform thickness profiles. Other studies (for example, Debbaut et al., 1995; Beaulne and Mitsoulis, 1999) include viscoelasticity to model polymer film casting more accurately. Smith and Stolle (2000) use numerical simulations to show that edge thickening can be reduced by using a non-rectangular extrusion die.

In this chapter we develop a model for the redraw process in the limit where the heater zone is short compared with the sheet width, and predict and quantify the phenomenon of edge thickening. In §§3.2–3.3 we exploit several features of the problem to facilitate our analysis and gain insight. First we use the fact that the Reynolds number is typically small ($\mathrm{Re} \lesssim 10^{-4}$) to neglect inertia and model the flow using the three-dimensional Stokes equations. Second, we exploit the geometrical property that the preform thickness is small compared with the heater zone length, which in turn is short compared with the preform width. (We use the terms thickness, width and length as defined in figures 1.1 and 3.2). We use asymptotic analysis to examine the structure of the flow and capture the one-dimensional behaviour in the bulk, with two-dimensional behaviour in a boundary layer at the sheet edge. This represents an advance on previous work by authors such as d'Halewyu et al. (1990), Silagy et al. (1999) and Filippov and Zheng (2010), as we demonstrate that the distance over which edge thickening persists scales with the length of the heater zone, and that the edge thickening phenomenon is described by a canonical two-dimensional boundary layer problem. Only the boundary-layer problem requires numerical solution, and our approach thus removes the numerical stiffness associated with the large separation of lengthscales in the full free-boundary problem.

In §3.3.2 we present numerical solutions to this boundary-layer problem. In our solutions, the final thicknesses at the centre and at the edge of the sheet depend on the draw ratio D(= draw speed/feed speed) through the universal power laws (3.1), as proposed by Dobroth and Erwin (1986). The corresponding exponents are explained in §3.4 through an exact conservation property of the thin-sheet equations at a stress-free edge, thus providing a more systematic justification than that of Dobroth and Erwin (1986). In §3.5 we compare the predictions of our model with numerical solutions to the full three-dimensional problem and with experimental data. In §3.6 we extend the idea of Smith and Stolle (2000) of modifying the preform shape with the aim of producing a perfectly rectangular final cross-section, by presenting and illustrating a simple method for calculating the exact preform shape required. In §3.7 we discuss the validity of our main assumptions (namely that heat flow is decoupled from fluid flow and that surface tension is not important) and the extension of the model to include a fully coupled temperature equation and surface-tension effects. Finally, in §3.8 we discuss our findings and their implications.

3.2 Mathematical model

3.2.1 Full dimensional problem

We use Cartesian coordinates $\boldsymbol{x} = (x, y, z)$, with the x-axis aligned with the direction of drawing, the y-axis spanning the width of the sheet as it enters the heater zone, and z in the transverse direction as shown in figure 3.2. We consider a planar sheet of glass, of width $2b(x)$ in the y-direction and thickness $2h(x, y)$ in the z-direction, undergoing redraw through a furnace of length d in the x-direction. The sheet enters the heater zone across the $x = 0$ plane and exits through the $x = d$ plane. We assume that the mid-surface of the sheet is flat so that the glass surfaces are located at $z = \pm h(x, y)$ for $-b(x) < y < b(x)$ and $0 < x < d$. In industrial processes of interest, the Reynolds number is small, the sheet is thin compared with other lengthscales, and the heater zone is short compared with the preform width. We will exploit these features to derive a simplified model governing the behaviour of the sheet.

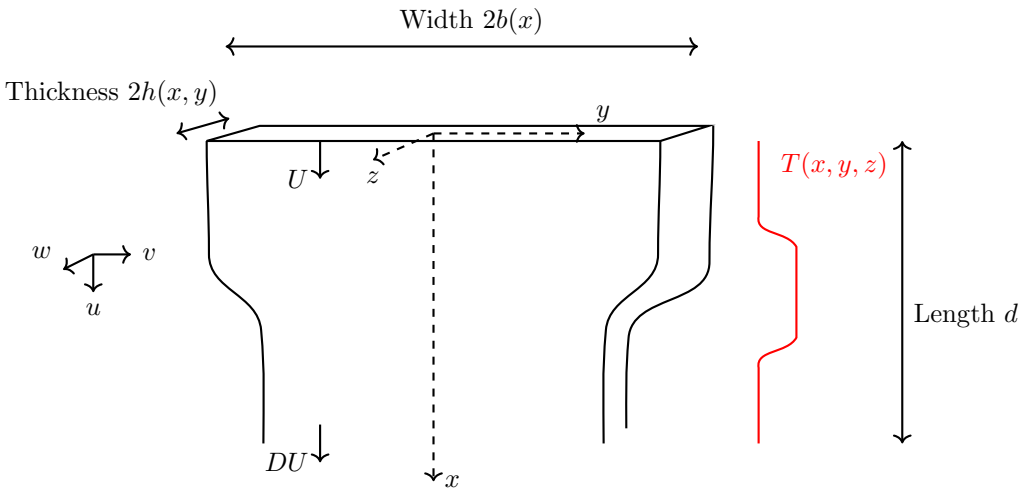

Figure 3.2: Three-dimensional glass sheet with width $2b(x)$ and thickness $2h(x, y)$ undergoing redraw in the x-direction subject to an imposed temperature profile $T(x, y, z)$. The sheet has velocity $\boldsymbol{u} = (u, v, w)$, with feed speed $u = U$ and draw speed $u = DU$.

We assume that the flow is steady and governed by the Stokes equations

$$\nabla \cdot \boldsymbol{u} = 0, \quad \nabla \cdot \boldsymbol{\sigma} = \boldsymbol{0}. \tag{3.2}$$

Here $\boldsymbol{u} = (u, v, w)$ is the velocity vector, $\nabla = (\partial/\partial x, \partial/\partial y, \partial/\partial z)$ and

$$\boldsymbol{\sigma} = -p\mathbb{I} + \mu\left(\nabla \boldsymbol{u} + (\nabla \boldsymbol{u})^T\right) \tag{3.3}$$

is the stress tensor, with p denoting the pressure, μ the viscosity, and $\mathbb{I}$ the identity matrix.

We initially consider a preform with rectangular cross-section. The preform has half-thickness h_{in} and half-width b_{in}, and is pushed slowly into the heater zone by the preform clamp, moving at speed U, so that the inlet conditions read

$$h = h_{in}, \quad b = b_{in}, \quad u = U, \quad v = 0 \tag{3.4}$$

at $x = 0$. Over the length of the heater zone the speed is increased by a factor of the draw ratio D by the use of draw rollers at the bottom of the heater zone, so that the final velocity is given by

$$u = DU, \quad v = 0 \tag{3.5}$$

at $x = d$. The sheet moves like a rigid body upstream and downstream of the heater zone. In principle one should also specify boundary conditions at $x = 0$ and $x = d$ for w, the velocity out of the xy-plane, such as

$$w = 0 \quad \text{on} \quad x = 0,\ d. \tag{3.6}$$

However, we will see later that this is no longer necessary when a thin-sheet approximation is made. On the free surfaces $z = \pm h(x, y)$, we impose no-flux and no-stress conditions

$$\boldsymbol{u} \cdot \hat{\boldsymbol{n}} = 0, \tag{3.7a}$$

$$\boldsymbol{\sigma} \cdot \hat{\boldsymbol{n}} = \boldsymbol{0}, \tag{3.7b}$$

where $\hat{\boldsymbol{n}}$ is the unit normal to the surface. We neglect the effect of surface tension since the capillary number $\mathrm{Ca} = \mu_s U/\gamma \gg 1$, where γ is the surface-tension coefficient at the glass–air interface and μ_s is the minimal viscosity (here the viscosity varies along the sheet as a function of temperature; we will discuss this in more detail in §3.3.2). We note that this assumption will break down in a very small region near the edge of the sheet, and we will discuss the effects of surface tension further in §3.7.

3.2.2 Non-dimensionalization

We define two aspect ratios

$$\epsilon = \frac{\text{preform thickness}}{\text{preform width}} = \frac{2h_{in}}{2b_{in}}, \tag{3.8a}$$

$$\delta = \frac{\text{length of heater zone}}{\text{preform half-width}} = \frac{d}{b_{in}}. \tag{3.8b}$$

In manufacture of glass sheets, the sheet thickness is invariably much smaller than the length and the width, and it follows that both $\epsilon \ll 1$ and $\epsilon \ll \delta$ must be satisfied. In this chapter, we focus on industrial processes where the heater zone is short relative to the sheet width, and therefore we assume that the two parameters ϵ and δ satisfy

$$0 < \epsilon \ll \delta \ll 1. \tag{3.9}$$

We now non-dimensionalize the system and exploit these two small parameters by introducing

$$(x', y', z') = \left(\frac{x}{\delta b_{in}}, \frac{y}{b_{in}}, \frac{z}{\epsilon b_{in}}\right), \quad (b', h') = \left(\frac{b}{b_{in}}, \frac{h}{\epsilon b_{in}}\right), \tag{3.10a}$$

$$(u', v', w') = \left(\frac{u}{U}, \frac{v}{\delta U}, \frac{w}{\epsilon U}\right), \tag{3.10b}$$

$$p' = \frac{\delta b_{in}}{\mu_s U} p, \quad T' = \frac{T}{T_s}, \quad \mu' = \frac{\mu}{\mu_s}. \tag{3.10c}$$

Here T_s is the maximum temperature attained by the glass inside the furnace, and $\mu_s = \mu(T_s)$. Inserting these new variables into the governing equations (3.2) and dropping the primes from the notation yields

$$u_x + \delta^2 v_y + \delta w_z = 0, \tag{3.12a}$$

$$\epsilon^2(-p + 2\mu u_x)_x + \epsilon^2\delta^2 \left(\mu u_y + \mu v_x\right)_y + \left(\delta^2 \mu u_z + \epsilon^2 \delta \mu w_x\right)_z = 0, \tag{3.12b}$$

$$\epsilon^2 \left(\mu u_y + \mu v_x\right)_x + \epsilon^2 \left(-p + 2\delta^2 \mu v_y\right)_y + \left(\delta^2 \mu v_z + \epsilon^2 \delta \mu w_y\right)_z = 0, \tag{3.12c}$$

$$\left(\delta \mu u_z + \epsilon^2 \mu w_x\right)_x + \delta^2 \left(\delta \mu v_z + \epsilon^2 \mu w_y\right)_y + \left(-\delta p + 2\delta^2 \mu w_z\right)_z = 0, \tag{3.12d}$$

where subscripts denote differentiation.

The kinematic and dynamic conditions (3.7) become

$$\pm \left(u h_x + \delta^2 v h_y\right) = \delta w, \tag{3.13a}$$

$$\pm\epsilon^2 h_x \left(-p + 2\mu u_x\right) \pm \epsilon^2\delta^2 h_y \left(\mu u_y + \mu v_x\right) = \delta^2 \mu u_z + \epsilon^2 \delta \mu w_x, \tag{3.13b}$$

$$\pm\epsilon^2 h_x \left(\mu u_y + \mu v_x\right) \pm \epsilon^2 h_y \left(-p + 2\delta^2 \mu v_y\right) = \delta^2 \mu v_z + \epsilon^2 \delta \mu w_y, \tag{3.13c}$$

$$\pm h_x \left(\delta \mu u_z + \epsilon^2 \mu w_x\right) \pm \delta^2 h_y \left(\delta \mu v_z + \epsilon^2 \mu w_y\right) = -\delta p + 2\delta^2 \mu w_z, \tag{3.13d}$$

on $z = \pm h(x, y, t)$. Finally, our choice of non-dimensionalization yields the feed and draw conditions

$$u = h = b = 1, \quad v = 0 \quad \text{on} \quad x = 0, \tag{3.14a}$$

$$u = D, \quad v = 0 \quad \text{on} \quad x = 1. \tag{3.14b}$$

3.2.3 Thin-sheet limit

We now consider the thin-sheet limit $\epsilon \to 0$, with δ held fixed for the moment. The details of the asymptotic analysis may be found in Howell (1994, 1996) and are omitted here. The leading-order flow is found to be extensional, meaning that the in-plane velocity is uniform across the sheet, i.e.,

$$u = u(x, y), \qquad v = v(x, y). \tag{3.15}$$

Net conservation of mass and momentum then yield the leading-order governing equations

$$(uh)_x + \delta^2 (vh)_y = 0, \tag{3.16a}$$

$$\left(4\bar{\mu}hu_x + 2\delta^2\bar{\mu}hv_y\right)_x + \delta^2\left(\bar{\mu}hu_y + \bar{\mu}hv_x\right)_y = 0, \tag{3.16b}$$

$$\left(\bar{\mu}hu_y + \bar{\mu}hv_x\right)_x + \left(2\bar{\mu}hu_x + 4\delta^2\bar{\mu}hv_y\right)_y = 0, \tag{3.16c}$$

where

$$\bar{\mu}(x, y) = \frac{1}{2h}\int_{-h}^{h} \mu(x, y, z)\mathrm{d}z \tag{3.17}$$

is the viscosity averaged across the sheet thickness.

We assume symmetry about the x-axis and hence impose the conditions

$$v = u_y = 0 \quad \text{at } y = 0. \tag{3.18}$$

Net conservation of mass and momentum at the edge of the sheet lead to the boundary conditions

$$\delta^2 v = ub'(x), \tag{3.19a}$$

$$\delta^2\left(u_y + v_x\right) = \left(4u_x + 2\delta^2 v_y\right)b'(x), \tag{3.19b}$$

$$2u_x + 4\delta^2 v_y = \left(u_y + v_x\right)b'(x) \tag{3.19c}$$

at $y = b(x)$. The feed and draw conditions are

$$u = h = b = 1, \quad v = 0 \quad \text{on} \quad x = 0, \tag{3.20a}$$

$$u = D, \quad v = 0 \quad \text{on} \quad x = 1. \tag{3.20b}$$

We note that (3.16)–(3.20) are equivalent to the equations used by Filippov and Zheng (2010) to model redraw, when gravity is neglected from their model

The equations (3.16)–(3.20) should be supplemented by an equation for the thickness-averaged viscosity $\bar{\mu}$, which depends on the glass temperature. In principle the temperature and flow of the glass are coupled. However, in Chapter 2 we presented a

model for the coupled temperature and flow in a two-dimensional thin sheet and found that, in the industrially relevant limit where one or both of α, β (defined by 2.24) are large, the temperature is uniform across the sheet thickness and is not affected by the thickness or velocity of the sheet. We therefore assume that the viscosity is a known function, and does not vary across the sheet thickness. A full discussion of this assumption and the role of heat transfer in the system will be presented in §3.7.

3.2.4 Short-heater-zone limit

We now apply the additional industrially relevant asymptotic limit $\delta \ll 1$, in which the heater-zone length is short relative to the preform width (but still much larger than the preform thickness), by writing the variables u, v, h and b as asymptotic expansions in δ^2, i.e.,

$$\psi = \psi_0 + \delta^2 \psi_1 + \cdots . \tag{3.21}$$

Note that the subscripts refer to an expansion in δ about the leading-order (in ϵ) solution.

In addition to our assumption that the temperature profile in the sheet is prescribed, we will restrict our consideration to temperature profiles that vary along the length of the sheet only, i.e., $T = T(x)$, and $\bar{\mu} = \mu(x)$. This is valid provided the furnace temperature is constant in the y-direction.

At leading order, conservation of mass (3.16a) and x-momentum (3.16b) with boundary conditions (3.20) imply that the axial velocity and film thickness are independent of y, i.e.,

$$u_0 = u_0(x), \qquad h_0 = h_0(x), \tag{3.22}$$

and satisfy the familiar one-dimensional model (2.39)

$$u_0(x) = \exp\left(\log(D)\frac{\int_0^x \mu^{-1}\mathrm{d}s}{\int_0^1 \mu^{-1}\mathrm{d}s}\right), \qquad h_0(x) = \frac{1}{u_0(x)}. \tag{3.23}$$

The y-component of momentum conservation (3.16c) at leading order yields an equation for v_0. Integrating twice and applying homogeneous Dirichlet conditions (3.20), we find that the leading-order lateral velocity is zero:

$$v_0 \equiv 0. \tag{3.24}$$

Continuing to $O(\delta^2)$, one can quickly find that the first corrections u_1, h_1, v_1 are all zero and, indeed, that all algebraic corrections are zero. Hence the leading-order outer solution (3.23)–(3.24) is exponentially accurate in δ.

Finally, evaluating the no-flux condition (3.19a) we see that $b(x) \sim 1$ at leading order, while the no-stress conditions (3.19b)–(3.19c) can only be satisfied by (3.23), (3.24) in the trivial case of no stretching (i.e., $D = 1$). From this result we infer that there must be a boundary layer in the region near $y = b(x)$, in which a different scaling is required.

3.3 Boundary-layer behaviour

3.3.1 Rescaled problem

To satisfy the free-boundary conditions on $y = b(x)$ we must introduce a boundary layer at the sheet edge where the fluid behaviour changes rapidly. We therefore perform the rescaling

$$b = 1 + \delta B, \qquad y = 1 + \delta Y, \qquad v = \delta^{-1} V, \tag{3.25}$$

so that the free surface is now located at $Y = B(x)$ and the outer flow (3.23) is recovered as $Y \to -\infty$. The quantity δB may be interpreted as the displacement of the preform edge in the y-direction from its position at the top of the heater zone. The rescaling of the lateral velocity v reflects the expectation that the velocity components should be comparable in the boundary layer.

The conservation laws (3.16) become

$$(uh)_x + (Vh)_Y = 0, \tag{3.26a}$$

$$(4\mu h u_x + 2\mu h V_Y)_x + (\mu h u_Y + \mu h V_x)_Y = 0, \tag{3.26b}$$

$$(\mu h u_Y + \mu h V_x)_x + (2\mu h u_x + 4\mu h V_Y)_Y = 0, \tag{3.26c}$$

and we recover the fully two-dimensional problem, as expected. The feed and draw conditions are

$$u = h = 1, \quad V = B = 0 \quad \text{on} \quad x = 0, \tag{3.27a}$$

$$u = D, \quad V = 0 \quad \text{on} \quad x = 1, \tag{3.27b}$$

and the boundary conditions (3.19) on the sheet edge $Y = B(x)$ are now given by

$$V = u B_x, \tag{3.28a}$$

$$u_Y + V_x = (4u_x + 2V_Y) B_x, \tag{3.28b}$$

$$2u_x + 4V_Y = (u_Y + V_x) B_x. \tag{3.28c}$$

This system is closed by matching to the outer solution (3.23)–(3.24), i.e.,

$$u \to u_0(x), \quad V \to 0, \quad h \to 1/u_0(x) \qquad \text{as } Y \to -\infty. \tag{3.29}$$

3.3.2 Numerical solution

We now present numerical solutions of the boundary-layer problem (3.26)–(3.29) obtained using the finite-element software FEniCS (Logg and Wells, 2010; Logg et al., 2012). To enable solution with FEniCS, the domain is transformed from $(X, Y) \in [0, 1] \times (-\infty, B(X)]$ onto a fixed rectangle $[0, 1] \times [-L, 0]$, with $L \gg 1$. We use a regular triangular mesh with Lagrange elements of degree 1, and the resulting nonlinear problem is solved using a built-in Newton solver. For the case when $\mu = 1$ and $D = 20$, we find that 300×260 nodes with $L = 3.5$ suffice to give solutions correct to two significant figures.

For the moment we focus on the case of constant viscosity $\mu \equiv 1$, so that the solution depends on a single parameter D. A typical spatially varying viscosity profile used in industrial simulations will be considered in §3.5.

In figure 3.3 we show the thickness profile in the boundary later for a sheet redrawn at draw ratio $D = 20$. As the sheet moves through the heater zone (x increasing), we see that the cross-sectional area decreases, as expected, as the velocity increases. We also observe a departure from uniform thickness. The location of the sheet edge moves inwards and as a result the thickness at the edge increases relative to the bulk. In §3.4 we will argue that this is a universal consequence of conservation of mass near a stress-free surface.

In figure 3.4 we show the velocity profile in the sheet, as well as the evolution of the sheet edge, during drawing at $D = 20$. Comparing figures 3.3 and 3.4 we see that the sheet necks inwards in both the y- and z-directions during drawing. Far from the sheet edge, the solution approaches the one-dimensional far-field behaviour (3.29), which depends only on x, and the velocity vector points strictly in the x-direction. However, close to the sheet edge the velocity points inwards, and this results in the necking in of the sheet as well as the observed difference between the edge and bulk thicknesses.

Finally, we ask how this behaviour depends on the draw ratio D. Since draw resonance is not a concern (see §2.4), it is sensible to study (3.26)–(3.29) even for large D. Figure 3.5(a) shows the final edge displacement $B(1)$ as a function of draw ratio; as D increases so too does the magnitude of the change in edge position, with the rate of change decreasing for large draw ratios. Figure 3.5(c) shows the final sheet thickness $h(1, Y)$ at varying distances from the sheet edge. We observe that the difference between the edge and bulk thickness increases with increasing draw ratio. We also note the appearance of two power laws as predicted by Dobroth and Erwin (1986) and given in (3.1). Far from the edge the final thickness scales with $1/D$; this

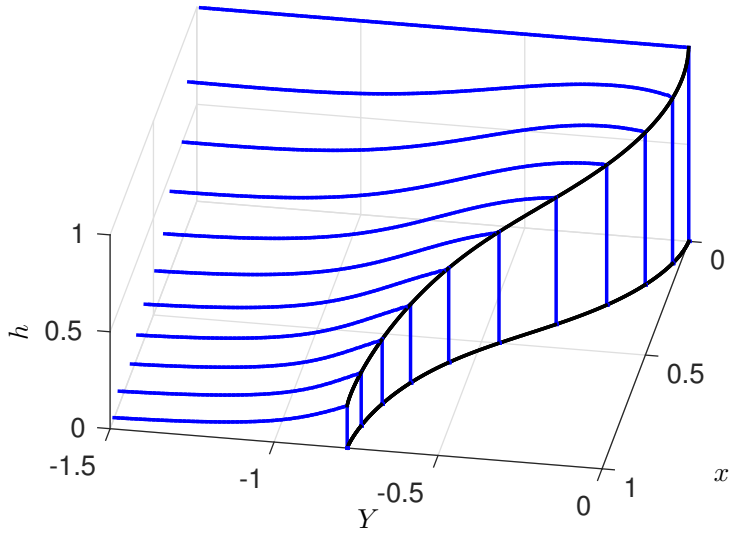

Figure 3.3: Thickness profiles inside the boundary layer for a constant-viscosity sheet drawn at a draw ratio $D = 20$.

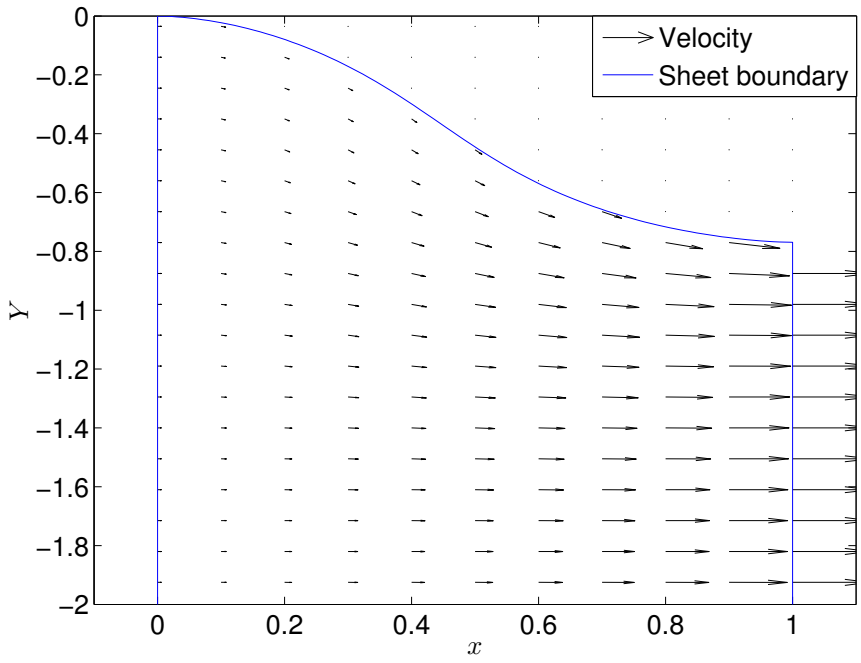

Figure 3.4: Velocity profile inside the boundary layer of a sheet undergoing redraw at draw ratio $D = 20$ under constant viscosity conditions, with free surface $Y = B(x)$ shown.

corresponds to the one-dimensional behaviour described by (3.23). Close to the edge the final thickness scales with $1/\sqrt{D}$; we discuss this further in §3.4. We also note that as D grows large small oscillations occur as the thickness profile decays away from the sheet edge; the first minimum is highlighted in figure 3.5(b) for a draw ratio of 80.

3.4 Edge behaviour

We investigate the phenomenon of edge thickening in a more general setting by returning to the governing equations (3.16)–(3.20) and considering the behaviour of the fluid at the free surface $y = b(x)$. Close to this free surface it is natural to use a local curvilinear coordinate system; we let s parametrize arc-length along the free surface and n be the normal distance from the free surface, so that

$$\tilde{\boldsymbol{x}} = (\delta x, y) = s\hat{\boldsymbol{t}} + n\hat{\boldsymbol{n}}, \tag{3.30}$$

where $\hat{\boldsymbol{t}}$ and $\hat{\boldsymbol{n}}$ are the unit tangent and normal to the sheet edge. We also define tangential and normal velocity components u_s and u_n respectively by

$$\tilde{\boldsymbol{u}} = (u, \delta v) = u_s(s, n)\hat{\boldsymbol{t}} + u_n(s, n)\hat{\boldsymbol{n}}. \tag{3.31}$$

The factors of δ in the definitions (3.30) and (3.31) account for the fact that x and y variables were non-dimensionalized using different scalings.

The conservation-of-mass equation (3.16a) may now be rewritten as

$$\tilde{\nabla} \cdot (h\tilde{\boldsymbol{u}}) = 0. \tag{3.32}$$

In terms of the new coordinates, the kinematic boundary condition (3.19a) and the normal component of the no-stress condition (3.19b)–(3.19c) at the sheet edge take the forms

$$u_n = 0, \quad \frac{\partial u_s}{\partial s} + 2\frac{\partial u_n}{\partial n} = 0 \quad \text{at } n = 0. \tag{3.33}$$

Now, by evaluating equation (3.32) at the free surface $n = 0$ and using the boundary conditions (3.33), we obtain the exact relation

$$\frac{\partial}{\partial s}\left(h\sqrt{u_s}\right) = 0 \quad \text{at } n = 0. \tag{3.34}$$

Thus the product of the sheet thickness and the square root of the fluid speed at the sheet edge is a conserved quantity. From the inlet conditions $h = u = u_s = 1$ at

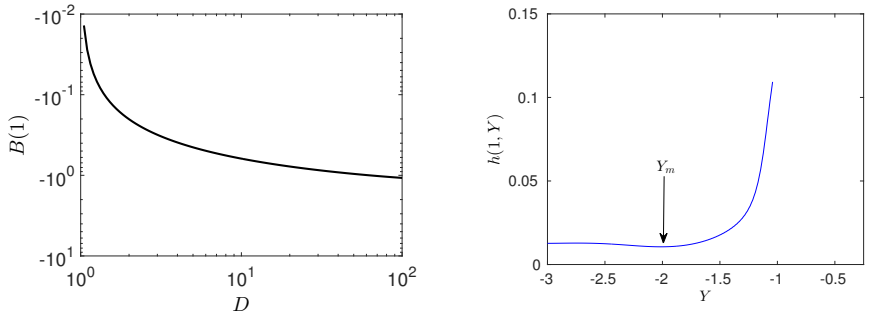

(a) (b)

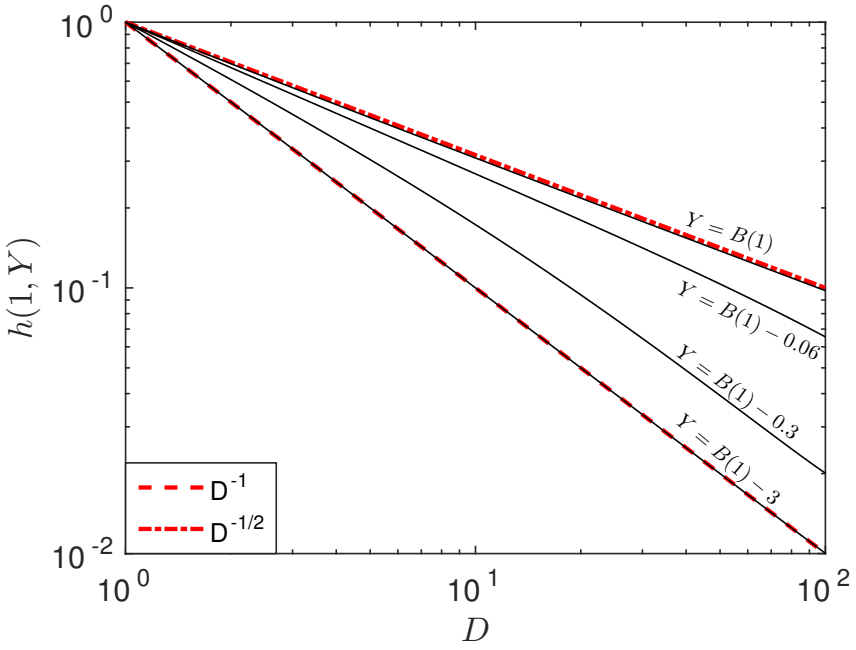

(c)

Figure 3.5: Dependence of sheet behaviour on draw ratio D : (a) Scaled displacement of sheet edge at the bottom of the heater zone $B(1)$ as a function of D, (b) final thickness profile for draw ratio 80, with a local minimum in thickness at Y_m, (c) final sheet thickness as a function of D at varying distances from the sheet edge $Y = B(x)$ are shown in black, while plots of D^{-1} (dashed line) and $D^{-1/2}$ (dot-dashed) are shown in red.

$x = 0$ and outlet condition $u = u_s = D$ at $x = 1$, we deduce that the final sheet edge thickness is given by

$$h\big(1, b(1)\big) = 1/\sqrt{D}. \tag{3.35}$$

Dobroth and Erwin (1986) give the following simple physical argument for this result. In the direction of drawing, x, the elongation ratio is equal to the draw ratio D. At the edge of the sheet there is no stress either across the sheet thickness or across the sheet width, so the elongation ratios in these directions must be the same and equal to $1/\sqrt{D}$. In contrast, the outer solution (3.23) yields $h(1, y) \sim 1/D$ at the centre of the sheet, since the behaviour here is equivalent to that of an infinitely wide sheet, with no flow in the y-direction. These are exactly the power-law behaviours observed in figure 3.5(c). It is thus clear that the final sheet thickness will always be larger at the edges than in the middle, with the disparity increasing as the draw ratio increases. Hence we provide a systematic derivation of the same power-law relationships proposed by Dobroth and Erwin (1986) for casting of a polymer film.

It is worth emphasizing that the relation (3.35) is *exact* for any thin viscous sheet under tension with no stress at the edges. In contrast, the one-dimensional outer solution (3.23) is valid only in the limit $\delta \to 0$, i.e., in the regime where the heater zone is short compared with the sheet width. In the regime where $\delta = O(1)$, the inward retraction of the edge would affect the whole sheet and cause the thickness at the centre to be larger than the one-dimensional result $h \sim 1/D$. At the other extreme where $\delta \gg 1$, so the sheet is long and narrow, the edge-thickening effect would be eliminated at leading order: the sheet thickness would remain approximately uniform and scale with $1/\sqrt{D}$ everywhere (Howell, 1994). We address this scenario in Chapter 4.

3.5 Comparison with three-dimensional model and with redraw data

We now test the validity of our model by comparing our predictions with numerical solutions to the full three-dimensional problem (3.2)–(3.7) and with measurements from a redraw plant at Schott AG. We impose a typical dimensionless temperature profile used in industrial simulations to mimic the effects of furnace heating, namely

$$T(x) = \theta_0 + (1 - \theta_0)\left(\frac{1}{1 + \exp[-k(x - x_L)]} + \frac{1}{1 + \exp[k(x - x_R)]} - 1\right), \tag{3.36}$$

where $x_L < x_R$, $\theta_0 < 1$ and $k \gg 1$ are parameters, with $k = 20$, $x_L = 0.25$, $x_R = 0.75$ and $\theta_0 = 0.8$, and the dimensionless viscosity

$$\mu = \exp\left[\frac{1}{\nu}\left(\frac{1}{T - T_c} - \frac{1}{1 - T_c}\right)\right], \tag{3.37}$$

with $\nu = 0.1$ and $T_c = 0.34$.

In figure 3.6 we show the final sheet profile calculated numerically by U. Lange at Schott AG. These numerical solutions were obtained by solving the dimensionless version of the full three-dimensional Stokes equations (3.2)–(3.3) with associated boundary conditions (3.4)–(3.7) using the finite-element package Polyflow (Ansys Inc. Polyflow, 2013). The temperature profile (3.36) is prescribed on the free surface and at the inlet boundary, and the temperature in the bulk is then calculated by solving the energy equation (13.1–4 in Ansys Inc. Polyflow, 2013). The corresponding viscosity is then determined using equation (3.37), as this was found to be numerically more stable than imposing the viscosity field directly in the bulk. The other parameter values are $\epsilon = 0.01$, $D = 20$ and two different small values of $\delta \in \{0.1, 0.2\}$. In all cases, the sheet was discretized using linear elements for temperature and mini-elements for velocity and pressure (for details see Ansys Inc. Polyflow, 2013; Fortin, 1981). Remeshing was carried out via a streamwise method, full details of which may be found in Ansys Inc. Polyflow (2013). Grid independence was established for typical grid sizes of $100 \times 50 \times 4$.

Figure 3.6 demonstrates that the scalings from (3.25) collapse the two thickness profiles onto a single curve in a neighbourhood of the edge $y = b(x)$. We have also plotted the Polyflow numerical solutions to the three-dimensional problem when surface tension is included (with $\mathrm{Ca} = 80$), and these collapse onto the same curve, verifying that surface-tension effects are not important in the inner region for this process.

In figure 3.6, we also plot the numerical solution to the boundary-layer problem (3.26)–(3.29), calculated using the same viscosity profile. The agreement between the full numerical solution and the boundary-layer solution is extremely good, despite the values of δ not being especially small. This is because we retain all of the terms in the governing equations (3.16)–(3.20) inside the boundary layer near the edge, and the influence of the free surface decays exponentially away from the edge (cf. §3.2.4). The thin-sheet model surely breaks down very close to the sheet edge but nevertheless gives an excellent approximation to the thickness profile everywhere else. In summary, figure 3.6 demonstrates that, provided the heating zone is sufficiently short, the edge thickening effect is independent of the sheet width. The details of the thickness

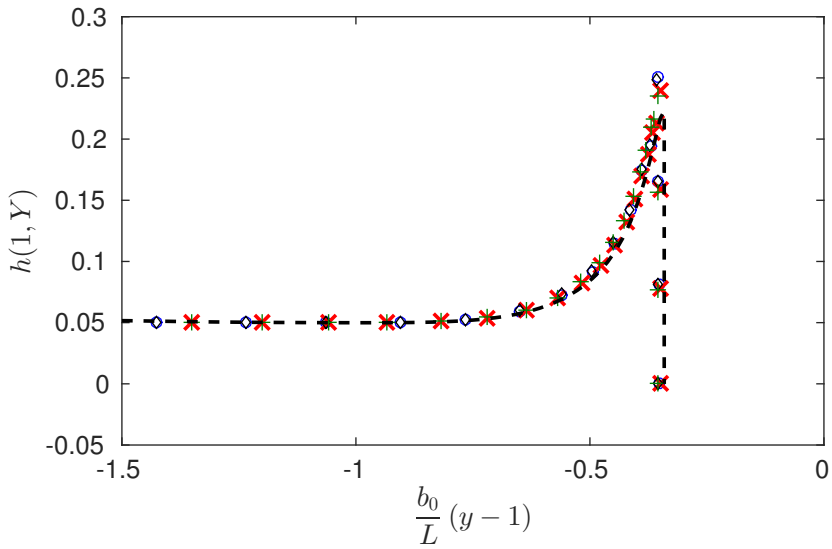

Figure 3.6: Final thickness profile $h(1, y)$ at the bottom of the heater zone for a draw ratio $D = 20$ and temperature and viscosity profiles (3.36), (3.37). The coloured data points are numerical solutions to the full three-dimensional Stokes problem calculated using software package Polyflow for $\epsilon = 0.01$. The blue circles correspond to $\delta = 0.1$ and the red $\times$ symbols to $\delta = 0.2$. The black diamonds and green plus signs are for cases with surface tension $\mathrm{Ca} = 80$, for $\delta = 0.1$ and $\delta = 0.2$ respectively. The data is scaled so that the profiles collapse onto the black dashed curve which is the numerical solution to the boundary-layer problem (3.26)–(3.28).

profile plotted in figure 3.6 do depend on the draw ratio and on the viscosity profile, but the asymptotic variations $h \sim 1/D$ in the bulk and $h \sim 1/\sqrt{D}$ at the edge are universal. We note a small discrepancy between the thicknesses predicted by the boundary-layer solution and by the three-dimensional solution near the sheet edge. The numerical solution of the three-dimensional problem is more challenging than the two-dimensional boundary-layer problem, due to the presence of very small and large parameters, and the discrepancy may be to numerical error arising in Polyflow, or it may be a failure of the thin-sheet approximation $\epsilon \to 0$.

We were also kindly provided with thickness data and corresponding process parameters from a redraw plant at Schott AG (see figure 3.7). By measurements with thermocouples fixed on a plate travelling through the heater zone, it was established that this heater zone corresponds to a dimensionless length of $\delta = 0.4$ and that the induced glass temperature profile can be roughly approximated by a function of type (3.36). The glass thickness was measured offline using a contact profilometer, and measurements were taken for three different times during redraw of a borosilicate glass sheet with aspect ratio $\epsilon = 0.01$ at draw ratio $D = 38$. We compare this to

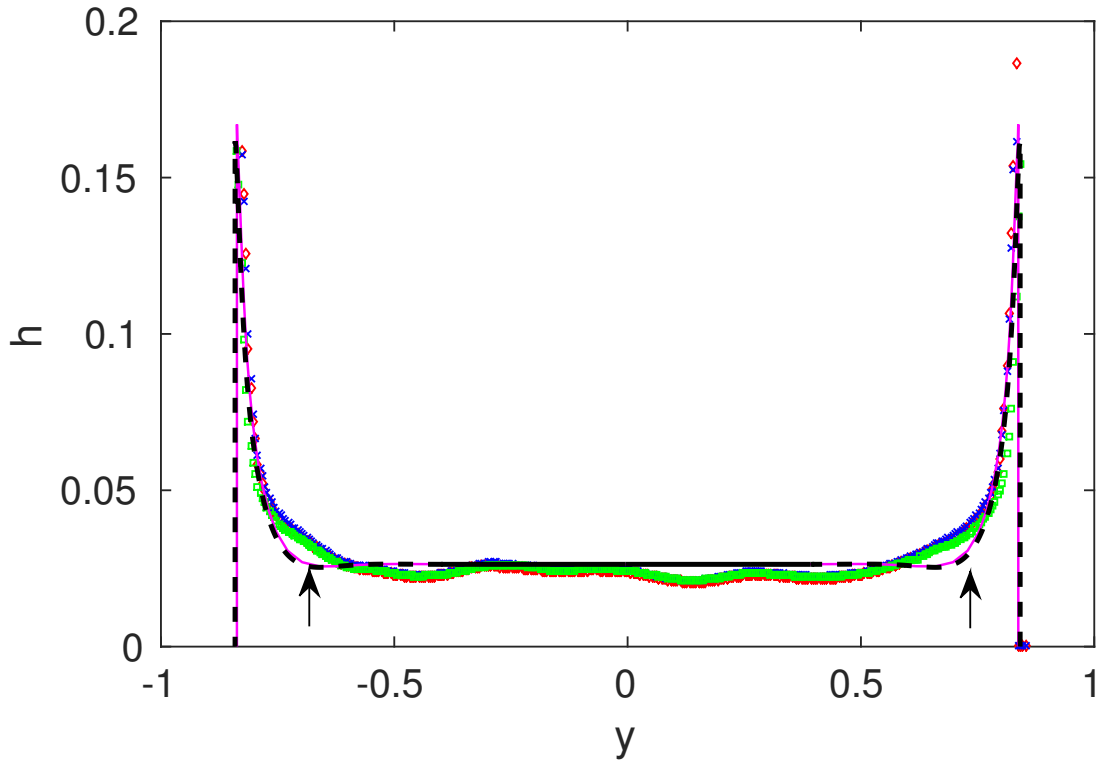

Figure 3.7: Thickness profile $h(1, y)$ at the bottom of the heater zone for a draw ratio $D = 38$ and temperature and viscosity profiles given by (3.36) and (3.37). The blue, red and green data points show thickness profiles measured at three different times during an experimental run of the redraw process whose parameters correspond to $\epsilon = 0.01$ and $\delta = 0.4$. The black dashed lines show the solution of the boundary-layer problem (3.26)–(3.28), and the black solid line in the centre, located at $h = 1/38$, is the one-dimensional bulk solution (3.23). The thin pink line shows the numerical solution to the full three-dimensional problem (3.12)–(3.14) calculated using Polyflow. The arrows highlight regions where the discrepancy between experimental data and the numerical solutions is significant.

our asymptotic solution, composed of the numerical solution to the boundary-layer problem (3.26)–(3.29) matched with the one-dimensional bulk solution (3.23), and to the numerical solution to the full three-dimensional problem (3.12)–(3.14), calculated U. Lange. Even for such a moderate value of δ, the agreement between the three-dimensional and thin-sheet models is very good. Our asymptotic solution gives an excellent prediction of the final sheet width as well as the edge and bulk thicknesses observed experimentally. However, the physical sheet is not completely flat in the bulk, and there appears to be a significant discrepancy between the predicted and measured profiles in the regions indicated by arrows in figure 3.7. One possible source of error is an over-simplification of the temperature profile. The two- and three-dimensional simulations assume that the temperature is a known function of x; in reality, the temperature will vary across the sheet width (and may also vary across the thickness). A more accurate, two-dimensional temperature profile would better reflect the industrial process and improve the prediction of the thickness transition between the bulk and edge, in particular in the region highlighted in figure 3.7.

3.6 Non-rectangular preforms

The ubiquitous edge-thickening effect demonstrated in figures 3.3–3.7 is a nuisance for glass manufacturers, and it is natural to ask whether the shape of the preform might be modified to counteract the accumulation of glass at the sheet edges. From the analysis performed in §3.4 we know that the final edge thickness scales with $1/\sqrt{D}$ while the bulk thickness scales with $1/D$. This suggests that a tapered preform whose edges have reduced thickness $1/\sqrt{D}$ will provide a final product with edge thickness $1/D$, in line with that of the bulk of the sheet. It is not obvious, however, exactly what the shape or extent of the taper should be.

The analysis presented in this chapter is valid for non-rectangular preforms, provided the preform is only doctored over a length $O(\delta)$ at the edge, i.e., provided the imposed non-uniformity is confined to the naturally occurring boundary layer. One can therefore conduct numerical experiments by solving the boundary-layer problem from §3.3 with different preform thickness profiles imposed at $x = 0$ and discover the corresponding final thickness profiles produced at $x = 1$; an approach similar to this was adopted by Smith and Stolle (2000). Alternatively, one could impose the condition of a uniform final sheet thickness at $x = 1$ and then try to determine the required preform profile $h(0, y)$. At first glance, one would expect the resulting inverse problem to be ill posed. However, we can exploit the scaling and reflectional

symmetries of the governing equations (3.26) to translate the inverse problem into a version of the forward problem already solved in §3.3.

The idea is to solve the boundary-layer problem (3.26)–(3.29) numerically for draw ratio $D = D^* < 1$. While physical compression of the sheet would certainly lead to a mid-surface instability, the purely in-plane thin-sheet model (3.26)–(3.29) is mathematically well posed regardless of whether D is greater or smaller than unity. A suitable reflection and scaling of the resulting forward (starred) solution, namely

$$x = 1 - x^*, \quad h(x, Y) = D^* h^*(x^*, Y), \quad u(x, Y) = \frac{1}{D^*} u^*(x^*, Y), \tag{3.38a}$$

$$V(x, Y) = -\frac{1}{D^*} V^*(x^*, Y), \qquad B(x) = B^*(x^*) - B^*(1), \tag{3.38b}$$

gives a solution of the inverse problem with draw ratio $D = 1/D^* > 1$ and uniform thickness at the downstream end $x = 1$. Therefore, to find the optimal taper for a given draw ratio D, we simply impose a uniform thickness at $x^* = 0$, solve the forward problem for draw ratio $1/D$ and an appropriately reflected temperature profile, and record the thickness profile produced at $x^* = 1$. Such an "optimal preform" is shown in figure 3.8 for three different draw ratios, $D = 10$, 20, and 40 and constant temperature and viscosity. We see that the edge thickness is $1/\sqrt{D}$ as expected, increasing to 1 away from the sheet edge.

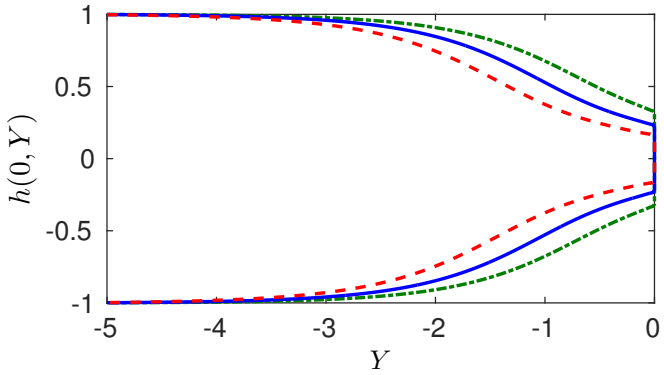

Figure 3.8: Optimal preform shape to draw a rectangular product at draw ratios 10 (green dot-dashed), 20 (blue solid) and 40 (red dashed) with constant viscosity.

Drawing of the optimal preform at $D = 20$ is illustrated in figure 3.9(a), and we see that it does indeed produce a rectangular thin sheet. While it is likely to be impractical and expensive to create a preform with a precisely specified smooth taper, it is relatively easy via a cutting process to produce a piecewise linear preform profile. The result of drawing such a linear preform is shown in figure 3.9(b).

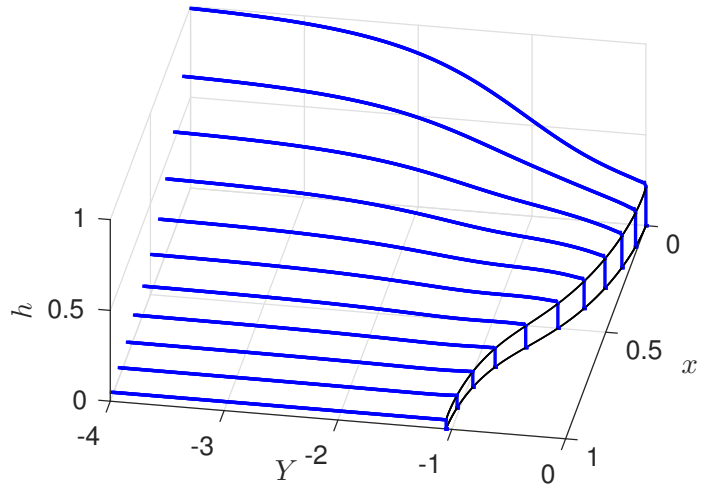

(a)

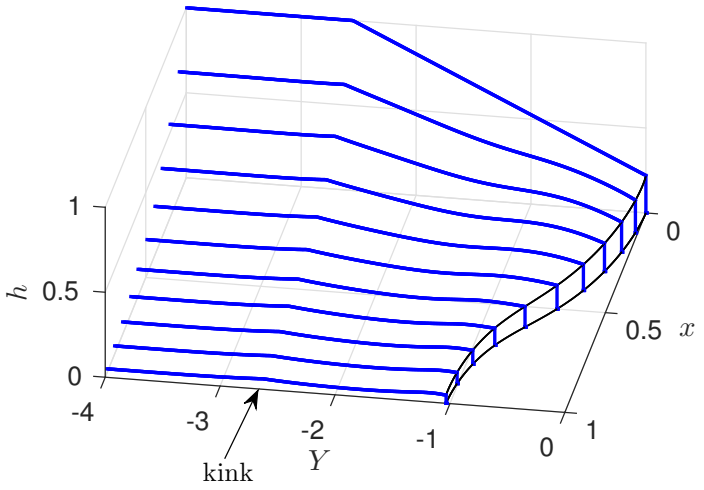

(b)

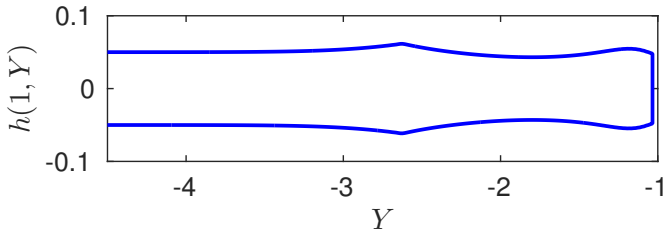

(c)

Figure 3.9: Drawing of (a) sheet with optimal initial thickness profile, (b) sheet with linear taper, at draw ratio $D = 20$ at constant viscosity, (c) final cross-section of tapered sheet shown in (b).

We see that the shape of the final product is greatly improved compared with that shown in figure 3.3, but that the sharp corner in the preform results in a kink in the final product as indicated by the arrow, and shown more clearly in 3.9(c). The exact inverse-problem solutions shown in figure 3.8 would provide a valuable guide in designing a preform shape that reduces the thickness variations in the final product while satisfying manufacturing constraints.

3.7 Redraw of a thin viscous sheet including fully coupled heat transfer and surface tension

The model used in this chapter relies on three basic assumptions, namely that (i) inertia effects are negligible, (ii) the temperature is a known function of position in the heater zone, (iii) surface-tension effects are negligible. The Reynolds number in industrial processes of interest is almost always small, and therefore inertia effects are indeed unlikely to be significant. However, situations may arise in which it is prudent to include coupled heat transfer and/or surface tension effects in the model. In this section we will briefly discuss the implications of each.

3.7.1 Heat transfer

Models for coupled heat transfer are discussed in §2.3, and for a two-dimensional sheet heat flow decouples from fluid flow to a first approximation in regimes of interest. For a three-dimensional sheet the temperature in the glass is known *a priori* provided heat transfer between the glass sheet and the surrounding atmosphere is effectively instantaneous (see §2.3.4), i.e. provided one or both of the reduced Stanton number

$$a = \frac{k_{\mathrm{h}} d}{\rho c_p U h_0} = \frac{\delta}{\epsilon} \frac{k_{\mathrm{h}}}{\rho c_p U}, \tag{3.39}$$

and the parameter

$$b = \frac{\sigma_{SB} \epsilon_R T_0^3 d}{\rho c_p U h_0} = \frac{\delta}{\epsilon} \frac{\sigma_{SB} \epsilon_R T_0^3}{\rho c_p U}, \tag{3.40}$$

is sufficiently large. The representative parameters given in Tables 1.1 and 2.1 imply that $a \approx 5.7$ and $b \approx 5.1$. While these values are sufficiently large to indicate that the heat-flow problem decouples to a first approximation, the effects of coupling may be important, especially near the edges. In this case we would extend the models derived in §2.3 to three spatial dimensions.

3.7.2 Surface tension

The parameter values listed in Table 1.1 indicate that the capillary number $\mathrm{Ca} = \mu_0 U/\gamma \approx 80$. Including surface tension in the model requires the imposition of a normal force on the free surface. In the thin-sheet limit the bulk momentum equations (3.26) remain unchanged, and only the boundary conditions (3.28b) and (3.28c) on $y = \pm b(x,t)$ need be modified. At the sheet edge, a normal force balance in dimensional terms yields

$$\frac{-2\gamma}{\sqrt{1+h_n^2}} = \int_{-h}^{h} \hat{\boldsymbol{n}} \cdot (\boldsymbol{\sigma} \cdot \hat{\boldsymbol{n}}) \, \mathrm{d}z, \tag{3.41}$$

where $h_n = \hat{\boldsymbol{n}} \cdot \nabla h$ is the normal derivative of the sheet thickness at the sheet edge. Non-dimensionalizing and integrating provides a normal stress condition

$$\frac{2\mu}{1+B_x^2}\left[B_x^2(2u_x + V_Y) - B_x(u_Y + V_x) + (u_x + 2V_Y)\right] = -\frac{\delta}{\epsilon\,\mathrm{Ca}}\frac{1}{h}, \tag{3.42}$$

along with the condition of zero tangential stress. These new boundary conditions could easily be incorporated into the numerical solution of the boundary-layer problem, and the presence of surface tension will act to exacerbate the problem of edge retraction. The size of the effect is $\delta/(\epsilon\,\mathrm{Ca})$ which may be $O(1)$ in processes of interest. However, in figure 3.6 we compare solutions to the full three-dimensional Stokes problem (3.12)–(3.14) with and without the inclusion of a surface tension term. The solutions are plotted in figure 3.6 for the cases $\epsilon = 0.01$, $\delta = 0.1$ and $\epsilon = 0.01$, $\delta = 0.2$ and temperature and viscosity profiles (3.36)–(3.37). We observe that the data are virtually indistinguishable and collapse onto the same curve in the boundary layer, so our assumption that surface tension may be neglected is accurate for the particular process of interest here, in which $\delta/(\epsilon\,\mathrm{Ca}) = 0.5$.

3.8 Conclusions

In this chapter we examine the glass redraw process when the heater zone through which the sheet is drawn is short compared with its width. We derive a mathematical model to predict how the thickness profile of the resulting final product depends on the process parameters and, in particular, to explain and quantify the anomalous thickening observed near the edges of the sheet. We find that the bulk flow is purely one-dimensional, with the axial velocity and sheet thickness varying in the direction of drawing only. Variations in the sheet thickness are confined to boundary layers near the edges of the sheet, where the flow is governed by a canonical free-boundary

problem. The inward displacement of the sheet edge and the local thickness profile depend on the draw ratio and on the temperature profile in the heater zone, but not on the width of the sheet. This finding should inform future manufacture of thin sheets by redraw: increasing the width of the preform while keeping the heater zone length constant will increase the yield of uniformly thin glass by the same amount, with no increase in the amount of waste due to edge thickening.

In the limit where the heater zone is very short compared with the preform width, mass conservation in the one-dimensional bulk flow implies that the ratio of final to initial bulk thickness is equal to the inverse of the draw ratio. On the other hand, the mass-conservation equation and stress-free edge conditions imply that the ratio of final to initial edge thickness is equal to the inverse square root of the draw ratio. This result holds for any thin sheet (i.e., regardless of the length of the heater zone), provided that surface tension is negligible. We thus provide a rigorous derivation of the draw-ratio relationships previously proposed by Dobroth and Erwin (1986).

We demonstrate that the inverse problem of how to determine the optimal preform shape that will redraw to a uniform-thickness sheet may be transformed to a version of the forward problem and then solved numerically in a straightforward way. This allows us to determine the required preform that achieves a uniformly thick sheet following redraw. In addition, we predict a preform shape that achieves a final product that is close to uniform in the case where we are only able to taper the preform linearly. Here we find that the final cross-sectional profile is close to uniform but possesses an unavoidable "kink" that arises from the gradient discontinuity in the preform where the taper begins. This second result provides insight into the optimization strategy given certain preform fabrication constraints.

Finally, we extend our theory to include surface tension. In principle surface tension will exacerbate the thick-edge phenomenon, but we find that it has little impact on the observed behaviour here.

Chapter 4

Redraw through a long heater zone

4.1 Introduction

In contrast to the process considered in Chapter 3, in this chapter we will consider the limit in which the heater zone is long compared with the sheet width. A long heater zone is used in processes where the aim is to redraw a thin sheet, but preserve the aspect ratio or even cross-sectional shape of the preform. Howell (1994) showed that, for a long rectangular sheet in the absence of surface tension, each cross-section preserves its aspect ratio to leading order as it convects along. However, in reality it is not economic to construct extremely long heater zones, and the finite length of the heater zone means that the cross-sectional profile of the sheet is not, in fact, preserved. A rectangular preform redraws to a product that is thick at the edges and thin in the centre (see figure 4.1), and both the width of the product and the thickness variation increase as the ratio of width to heater zone length increases. Furthermore, surface tension acts to pull in the sheet edges, decreasing the final width and increasing the final thickness, and the sharp corners in the preform become rounded (see figure 4.2). To determine how long a heater zone is required to yield final products acceptably close to rectangular, a clear understanding of the dependence of the final cross-section of the glass sheet on process parameters is required. In the case of a fibre whose radius is small compared with its length, the Trouton model describes the velocity and radius to leading order in the small aspect ratio. Schultz and Davis (1982) derived higher-order corrections to this model. The boundary conditions on the velocity at the sheet ends cannot be applied directly to the bulk velocity after the long narrow limit is taken, so they instead applied these conditions to the cross-sectional average of the bulk flow. This assumption yields correction terms which scale with the inverse heater zone length squared. However, numerical solutions of a three-dimensional model for

the thickness profile of a thin sheet (Lange, 2016) indicate that the deviation is linear in the inverse heater zone length, not quadratic.

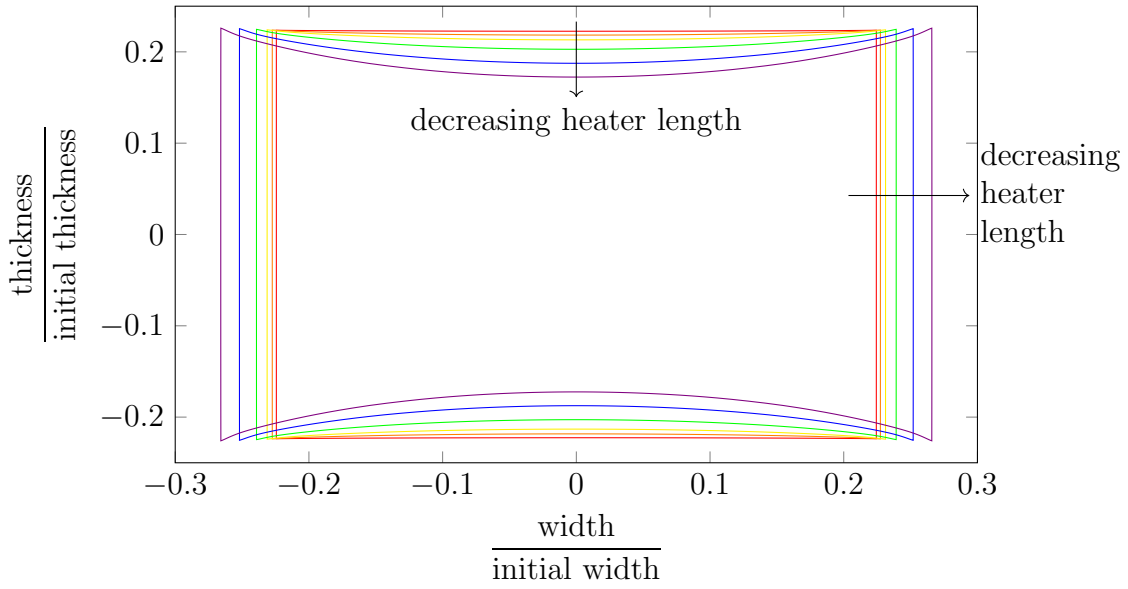

Figure 4.1: Final thickness profile of glass after redraw at draw ratio 20, with a ratio of preform half-width to heater zone length equal to 0.01 (red), 0.05 (orange), 0.1 (yellow), 0.2 (green), 0.35 (blue) and 0.5 (violet). These are numerical solutions to the three-dimensional Stokes equations calculated in Polyflow by U. Lange at Schott AG.

In this chapter we determine the cross-sectional profile of a glass sheet undergoing redraw through a long heater zone (as opposed to Chapter 3 where we considered a short heater-zone limit). We quantify the deviation in the final shape from the preform shape by calculating corrections to the leading-order asymptotic solution. In §4.2 we adapt the thin-sheet model to the case where the heater zone is long compared with the preform width. In this limit, the leading-order behaviour in the bulk of the sheet is one-dimensional, with boundary layers near the sheet ends where the flow is two-dimensional. We revisit the calculation of Howell (1994) in §4.3, considering the more general scenario in which the sheet has a non-uniform initial thickness profile, and show that its shape is preserved at leading order in the absence of surface tension. In regimes where surface tension plays a role at leading order, we calculate the relative change in the final thickness and width of the sheet. In §4.4 we proceed to next order in our asymptotic expansion to determine the first correction to the leading-order solution, quantifying the deviations from the preform shape when the heater zone has finite length. Matching between the bulk and boundary layers at the sheet ends

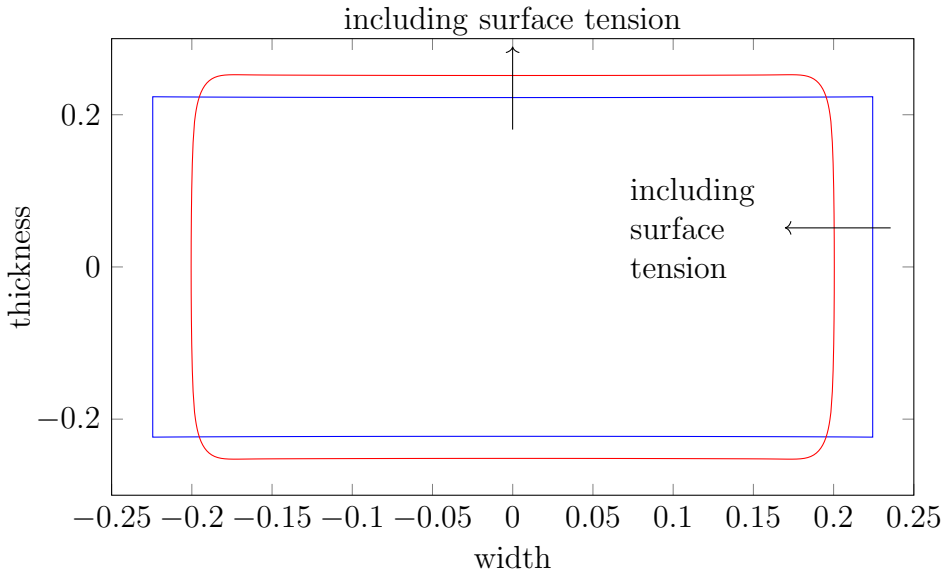

Figure 4.2: Final thickness profile of glass after redraw at draw ratio 20, with a ratio preform half-width to heater zone length equal to 0.01, with and without surface tension, calculated using Polyflow by U. Lange at Schott AG.

motivates an expansion in powers of the ratio of heater zone length to preform half-width, $\mathcal{B}$, as opposed to the $\mathcal{B}^2$ expansion often employed in the literature (Schultz and Davis, 1982). We thus show that corrections to the leading-order behaviour are larger than previously predicted, and that simply averaging the boundary conditions at the sheet ends and applying them to the bulk is not appropriate beyond leading order. In §4.5 we study the behaviour in the boundary layers at either end of the sheet and determine the matching conditions for the bulk problem. We present solutions to the higher-order correction problem and investigate the dependence on process parameters in §4.6, and we compare our predictions with numerical solutions to the full three-dimensional problem in §4.7. In §4.8 we discuss the inverse problem: what preform shape redraws to a rectangular final product?

4.2 Dimensionless model

The velocity, thickness and width in the bulk of the sheet are governed by the thin-sheet equations derived in Chapter 3, but in this scenario

$$\delta = \frac{\text{length of heater zone}}{\text{preform half-width}} \gg 1. \tag{4.1}$$

We define $\mathcal{B} = \delta^{-1} \ll 1$ and scale the horizontal velocity with $\mathcal{B}^2$ since it will be small. Then the governing equations (3.16) become

$$(uh)_x + (vh)_y = 0, \tag{4.2a}$$

$$\mathcal{B}^2 \left(4\mu h u_x + 2\mu h v_y\right)_x + \left(\mu h u_y + \mathcal{B}^2 \mu h v_x\right)_y = 0, \tag{4.2b}$$

$$\left(\mu h u_y + \mathcal{B}^2 \mu h v_x\right)_x + \left(2\mu h u_x + 4\mu h v_y\right)_y = 0. \tag{4.2c}$$

At the free edge $y = \pm b(x)$ we impose a no-flux condition, and include the effect of surface tension in the stress balance, so that

$$v = \pm b_x u, \tag{4.3a}$$

$$\begin{pmatrix} 4\mu h u_x + 2\mu h v_y & \mathcal{B}^{-1}\mu h u_y + \mathcal{B}\mu h v_x \\ \mathcal{B}^{-1}\mu h u_y + \mathcal{B}\mu h v_x & 2\mu h u_x + 4\mu h v_y \end{pmatrix} \begin{pmatrix} \mp\mathcal{B} b_x \\ 1 \end{pmatrix} = -\Gamma \begin{pmatrix} \mp\mathcal{B} b_x \\ 1 \end{pmatrix}, \tag{4.3b}$$

where

$$\Gamma = \frac{1}{\epsilon \mathcal{B}\,\mathrm{Ca}} = \frac{\text{heater length}}{\text{preform half-width}} \frac{\gamma}{\mu_s U} \tag{4.4}$$

measures the importance of surface tension relative to viscous effects, with

$$\mathrm{Ca} = \frac{\mu_s U}{\gamma} \tag{4.5}$$

the capillary number, μ_s a characteristic viscosity, U the feed speed and γ the surface tension. We will investigate the regime $\Gamma = O(1)$ in which surface tension effects play a role at leading order.

We expect the sheet to be symmetric about $y = 0$, i.e., the thickness h and lengthwise velocity u should be symmetric in y, and the transverse velocity v should be antisymmetric. In addition, we impose feed and draw conditions at the top and bottom of the heater zone. At the top of the heater zone, we impose the dimensionless velocity and sheet dimensions

$$u = b = 1, \quad h = h_{in}(y) \quad \text{on} \quad x = 0, \tag{4.6}$$

and at the bottom of the heater zone we impose the dimensionless velocity

$$u = D \quad \text{on} \quad x = 1. \tag{4.7}$$

In principle we should also impose boundary conditions on the transverse velocity $v(0, y) = v(1, y) = 0$. However, we shall see below that this is not straightforward in the limit $\mathcal{B} \to 0$, when the bulk velocity cannot fully satisfy the boundary conditions. The velocity adjusts rapidly in boundary layers at either end of the sheet from the

profile imposed by the feed and draw rollers to the bulk profile. At leading order, we may simply impose the feed speed $u(0, y) = 1$ and draw speed $u(1, y) = D$ and disregard the transverse velocity conditions. However, the boundary-layer behaviour must be properly resolved for accurate determination of higher-order corrections; we return to this in §4.5.

In principle the viscosity μ of the glass varies spatially due to temperature variations as the sheet moves through the heater zone. In this chapter we will assume $\mu \equiv 1$ and focus our attention on the boundary-layer structure of the sheet, although most of the results that follow can also be extended to the case $\mu = \mu(x)$.

4.3 Leading-order behaviour

We examine the behaviour for a very long heater zone by considering the limit $\mathcal{B} \to 0$ and expanding variables in powers of $\mathcal{B}$ (the necessity for expansion in powers of $\mathcal{B}$ as opposed to $\mathcal{B}^2$ arises from the boundary layers at either end of the sheet, as we shall see in §4.5). Evaluating the x-momentum equation (4.2b) at leading order and integrating using the stress condition (4.3b) at the free edge, we find that the leading-order velocity varies only along the length of the sheet, i.e.,

$$u_0 = u_0(x), \tag{4.8}$$

and, as usual, the flow is extensional. Evaluating the y-momentum equation (4.2c) at leading order and integrating using the free-boundary condition (4.3b) we find

$$2h_0 u_{0x} + 4h_0 v_{0y} = -\Gamma, \tag{4.9}$$

which represents a net lateral stress balance. Solving for v_0 and integrating (requiring symmetry) yields

$$v_0 = -\frac{1}{2} u_{0x} y - \frac{\Gamma}{4} \int_0^y \frac{1}{h_0} \, \mathrm{d}y. \tag{4.10}$$

Integrating the mass conservation equation (4.2a) across the sheet width and using no-flux condition (4.3a) and inlet conditions (4.6) yields

$$u_0 \int_0^{b_0} h_0 \, \mathrm{d}y = 1, \tag{4.11}$$

implying a constant net flux along the sheet. Integrating force balance (4.2b) across the sheet width and using no-stress condition (4.3b) yields a cross-averaged longitudinal force balance, which may be simplified using (4.10) to give

$$\frac{\partial}{\partial x} \int_{-b_0}^{b_0} 3h_0 u_{0x} \, \mathrm{d}y = -\Gamma b_{0x}. \tag{4.12}$$

We note that the Trouton ratio in this regime is 3; this is to be expected since in the limit of a long heater zone the sheet is quasi one-dimensional. A further discussion of this point may be found in Chapter 8 of Howell (1994).

We obtain a third equation for u_0, h_0, b_0 by applying the no-flux condition (4.3a) at leading order to obtain

$$u_0 b_{0x} + \frac{1}{2} u_{0x} b_0 + \frac{\Gamma}{4} \int_0^{b_0} \frac{1}{h_0} \, \mathrm{d}y = 0. \tag{4.13}$$

In the absence of surface tension ($\Gamma = 0$) the governing equations are simplified significantly. We can eliminate between (4.11)–(4.13) to determine a differential equation for u_0 only, which may be integrated subject to (4.6)–(4.7), yielding

$$u_0 = \mathrm{e}^{\log(D)x}, \tag{4.14}$$

and similarly

$$b_0 = \mathrm{e}^{-\log(D)x/2}. \tag{4.15}$$

To determine h_0, we return to mass balance (4.2a) at leading order and substitute in our leading-order velocities to find

$$h_{0x} - \frac{1}{2} \log(D) y h_{0y} = -\frac{1}{2} \log(D) h_0, \tag{4.16}$$

which has solution

$$h_0 = h_{in}\left(y \mathrm{e}^{\log(D)x/2}\right) \mathrm{e}^{-\log(D)x/2}, \tag{4.17}$$

where $h_{in}(y)$ is the initial thickness profile of the sheet at the top of the heater zone. Thus the thickness of the sheet decreases with the inverse square root of the velocity, and any variation in the initial thickness profile is retained. The width and thickness results (4.15) and (4.17) together confirm that, in the absence of surface tension, the aspect ratio and initial shape are preserved in the limit of a long heater zone.

For $\Gamma \neq 0$ we can make progress by assuming that the initial thickness profile is uniform, i.e., $h(0, y) = h_{in}(y) \equiv 1$. It can then be shown (see, for example Howell, 1994) that $h_0 = h_0(x)$, so that the leading-order governing equations (4.11)–(4.13) reduce to

$$u_0 b_0 h_0 = 1, \tag{4.18a}$$

$$\frac{\mathrm{d}}{\mathrm{d}x}\left(3\frac{u_{0x}}{u_0}\right) = -\frac{\Gamma}{2} b_{0x}, \tag{4.18b}$$

$$\frac{b_{0x}}{b_0} = -\frac{1}{2}\frac{u_{0x}}{u_0} - \frac{\Gamma}{4} b_0, \tag{4.18c}$$

with boundary conditions

$$u_0(0) = h_0(0) = b_0(0) = 1, \quad u_0(1) = D. \tag{4.19}$$

This leading-order problem has solution

$$u_0 = \frac{3\kappa}{\Gamma + 3\kappa - \Gamma \mathrm{e}^{-\kappa x/2}} \mathrm{e}^{\kappa x}, \tag{4.20a}$$

$$h_0 = \left(\frac{\Gamma + 3\kappa - \Gamma \mathrm{e}^{-\kappa x/2}}{3\kappa} \right)^2 \mathrm{e}^{-\kappa x/2}, \tag{4.20b}$$

$$b_0 = \frac{3\kappa}{\Gamma + 3\kappa - \Gamma \mathrm{e}^{-\kappa x/2}} \mathrm{e}^{-\kappa x/2}, \tag{4.20c}$$

where $\kappa > \log(D)$ satisfies the transcendental equation

$$\Gamma = \frac{3\kappa \left(\mathrm{e}^{\kappa} - D \right)}{D(1 - \mathrm{e}^{-\kappa/2})}. \tag{4.21}$$

The ratio between the thickness/width of the cross-section with and without surface tension can thus be quantified by

$$\frac{h_0(1)}{D^{-1/2}} = \left(\frac{b_0(1)}{D^{-1/2}} \right)^{-1} = \mathrm{e}^{3(\kappa - \log(D))/2}. \tag{4.22}$$

The ratio $\mathrm{e}^{3(\kappa - \log(D))/2}$ is plotted in figure 4.3 as a function of the surface-tension coefficient Γ for a range of values of the draw ratio D. As expected, $\kappa \to \log(D)$ in the limit $\Gamma \to 0$ where surface tension is not important, while the final thickness increases and the final width decreases as surface tension becomes more dominant.

4.4 Correction terms

We calculate corrections to the leading-order behaviour by proceeding to $O(\mathcal{B})$ in our asymptotic expansion. We limit our attention to the case $h_{in}(y) = 1$ to allow further analytical progress. We return to the x-momentum equation (4.2b), integrating and applying (4.3b) to obtain $u_1 = u_1(x)$. Evaluating the y-momentum equation (4.2c) at $O(\mathcal{B})$ and integrating, we obtain

$$2h_0 v_{1y} + 2h_1 v_{0y} = -h_0 u_{1x} - h_1 u_{0x}, \tag{4.23}$$

so that substituting in (4.10) and solving for v_1 yields

$$v_1 = -\frac{1}{2} u_{1x} y + \frac{\Gamma}{4} \frac{1}{h_0^2} \int_0^y h_1 \, \mathrm{d}y. \tag{4.24}$$

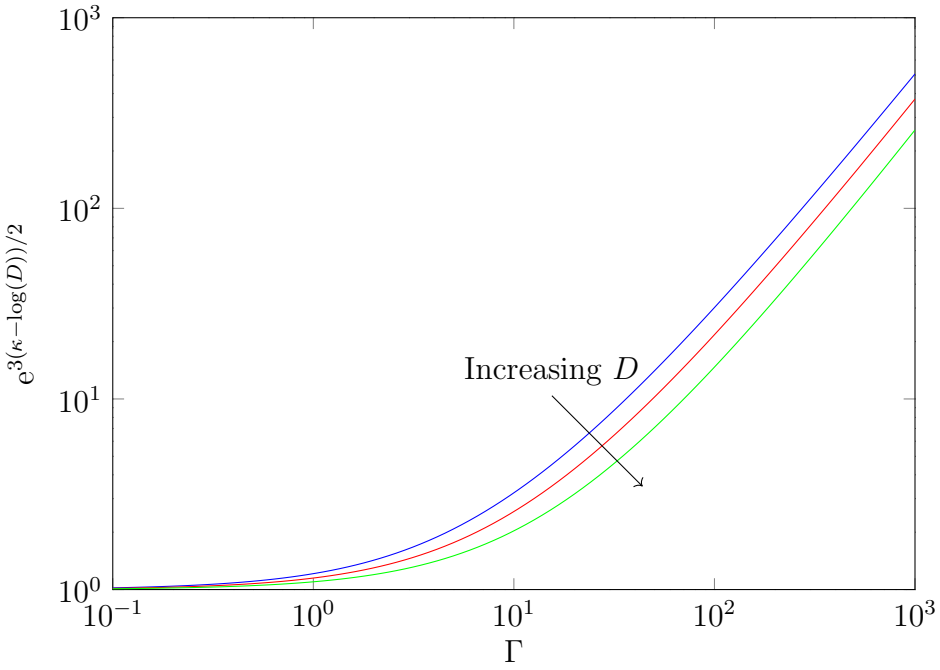

Figure 4.3: Change in final cross-section due to surface tension for $D = 2$ (blue), $D = 10$ (red) and $D = 100$ (green). The leading-order final thickness relative to that in the absence of surface tension is given by $e^{3(\kappa-\log(D))/2}$, with $\kappa(\Gamma)$ the solution to (4.21), while the ratio for width is given by the reciprocal of this.

Integrating the mass equation (4.2a) across the sheet thickness and evaluating at $O(\mathcal{B})$ yields

$$u_0 \int_0^{b_0} h_1 \, \mathrm{d}y = -h_0 b_0 u_1 - u_0 h_0 b_1. \tag{4.25}$$

We again integrate the x-momentum (4.2b) equation across the sheet thickness, and use (4.25) to eliminate h_1 to obtain

$$\left(3\frac{u_1}{u_0}\right)_{xx} = -\frac{\Gamma}{2} b_{1x}. \tag{4.26}$$

Meanwhile, the no-flux boundary condition (4.3a) together with (4.24)–(4.25) and leading-order solutions (4.20) yields

$$\left(\frac{b_1}{b_0}\right)_x + \frac{1}{2}\left(\frac{u_1}{u_0}\right)_x + \frac{\Gamma}{4} b_1 = 0. \tag{4.27}$$

In the special case $\Gamma = 0$ these equations simplify significantly, and we obtain

$$u_1 = u_0 \log(D)\,(c_1 x + c_2)\,, \tag{4.28a}$$

$$b_1 = b_0 \log(D)\left(-\frac{c_1}{2} x + c_3\right), \tag{4.28b}$$

where c_1, c_2 and c_3 are constants of integration to be determined by the boundary conditions, which will be obtained in §4.5 by examining the boundary layers at either end of the sheet. Still with $\Gamma = 0$, we evaluate the mass equation (4.2a) to obtain

$$h_{1x} - \frac{1}{2}\log(D) y h_{1y} = -\frac{1}{2}\log(D) h_1 - c_1 \frac{\log(D)}{2} \mathrm{e}^{-\log(D)x/2}, \tag{4.29}$$

with solution

$$h_1 = \log(D) f\left(y \mathrm{e}^{\log(D)x/2}\right) \mathrm{e}^{-\log(D)x/2} - c_1 \frac{\log(D)}{2} x \mathrm{e}^{-\log(D)x/2}, \tag{4.30}$$

with the function f also to be determined by the boundary conditions.

For $\Gamma \neq 0$, the momentum balance (4.26) and no-flux condition (4.27) are satisfied by

$$b_1(x) = b_0(x)\left[d_1 x + \Gamma\left(\frac{\frac{2d_1}{\kappa}\mathrm{e}^{-\kappa x/2} + d_1 x \mathrm{e}^{-\kappa x/2} + d_2}{\Gamma + 3\kappa - \Gamma \mathrm{e}^{-\kappa x/2}}\right)\right], \tag{4.31a}$$

$$u_1(x) = u_0(x)\left[d_3 - 2d_1 x + \Gamma\left(\frac{\frac{2d_1}{\kappa}\mathrm{e}^{-\kappa x/2} + d_1 x \mathrm{e}^{-\kappa x/2} + d_2}{\Gamma + 3\kappa - \Gamma \mathrm{e}^{-\kappa x/2}}\right)\right], \tag{4.31b}$$

where d_1, d_2 and d_3 are constants of integration. The mass equation (4.2a) then yields

$$\frac{1}{2}\frac{u_{0x}}{u_0} h_1 + h_{1x} - \left(\frac{1}{2}\frac{u_{0x}}{u_0} + \frac{\Gamma}{4}\frac{1}{u_0 h_0}\right) y h_{1y} = -\frac{1}{2}\frac{u_{1x}}{u_0} h_0 - \frac{u_1}{u_0} h_{0x}, \tag{4.32}$$

with solution

$$h_1(x,y) = h_0(x)\left[d_1 x - d_3 - 2\Gamma\left(\frac{\frac{2d_1}{\kappa}\mathrm{e}^{-\kappa x/2} + d_1 x \mathrm{e}^{-\kappa x/2} + d_2}{\Gamma + 3\kappa - \Gamma \mathrm{e}^{-\kappa x/2}}\right)\right] + \mathrm{e}^{-\kappa x/2}\sqrt{\Gamma + 3\kappa - \Gamma \mathrm{e}^{-\kappa x/2}} f^*\left(\frac{y}{b_0(x)}\right), \tag{4.33}$$

where f^* arises from the integration and is to be determined by the boundary conditions.

We now must apply appropriate boundary conditions to the correction terms (4.28) and (4.30) to determine c_1, c_2, c_3 and f in the surface-tension-free case or to (4.31) and (4.33) to determine d_1, d_2, d_3 and f^* when surface tension is included. However, these correction terms cannot satisfy all of the boundary conditions (4.6)–(4.7); there are boundary layers at either end of the sheet where the solution adjusts from its bulk behaviour to that at the boundaries, and we must examine these boundary layers in order to determine the correct boundary conditions for the bulk solution.

4.5 Boundary-layer behaviour

4.5.1 Without surface tension

To obtain the correct boundary conditions for the bulk solution at $x = 0$ and $x = 1$ we must investigate the behaviour in the boundary layers around these regions, where the behaviour is two-dimensional and the solution adjusts from that imposed by the draw rollers to the bulk profile. For clarity, we first present a detailed account of the special case $\Gamma = 0$, and subsequently extend the analysis to include surface tension. We examine the behaviour in the boundary layer near $x = 0$ by scaling $x = \mathcal{B}\hat{x}$ and re-examine the governing equations (4.2)–(4.7), using hats to denote variables inside the boundary layer. Matching between the bulk and boundary regions verifies that the correction terms must indeed be of $O(\mathcal{B})$, not $O(\mathcal{B}^2)$ as proposed by Schultz and Davis (1982). We propose solutions of the form

$$\begin{aligned} \hat{u} &= 1 + \mathcal{B}\log(D)\hat{u}_1(\hat{x}, y) + \cdots, \\ \hat{v} &= \log(D)\hat{v}_0(\hat{x}, y) + O(\mathcal{B}), \\ \hat{h} &= 1 + \mathcal{B}\log(D)\hat{h}_1(\hat{x}, y) + \cdots, \\ \hat{b} &= 1 + \mathcal{B}\log(D)\hat{b}_1(\hat{x}) + \cdots. \end{aligned} \tag{4.34}$$

The extra factors of $\log(D)$ are included to allow D to be scaled out of the boundary-layer problem entirely. We thus obtain from (4.2) governing equations for $\hat{u}_1$, $\hat{v}_0$, $\hat{h}_1$ and $\hat{b}_1$, namely

$$\hat{u}_{1\hat{x}} + \hat{h}_{1\hat{x}} + \hat{v}_{0y} = 0, \tag{4.35a}$$

$$(4\hat{u}_{1\hat{x}} + 2\hat{v}_{0y})_{\hat{x}} + (\hat{u}_{1y} + \hat{v}_{0\hat{x}})_y = 0, \tag{4.35b}$$

$$(\hat{u}_{1y} + \hat{v}_{0\hat{x}})_{\hat{x}} + (2\hat{u}_{1\hat{x}} + 4\hat{v}_{0y})_y = 0. \tag{4.35c}$$

The boundary conditions (4.3) at the free edge $y = \pm 1$ are transformed to

$$\hat{v}_0 = \pm b_{1\hat{x}}, \tag{4.36a}$$

$$\hat{u}_{1y} + \hat{v}_{0\hat{x}} = 0, \tag{4.36b}$$

$$2\hat{u}_{1\hat{x}} + 4\hat{v}_{0y} = 0, \tag{4.36c}$$

while the feed conditions (4.6) become

$$\hat{u}_1 = \hat{v}_0 = \hat{h}_1 = \hat{b}_1 = 0 \quad \text{on} \quad \hat{x} = 0. \tag{4.37}$$

Matching with the bulk solutions (4.28) and (4.30) yields

$$\hat{u}_1 \sim \hat{x} + c_2, \tag{4.38a}$$

$$\hat{v}_0 \sim -\frac{1}{2}y, \tag{4.38b}$$

$$\hat{h}_1 \sim -\frac{1}{2}\hat{x} + f(y), \tag{4.38c}$$

$$\hat{b}_1 \sim -\frac{1}{2}\hat{x} + c_3 \tag{4.38d}$$

as $\hat{x} \to \infty$, and the force integrated across the sheet width should be fixed, so

$$4\hat{u}_{1\hat{x}} + 2\hat{v}_{0y} = 3 \quad \text{as} \quad \hat{x} \to \infty. \tag{4.39}$$

We note that our scalings (4.34) ensure the draw ratio D does not appear in the boundary-layer equations (4.35)–(4.39), so we only need to solve this problem once.

We may solve the linear equations (4.35b)–(4.35c) together with boundary conditions (4.36b)–(4.36c), (4.37), (4.38b) and force condition (4.39) on the fixed domain $[0, \infty) \times [-1, 1]$ for velocity components $\hat{u}_1$, $\hat{v}_0$. We can then solve the mass and no-flux equations (4.35a) and (4.36a) together with input conditions (4.37) for the size components h_1 and b_1. Finally, we infer the integration constants c_2, c_3 and function f by matching with the bulk using (4.38). We must then examine the boundary layer near the bottom of the sheet to determine the final constant c_1.

We solve the system of equations (4.35)–(4.39) numerically using finite-element software FEniCS. Since the system is symmetric about $y = 0$, we solve in $y \geq 0$ only. A convergence check shows that the solution may be determined to three significant figures with a 1000×400 mesh and the domain truncated at $\hat{x} = 5$. This yields the integration constants

$$c_2 = -0.064, \quad c_3 = 0.129, \tag{4.40}$$

along with the function $f(y)$, which is plotted in figure 4.4.

In the neighbourhood of $x = 1$ we scale into the boundary layer via $x = 1 - \mathcal{B}\bar{x}/\sqrt{D}$, also scaling $y = -\bar{y}/\sqrt{D}$, and denote variables inside the boundary layer with bars. The factors of $\sqrt{D}$ are included to rescale the domain width to $\bar{y} \in [-1, 1]$. We propose solutions of the form

$$\begin{aligned}
\bar{u} &= D\left(1 - \mathcal{B}\log(D)\frac{\bar{u}_1(\bar{x}, \bar{y})}{\sqrt{D}} + \cdots\right), \\
\bar{v} &= D\left(-\log(D)\frac{\bar{v}_0(\bar{x}, \bar{y})}{\sqrt{D}} + O(\mathcal{B})\right), \\
\bar{h} &= \frac{1}{\sqrt{D}}\left(1 - \mathcal{B}\log(D)\frac{\bar{h}_1(\bar{x}, \bar{y})}{\sqrt{D}} + \cdots\right), \\
\bar{b} &= \frac{1}{\sqrt{D}}\left(1 - \mathcal{B}\log(D)\frac{\bar{b}_1(\bar{x})}{\sqrt{D}} + \cdots\right),
\end{aligned} \tag{4.41}$$

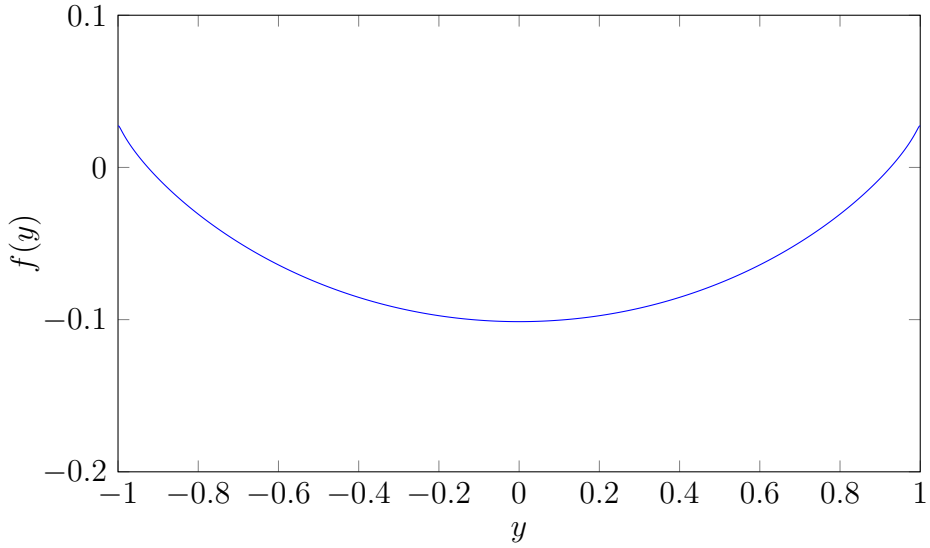

Figure 4.4: Numerical solution $f(y)$ to boundary-layer problem (4.35)–(4.39), which contributes to the correction to the thickness profile (4.30).

where again extra scaling factors have been introduced to remove dependence on D from the resulting problem. Substituting these expansions into the governing equations, we find that the barred variables in the lower boundary layer near $x = 1$ satisfy analogous governing equations to the hatted variables in the upper boundary layer near $x = 0$, and so a second computation to solve these equations in the lower boundary layer is not necessary. Comparing governing equations and boundary conditions for the velocity components, we observe

$$\bar{u}_1(\bar{x}, \bar{y}) = \hat{u}_1(\hat{x}, y), \tag{4.42a}$$

$$\bar{v}_0(\bar{x}, \bar{y}) = \hat{v}_0(\hat{x}, y). \tag{4.42b}$$

Matching the velocity in the lower boundary layer with the bulk velocity as $x \to 1$, we find

$$c_1 = -c_2 \left(1 + \frac{1}{\sqrt{D}}\right). \tag{4.43}$$

We examine the width and thickness in the lower boundary layer by introducing h^* and b^* such that

$$\bar{b}_1(\bar{x}, \bar{y}) = \hat{b}_1(\hat{x}, y) + b^*, \quad \bar{h}_1(\bar{x}, \bar{y}) = \hat{h}_1(\hat{x}, y) + h^*. \tag{4.44}$$

Comparing the governing equations for the barred and hatted quantities we determine that b^* is a constant while h^* is a function of $\bar{y}$ only, and these may be determined by

comparing the far-field matching conditions for the two boundary layers. This then provides the final glass width and thickness,

$$h(1,y) = \frac{1}{\sqrt{D}}\left\{1 + \mathcal{B}\log(D)\left[f(y\sqrt{D}) + \frac{c_2}{2}\right]\left(1 + \frac{1}{\sqrt{D}}\right) + O\left(\mathcal{B}^2\right)\right\}, \tag{4.45a}$$

$$b(1) = \frac{1}{\sqrt{D}}\left\{1 + \mathcal{B}\log(D)\left[c_3 + \frac{c_2}{2}\right]\left(1 + \frac{1}{\sqrt{D}}\right) + O\left(\mathcal{B}^2\right)\right\}, \tag{4.45b}$$

where f is the numerically-determined function plotted in figure 4.4. We note that the thickness variation across the sheet width scales with $\log(D)(1/\sqrt{D} + 1/D)$, which has a maximum at $D = 4.56$ and decreases as D increases beyond this value (see figure 4.5c).

4.5.2 Including surface tension

We can extend the analysis performed in §4.5.1 to the case $\Gamma \neq 0$. In the upper boundary layer we rescale $x = \mathcal{B}\hat{x}$. Adapting the expansions proposed in (4.34) and scaling out the linear terms in the far-field conditions (4.38), we propose solutions of the form

$$\begin{aligned}
\hat{u} &= 1 + \mathcal{B}\kappa\left[\left(1 - \tfrac{\Gamma}{6\kappa}\right)\hat{x} + \left(1 + \tfrac{\Gamma}{3\kappa}\right)\hat{\hat{u}}(\hat{x},y)\right] + \cdots, \\
\hat{v} &= \kappa\left[-\left(\tfrac{1}{2} + \tfrac{\Gamma}{6\kappa}\right)y + \left(1 + \tfrac{\Gamma}{3\kappa}\right)\hat{\hat{v}}(\hat{x},y)\right] + O(\mathcal{B}), \\
\hat{h} &= 1 + \mathcal{B}\kappa\left[-\left(\tfrac{1}{2} - \tfrac{\Gamma}{3\kappa}\right)\hat{x} + \left(1 + \tfrac{\Gamma}{3\kappa}\right)\hat{\hat{h}}(\hat{x},y)\right] + \cdots, \\
\hat{b} &= 1 + \mathcal{B}\kappa\left[-\left(\tfrac{1}{2} + \tfrac{\Gamma}{6\kappa}\right)\hat{x} + \left(1 + \tfrac{\Gamma}{3\kappa}\right)\hat{\hat{b}}(\hat{x})\right] + \cdots,
\end{aligned} \tag{4.46}$$

where the factors $(1 + \Gamma/3\kappa)$ are included to ensure the boundary condition on $\hat{v}$ does not depend on Γ and κ. Similarly, in the lower boundary layer we rescale $x = 1 - \mathcal{B}b_0(1)\bar{x}$, $y = -b_0(1)\bar{y}$ and adapt (4.41) and propose solutions of the form

$$\begin{aligned}
\bar{u} &= D\left(1 - \mathcal{B}\kappa b_0(1)\left[\left(1 - \tfrac{\Gamma b_0(1)}{6\kappa}\right)\bar{x} + \left(1 + \tfrac{\Gamma b_0(1)}{3\kappa}\right)\bar{\bar{u}}(\bar{x},\bar{y})\right] + \cdots\right), \\
\bar{v} &= D\left(-\kappa b_0(1)\left[-\left(\tfrac{1}{2} + \tfrac{\Gamma b_0(1)}{6\kappa}\right)\bar{y} + \left(1 + \tfrac{\Gamma b_0(1)}{3\kappa}\right)\bar{\bar{v}}(\bar{x},\bar{y})\right] + O(\mathcal{B})\right), \\
\bar{h} &= \frac{1}{\sqrt{D}}\left(1 - \mathcal{B}\kappa b_0(1)\left[-\left(\tfrac{1}{2} - \tfrac{\Gamma b_0(1)}{3\kappa}\right)\bar{x} + \left(1 + \tfrac{\Gamma b_0(1)}{3\kappa}\right)\bar{\bar{h}}(\bar{x},\bar{y})\right] + \cdots\right), \\
\bar{b} &= \frac{1}{\sqrt{D}}\left(1 - \mathcal{B}\kappa b_0(1)\left[-\left(\tfrac{1}{2} + \tfrac{\Gamma b_0(1)}{6\kappa}\right)\bar{x} + \left(1 + \tfrac{\Gamma b_0(1)}{3\kappa}\right)\bar{\bar{b}}(\bar{x})\right] + \cdots\right).
\end{aligned} \tag{4.47}$$

In the upper boundary layer the governing equations (4.2) become

$$\hat{\hat{u}}_{\hat{x}} + \hat{\hat{h}}_{\hat{x}} + \hat{\hat{v}}_y = 0, \tag{4.48a}$$

$$\left(4\hat{\hat{u}}_{\hat{x}} + 2\hat{\hat{v}}_y\right)_{\hat{x}} + \left(\hat{\hat{u}}_y + \hat{\hat{v}}_{\hat{x}}\right)_y = 0, \tag{4.48b}$$

$$\left(\hat{\hat{u}}_y + \hat{\hat{v}}_{\hat{x}}\right)_{\hat{x}} + \left(2\hat{\hat{u}}_{\hat{x}} + 4\hat{\hat{v}}_y\right)_y = 0. \tag{4.48c}$$

The free-boundary conditions (4.3) on $y = b(x)$ are transformed to

$$\hat{\hat{v}} = \pm\hat{\hat{b}}_{\hat{x}}, \tag{4.49a}$$

$$\hat{\hat{u}}_y + \hat{\hat{v}}_{\hat{x}} = 0, \tag{4.49b}$$

$$2\hat{\hat{u}}_{\hat{x}} + 4\hat{\hat{v}}_y = 0 \tag{4.49c}$$

on $y = \pm 1$. The feed conditions (4.6) become

$$\hat{\hat{u}} = \hat{\hat{h}} = \hat{\hat{b}} = 0, \quad \hat{\hat{v}} = \frac{y}{2} \tag{4.50}$$

on $\hat{x} = 0$, and the far-field matching conditions as $\hat{x} \to \infty$ are

$$4\hat{\hat{u}}_{\hat{x}} + 2\hat{\hat{v}}_y \sim 0, \tag{4.51a}$$

$$\hat{\hat{u}}_y + \hat{\hat{v}}_{\hat{x}} \sim 0, \tag{4.51b}$$

so the dependence on D and Γ is removed from the upper-boundary-layer problem. In the lower boundary layer the velocity components are again governed by analogous equations to the upper-boundary-layer velocity, with

$$\bar{\hat{u}}(\bar{x}, \bar{y}) = \hat{\hat{u}}(\hat{x}, y), \tag{4.52a}$$

$$\bar{\hat{v}}(\bar{x}, \bar{y}) = \hat{\hat{v}}(\hat{x}, y). \tag{4.52b}$$

The upper-boundary-layer variables $\hat{\hat{u}}$, $\hat{\hat{v}}$, $\hat{\hat{h}}$ and $\hat{\hat{b}}$ and the lower-boundary-layer velocity components $\bar{\hat{u}}$, $\bar{\hat{v}}$ must now be calculated only once. The integration coefficients d_1, d_2, d_3 and $f^*(y)$ may then be inferred from the matching conditions

$$\hat{u}_1 \sim \frac{d_3}{\kappa} + \frac{\Gamma}{\kappa}\left(\frac{2d_1/\kappa + d_2}{3\kappa}\right) \sim c_2, \tag{4.53a}$$

$$\hat{b}_1 \sim \frac{\Gamma}{\kappa}\left(\frac{2d_1/\kappa + d_2}{3\kappa}\right) \sim c_3, \tag{4.53b}$$

$$\hat{h}_1 \sim -\frac{d_3}{\kappa} - \frac{2\Gamma}{\kappa}\left(\frac{2d_1/\kappa + d_2}{3\kappa}\right) + \sqrt{\frac{3}{\kappa}} f^*(y) \sim f(y) \tag{4.53c}$$

as $\hat{x} \to \infty$, and

$$\bar{u}_1 \sim \frac{2d_1 - d_3}{\kappa b_0(1)} - \frac{\Gamma}{\kappa}\left(\frac{2d_1/\kappa + d_1 + d_2 \mathrm{e}^{\kappa/2}}{3\kappa}\right) \sim c_2 \tag{4.54}$$

as $\bar{x} \to \infty$. Meanwhile, the width and thickness components in the lower boundary layer are governed by

$$\bar{\bar{u}}_{\bar{x}} + \bar{\bar{h}}_{\bar{x}} + \bar{\bar{v}}_{\bar{y}} = 0, \tag{4.55a}$$

$$\bar{\bar{v}}(\bar{y} = \pm 1) = \pm \bar{\bar{b}}_{\bar{x}}, \tag{4.55b}$$

together with far-field matching conditions, which may be written

$$\bar{\bar{b}} \sim \frac{1}{1 + \frac{\Gamma b_0(1)}{3\kappa}} \left[-\frac{d_1}{b_0(1)\kappa} - \frac{\Gamma}{\kappa} \left(\frac{2d_1/\kappa + d_1 + d_2 \mathrm{e}^{\kappa/2}}{3\kappa} \right) \right], \tag{4.56a}$$

$$\bar{\bar{h}} \sim \frac{1}{1 + \frac{\Gamma b_0(1)}{3\kappa}} \left[\frac{d_3 - d_1}{b_0(1)\kappa} + \frac{2\Gamma}{\kappa} \left(\frac{2d_1/\kappa + d_1 + d_2 \mathrm{e}^{\kappa/2}}{3\kappa} \right) - \sqrt{D} \sqrt{\frac{3}{\kappa}} f^*(\bar{y}) \right]. \tag{4.56b}$$

Finally, we repeat the procedure used in §4.5.1 in the absence of surface tension, and introduce h^* and b^* such that

$$\bar{\bar{b}}(\bar{x}, \bar{y}) = \hat{\bar{b}}(\hat{x}, y) + b^*, \quad \bar{\bar{h}}(\bar{x}, \bar{y}) = \hat{\bar{h}}(\hat{x}, y) + h^*. \tag{4.57}$$

As before, b^* is a constant and h^* is a function of $\bar{y}$ only, and comparing the boundary conditions for the barred and hatted variables we find that the final width and thickness are given by

$$b(1) = b_0(1) \left\{ 1 - \mathcal{B}\kappa b_0(1) \left[-\left(\frac{1}{2} - \frac{\Gamma b_0(1)}{3\kappa} \right) \bar{x} + \left(1 + \frac{\Gamma b_0(1)}{3\kappa} \right) b^* \right] \right\}, \tag{4.58a}$$

$$h(1, y) = h_0(1) \left\{ 1 - \mathcal{B}\kappa b_0(1) \left[-\left(\frac{1}{2} + \frac{\Gamma b_0(1)}{6\kappa} \right) \bar{x} + \left(1 + \frac{\Gamma b_0(1)}{3\kappa} \right) h^* \right] \right\}, \tag{4.58b}$$

where b^* and h^* are given by

$$b^* = \frac{1}{1 + \frac{\Gamma b_0(1)}{3\kappa}} \left[-\frac{d_1}{b_0(1)\kappa} - \frac{\Gamma}{\kappa} \left(\frac{2d_1/\kappa + d_1 + d_2 e^{\kappa/2}}{3\kappa} \right) \right] - \frac{1}{1 + \frac{\Gamma}{3\kappa}} \frac{\Gamma}{\kappa} \left(\frac{2d_1/\kappa + d_2}{3\kappa} \right), \tag{4.59a}$$

$$h^* = \frac{1}{1 + \frac{\Gamma b_0(1)}{3\kappa}} \left[\frac{d_3 - d_1}{b_0(1)\kappa} + \frac{2\Gamma}{\kappa} \left(\frac{2d_1/\kappa + d_1 + d_2 e^{\kappa/2}}{3\kappa} \right) - \sqrt{D} \sqrt{\frac{3}{\kappa}} f^*(y) \right] - \frac{1}{1 + \frac{\Gamma}{3\kappa}} \left[-\frac{d_3}{\kappa} - \frac{2\Gamma}{\kappa} \left(\frac{2d_1/\kappa + d_2}{3\kappa} \right) + \sqrt{\frac{3}{\kappa}} f^*(y) \right], \tag{4.59b}$$

and d_1, d_2, d_3 and $f^*(y)$ are given by (4.53) and (4.54).

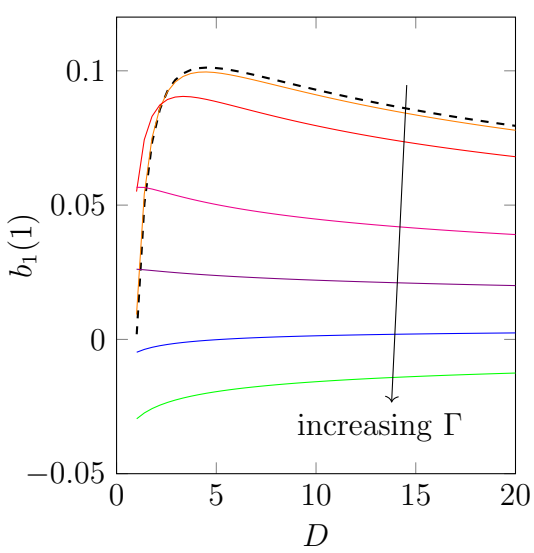

(a) Correction to final sheet width.

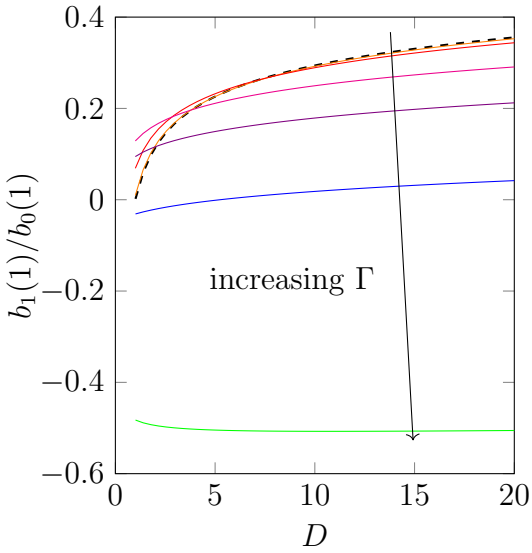

(b) Normalized width correction.

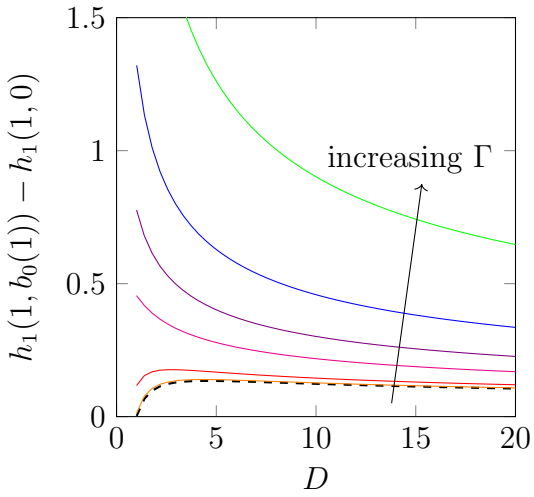

(c) Variation in thickness correction.

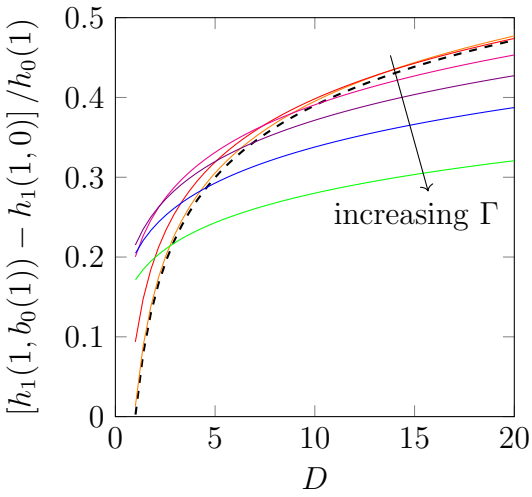

(d) Normalized thickness variation.

Figure 4.5: Correction to final sheet width and thickness (4.45) & (4.58) as a function of draw ratio D for surface tension coefficient $\Gamma = 0.0$ (black dashed), 0.1 (orange), 1.0 (red), 5.0 (magenta), 10.0 (violet), 20.0 (blue) and 50.0 (green).

4.6 Results

For small to moderate values of the surface tension coefficient Γ, the width correction $b_1(1)$ attains a local maximum at some critical draw ratio D, beyond which it decreases (see figure 4.5a). As Γ increases, the correction $b_1(1)$ decreases, except for when the draw ratio $D \approx 1$. For sufficiently large values of Γ, the necking-in effect of surface tension outweighs that of drawing, and the correction $b_1(1)$ becomes negative. In this scenario, the size of the correction decreases monotonically with increasing $D \in [1.001, 20]$. The size of the width correction relative to the leading-order final width $b_1(1)/b_0(1)$ increases as D increases for scenarios where the correction is does not change sign, so that the effect of the finite heater zone is larger for larger draw ratios (see figure 4.5b).

The thickness variation across the sheet $h_1(1, b_0(1)) - h_1(1, 0)$ attains a local maximum at some critical draw ratio D when the surface tension coefficient Γ is small (see figure 4.5c), and for large draw ratios the thickness variation decreases as D increases. The thickness variation increases as the surface tension coefficient Γ increases. The relative thickness change across the sheet width $[h_1(1, b_0(1)) - h_1(1, 0)]/h_0(1)$ increases as the draw ratio D increases (see figure 4.5d), and is maximized at a critical value of surface tension coefficient Γ (see figure 4.6), beyond which it decreases as Γ increases.

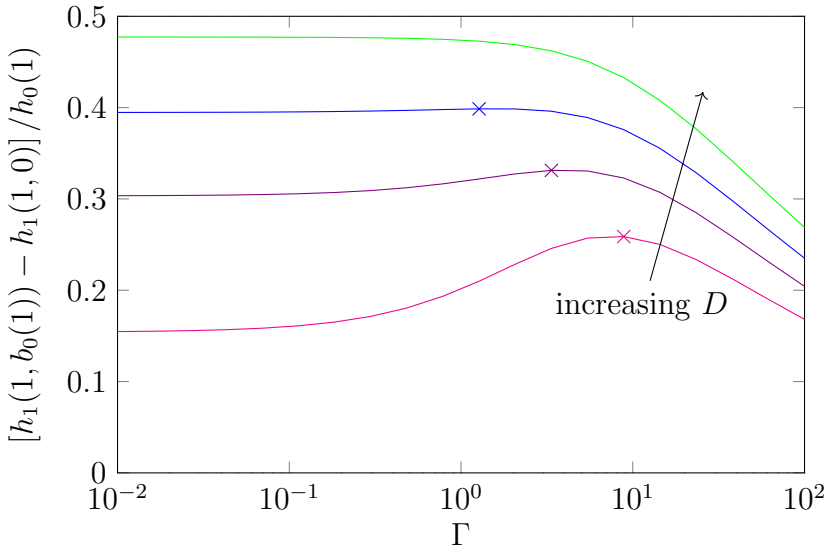

Figure 4.6: Change in thickness correction (4.58b) as a function of the surface tension coefficient Γ, scaled with the leading order thickness (4.20b) for draw ratios $D = 2.0$ (magenta), 5.0 (violet), 10.0 (blue) and 20.0 (green). Local maxima are marked with crosses.

4.7 Comparison with numerical experiments

We now test the validity of our model by comparing our predictions with numerical solutions to a full three-dimensional model for the glass redraw process, supplied by U. Lange at Schott AG. The final sheet profile was determined by solving the three-dimensional Stokes equations with appropriate boundary conditions using the finite-element package Polyflow (Ansys Inc. Polyflow, 2013). Uniform viscosity was prescribed throughout the sheet, and solutions calculated for a range of values of the small parameter $\mathcal{B}$ and draw ratio D, with the thin-sheet parameter $\epsilon = 0.05 \ll 1$.

We consider sheets redrawn at draw ratio $D = 20$ in the absence of surface tension, and plot the difference between the final thickness profile and a uniform profile for varying values of $\mathcal{B}$ (figure 4.7). The coloured lines are the same data as in figure 4.1, but the width and thickness of the sheet are scaled so that the profiles all collapse onto one curve. A black dashed line shows the thickness correction predicted by the asymptotics, given by (4.45a). We note that the agreement is good even when $\mathcal{B}$ is comparable with the thin-sheet parameter ϵ. The change in width as a function of $\mathcal{B}$ is plotted in figure 4.8, and compared with numerical solutions to the three-dimensional Stokes equations for a range of draw ratios D. The data is scaled so that it collapses onto one line for all values of D. The asymptotic prediction (4.45b) is shown as a black dashed line. The agreement between the asymptotics and full numerical solutions is good, especially for small values of $\mathcal{B}$ when the long-heater-zone approximation is valid.

We show the final thickness profile of sheets drawn with surface tension $\Gamma = 1$ in figure 4.9, for $\mathcal{B} = 0.01$, $\mathcal{B} = 0.05$ and $\mathcal{B} = 0.2$. (The data is scaled with $1/\sqrt{D}$ in both directions so that the scaled width and average thickness would both be 1 in the absence of surface tension.) The agreement between the full numerical solution and the two-term asymptotic solution (4.58) is good except for in a region of $O(\epsilon\mathcal{B})$ at the edge of the sheet, where surface tension smooths out the sharp corners. This is not captured by our model, which only gives the leading-order behaviour in the limit $\epsilon\mathcal{B} \ll 1$. This gives rise to an offset in the predicted width compared with the actual width, which persists over all values of $\mathcal{B}$ (see figure 4.9). We plot the final width as a function of draw ratio D for $\mathcal{B} = 0.01$ in figure 4.10, and our asymptotic solution (4.20) gives a good prediction of the trend, but again an offset is present due to the smoothing effect of surface tension in the corners.

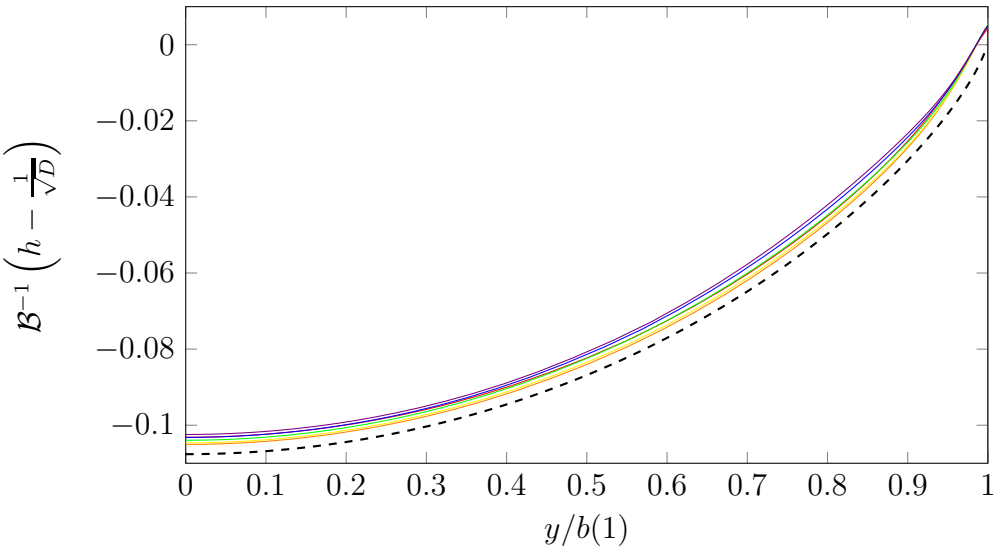

Figure 4.7: Scaled change in thickness for $\mathcal{B} = 0.01$ (red), 0.05 (orange), 0.1 (yellow), 0.2 (green), 0.35 (blue) and 0.5 (violet), with thin-sheet parameter $\epsilon = 0.05$, draw ratio $D = 20$ and $\Gamma = 0$ (no surface tension). The coloured lines are the numerical solution to the three-dimensional Stokes equations computed by U. Lange and the black dotted line gives the asymptotic solution in the limit $\mathcal{B} \to 0$, (4.45a).

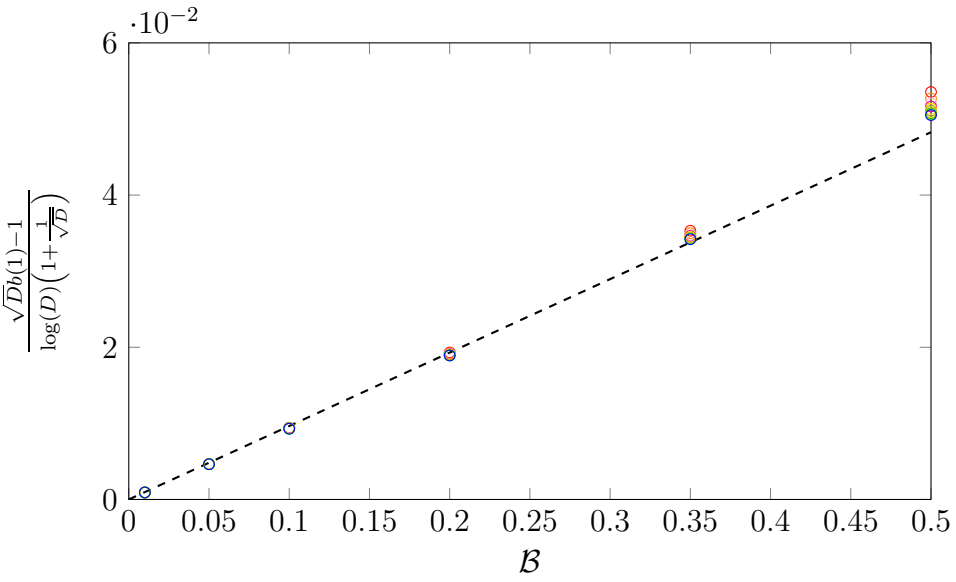

Figure 4.8: Scaled change in width as a function of $\mathcal{B}$. Numerical solutions to the three-dimensional Stokes equations computed by U. Lange are plotted as circles for $D = 5$ (red), $D = 10$ (orange), $D = 15$ (pink), $D = 20$ (magenta), $D = 25$ (yellow), $D = 30$, (brown), $D = 35$ (lime), $D = 40$ (olive), $D = 45$ (green), and $D = 50$ (blue). The asymptotic prediction (4.45b) for the change in width in the limit $\mathcal{B} \to 0$ is given by the black dashed line for the case $\epsilon = 0.05$, $\Gamma = 0$.

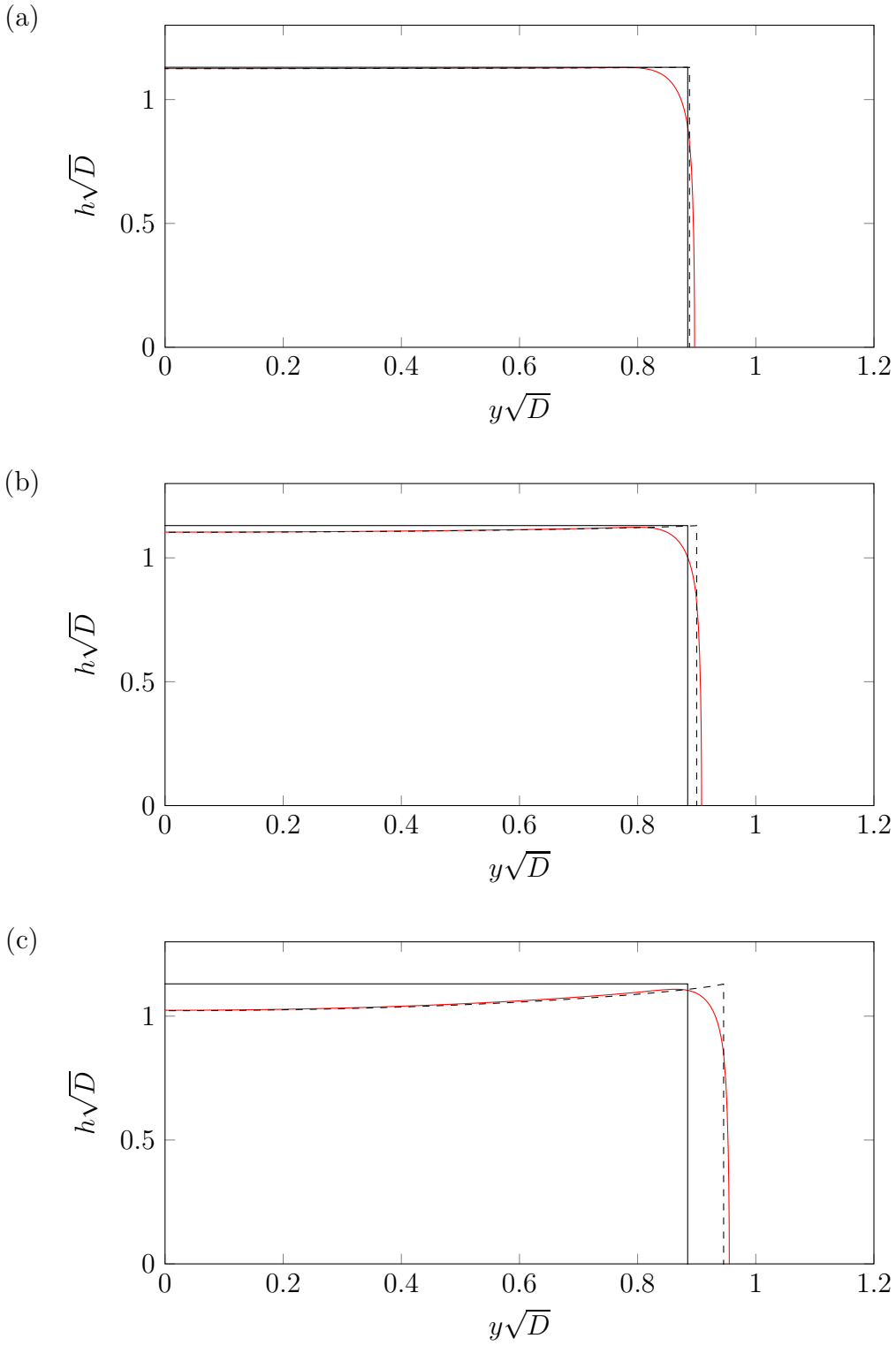

Figure 4.9: Final thickness profile of sheets drawn at draw ratio $D = 20$ with (a) $\mathcal{B} = 0.01$, (b) $\mathcal{B} = 0.05$ and (c) $\mathcal{B} = 0.2$ and surface tension $\Gamma = 1$. Numerical solutions to the full three-dimensional problem computed by U. Lange are shown in red, the black solid lines show the leading-order asymptotic solution in the limit $\mathcal{B} \to 0$ (4.20), and the black dashed lines show the two-term asymptotic solution (4.58).

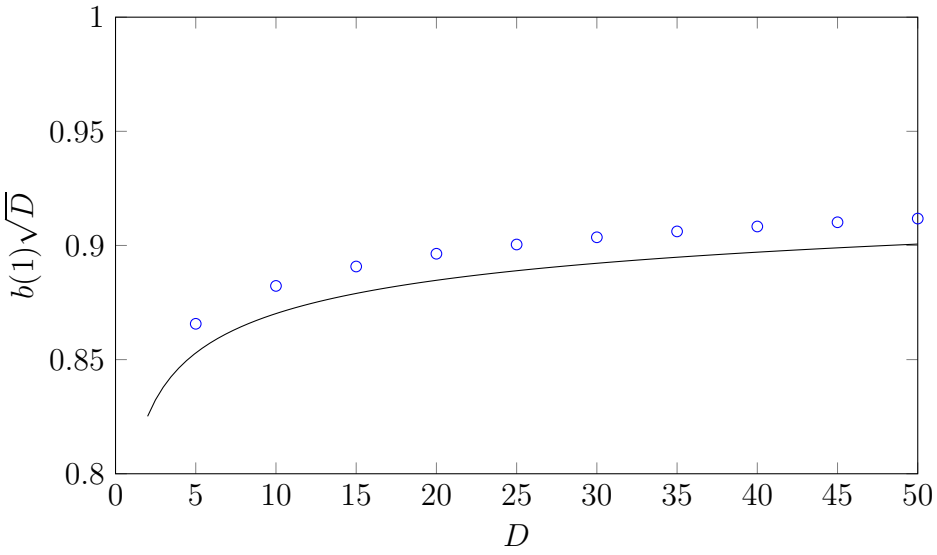

Figure 4.10: Final width of glass sheet redrawn with $\mathcal{B} = 0.01$ and surface tension $\Gamma = 1$ for varying draw ratio D, normalized with the expected final thickness in the absence of surface tension. The blue circles denote numerical solutions to the three-dimensional Stokes equations provided by U. Lange at Schott AG, and the black line gives the leading-order prediction (4.22) in the limit $\mathcal{B} \to 0$.

4.8 Inverse problem

It is natural to ask whether the preform can be modified so that a rectangular final product is obtained. In this long-heater-zone limit, since the thickness variation is of $O(\mathcal{B})$, we propose an optimal preform of dimensions

$$h(0, y) = 1 + \mathcal{B}h_p(y), \quad b(0) = 1 + \mathcal{B}b_p. \tag{4.60}$$

We exploit the fact that the upper and lower boundary layers are analogous, and simply impose boundary conditions on the sheet shape in the lower boundary layer instead of the upper boundary layer, i.e. we set

$$\bar{b} = \bar{h} = 0 \quad \text{at} \quad \bar{x} = 0, \tag{4.61}$$

instead of setting $\hat{h}$ and $\hat{b}$ at $\hat{x} = 0$ in (4.37). It is then straightforward to repeat the comparison between upper and lower boundary layers outlined in §4.5 to determine $h_p(y)$ and b_p. For example, in the absence of surface tension $h_p(y) = h^*(y)/\sqrt{D}$ and $b_p = b^*/\sqrt{D}$, so that the optimal preform is given by

$$h(0, y) = 1 - \mathcal{B}\log(D)\left(1 + \frac{1}{\sqrt{D}}\right)\left(f(y) + \frac{c_2}{2}\right), \tag{4.62a}$$

$$b(0) = 1 - \mathcal{B}\log(D)\left(1 + \frac{1}{\sqrt{D}}\right)\left(c_3 + \frac{c_2}{2}\right), \tag{4.62b}$$

where the constants c_2 and c_3 are given by (4.40) and $f(y)$ is shown in figure 4.4. We note that it is also possible to arrive at this optimal preform by the method employed for a short heater zone in §3.6, i.e. by introducing a "compressive" draw ratio $D^* = 1/D$ and rescaling the variables as appropriate. The linear nature of the long-heater-zone problem simplifies matters even further, and comparing the solutions to the forward (4.45) and inverse (4.62) problems, we see that from a practical point of view one may follow a straightforward procedure when surface tension is negligble: upon observing some thickness variation in a redrawn sheet, determine the thickness variation across its width and remove the same profile from the preform, scaled with a factor $\sqrt{D}$ and stretched across the preform width.

4.9 Discussion

In this chapter we examine the glass redraw process in the limit where the heater zone is long compared with the width of the preform, and investigate how thickness variations across the width of the final product are affected by the length of the heater zone. This analysis, together with the short-heater-zone analysis carried out in Chapter 3, illustrates that thick edges are an endemic problem in the redraw of thin glass sheets, and that a preform with uniform thickness will always redraw to a product that is thicker at the edge than in the centre, regardless of whether it is drawn through a long or short heater zone. We derive a mathematical model to predict how the thickness profile and width of the final product depend on the process parameters, and in particular to quantify the deviation from a preserved aspect ratio that arises in practice due to surface tension, the finite length of the heater zone or a combination of both. We first address the leading-order governing equations in the small aspect ratio of width to length, and find that the preform shape is preserved at leading order in the absence of surface tension, with necking-in of the sheet edges increasing as the importance of surface tension relative to viscous effects increases. In both cases, the final product has uniform thickness at leading order if the preform has uniform thickness. In the absence of surface tension we can make the more general statement that the leading-order final thickness profile matches that of the preform.

By matching between the bulk of the sheet and boundary layers at either end where the solution adjusts rapidly to satisfy the boundary conditions, we determine that the correction terms for a sheet of finite length are of $O(\mathcal{B})$, with $\mathcal{B} =$

preform half-width/heater zone length. Schultz and Davis (1982) have previously bypassed the solution of the boundary-layer problem for a fibre by applying an averaged version of the boundary conditions directly to the bulk solution, but our results indicate that this approach is flawed, as it fails to predict the existence of $O(\mathcal{B})$ terms, instead giving correction terms of $O(\mathcal{B}^2)$. The $O(\mathcal{B})$ corrections can be determined upon numerical solution of the two-dimensional boundary-layer problems at the sheet ends. We find that the governing equations in the two boundary layers are equivalent, and can be rescaled to be independent of the draw ratio and surface tension, so that the problem needs only to be solved once.

We compare our asymptotic results with numerical solutions to the three-dimensional Stokes equations. In the absence of surface tension, the agreement is excellent. Furthermore, the scalings predicted by the asymptotics mean all the numerical data can be collapsed onto one curve for any value of $\mathcal{B}$ and draw ratio D. When surface tension is included, the agreement between numerics and asymptotics is good except for near the corners of the sheet, which are smoothed out by surface tension. Our model relies on a thin-sheet approximation that breaks down in the region at the edge of the sheet where the smoothing effect occurs, and so smoothing can only be resolved by re-examining the governing equations inside this edge region.

We use the two-term asymptotic solution to the long-heater zone problem to investigate how the geometric properties of the final product depend on the process parameters. The size of the higher-order corrections relative to the leading-order solution increases as the draw ratio D increases (for industrially relevant values of D and Γ). The width correction is typically positive, except in the limit where surface tension dominates over drawing, in which case it may be negative. The relative thickness variation across the sheet width is maximized at a critical value of the surface tension coefficient, beyond which it decreases as the effect of surface tension increases. It may therefore be advantageous to increase the effect of surface tension (e.g. by increasing the furnace temperature) to decrease thickness variations, even though the aspect ratio of thickness to width will be altered, since it is more straightforward to alter the aspect ratio of the preform than it is to modify the initial thickness profile.

We restrict our attention to sheets with uniform viscosity in this chapter. An identical methodology may be followed for $\mu = \mu(x)$, and the bulk behaviour may be found in terms of constants to be determined by matching with the boundary layer, although the symmetry between the upper and lower boundary layers no longer holds, since the viscosity profile may be different in the two different boundary layers.

Finally, we address the inverse problem of how to determine the optimal preform shape that will redraw to a sheet of uniform thickness. Similarly to the short-heater-zone case (cf. §3.6), it is possible to pose this inverse problem in terms of the forward problem. In the long-heater-zone case studied here, the inverse problem may be solved in the same computation as the forward problem, with just some extra algebra required to determine the correct adjustment to the preform. Furthermore, in the absence of surface tension it is possible to simply measure the thickness variation in a product redrawn from a rectangular preform, and apply a straightforward scaling to determine the preform modification required, with no computation necessary.

Chapter 5

Gravity-driven buckling of a two-dimensional thin viscous sheet

5.1 Introduction

The buckling of thin viscous sheets has been studied extensively due to its prevalence in everyday life (Mahadevan et al., 1998), industrial manufacturing processes (Batty et al., 2012; Perdigou, 2015), and geophysical flows (Ribe, 2001). In the context of thin glass sheets, the presence of buckling or ripples is highly undesirable, motivating an investigation of the production of ripples during glass drawing. A three-dimensional thin sheet undergoing redraw will typically have regions in which there is pure tension in the plane of the sheet, as well as regions in which there is tension in one direction and compression in another. These compressive forces can, in some cases, give rise to an instability in the sheet shape, leading to out-of-plane buckling. The study of the buckling of such a sheet is complicated by the question of whether a sheet in a given process will buckle in the first place, as well as the feedback between the out-of-plane deformation and the evolving two-dimensional stress field. We begin by considering the simpler canonical problem of the buckling of a two-dimensional glass sheet in the presence of a sufficiently strong gravitational field, in which the sheet experiences tension in one region and compression in another.

The complexity of the mathematical model required for studying centreline deformation of a viscous sheet or thread depends on the size of the deformation. In particular, if the centreline deformation is comparable with the sheet thickness, then a relatively simple "nearly planar" model can be used, while if the deformation is comparable with the sheet length then a more complicated model must be derived, either using a curvilinear coordinate system aligned along the sheet centreline (Buckmaster

et al., 1975) or by performing a transformation to allow continued use of Cartesian coordinates (Howell, 1994).

Buckmaster et al. (1975) consider buckling of a two-dimensional thin viscous sheet whose ends are pushed together at a constant speed (sufficiently slowly that inertia can be neglected) and derive a model for the sheet centreline as a function of time and position. For a small centreline deformation, they note that buckling takes place on a timescale which is a factor ϵ^2 shorter than that associated with stretching of the sheet, where ϵ is the aspect ratio of the sheet, and show that at late times the amplitude of the buckled centreline grows with the square root of time. When the centreline deformation is comparable with the sheet length, an alternative scaling is required and the resulting governing equations are solved numerically. Howell (1994, 1996) notes that even small inertia effects dramatically change the behaviour in the model of Buckmaster et al. (1975), and a buckling lengthscale shorter than the sheet length must be introduced to resolve the behaviour. By identifying the wavelength and growth rate of the fastest-growing mode in a simplified linear centreline equation, Howell (1994, 1996) proposes that the dominant lengthscale is of $O(\epsilon^{2/3}\,\mathrm{Re}^{-1/6})$, where $\mathrm{Re} = \rho LU/\mu$ is the Reynolds number (where ρ is density, L sheet length, U characteristic velocity and μ viscosity), and that the corresponding linear growth rate is of $O(\epsilon^{-2/3}\,\mathrm{Re}^{-1/3})$. Le Merrer et al. (2012) carry out an experimental investigation of the behaviour of a viscous rod whose ends are slowly pushed together in a regime where inertia and gravity are not important, and observe that the rod buckles if its aspect ratio is sufficiently small and surface tension effects are sufficiently weak.

Equations governing the dynamics of a nearly planar three-dimensional thin viscous sheet were derived by Howell (1994, 1996). Pfingstag et al. (2011a) extend this model to include arbitrary external forces, and derive equations governing the stability and response of a planar sheet subject to arbitrary in-plane strain. They find that, in the unstable case, for a fixed, uniform strain rate, the sheet deformation undergoes exponential growth at early times, and at late times grows with the square root of time as predicted by Buckmaster et al. (1975). Pfingstag et al. (2011b) include spatially varying viscosity and show that, if a sheet with a varying viscosity profile that is not symmetric about its centreline is subjected to a prescribed tension, the centreline becomes non-planar even if the tension is positive. They calculate the steady-state centreline shape of such a sheet in the cases of both stretching and compression. Meanwhile, Filippov and Zheng (2010) hypothesize that compressive forces are linked to a change of type in the governing equations from elliptic to hyperbolic,

and calculate 'hyperbolic zones' for a planar three-dimensional thin glass sheet undergoing redraw for two different heater zones. The parts of the sheet under compression are associated with buckling, and so a hyperbolic zone is indicative that ripples may form in that part of the sheet.

Benjamin and Mullin (1988) study buckling of a thin viscous sheet due to shearing in an axisymmetric Couette geometry. Shear is induced in the sheet by rotating one of the boundaries, and ripples appear in the sheet above a threshold speed. Slim et al. (2012) develop a model for this phenomenon in a rectangular geometry and present numerical solutions for the growth rate and phase speed of unstable modes, noting, like Howell (1996), that there is a most unstable mode at an intermediate wavelength.

A substantial body of work has been developed on the buckling of a viscous sheet or jet impinging on a perpendicular plate since the experimental study of Cruickshank and Munson (1981), who measure the periods of folding and coiling of thin sheets and jets of viscous fluid and record the increase of folding/coiling frequency with the length of the falling jet. Cruickshank (1988) and Tchavdarov et al. (1993) develop mathematical models for this buckling phenomenon and predict the heights at which a plane jet and an axisymmetric jet become unstable along with the corresponding period of folding/coiling. Chiu-Webster and Lister (2006) and Morris et al. (2008) modify the standard impinging-jet experiments to observe a falling jet impinging on a perpendicular moving belt, so that the jet is draped along the surface. The unstable buckling modes depend on the fall height, belt speed and viscosity, and the large range of observed modes has caused the apparatus to be dubbed a "fluid-mechanical sewing machine."

In this chapter we consider the buckling of a two-dimensional thin sheet undergoing drawing in the presence of gravity. In a sufficiently weak gravitational field the sheet will experience a positive tension everywhere due to the combined effects of gravity and draw rollers, and undergo steady extensional flow. As the effect of gravity is increased, the sheet velocity increases beyond the draw velocity, and an instability forms. Because the glass sheet cannot escape through the draw rollers as quickly as it arrives, the sheet centreline increases in length and buckles out of plane (cf. figure 5.1), which in turn modifies the tension/compression in the sheet. In this scenario the location of the sheet centreline is fixed by rollers at the top and bottom of the heater zone, in contrast to the studies carried out by authors such as Cruickshank and Munson (1981), in which the point of contact of the sheet (or jet) is free to move across a perpendicular surface. In §5.2 we present a mathematical model for the dynamics of a two-dimensional thin glass sheet buckling due to gravity

while undergoing redraw, and determine the appropriate length and timescales for the study of buckling (reproducing the findings of Howell, 1996). We focus on the special case in which the buckling lengthscale is comparable with the length of the sheet, and discuss suitable initial conditions for the onset of buckling. In §5.3 we determine the steady-state solution, and investigate the effect of process parameters on centreline stability. In §5.4 we present numerical solutions of our simplified model, and analyse the behaviour of the sheet in early- and late-time regimes. The form of the late-time problem is reminiscent of low-Reynolds-number flow past a cylindrical body (Boyd, 1999), in which the appropriate asymptotic expansion is a double series in powers of the small parameter and the logarithm of this small parameter. We adapt the approach of Kropinski et al. (1995), using a hybrid asymptotic–numerical scheme to determine the late-time centreline shape. Finally, in §5.5 we discuss our findings and their implications for a more general study of buckling processes in thin viscous sheets.

5.2 Model derivation

5.2.1 Full dimensional model

We consider a two-dimensional (infinitely wide) nearly planar sheet, and use Cartesian coordinates $\boldsymbol{x} = (x, z)$, with the x-axis aligned with the direction of drawing and z in the transverse direction, as shown in figure 5.1. We consider a sheet with thickness $2h(x,t)$, which undergoes drawing over a distance L in the x-direction, with gravity also acting in the positive x-direction. We denote the sheet centreline by $H(x,t)$, so that the glass surfaces are located at $z = z^{\pm} := H(x,t) \pm h(x,t)$ for $0 < x < L$. In industrial processes of interest, the Reynolds number is invariably small ($\mathrm{Re} \lesssim 10^{-4}$), and the sheet is thin compared with the length over which it is drawn. We exploit the geometry of the sheet to derive a simplified model for out-of-plane buckling, noting that inertia terms may be promoted to leading order if buckling takes place over a sufficiently short timescale.

We assume the glass is Newtonian and incompressible, and therefore governed by the Navier–Stokes equations

$$\nabla \cdot \boldsymbol{u} = 0, \tag{5.1a}$$

$$\rho \frac{\mathrm{D}\boldsymbol{u}}{\mathrm{D}t} = \nabla \cdot \boldsymbol{\sigma} + \rho g \hat{\boldsymbol{\imath}}. \tag{5.1b}$$

Here $\boldsymbol{u} = (u, w)$ is the velocity vector, $\nabla = (\partial/\partial x, \partial/\partial z)$ is the two-dimensional gradient operator, $\mathrm{D}/\mathrm{D}t = \partial/\partial t + \boldsymbol{u} \cdot \nabla$ is the convective derivative and $\hat{\boldsymbol{\imath}}$ is a unit

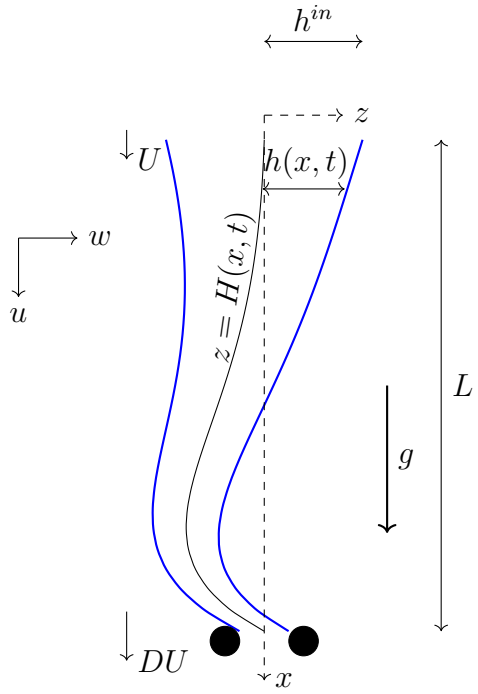

Figure 5.1: Two-dimensional glass sheet with thickness $2h(x,t)$ undergoing redraw over a distance L in the x-direction subject to gravity g, also acting in the x-direction. The sheet has velocity $\boldsymbol{u} = (u, w)$ with feed speed $u = U$ and draw speed $u = DU$, and centreline $z = H(x,t)$.

vector in the x-direction. The stress tensor is given by

$$\boldsymbol{\sigma} = -p\mathbb{I} + \mu\left(\nabla\boldsymbol{u} + (\nabla\boldsymbol{u})^T\right), \tag{5.2}$$

with p denoting pressure, $\mathbb{I}$ the identity matrix and μ the viscosity. In practice glass has a strongly temperature-dependent viscosity (cf. Chapter 2). However, our focus here is on the fundamental fluid-mechanical processes involved in buckling, and we assume for simplicity that the sheet has uniform viscosity μ throughout this chapter.

A glass sheet with initial thickness $2h_{in}$ is fed into the stretching zone at a speed U. We assume it is "simply-supported", that is, no bending moment is applied, so that the inlet conditions are

$$h = h_{in}, \quad u = U, \quad H = H_{xxt} = 0 \quad \text{at} \quad x = 0. \tag{5.3}$$

Over the length of the stretching zone the velocity is increased by a factor D through the combined action of gravity and draw rollers applied to the sheet at $x = L$. We assume the sheet is again simply-supported at the draw rollers so that

$$u = DU, \quad H = H_{xxt} = 0 \quad \text{at} \quad x = L. \tag{5.4}$$

On the free surfaces $z = z^{\pm}$, we impose kinematic and no-stress conditions

$$\frac{\mathrm{D}}{\mathrm{D}t}\left(z - z^{\pm}\right) = 0, \quad \boldsymbol{\sigma} \cdot \hat{\boldsymbol{n}} = \mathbf{0}, \tag{5.5}$$

where $\hat{\boldsymbol{n}}$ is the unit vector normal to the free surface. We neglect the effect of surface tension under the assumption that the capillary number $\mathrm{Ca} = \mu U/\gamma \gg 1$, where γ is surface tension (typically $\mathrm{Ca} \approx 10^2$).

We also need initial conditions for this time-dependent problem; we will discuss how these might be chosen in §5.3.

5.2.2 Non-dimensionalization

We define the aspect ratio of the sheet

$$\epsilon = \frac{\text{initial half-thickness}}{\text{length of drawing process}} = \frac{h_{in}}{L}. \tag{5.6}$$

The thickness is always much smaller than the length in glass drawing processes, so we assume that $\epsilon \ll 1$. We introduce dimensionless length variables

$$(x', z') = \left(\frac{x}{L}, \frac{z}{\epsilon L}\right), \quad h' = \frac{h}{\epsilon L}, \quad H' = \frac{H}{\epsilon L}, \quad (z^{\pm})' = \frac{z^{\pm}}{\epsilon L}. \tag{5.7}$$

However, the wavelength of buckling may be much shorter than the length of the sheet L, so we introduce an additional length variable

$$\xi = \epsilon^{-\theta}\frac{x}{L}, \tag{5.8}$$

where θ is an unknown scalar which characterizes the buckling wavelength. We will assume all variables with x-dependence now depend on x' and ξ and perform a multiple scales analysis. The feed speed U provides a natural choice for the non-dimensionalization of speed in the x-direction. If the sheet were undergoing stretching with a fixed centreline, a sensible scaling for transverse motion would be ϵU, but when the sheet undergoes centreline deformation it is not obvious *a priori* how large the out-of-plane velocity w will be, so we introduce

$$(u', w') = \left(\frac{u}{U}, \epsilon^{\beta}\frac{w}{\epsilon U}\right), \tag{5.9}$$

where β, along with the length scaling exponent θ, will be determined by requiring a dominant balance in the governing equations. The two different velocity scalings provide two natural timescales

$$t' = \frac{t}{L/U}, \quad \tau = \epsilon^{-\beta}\frac{t}{L/U}, \tag{5.10a,b}$$

the first associated with the time taken for glass to move through the heater zone, and the second a characteristic timescale for buckling of the sheet. This motivates a multiple scales analysis with two separate timescales as well as two separate lengthscales. Finally, we non-dimensionalize pressure according to

$$p' = \frac{p}{\mu U/L}. \tag{5.11}$$

In the absence of inertia only one lengthscale is needed ($\theta = 0$), and it is well known (see, for example Buckmaster et al., 1975) that the correct scaling for time is ϵ^2 (i.e. $\beta = 2$). This can be explained physically by considering the role of the in-plane velocity in buckling of a thin sheet or filament. When the leading-order in-plane velocity is uniform across the sheet thickness, the flow is extensional and the glass moves in the x-direction. For the sheet to bend, the velocity must be larger at one surface than the other. Returning to the Trouton model derived for a two-dimensional thin sheet undergoing extensional flow in §2.2, we see that the leading-order in-plane velocity is uniform across the sheet thickness by the in-plane momentum equation (2.10b). By contrast, if the size of the out-of-plane velocity w is increased by a factor ϵ^{-2}, the leading-order in-plane velocity may vary across the sheet thickness and the sheet bends. Since the out-of-plane velocity is larger by a factor ϵ^{-2} in problems with buckling than problems with extensional flow, the timescale for out-of-plane buckling is shorter than the timescale for stretching by a factor ϵ^2. When inertia is included in the problem the correct scalings are less obvious, and we take a more careful approach. However, we expect the same principle to apply, namely that bending only occurs if the in-plane velocity varies across the sheet thickness in the correct way.

Inserting the new dimensionless variables into the governing equations (5.1) and dropping primes from the notation yields

$$\epsilon^{-\theta} u_\xi + u_x + \epsilon^{-\beta} w_z = 0, \tag{5.12a}$$

$$\begin{aligned}\epsilon^{\phi}\overline{\mathrm{Re}}\left(\epsilon^{-\beta}u_\tau + u_t + \epsilon^{-\theta}uu_\xi + uu_x + \epsilon^{-\beta}wu_z\right) = \\ \left(-\epsilon^{-\theta}p + 2\epsilon^{-2\theta}u_\xi + 2\epsilon^{-\theta}u_x\right)_\xi + \left(-p + 2\epsilon^{-\theta}u_\xi + 2u_x\right)_x \\ + \left(\epsilon^{-2}u_z + \epsilon^{-\beta-\theta}w_\xi + \epsilon^{-\beta}w_x\right)_z + \mathrm{St},\end{aligned} \tag{5.12b}$$

$$\begin{aligned}\epsilon^{\phi+2}\overline{\mathrm{Re}}\left(\epsilon^{-\beta}w_\tau + w_t + \epsilon^{-\theta}uw_\xi + uw_x + \epsilon^{-\beta}ww_z\right) = (-\epsilon^{\beta}p + 2w_z)_z + \\ (\epsilon^{\beta-\theta}u_z + \epsilon^{2-2\theta}w_\xi + \epsilon^{2-\theta}w_x)_\xi + (\epsilon^{\beta}u_z + \epsilon^{2-\theta}w_\xi + \epsilon^{2}w_x)_x,\end{aligned} \tag{5.12c}$$

where $\phi > 0$ is chosen to characterize the smallness of the Reynolds number

$$\mathrm{Re} = \frac{\rho L U}{\mu} = \epsilon^{\phi}\overline{\mathrm{Re}} \ll 1, \tag{5.13}$$

with $\overline{\mathrm{Re}} = O(1)$, and the Stokes number

$$\mathrm{St} = \frac{\rho g L^2}{\mu U} \tag{5.14}$$

gives the ratio of gravity to viscous forces. We anticipate that, even if $\mathrm{Re} \ll 1$, inertia may play a role on the short buckling timescale τ given by (5.10b) (Howell, 1994, 1996).

The inlet conditions (5.3) on $x = 0$ become

$$u = h = 1, \quad H = \left(\epsilon^{-\beta}\frac{\partial}{\partial\tau} + \frac{\partial}{\partial t}\right)\left(\epsilon^{-\theta}\frac{\partial}{\partial\xi} + \frac{\partial}{\partial x}\right)^2 H = 0, \tag{5.15}$$

while the outlet conditions (5.4) are transformed to

$$u = D, \quad H = \left(\epsilon^{-\beta}\frac{\partial}{\partial\tau} + \frac{\partial}{\partial t}\right)\left(\epsilon^{-\theta}\frac{\partial}{\partial\xi} + \frac{\partial}{\partial x}\right)^2 H = 0, \tag{5.16}$$

on $x = 1$. The no-flux and no-stress conditions (5.5) on the free surfaces $z = z^{\pm}$ become

$$\left(\epsilon^{-\beta}z_{\tau}^{\pm} + z_t^{\pm}\right) + \left(\epsilon^{-\theta}z_{\xi}^{\pm} + z_x^{\pm}\right)u = \epsilon^{-\beta}w, \tag{5.17a}$$

$$\left(\epsilon^{-\theta}z_{\xi}^{\pm} + z_x^{\pm}\right)\left(-p + 2\epsilon^{-\theta}u_{\xi} + 2u_x\right) = (\epsilon^{-2}u_z + \epsilon^{-\beta-\theta}w_{\xi} + \epsilon^{-\beta}w_x), \tag{5.17b}$$

$$\left(\epsilon^{-\theta}z_{\xi}^{\pm} + z_x^{\pm}\right)(\epsilon^{\beta}u_z + \epsilon^{2-\theta}w_{\xi} + \epsilon^2 w_x) = (-\epsilon^{\beta}p + 2w_z). \tag{5.17c}$$

5.2.3 Characteristic lengthcales and timescales

An equation governing the motion of the centreline of the sheet $H(x, t, \xi, \tau)$ may be derived by multiplying both sides of the momentum balance in the direction of drawing (5.12b) by $(z-H)$ and integrating across the sheet thickness (using boundary condition (5.17b)). Omitting the workings for brevity, we differentiate in the direction of drawing and apply the transverse momentum equation (5.12c) and corresponding

boundary condition (5.17c), to give

$$\begin{aligned}
&\epsilon^{\phi}\bar{\mathrm{Re}}\left(\epsilon^{-\theta}\frac{\partial}{\partial\xi}+\frac{\partial}{\partial x}\right)\int_{z^-}^{z^+}\left(\epsilon^{-\beta}u_\tau+u_t\right)(z-H)\,\mathrm{d}z\\
&\quad+\epsilon^{\phi}\bar{\mathrm{Re}}\left(\epsilon^{-\theta}\frac{\partial}{\partial\xi}+\frac{\partial}{\partial x}\right)\int_{z^-}^{z^+}\left(\epsilon^{-\theta}uu_\xi+uu_x+\epsilon^{-\beta}wu_z\right)(z-H)\,\mathrm{d}z=\\
&\qquad\left(\epsilon^{-\theta}\frac{\partial}{\partial\xi}+\frac{\partial}{\partial x}\right)^2\int_{z^-}^{z^+}(z-H)\left(-p+2\epsilon^{-\theta}u_\xi+2u_x\right)\mathrm{d}z\\
&\quad+\left(\epsilon^{-\theta}\frac{\partial}{\partial\xi}+\frac{\partial}{\partial x}\right)\left[\left(\epsilon^{-\theta}H_\xi+H_x\right)\int_{z^-}^{z^+}\left(-p+2\epsilon^{-\theta}u_\xi+2u_x\right)\mathrm{d}z\right]\\
&\qquad-\epsilon^{\phi-\beta}\overline{\mathrm{Re}}\int_{z^-}^{z^+}\left(\epsilon^{-\beta}w_\tau+w_t+\epsilon^{-\theta}uw_\xi+uw_x+\epsilon^{-\beta}ww_z\right)\mathrm{d}z. \quad (5.18)
\end{aligned}$$

On the left-hand side of this centreline equation are inertia terms, while on the right-hand side the first term is a bending term, the second a tension/compression term and the third an inertia term. Examining the bending term we observe that, if the pressure and in-plane velocity are symmetric about the centreline, then this term will integrate to zero and there will be no bending – this is consistent with our observation that we must choose scalings so that u has the correct z-dependence. We seek the lengthscale and timescale for which bending, tension and inertia balance at leading order. We investigate this by performing an asymptotic analysis in the thin-sheet limit $\epsilon \to 0$ for an arbitrary choice of short lengthscale and short timescale. We quote the main results here, and give details in Appendix A.

Note that we only consider regimes in which $\phi > 0$, so that the Reynolds number $\mathrm{Re} \ll 1$, and in which $\beta, \theta \geq 0$, so that the timescale and lengthscale for buckling are shorter than or the same as those for stretching. If $\beta < 0$ buckling would be extremely slow (in particular, the buckling timescale would be longer than the stretching timescale), while if $\theta < 0$ the predicted lengthscale would be much longer than the distance between the rollers holding the sheet in place, which is inconsistent. In that case the buckling lengthscale is controlled by the distance between the draw rollers rather than a balance between the three effects in (5.18).

The largest contribution from the inertia terms in the centreline equation (5.18) is $O\left(\max\left(\epsilon^{\phi-2\theta}, \epsilon^{\phi-2\beta}\right)\right)$, depending on whether θ or β is larger. For inertia, bending and tension to balance, we require

$$\max\left(\epsilon^{\phi-2\theta}, \epsilon^{\phi-2\beta}\right) \sim \left(\epsilon^{-\theta}\frac{\partial}{\partial\xi}+\frac{\partial}{\partial x}\right)^2\mathcal{M} \sim \left(\epsilon^{-\theta}\frac{\partial}{\partial\xi}+\frac{\partial}{\partial x}\right)\left[\left(\epsilon^{-\theta}H_\xi+H_x\right)\mathcal{T}\right], \quad (5.19)$$

where

$$\mathcal{T} = \int_{z^-}^{z^+} \left(-p + 2\epsilon^{-\theta} u_\xi + 2u_x\right) \mathrm{d}z \tag{5.20}$$

is the tension in the sheet and

$$\mathcal{M} = \int_{z^-}^{z^+} (z - H) \left(-p + 2\epsilon^{-\theta} u_\xi + 2u_x\right) \mathrm{d}z \tag{5.21}$$

is the bending moment.

By careful asymptotic analysis of the governing equations (5.12)–(5.17) (see Appendix A), we can show that $\theta < \beta$, and that either

- $\theta = 0$ so there is only one lengthscale, or
- $0 < \theta < 1$ so the buckling lengthscale is between the sheet length and the sheet thickness. In this case the leading-order velocity does not change over the short (buckling) lengthscale.

In both scenarios, we find that the tension $\mathcal{T} = O(1)$, so that inertia and tension balance in (5.19) if

$$\phi - 2\beta = -2\theta. \tag{5.22}$$

The bending term in (5.19) only balances with the tension and inertia terms if the bending moment $\mathcal{M} = O(1)$, i.e. if the in-plane velocity varies across the sheet thickness. Comparing the two σ_{xz} terms in (5.12c) we observe that this corresponds to (see Appendix A for details)

$$\beta + 2\theta - 2 = 0. \tag{5.23}$$

Combining the two balance conditions (5.22) and (5.23), we find

$$\theta = \frac{2}{3} - \frac{\phi}{6}, \quad \beta = \frac{2}{3} + \frac{\phi}{3}, \tag{5.24}$$

provided $\phi \leq 4$, so the lengthscale and timescale associated with buckling for a given Reynolds number are

$$\text{lengthscale} \sim \epsilon^{2/3}\,\mathrm{Re}^{-1/6}, \quad \text{timescale} \sim \epsilon^{2/3}\,\mathrm{Re}^{1/3}\,. \tag{5.25}$$

These are the same scalings obtained by Howell (1994) by examining the fastest-growing mode in a simplified linear-stability problem. Increasing the Reynolds number gives buckling with shorter wavelengths and shorter timescales. For sufficiently small Reynolds numbers, $\mathrm{Re} = o(\epsilon^4)$, the predicted lengthscale is longer than the size of the sheet, and we cannot balance all three effects. In particular, the inertia term

does not enter the centreline equation at leading order, and tension and bending are balanced by the timescale choice

$$\text{timescale} \sim \epsilon^2. \tag{5.26}$$

This is the scaling proposed by Buckmaster et al. (1975) for scenarios where inertia is not important.

5.2.4 $\mathrm{Re} = O(\epsilon^4)$ regime

In the remainder of this chapter we will consider the regime in which $\mathrm{Re} = O(\epsilon^4)$ (i.e. $\phi = 4$), so that inertia plays a role on the bending timescale, but the lengthscale for buckling is the same as the length of glass undergoing drawing. This corresponds to the choice $\beta = 2$, $\theta = 0$ in the non-dimensionalization (5.6)–(5.11). We determined these scalings by focusing on the moment balance in the sheet, and we now consider the mass and force balances in the sheet to derive a full system of governing equations in the thin-sheet limit. In the $\mathrm{Re} = O(\epsilon^4)$ regime, the mass and momentum equations (5.12) may be rewritten

$$u_x + \epsilon^{-2} w_z = 0, \tag{5.27a}$$

$$\epsilon^4 \bar{\mathrm{Re}} \left(\epsilon^{-2} u_\tau + u_t + u u_x + \epsilon^{-2} w u_z\right) = \left(-p + 2u_x\right)_x + \epsilon^{-2} \left(u_z + w_x\right)_z + \mathrm{St}, \tag{5.27b}$$

$$\epsilon^4 \bar{\mathrm{Re}} \left(\epsilon^{-2} w_\tau + w_t + u w_x + \epsilon^{-2} w w_z\right) = \left(u_z + w_x\right)_x + \left(-p + 2\epsilon^{-2} w_z\right)_z \tag{5.27c}$$

and the free-boundary conditions (5.17) become

$$\epsilon^{-2} z^\pm_\tau + z^\pm_t + u z^\pm_x = \epsilon^{-2} w, \tag{5.28a}$$

$$z^\pm_x \left(-p + 2u_x\right) = \epsilon^{-2} \left(u_z + w_x\right), \tag{5.28b}$$

$$z^\pm_x \left(u_z + w_x\right) = \left(-p + 2\epsilon^{-2} w_z\right). \tag{5.28c}$$

The centreline equation (5.18) is simplified to

$$\begin{aligned} \epsilon^4 \bar{\mathrm{Re}} \frac{\partial}{\partial x} \int_{z^-}^{z^+} (z - H) \left(\epsilon^{-2} u_\tau + u_t + u u_x + \epsilon^{-2} w u_z\right) \,\mathrm{d}z = \\ \frac{\partial^2}{\partial x^2} \int_{z^-}^{z^+} (z - H) \left(-p + 2u_x\right) \mathrm{d}z + \frac{\partial}{\partial x} \left[H_x \int_{z^-}^{z^+} \left(-p + 2u_x\right) \mathrm{d}z\right] \\ - \epsilon^2 \overline{\mathrm{Re}} \int_{z^-}^{z^+} \left(\epsilon^{-2} w_\tau + w_t + u w_x + \epsilon^{-2} w w_z\right) \,\mathrm{d}z. \end{aligned} \tag{5.29}$$

Integrating the mass equation (5.27a) across the sheet thickness and applying the no-flux condition (5.28a) we find

$$w^{(0)} = H_\tau^{(0)}, \quad h_\tau^{(0)} = 0, \tag{5.30}$$

so the sheet thickness remains fixed over the buckling timescale. The thickness profile is therefore given by the initial conditions. In reality these initial conditions may be quite difficult to determine, as they are a solution of a time-dependent problem on the original stretching timescale, and this problem depends on the route by which the system approaches the unstable regime. We consider three idealized scenarios:

(i) Redraw is attempted on a sheet of uniform thickness in the presence of gravity. This configuration is unstable and immediately undergoes buckling, with $h^{(0)} \equiv 1$.

(ii) Redraw is performed on a sheet in the presence of gravity, with the centreline held fixed so that the thickness and velocity reach steady-state profiles. At $t = 0$ the centreline is released and the sheet undergoes buckling. This scenario is appropriate if the centreline is held fixed by some mechanism, or if the sheet first reaches steady-state drawing at a stable draw ratio, which is then gradually decreased towards instability.

(iii) Redraw is performed on a sheet in the absence of gravity, so that the thickness and velocity acquire steady-state profiles for gravity-free drawing. At $t = 0$ gravity is "switched on" and the sheet buckles. Although this scenario is unlikely in the case of glass manufacture, this or a similar setup may be relevant in other systems in which a sheet is drawn or a fibre spun in a bath of another liquid, e.g. spinning of polymer fibres for use in tissue engineering, where water is used as as coagulant during the spinning process (see, for example Wang et al., 1996).

Interestingly, the threshold for instability is slightly different in each of these scenarios; we discuss this further in §5.3.

Evaluating the force balance in the direction of drawing (5.27b) and corresponding no-stress condition (5.28b) we find

$$u_z^{(0)} + w_x^{(0)} = 0, \tag{5.31}$$

so that integrating across the sheet thickness and using (5.30) to substitute for the out-of-plane velocity yields

$$u^{(0)} = \bar{u}^{(0)} - (z - H^{(0)})H_{x\tau}^{(0)}, \tag{5.32}$$

where

$$\bar{u}^{(0)} = \frac{1}{2h^{(0)}} \int_{z^{-(0)}}^{z^{+(0)}} u^{(0)} \, \mathrm{d}z \tag{5.33}$$

is the velocity averaged across the sheet thickness, so the leading-order in-plane velocity now varies linearly across the sheet thickness. We determine the leading-order pressure by evaluating the out-of-plane momentum equation (5.27c) and applying no-stress condition (5.28c) to find

$$p^{(0)} = -2\left[\bar{u}_x^{(0)} + H_x^{(0)} H_{x\tau}^{(0)} - (z - H^{(0)}) H_{xx\tau}^{(0)}\right], \tag{5.34}$$

so that integrating the in-plane momentum equation (5.27b) over the sheet thickness and applying (5.28b) yields

$$\left[4h^{(0)}\left(\bar{u}_x^{(0)} + H_x^{(0)} H_{x\tau}^{(0)}\right)\right]_x = -\,\mathrm{St}\, h^{(0)}, \tag{5.35}$$

and the centreline equation (5.29) yields

$$\overline{\mathrm{Re}} h^{(0)} H_{\tau\tau}^{(0)} + \left(\frac{4}{3} h^{(0)3} H_{xx\tau}^{(0)}\right)_{xx} = \left[4h^{(0)} H_x^{(0)}\left(\bar{u}_x^{(0)} + H_x^{(0)} H_{x\tau}^{(0)}\right)\right]_x. \tag{5.36}$$

Evaluating the boundary conditions (5.15) and (5.16) on the velocity and thickness at leading order, we find

$$u^{(0)} = h^{(0)} = 1 \quad \text{on} \quad x = 0, \tag{5.37a}$$

$$u^{(0)} = D \quad \text{on} \quad x = 1. \tag{5.37b}$$

Integrating (5.35) in the direction of drawing x, we find that the tension in the sheet is

$$4h^{(0)}\left(\bar{u}_x^{(0)} + H_x^{(0)} H_{x\tau}^{(0)}\right) = \mathrm{St} \int_x^1 h^{(0)}(s)\mathrm{d}s + c(\tau), \tag{5.38}$$

where $c(\tau)$ corresponds to the force on the sheet at $x = 1$: if $c(\tau) < 0$ then the force is in the upward direction so some portion of the sheet is under compression, and the centreline is susceptible to buckling. (This may be confirmed by solving the associated linear-stability problem given by (5.63).) Integrating (5.38) and applying boundary conditions (5.37), we find that this force is given by

$$c(\tau) = \frac{D - 1 - \int_0^1 \frac{1}{4h^{(0)}} \left(\int_x^1 \mathrm{St}\, h^{(0)} \mathrm{d}s\right) \mathrm{d}x + \int_0^1 H_x^{(0)} H_{x\tau}^{(0)} \mathrm{d}x}{\int_0^1 \mathrm{d}x / 4h^{(0)}}. \tag{5.39}$$

We may obtain a single non-local equation for the centreline $H^{(0)}$ by substituting (5.38), (5.39) into the moment balance (5.36) to give

$$\overline{\mathrm{Re}} h^{(0)} H_{\tau\tau}^{(0)} + \left(\frac{4}{3} h^{(0)3} H_{xx\tau}^{(0)}\right)_{xx} = \left[H_x^{(0)}\left(\int_x^1 \mathrm{St}\, h^{(0)}(s)\mathrm{d}s + c(\tau)\right)\right]_x. \tag{5.40}$$

Finally, evaluating the boundary conditions (5.15) and (5.16) on the centreline at leading order, we find

$$H^{(0)} = H^{(0)}_{xx\tau} = 0 \quad \text{on} \quad x = 0,\ 1. \tag{5.41}$$

We drop superscripts from the notation and use leading-order (in ϵ) equations only in the remainder of this chapter.

We note that the model derived here will break down once the centreline deformation is sufficiently large that $H = O(1/\epsilon)$. Once that regime is reached, the centreline deformation should be scaled with the sheet length rather than its thickness, and additional nonlinearities are promoted into the leading-order governing equations (see Chapter 3 of Howell, 1994, for details of the nonlinearities).

5.3 Steady state

On the timescale for buckling, the thickness of the sheet does not change while the velocity of the sheet evolves from an initial profile. The thickness and initial velocity are determined by the behaviour of the sheet on the longer stretching timescale. In this section, we will determine the steady-state solution on this longer stretching timescale, when $H \equiv 0$, and the velocity and thickness are the solution to

$$\bar{u}h = 1, \tag{5.42a}$$

$$(4h\bar{u}_x)_x = -\operatorname{St} h, \tag{5.42b}$$

with boundary conditions

$$\bar{u} = h = 1 \quad \text{on} \quad x = 0, \tag{5.43a}$$

$$\bar{u} = D \quad \text{on} \quad x = 1. \tag{5.43b}$$

We note that these equations correspond to a steady-state Trouton model with gravity (Howell, 1994). In the absence of gravity, $\operatorname{St} = 0$, the thickness and velocity profiles are well known (Scheid et al., 2009) and given by

$$\bar{u} = D^x, \quad h = D^{-x}, \tag{5.44}$$

while for $\operatorname{St} \neq 0$,

$$\bar{u} = \left(\frac{\operatorname{St}}{2a}\right) \sin^2\left(\frac{\sqrt{a}}{2}x + \sin^{-1}\sqrt{\frac{2a}{\operatorname{St}}}\right), \tag{5.45a}$$

$$h = \left(\frac{2a}{\operatorname{St}}\right) \frac{1}{\sin^2\left(\frac{\sqrt{a}}{2}x + \sin^{-1}\sqrt{\frac{2a}{\operatorname{St}}}\right)}, \tag{5.45b}$$

where a satisfies the transcendental equation

$$D = \left(\frac{\mathrm{St}}{2a}\right) \sin^2 \left(\frac{\sqrt{a}}{2} + \sin^{-1} \sqrt{\frac{2a}{\mathrm{St}}} \right). \tag{5.46}$$

The stability of this steady-state solution depends on whether or not a portion of the sheet is under compression. This is most likely to occur near $x = 1$, as the contribution to the tensile force due to gravity is minimized. At $x = 1$, the force on the sheet is given by

$$c = \frac{D - 1 - \int_0^1 \frac{1}{4h} \left(\int_x^1 \mathrm{St}\, h \, \mathrm{d}s \right) \mathrm{d}x}{\int_0^1 \mathrm{d}x/4h}. \tag{5.47}$$

If $c > 0$, the force is positive and the whole sheet is under tension, and therefore stable to centreline perturbations. If $c < 0$ then at least some of the sheet is under compression, and the sheet is unstable to centreline perturbations. We determine the neutral stability curve separating regions of stability and instability by finding the draw ratio D for which $c = 0$ for each of the idealized scenarios (i)–(iii) introduced in §5.2.4 (see figure 5.2). We note that the neutral stability curve is determined by the interplay between drawing and gravity, i.e. the parameters St and D; inertia does not affect whether the sheet is stable or unstable. When $\mathrm{St} \lesssim 10$, the neutral stability curves are almost indistinguishable for the three scenarios, and the critical draw ratio below which the sheet is unstable is close to 1. As St increases further, the three curves diverge: the critical draw ratio is highest for scenario (i), in which the thickness $h \equiv 1$, and lowest for scenario (iii), in which the sheet evolves first in the absence of gravity. It is noteworthy that neutral stability curves for (i) (red dashed) and (ii) (blue) are significantly different: stable drawing can be achieved at much lower draw ratios (or much higher St) if the sheet first evolves to a steady-state thickness profile (5.45b) for a large draw ratio D, and D is then gradually decreased toward the blue curve. By contrast, even if scenario (iii) were physically realizable, stable drawing could not actually be achieved at the draw ratios on the green dot-dashed curve: once gravity was switched on, the thickness and velocity profiles would evolve towards (5.45a)–(5.45b), rendering the sheet unstable to buckling. The solid blue line corresponding to scenario (ii) is therefore an absolute lower bound on the draw ratio D at which stable drawing can be achieved for a given value of St.

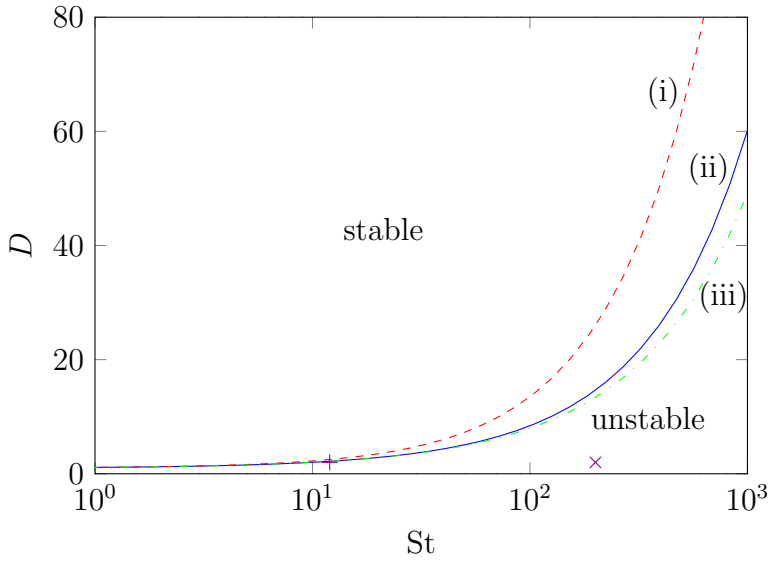

Figure 5.2: Neutral stability curve for an initially flat sheet with uniform viscosity for scenarios (i)–(iii) introduced in §5.2.4 (red dashed, blue solid and green dot-dashed lines respectively). Two particular unstable points are marked at $D = 2$, $\mathrm{St} = 12$ (+) and $D = 2$, $St = 200$ (×).

5.4 Buckling solutions

The tensile force acting on the sheet centreline has two components: a spatially varying downward force due to the weight of the sheet, and a time-dependent contribution $c(\tau)$ which is uniform throughout the sheet (cf. the centreline equation (5.40)). The centreline exhibits dramatically different behaviour depending on the sign of c and on whether the weight of the sheet is significant. We consider two distinct unstable scenarios: one in which gravity does not play a role and the entire sheet experiences uniform compression, and the other in which the buckling is gravity-driven. The first of these scenarios has been studied in detail by Buckmaster et al. (1975), and the relevant results are highlighted in §5.4.1. The major focus of this section will be on the latter, gravity-driven scenario. We consider an initially straight centreline, so that the force balance (5.39) may be rewritten

$$[c(\tau) - c_0)] \int_0^1 \frac{\mathrm{d}x}{4h} = \int_0^1 H_x H_{x\tau} \, \mathrm{d}x, \tag{5.48}$$

where $c_0 = c(0)$ is given by the planar-sheet solution (5.47). The early-time response to a small perturbation is investigated via a linear-stability analysis in §5.4.2, and full numerical solutions are presented in §5.4.3. The observation of self-similar, power-law behaviour of the centreline deformation H at late time in the numerical solutions

motivates an analysis of the governing equations in the limit $\tau \gg 1$, which we present in §§5.4.4–5.4.6.

5.4.1 Gravity-free buckling

In the absence of gravity and inertia, i.e. with $\mathrm{St} = \overline{\mathrm{Re}} = 0$, the sheet experiences a uniform tension $c(\tau)$. The thickness of the sheet D^{-x} is given by the steady-state solution (5.44), while the velocity and centreline deformation are governed by the force (5.39) and centreline (5.40) equations, which simplify to

$$c(\tau) = \frac{D - 1 + \int_0^1 H_x H_{x\tau} \mathrm{d}x}{\int_0^1 \mathrm{d}x/4h}, \tag{5.49a}$$

$$\frac{4}{3} D^{-3x} H_{xx\tau} = c(\tau) H, \tag{5.49b}$$

where boundary conditions (5.41) are used in integrating the centreline equation. If $c < 0$ then the entire sheet experiences a compressive force and undergoes buckling; this is true at time $\tau = 0$ if $D < 1$. This scenario was considered by Buckmaster et al. (1975) in the general case of a centreline of arbitrary amplitude. Here we summarize their findings in the special case when the centreline amplitude is small so that we can use Cartesian coordinates. We consider the unstable case $c < 0$ and introduce a new time-like variable $m(\tau)$ given by

$$\frac{4}{3} \frac{\mathrm{d}m}{\mathrm{d}\tau} = -c(\tau), \quad m(0) = 0. \tag{5.50}$$

We propose a solution to (5.49) of the form

$$H = \sum_{n=1}^{\infty} g_n e^{m(\tau)/\sigma_n} \Psi_n(x), \tag{5.51}$$

where the eigenmodes $\Psi_n(x)$ are normalized (for reasons we will see below) according to

$$\int_0^1 \left[\Psi_n'(x)\right]^2 \, \mathrm{d}x = 1, \tag{5.52}$$

and the coefficients $g_n e^{m(\tau)/\sigma_n}$ give the amplitude of the contribution of each mode to H. The momentum equation (5.49b) is linear and so may be simplified to

$$D^{-3x} \Psi_n''(x) = -\sigma_n \Psi_n(x), \tag{5.53}$$

which has solution

$$\Psi_n(x) = A_n J_0\left(\Sigma_n D^{3x/2}\right) + B_n Y_0\left(\Sigma_n D^{3x/2}\right), \tag{5.54}$$

where $\Sigma_n = 2\sqrt{\sigma_n}/3\log(D)$ and J_0 and Y_0 are Bessel functions of zeroth order. Applying the boundary conditions $\Psi_n(0) = \Psi_n(1) = 0$, we find the coefficients A_n and B_n are related by

$$A_n = -B_n \frac{Y_0(\Sigma_n)}{J_0(\Sigma_n)}, \tag{5.55}$$

and the Σ_n are constrained to satisfy

$$Y_0\left(\Sigma_n\right) J_0\left(\Sigma_n D^{3/2}\right) - J_0\left(\Sigma_n\right) Y_0\left(\Sigma_n D^{3/2}\right) = 0, \tag{5.56}$$

which, in turn, determines the σ_n. Finally, we can use the normalization condition (5.52) to find B_n.

We still need to calculate $c(\tau)$ to determine how quickly the centreline deforms. We note from (5.53) that the eigenmodes satisfy an appropriate orthogonality condition,

$$\int_0^1 \Psi_p'(x)\Psi_q'(x)\ \mathrm{d}x = 0, \quad p \neq q, \tag{5.57}$$

and are normalized according to (5.52), so the force condition (5.49a) reduces to

$$D - 1 + \sum_n g_n^2 \frac{1}{\sigma_n}\frac{\mathrm{d}m}{\mathrm{d}\tau} e^{2m/\sigma_n} = c(\tau)\int_0^1 \frac{\mathrm{d}x}{4h} = -\frac{1}{3}\frac{\mathrm{d}m}{\mathrm{d}\tau}\int_0^1 \frac{\mathrm{d}x}{h}, \tag{5.58}$$

which gives a first-order ODE for m and hence c. In the limit $m \to \infty$ the fastest-growing eigenmode dominates, and

$$H \sim g_1 e^{m/\sigma_1}\Psi_1(x). \tag{5.59}$$

If $c(\tau) = -\mathrm{d}m/\mathrm{d}\tau$ is small, then integrating the length equation (5.58) yields

$$(1 - D)\tau \sim \frac{g_1^2}{2} e^{2m/\sigma_1}, \tag{5.60}$$

so that

$$H \sim \sqrt{2(1-D)\tau}\Psi_1(x). \tag{5.61}$$

Note that this does indeed satisfy the requirement $\mathrm{d}m/\mathrm{d}\tau \to 0$ as $m \to \infty$. The amplitude of the centreline grows with $\tau^{1/2}$ in agreement with Buckmaster et al. (1975) and is proportional to $\sqrt{1-D}$, which is a measure of excess loading.

5.4.2 Early-time behaviour

For the gravity-driven buckling case, we perform a linear-stability analysis of an initially planar centreline by considering a perturbation with $|H(x,\tau)| \ll 1$. Linearizing the governing equations, the force balance (5.38) reduces to

$$4h\bar{u}_x = \int_x^1 \mathrm{St}\, h \, \mathrm{d}s + c(0), \tag{5.62}$$

subject to boundary conditions $\bar{u}(0,\tau) = 1$, $\bar{u}(1,\tau) = D$. We note that the velocity profile does not change so long as the centreline deviation is small. Upon linearizing the centreline equation (5.39)–(5.40), we may decompose H into Fourier modes $e^{\lambda\tau}\psi(x)$,which grow if $\lambda > 0$ and decay if $\lambda < 0$. We also introduce corresponding modes $e^{\lambda\tau}\Omega(x)$ for $w = H_\tau$, which turns (5.40) into the eigenvalue problem

$$\lambda\overline{\mathrm{Re}}h\Omega = -\left(\frac{4}{3}h^3\Omega_{xx}\right)_{xx} + \left(4h\bar{u}_x\psi_x\right)_x, \tag{5.63a}$$

$$\lambda\psi(x) = \Omega(x), \tag{5.63b}$$

with boundary conditions $\Omega = \Omega_{xx} = 0$ on $x = 0$, 1.

In figure 5.3 we present numerical solutions to the eigenvalue problem (5.63) for $D = 2$, $\mathrm{St} = 12$ (marked with a purple + in figure 5.2) and $D = 2$, $\mathrm{St} = 200$ (purple $\times$ in figure 5.2), for $\overline{\mathrm{Re}} = 0$ (blue) and $\overline{\mathrm{Re}} = 100$ (red, dashed). Numerical solutions are calculated by using second-order finite differencing to give a matrix equation which is solved with `eig` in MATLAB. In each case we plot the fastest-growing mode, corresponding to the largest value of λ. Note that $D = 2$, $\mathrm{St} = 12$ is close to the stability threshold, so we anticipate growth rate $\lambda \ll 1$, i.e. slow centreline growth, while $D = 2$, $\mathrm{St} = 200$ is far from the stability boundary and we expect fast buckling. In figures 5.3(a) and (b), we show the eigenmodes for scenario (i) described in §5.3, in which the sheet has uniform thickness, while figures 5.3(c) and (d) correspond to scenario (ii), in which the sheet reaches a steady-state thickness profile before undergoing buckling. In the almost-stable regime the upward force at the draw rollers is small, $|c| \ll 1$, and only dominates over the downward force from gravity in a small portion of the sheet where $|1 - x| \ll 1$ (cf. force balance (5.62)). As a result, only a small segment of the sheet near $x = 1$ experiences compression, and the growth rate is small: for scenario (ii) $\lambda = 4.62 \times 10^{-3}$ when $\overline{\mathrm{Re}} = 0$ and $\lambda = 4.63 \times 10^{-3}$ when $\overline{\mathrm{Re}} = 100$. We also observe that the rescaled Reynolds number $\overline{\mathrm{Re}}$ appears to have very little impact on the sheet dynamics: the fastest-growing eigenmodes are almost indistinguishable for $\overline{\mathrm{Re}} = 0$ and $\overline{\mathrm{Re}} = 100$ (figure 5.3a,c).

By contrast, in the far-from-stability case a substantial portion of the almost-flat sheet experiences compression, and since the compressive force is larger (cf. (5.47)), so too is the corresponding growth rate: in scenario (ii) $\lambda = 20.9$ for $\overline{\mathrm{Re}} = 0$ and $\lambda = 3.74$ for $\overline{\mathrm{Re}} = 100$. We note that the Reynolds number plays a more significant role in this regime. In scenario (ii), we observe two turning points rather than one in the fastest-growing eigenmode for $\overline{\mathrm{Re}} \gg 1$ (figure 5.3d), and the growth rate is slower, so the lengthscale is shorter and the timescale is longer, as predicted by (5.25). However, for scenario (i), increasing the rescaled Reynolds number to $\overline{\mathrm{Re}} = 100$ does not change the sheet shape significantly even at large St (figure 5.3b). This is due to the difference in the bending stiffnesses of the sheets. Bending stiffness opposes the formation of high-curvature regions required for shorter wavelengths. In scenario (i) the sheet has uniform thickness and better resists bending than in scenario (ii), where the sheet gets thinner, making the lower portion less resistant to bending. Even more disparate values of $\overline{\mathrm{Re}}$ are required to effect a significant change in the early-time centreline shape in scenario (i).

5.4.3 Numerical solution

Beyond very small centreline perturbations, numerical solution of (5.39)–(5.41) is required to fully determine the evolution of the centreline profile. Unlike in the gravity-free case (cf. §5.4.1), we cannot simplify the gravity-driven problem by decomposing into modes except at very early time (see §5.4.2) because the tension has both a spatially varying part and a time-dependent part. Instead we solve (5.39)–(5.41) numerically using the method of lines, with second-order finite differencing in space to give a series of ODEs, which are then integrated in time using MATLAB's built-in solver `ode15s`. All the numerical solutions presented here are for scenario (ii) (cf. §5.2.4), with thickness profile (5.45b) and an initial centreline deformation (5.63). We illustrate the evolution of the sheet in time by plotting a series of snapshots of a sheet centreline with $D = 2$, $\mathrm{St} = 200$, for both $\overline{\mathrm{Re}} = 0$ and $\overline{\mathrm{Re}} = 100$ (figure 5.4). The early-time solutions are dramatically different for different $\overline{\mathrm{Re}}$, with the larger $\overline{\mathrm{Re}}$ case corresponding to much slower initial growth, as expected. However, as time proceeds, solutions for different values of $\overline{\mathrm{Re}}$ appear to converge: by time $\tau = 100$ the sheet centreline appears to have the same shape for $\overline{\mathrm{Re}} = 0$ and $\overline{\mathrm{Re}} = 100$ (figure 5.4e,f). We investigate further by plotting the amplitude of the centreline (defined as $\max_x |H|$) as a function of time (figure 5.5). For $\tau \gg 1$ the curves for $\overline{\mathrm{Re}} = 0$ and $\overline{\mathrm{Re}} = 100$ are in good agreement, and fall on a line whose slope is close to $1/3$ on a loglog plot. As time proceeds the centreline amplitude grows larger, and the peak

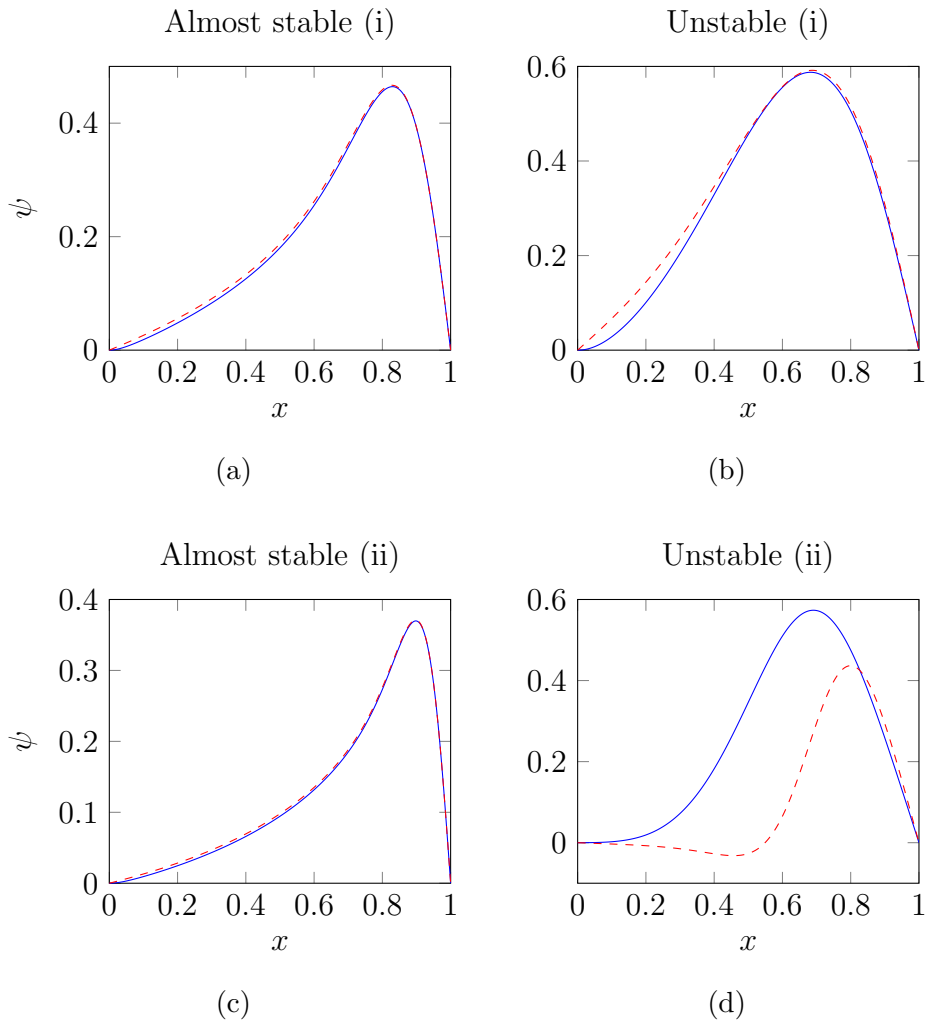

Figure 5.3: Fastest-growing eigenmodes of (5.63) corresponding to centreline shape at early times for $D = 2$, St $= 12$, (a,c) and $D = 2$, St $= 200$, (b,d) in scenarios (i) (a,b) and (ii) (c,d). In each case blue is for $\overline{\mathrm{Re}} = 0$ and dashed red is for $\overline{\mathrm{Re}} = 100$. Corresponding growth rates are (a) 6.58×10^{-3} for $\overline{\mathrm{Re}} = 0$ and 6.66×10^{-3} for $\overline{\mathrm{Re}} = 100$, (b) 1.41 and 1.22 respectively, (c) 4.62×10^{-3} and 4.65×10^{-3} respectively, and (d) 20.9 and 3.74 respectively.

moves closer to $x = 1$ (figure 5.6). The resulting large gradients in the region near $x = 1$ necessitate the use of an increasingly fine grid to maintain accuracy; at $\tau = 10^5$, the peak is located in $x \in [0.99, 1]$ and a mesh spacing of 1.25×10^{-3} gives a relative error of 10^{-2}.

5.4.4 Overview of late-time analysis

The late-time analysis of the centreline equations poses a challenging asymptotics problem. Since this analysis becomes quite involved, we first present an outline of the main steps and results, and then lay out the analysis in full in the sections that follow.

- We assume (and subsequently verify) that inertia does not play a role at leading order.
- On rescaling the centreline equation (5.40) for $\tau \gg 1$, it becomes clear that the bending moment is only significant in boundary layers at each end of the sheet.
- We find that the centreline is almost flat in the boundary layer near $x = 0$, although bending is significant here.
- Buckling is driven by the boundary layer near $x = 1$, where the sheet is under compression, and this also gives rise to leading-order centreline motion in the bulk of the sheet.
- We use the method of matched asymptotic expansions to derive expressions for the centreline in the $x \approx 1$ boundary layer and in the bulk of the sheet. The appropriate asymptotic expansion for the late-time buckling of the sheet involves both powers of $\tau^{1/3}$ and powers of $\log(\tau^{1/3})$.
- We calculate consecutive terms in this expansion individually, but find that this logarithmic approximation is only accurate at extremely late times.
- We improve on this by using a hybrid asymptotic–numerical method.
- We determine that the sheet thickness is almost uniform inside the boundary layer near $x = 1$. This allows us to rescale in such a way that we only need to solve the late-time problem inside the boundary layer once and rescale to find the boundary-layer solution for any thickness profile.

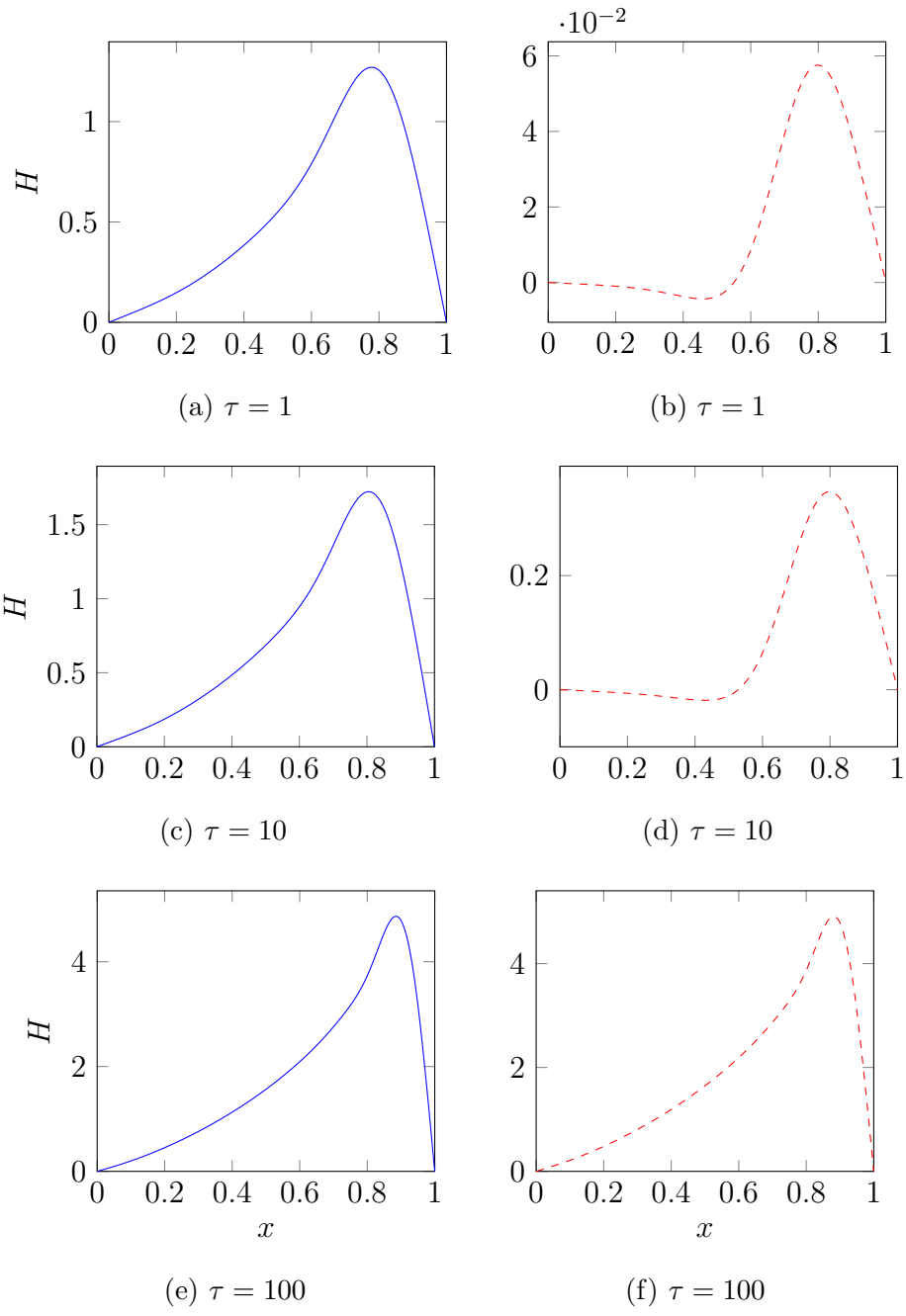

(a) $\tau = 1$ (b) $\tau = 1$

(c) $\tau = 10$ (d) $\tau = 10$

(e) $\tau = 100$ (f) $\tau = 100$

Figure 5.4: Numerical solutions to (5.39)–(5.41) for $D = 2$, St $= 200$ for scaled Reynolds numbers $\overline{\mathrm{Re}} = 0$ (a,c,d) and $\overline{\mathrm{Re}} = 100$ (b,d,f).

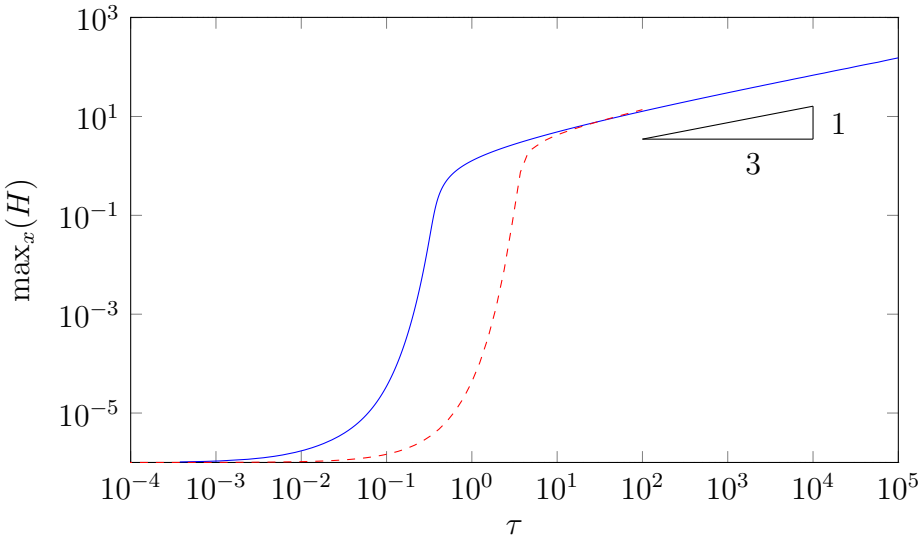

Figure 5.5: Loglog plot of centreline amplitude as a function of time for $D = 2$, $\mathrm{St} = 200$, $\overline{\mathrm{Re}} = 0$ (blue) and $\overline{\mathrm{Re}} = 100$ (red, dashed). A line of slope 1/3 is shown for comparison.

5.4.5 Late-time analysis

Since the numerical solutions to the system (5.39)–(5.41) shown in figures 5.4 and 5.5 indicate that inertia does not play a role in the late-time behaviour (cf. §5.4.3), we will neglect this term in our analysis of the equations, and justify this simplification *a posteriori*. We compare the size of the bending stiffness and inertia terms in the centreline equation (5.40) at late times by scaling $\tau = \delta^{-1}S$, where $\delta \ll 1$ is an arbitrary small parameter and $S = O(1)$ to give

$$\delta\left(\frac{4}{3}h^3H_{xxS}\right)_{xx} = \left[H_x\left(\int_x^1 \mathrm{St}\,h\mathrm{d}s + c(\delta^{-1}S)\right)\right]_x. \tag{5.64}$$

We see that the bending term on the left-hand side of (5.64) will not play a role at leading order in the majority of the sheet. Since there are then two fewer spatial derivatives in the leading-order governing equations, the boundary conditions (5.41) cannot all be satisfied. There will be boundary layers near either end of the sheet where the bending term is significant, and the sheet adjusts rapidly. By seeking a balance between bending and tension in (5.64), we observe that the effect of the bending moment is comparable in size to tension in a boundary layer of size $\delta^{1/2}$ (i.e. $\tau^{-1/2}$) near $x = 0$. Near $x = 1$ the positive contribution to the tension from gravity is small, and a balance exists between bending stiffness, the uniform upward force from the draw rollers and the spatially-varying downward force from gravity if

$$\delta|1-x|^{-4} \sim |1-x|^{-1} \sim c|1-x|^{-2} \tag{5.65}$$

i.e. the bending moment, gravity and the compression from the draw rollers balance for $c(\tau) \sim O(\delta^{1/3})$ in a boundary layer of $O(\delta^{1/3})$ (i.e. $O(\tau^{-1/3})$). This implies that, at late times, the size of the region under compression and the magnitude of the compressive force both decay like $\tau^{-1/3}$.

We know from (5.30) that the thickness profile of the sheet does not change on the buckling timescale, and is given by the initial conditions, which are the solution to the corresponding problem on the longer stretching timescale, as discussed in §5.2.4. Since the size of the boundary layers shrinks in time, at late times the thickness should be almost uniform inside the boundary layers. This suggests that it should be possible to write the governing equations in the boundary layers in a way that does not depend on the exact thickness profile. To this end, and with the benefit of hindsight, it is useful to introduce rescaled variables $\tilde{h}$, $\tilde{H}$, $\tilde{\tau}$, $\tilde{c}$ in the whole sheet defined by

$$h = h_1 \tilde{h}, \tag{5.66a}$$

$$\tilde{H}_x \, (1-x) \, \frac{h_1 \sqrt{d}}{\sqrt{3}} \sqrt{1-2b} = H_x \int_x^1 \tilde{h} \mathrm{d}s, \quad \tilde{H}(1) = 0, \tag{5.66b}$$

$$\tau = \frac{4h_1^2}{3\,\mathrm{St}} \tilde{\tau}, \tag{5.66c}$$

$$c = \mathrm{St}\, h_1 \tilde{c}, \tag{5.66d}$$

where $h_1 = h(1)$ is the final thickness and b and d are defined by

$$b = \frac{4(D-1)}{\mathrm{St}\, d}, \quad d = 2 \int_0^1 \tfrac{1}{\tilde{h}} \left(\int_x^1 \tilde{h} \mathrm{d}s \right) \mathrm{d}x. \tag{5.67}$$

Substituting this change of variables into the governing equations (5.39)–(5.40), it is straightforward to integrate the centreline equation (5.40) (in the absence of inertia) with respect to x twice and apply boundary conditions (5.41) to arrive at

$$\tilde{h}^3 \left(\tilde{H}_x \frac{1-x}{\int_x^1 \tilde{h} \mathrm{d}s} \right)_{x\tilde{\tau}} = \tilde{c}(\tilde{\tau}) \int_1^x \tilde{H}_{x'} \frac{1-x'}{\int_{x'}^1 \tilde{h} \mathrm{d}s} \mathrm{d}x' + (1-x) \int_0^1 \tilde{H}_x (1-x) \mathrm{d}x + \int_1^x \tilde{H}_{x'} (1-x') \mathrm{d}x', \tag{5.68}$$

while the force balance condition (5.39) may be rewritten as

$$\frac{\partial}{\partial \tilde{\tau}} \int_0^1 \tilde{H}_x^2 \left(\frac{1-x}{\int_x^1 \tilde{h} \mathrm{d}s} \right)^2 \mathrm{d}x = 1 + \frac{2\tilde{c}}{d(1-2b)} \int_0^1 \frac{\mathrm{d}x}{\tilde{h}}. \tag{5.69}$$

We may interpret the integral constraint (5.69) as a condition governing the increase in the length of the sheet.

We scale into the boundary layer near $x = 1$ by introducing a new variable $\eta = (1-x)\tilde{\tau}^{1/3}$. Substituting this rescaling into the centreline equation (5.68) and comparing terms, we confirm that the force on the end of the sheet must be of $O(\tilde{\tau}^{-1/3})$, i.e.

$$\tilde{c}(\tilde{\tau}) = \tilde{\tau}^{-1/3} K(\tilde{\tau}), \tag{5.70}$$

with $K(\tilde{\tau}) = O(1)$.

Next we consider the boundary layer near $x = 0$. For this purpose it is useful to rewrite the right-hand-side of the centreline equation (5.68) as

$$\tilde{h}^3 \left(\tilde{H}_x \frac{1-x}{\int_x^1 \tilde{h} \mathrm{d}s} \right)_{x\tilde{\tau}} = \tilde{\tau}^{-1/3} K(\tilde{\tau}) \int_0^x \tilde{H}_{x'} \frac{1-x'}{\int_{x'}^1 \tilde{h} \mathrm{d}s} \mathrm{d}x' + \int_0^x \tilde{H}_{x'}(1-x') \mathrm{d}x' - x \int_0^1 \tilde{H}_x (1-x) \mathrm{d}x, \tag{5.71}$$

where definition (5.66b) has been used to change the lower limit in the first integral on the right hand side. We rescale by introducing $\zeta = \tilde{\tau}^{1/2} x$ and use $\tilde{H}^{top}$ to denote the scaled centreline variable $\tilde{H}$ inside the $x \approx 0$ boundary layer. We compare terms in (5.71) to relate the size of the centreline deformation inside the $x \approx 0$ boundary layer to the bulk. On the left-hand side, the bending stiffness is of $O(\tilde{H}^{top})$. On the right hand side, the first tension term is of $O(\tilde{\tau}^{-1/3} \tilde{H}^{top})$. Finally, the two gravity terms are of $O(\tilde{H}^{top})$ and $O(\tilde{\tau}^{-1/2} \tilde{H})$ respectively, where $\tilde{H}$ refers to the solution away from $x = 0$. Balancing terms, we deduce that $\tilde{H}^{top} = O(\tilde{\tau}^{-1/2} \tilde{H})$.

Finally, we split the integral on the left-hand side of the length condition (5.69) into three components corresponding to the three regions. Requiring a balance with the force term on the right-hand side of the length condition (5.69) motivates the scaling

$$\tilde{H}(x \approx 1, \tilde{\tau}) = \tilde{\tau}^{1/3} F(\eta, \tilde{\tau}) \tag{5.72}$$

when $|1-x| \ll 1$, where $F(\eta, \tilde{\tau}) = O(1)$. Since we will match between the boundary layer near $x = 1$ and the bulk, we also scale

$$\tilde{H}(x, \tilde{\tau}) = \tilde{\tau}^{1/3} \Theta(x, \tilde{\tau}), \tag{5.73}$$

in the bulk of the sheet. We can now verify our assumption that inertia is not important, since at late times the inertia term will not affect the solution before corrections of $O(\tilde{\tau}^{-5/3})$.

We determine the bulk behaviour by substituting scaling (5.73) into centreline equation (5.68) and evaluating at leading order to find

$$\Theta = \alpha(\tilde{\tau}) \left[-\log|1-x| + \mathcal{C} \right] + O(\tilde{\tau}^{-1/3}), \tag{5.74}$$

where $\mathcal{C}$ is an integration constant which may be determined by imposing $H(0,\tau) = 0$. (Note from definition (5.66b) that $\mathcal{C}$ may be non-zero if the thickness is non-uniform.) To match between regions we must rewrite the bulk solution (5.74) in terms of η, to give

$$\Theta = \alpha(\tilde{\tau}) \left[-\log(\eta) + \log(\tilde{\tau}^{1/3}) + \mathcal{C} \right] + O(\tilde{\tau}^{-1/3}). \tag{5.75}$$

Matching between the boundary layer and bulk solutions (5.72)–(5.73) suggests that the amplitude $\alpha(\tilde{\tau})$ is of $O(1/\log(\tilde{\tau}^{1/3}))$, and that the boundary layer has terms of $O(\tilde{\tau}^{1/3})$, $O(\tilde{\tau}^{1/3}/\log(\tilde{\tau}^{1/3}))$ and so on. Inspecting the centreline equation (5.68) and scalings (5.72)–(5.73), we determine that the correct asymptotic expansions are

$$\alpha(T) = \frac{\alpha_1}{T} + \frac{\alpha_2}{T^2} + \cdots, \tag{5.76a}$$

$$F(\eta, T) = F_0(\eta) + \frac{1}{T} F_1(\eta) + \cdots, \tag{5.76b}$$

$$K(T) = K_0 + \frac{1}{T} K_1 + \cdots. \tag{5.76c}$$

where $T = \log(\tilde{\tau}^{1/3}) + \mathcal{C}$. It is not strictly necessary to include $\mathcal{C}$ in T, but it helps our aim of writing the boundary-layer problem in such a way that it does not depend on the thickness profile.

Scaling into the boundary layer $x = 1 - \eta\tilde{\tau}^{-1/3}$ in (5.68) yields an equation in terms of $F(\eta, T)$, which may be simplified by rewriting in terms of $G = F_\eta$. Performing the asymptotic expansion (5.76) and evaluating at leading order, we find

$$\frac{1}{3}\left(4G_{0\eta\eta} + \eta G_{0\eta\eta\eta}\right) - \left(K_0 + \eta\right) G_0 = 0. \tag{5.77}$$

The simple-support boundary condition (5.41) on $x = 1$ is transformed to

$$G_{0\eta} = 0 \quad \text{at} \quad \eta = 0, \tag{5.78}$$

and requiring the bending stress to decay as $\eta \to \infty$, we find

$$G_0 \sim 0 \quad \text{as} \quad \eta \to \infty. \tag{5.79}$$

Non-trivial solutions to the homogeneous linear problem (5.77)–(5.79) will only exist for particular values of the force component K_0, and the corresponding G_0 should then be normalized according to (5.69) at leading order, i.e.

$$\int_0^\infty G_0^2 \mathrm{d}\eta = 1. \tag{5.80}$$

We calculate the shape F_0 by integrating G_0 subject to $F_0(0) = 0$, and the outer amplitude α_1 can then be inferred from the far-field condition

$$F_0 \sim \alpha_1 \quad \text{as} \quad \eta \to \infty. \tag{5.81}$$

To enable the calculation of higher-order corrections, we must also solve the adjoint problem

$$\frac{1}{3}\left(\phi_{\eta\eta} - \eta\phi_{\eta\eta\eta}\right) - \left(K_0 + \eta\right)\phi = 0, \tag{5.82}$$

subject to $\phi_\eta(0) = 0$ and $\phi \sim 0$ as $\eta \to \infty$. We can then calculate the first correction to the leading-order solution given by (5.77)–(5.81) by evaluating the centreline equation (5.68) inside the boundary layer at next order to give

$$\frac{1}{3}\left(4G_{1\eta\eta} + \eta G_{1\eta\eta\eta}\right) - \left(K_0 + \eta\right)G_1 = K_1 G_0 + \alpha_1. \tag{5.83}$$

Evaluating the simple-support condition (5.41) on $x = 1$ and matching the bending moment with the bulk, we find

$$G_{1\eta} = 0 \quad \text{at} \quad \eta = 0, \tag{5.84a}$$

$$G_1 \sim 0 \quad \text{as} \quad \eta \to \infty. \tag{5.84b}$$

and the length condition (5.69) yields

$$\int_0^\infty G_0 G_1 \mathrm{d}\eta = 0. \tag{5.85}$$

Multiplying (5.83) with the adjoint ϕ and integrating over $[0, \infty)$ yields a condition for the correction to the force, namely

$$K_1 = -\alpha_1 \frac{\int_0^\infty \phi \, \mathrm{d}\eta}{\int_0^\infty \phi G_0 \, \mathrm{d}\eta}. \tag{5.86}$$

We then solve equations (5.83)–(5.85) for G_1, integrate as before to find F_1, and determine α_2 from the far-field condition

$$F_1 \sim -\alpha_1 \log\eta + \alpha_2 \quad \text{as} \quad \eta \to \infty. \tag{5.87}$$

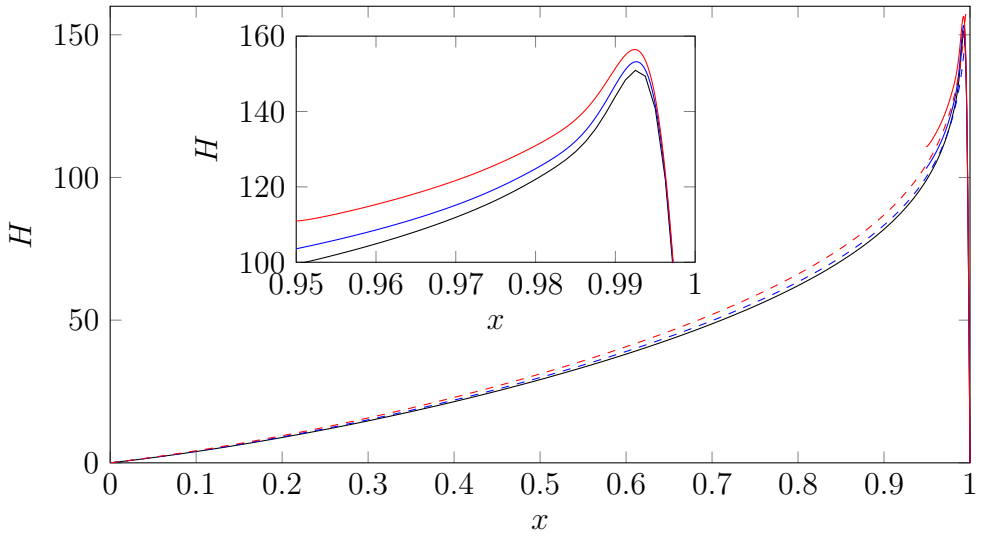

Figure 5.6: Late-time centreline shape for a sheet undergoing redraw at draw ratio $D = 2$ in a gravitational field $\mathrm{St} = 200$. The numerical solution to (5.39)–(5.41) is shown in black. The late-time asymptotic approximation (cf. §5.4.5) is shown in red, with a dashed line for the bulk solution and a solid line for the boundary-layer solution. A hybrid asymptotic–numerical solution (cf. §5.4.6) is shown in blue, with dashed and solid lines used for the bulk and boundary-layer solutions respectively.

Subsequent correction terms may be calculated by the same routine. The centreline shape in the bulk is then given by

$$H = \left(\frac{\alpha_1}{T} + \frac{\alpha_2}{T^2} + \cdots\right)\sqrt{d}\sqrt{1-2b}\left(\frac{\mathrm{St}\,h_1\tau}{4\sqrt{3}}\right)^{1/3}\int_0^x \frac{\mathrm{d}x'}{\int_0^{x'}\tilde{h}(s)\mathrm{d}s}, \tag{5.88}$$

with $T = (1/3)\log\left(3\,\mathrm{St}\,\tau/4h_1^2\right) + \mathcal{C}$. The integral on the right hand side of (5.88) may be calculated exactly in each of the three idealized scenarios laid out in §5.2.4, but for brevity we will omit the solutions here.

We solve the eigenvalue problems (5.77)–(5.81) and (5.83)–(5.87) together with the adjoint problem (5.82) numerically using Chebfun (Driscoll et al., 2014), and so determine two-term inner and outer asymptotic solutions for the sheet centreline at late times. The two-term asymptotic solution for a sheet undergoing redraw with draw ratio $D = 2$ and $\mathrm{St} = 200$ at time $\tau = 10^5$ shows reasonably good agreement with the full numerical solution to (5.39)–(5.41) (see figure 5.6). However, we observe that the two-term asymptotic prediction does deviate from the numerical solution even though $\tau = 10^5 \gg 1$, and further correction terms do not improve the accuracy.

5.4.6 Hybrid method

We have seen that, while one may in principle calculate successive terms in the series (5.76), such an approximation may not be very accurate unless τ is extremely large. A hybrid asymptotic–numerical scheme for a perturbed eigenvalue problem with gauge functions of the same form as in §5.4.5 has been developed by Ward et al. (1993) and adapted by Kropinski et al. (1995) for the case of low-Reynolds-number flow past a cylindrical body. In this scheme, rather than calculating individual terms in the logarithmic sequence separately, they are all calculated together as the function of a new variable which is the logarithm of the small parameter in the asymptotic expansion. We adopt this approach here by treating $T = \log(\tilde{\tau}^{1/3}) + \mathcal{C}$ as a new independent variable. Returning to our scalings (5.70)–(5.73) in the two regions of interest, and evaluating the centreline equation in the boundary layer at leading order in $\tilde{\tau}^{1/3}$ (remembering to treat T independently), we obtain a partial differential equation for F, namely

$$\frac{1}{3}\left[(\eta F)_{\eta\eta\eta} + F_{T\eta\eta}\right] = KF + \alpha\eta + \int_0^\eta \eta' F_{\eta'}\mathrm{d}\eta', \tag{5.89}$$

which must satisfy boundary conditions

$$F = F_{\eta\eta} = 0 \quad \text{on} \quad \eta = 0, \tag{5.90}$$

and match with the bulk solution (5.74) via

$$F \sim \alpha T - \alpha\log(\eta) \quad \text{as} \quad \eta \to \infty, \tag{5.91}$$

We also impose the normalization condition (5.69), that is

$$\int_0^\infty F_\eta^2 \mathrm{d}\eta = 1. \tag{5.92}$$

Although we must still solve a partial differential equation to determine the shape of the centreline, the rescaling into the inner region means the new boundary-layer problem (5.89)–(5.92) does not have the stiffness of the original problem (5.39)–(5.41), allowing much faster calculation at late times. Furthermore, we have removed any dependence on the process parameters, meaning that this boundary-layer problem must only be solved once, and the centreline shape and the force in the boundary layer may be deduced for any process by an appropriate rescaling. The centreline shape in the bulk is given by an equivalent rescaling to (5.88).

The boundary-layer equations (5.89)–(5.92) may be discretized in η using second-order finite differencing to give a system of ODEs in T supplemented by two algebraic

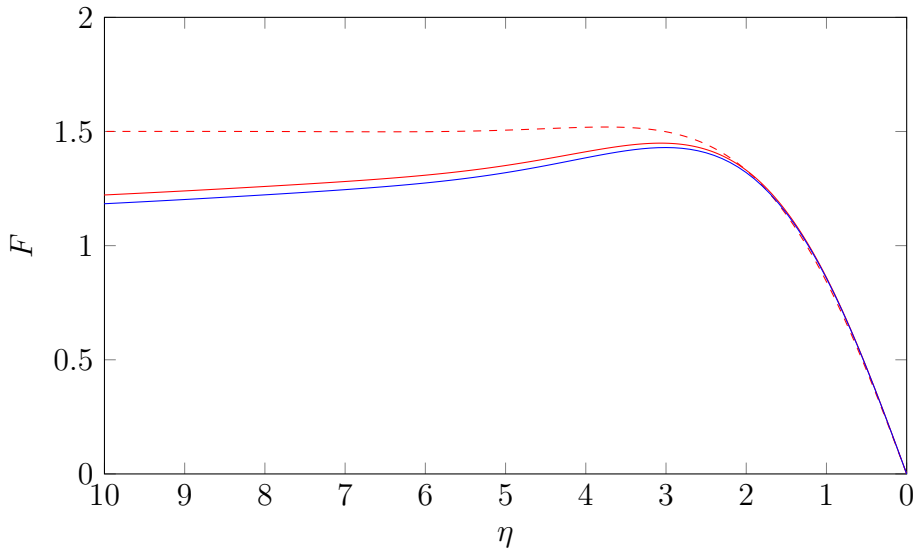

Figure 5.7: Late-time asymptotic solutions for the centreline shape at $T = 10$. The blue line shows the hybrid asymptotic–numerical solution (5.89)–(5.92). The solution $F_0 = \int_0^\eta G_0 \mathrm{d}\eta$ to (5.77)–(5.80) is illustrated with a dashed red line, and the two-term solution $F_0 + F_1/T$ (where the correction term F_1 may be determined using (5.83)–(5.85)) is plotted with a solid red line.

conditions. We solve this system of equations using MATLAB's built-in DAE solver `ode15i`. A suitable starting guess is provided to the solver from the straightforward asymptotic solution (cf. §5.4.5). This improved asymptotic–numerical solution shows better agreement with the full numerical solution than the straightforward two-term solution proposed in §5.4.5 (figure 5.6). The asymptotic–numerical solution is accurate up to $O(\tau^{-1/3})$ and, as expected, the agreement with the numerical solution to the centreline equation (5.39)–(5.41) is excellent at $\tau = 10^5$. In figure 5.7 we compare the straightforward late-time asymptotic solution for the centreline shape in the boundary layer near $x = 1$ presented in §5.4.5 (red) with the asymptotic–numerical scheme (5.89)–(5.92) (blue) for $T = 10$. Even at such a late time the performance of the one-term solution (dashed line) is poor; this is largely because it must tend to a constant as $\eta \to \infty$. We observe good agreement between the asymptotic-numerical solution and the two-term solution (solid line), but note that this plot corresponds to an extremely late time; for the scenario considered in §5.4.6 in which $\mathrm{St} = 200$ and $D = 10$, $T = 10$ corresponds to $\tau \approx 5 \times 10^7$.

5.4.7 Validity of late-time analysis

We conclude our study by returning to the question the validity of our nearly-planar assumption, in particular at late times when $H \sim \tau^{1/3}$. As noted in §5.2.4, our model breaks down when $H \sim 1/\epsilon$. Comparing the typical value $\epsilon \sim O(10^{-2})$ suggested by Table 1.1 with the numerical solution shown in figure 5.5 indicates that the late-time solution with $H \sim \tau^{1/3}$ is valid for $1 \ll \tau \ll 10^5$. However, we should also check the size of the curvature, which may be large in the boundary layer near $x = 1$. Inside this boundary layer, we require the curvature to satisfy $H_{xx} \sim \tau F_{\eta\eta} \ll 1/\epsilon$, so the late-time solution is valid for $1 \ll \tau \ll 1/\epsilon$.

Although the late-time analysis presented in this section breaks down eventually, it provides a valuable first step in the study of buckling in three-dimensional thin viscous sheets, because it demonstrates that the sheet is unstable to buckling in any process where some part of the sheet experiences compression, and that the stress profile and thus the out-of-plane deformation of the sheet will change significantly as it buckles. Furthermore, our late-time solution provides the matching conditions that would be needed to solve a geometrically nonlinear model for times $\tau \sim 1/\epsilon$.

5.5 Discussion

In this chapter we present a model for a two-dimensional thin viscous sheet undergoing redraw in the presence of a gravitational field, which may be sufficiently strong to render the sheet unstable to buckling. We derive a mathematical model to predict how the sheet centreline evolves, and in doing so provide a systematic derivation of the buckling lengthscale and timescale (also predicted by Howell, 1994), namely

$$\text{timescale} \sim \epsilon^{2/3}\,\mathrm{Re}^{1/3}, \quad \text{lengthscale} \sim \epsilon^{2/3}\,\mathrm{Re}^{-1/6}, \tag{5.93}$$

where ϵ is the aspect ratio of the sheet and Re the Reynolds number. Our multiple-scales analysis implies that for buckling of thin viscous sheets, the wavelength and growth rate/frequency will be governed by the relationship (5.93).

In this chapter we focus on the scenario where the Reynolds number $\mathrm{Re} \sim O(\epsilon^4)$, in which the buckling lengthscale is the sheet length and the buckling timescale is shorter than that for stretching by a factor ϵ^2. As a consequence the thickness profile of the sheet evolves relatively slowly, and only the centreline and velocity profile change on the buckling timescale. During redraw in the direction of gravity, gravity accelerates the sheet in conjunction with the draw rollers as it moves through the heater zone. The upper part of the sheet experiences positive tension but, if gravity is sufficiently

strong, a region near the bottom of the heater zone experiences compression, causing the sheet to buckle.

We first address the question of stability, and plot the neutral stability curves of the sheet by determining the direction of the vertical force acting on the sheet as it exits the drawing region. Our results demonstrate that the stability of the sheet to centreline perturbations depends on the thickness profile of the sheet before it is perturbed – a sheet of uniform thickness becomes unstable at a higher draw ratio D (or lower Stokes number St) than one which has been allowed to reach its equilibrium profile.

We determine a system of equations governing the buckling behaviour of the sheet centreline when it is unstable, depending on a rescaled Reynolds number $\overline{\mathrm{Re}} = \epsilon^4\,\mathrm{Re}$, the Stokes number St and the draw ratio D. Straightforward numerical solution of these equations as well as the linearized early-time version yields some insight into the parameter dependence of the process. If the effect of gravity is sufficiently large, the Reynolds number dramatically changes the early-time behaviour, with larger Reynolds numbers corresponding to shorter wavelengths and slower growth, in line with the predictions of our scaling analysis (5.93). At later times, inertia becomes negligible and the sheet adopts a self-similar shape, with the maximum of the centreline continuing to grow and moving towards the end of the drawing domain as time proceeds. Increasing the effect of gravity modifies the centreline shape and increases the growth rate by increasing both the size of the region under compression and the magnitude of the compressive force.

Analysis of the late-time problem illustrates that the sheet centreline responds to compression in such a way as to expel that compression from the system: as the sheet buckles, the size of the region under compression shrinks, and so too does the magnitude of the compressive force. The sheet may therefore be split into two regions, a bulk region in which the sheet is under tension, and a boundary layer in which the sheet is under compression and which drives the centreline motion. Matching between these regions reveals that the appropriate asymptotic expansion for large values of time $\tilde{\tau}$ is a double series in powers of $\tilde{\tau}^{1/3}$ and $\log(\tilde{\tau}^{1/3})$. We circumvent this by instead writing an expansion with $\tilde{\tau}^{1/3}$ times a function of $T = \log(\tilde{\tau}^{1/3}) + \mathcal{C}$ as its first term (with $\mathcal{C}$ a constant). We then solve numerically the partial differential equation that appears at leading order in $\tilde{\tau}^{1/3}$. This hybrid asymptotic–numerical scheme yields excellent agreement with numerics at late times, significantly better than an approximate solution derived by considering only the first two terms in the sum.

Our model does not display the periodic folding behaviour investigated by authors such as Cruickshank and Munson (1981), or observed in the often-cited scenario of cake batter poured from a height (Skorobogatiy and Mahadevan, 2000; Batty et al., 2012). This is due to a difference in the treatment of the sheet at the bottom of the domain. Folding occurs in scenarios where the sheet impacts a surface, deforms, and the point of contact moves across the surface as the deformation evolves. In the case of glass redraw, the glass is removed from the stretching region at a fixed speed, and its position at the point of removal is fixed in space by draw rollers, so folding behaviour does not emerge. This is reflected in the choice of boundary conditions in our model. Furthermore, our "nearly-planar" model does not predict the sagging behaviour one might expect at extremely late times, when the weight of glass at the apex of the deformed sheet is large enough to pull it down past the draw rollers. The use of Cartesian coordinates is appropriate as long as the centreline deformation is smaller than, or comparable with, the sheet thickness; when the centreline deformation is significantly larger than the sheet thickness the governing equations should be reformulated in terms of a curvilinear coordinate system embedded in the sheet, which evolves with the sheet centreline.

The velocity profile in the sheet and the dynamics of its centreline are fully coupled during buckling. The equilibrium velocity profile of the sheet, and in particular whether it decelerates, determines whether the sheet buckles out of plane. As the sheet centreline grows, it affects the velocity of the sheet, which decreases the magnitude of the compressive force experienced by the sheet and curtails the growth rate of the centreline. The shape of the sheet also changes dramatically from the initial fastest-growing eigenmode of a linearized problem at early times, and at late times we observe a self-similar shape in a shrinking boundary layer near the bottom of the sheet, while in the bulk only the amplitude of the centreline changes, with the shape remaining fixed.

Chapter 6

Buckling of a three-dimensional glass sheet

6.1 Introduction

Out-of-plane ripples are sometimes observed in a thin glass sheet that has undergone redraw (see figure 6.1). Understanding how and why these ripples form is a necessary first step in eliminating them. The origin of these ripples is not clear, nor is it easy to determine whether a given choice of process parameters will give rise to ripples in the final product. Observation of ripple formation inside the heater zone is challenging due to the very high operating temperatures. However, inspection of sheets with ripples after redraw suggests that the ripples travel inward from the sheet edge, and that the angle relative to the sheet edge in the product remains fixed during the course of a run, giving rise to a very regular pattern of ripples known as "tyre tracks" (see figure 6.1).

Filippov and Zheng (2010) calculate the "hyperbolic zones" in a glass sheet during redraw in an effort to learn about instabilities. A transition in the stress profile of the sheet from tension to compression corresponds to a change in the equation for the mid-surface from elliptic to "mixed type", i.e. hyperbolic in parts of the domain. The authors suggest that these hyperbolic zones are directly linked to out-of-plane buckling of the sheet, but do not solve for the buckling profile. Perdigou and Audoly (2016) perform a linear-stability analysis of an almost-rectangular thin viscous sheet stretched by a very weak gravitational field, and determine numerically the fastest-growing buckling modes in this scenario. Srinivasan et al. (2017) perform a linear-stability analysis of redraw of a thin glass sheet with aspect ratio of length to width of $O(1)$, and determine the buckling modes and corresponding growth rates for a range of heater-zone profiles. The observed eigenmodes and (positive) growth rates

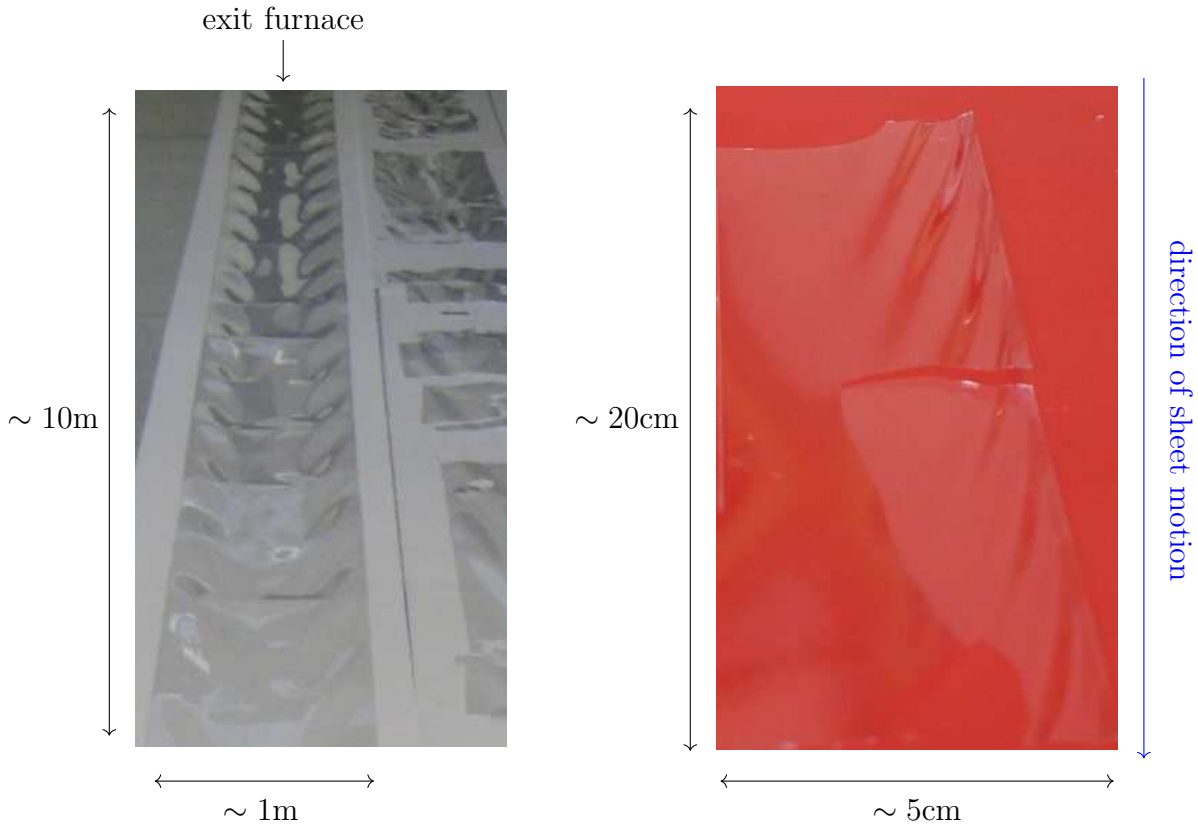

(a) Photo taken in Schott pilot plant

(b) Photo by Peter Tisdall

Figure 6.1: Photographs of glass sheets with ripples after undergoing redraw at Schott AG pilot plant.

support the proposition of Filippov and Zheng (2010) that a glass sheet undergoing redraw is inherently unstable to out-of-plane deformations. In regimes where there are two compression regions, the eigenmodes calculated by Srinivasan et al. (2017) fall into two separate groups corresponding to buckling in either region. The fastest-growing buckling modes in each region can, therefore, have different associated growth rates. Based on their analysis, Srinivasan et al. (2017) make two key observations about the relationship between buckling modes and the heater-zone profile, namely (i) compression regions always exist in the upper part of the heater zone (see figure 6.2 for a schematic), and (ii) for sufficiently short heater zones this compression region spans the width of the sheet, and a second compression zone may occur downstream. At the time of submission of this thesis, Srinivasan et al. (2017) had just been submitted for peer review. This chapter was developed in tandem, and as a result there is some overlap between the paper and the results presented in §§6.4–6.5, which we will highlight.

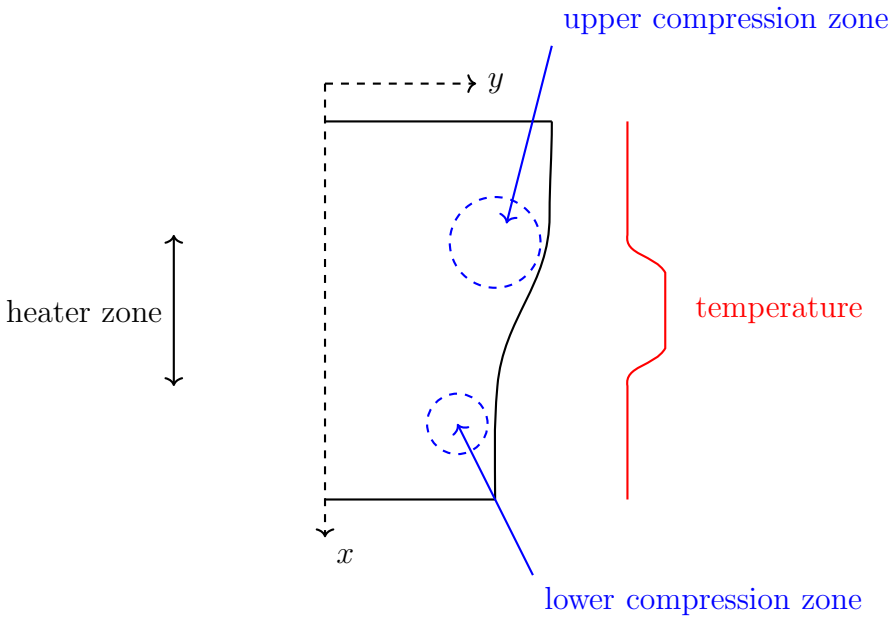

Figure 6.2: Schematic of a three-dimensional thin sheet undergoing redraw, showing the location of typical compression regions relative to the heater zone.

In this chapter, we will present a preliminary study of the stability of the mid-surface of a thin three-dimensional glass sheet during redraw. In §6.2 we derive equations governing the shape, velocity and mid-surface of a thin sheet, and in §6.3 we derive free-boundary conditions at the curved sheet edge. In §6.4 we investigate qualitatively the occurrence of compression zones in a glass sheet undergoing redraw in the short-heater-zone limit, and compare this with compression zones in a sheet whose aspect ratio of length to half-width is $O(1)$. We focus on sheets with aspect ratio $O(1)$ in the remainder of the chapter. In §6.5 we perform a linear-stability analysis of a thin sheet undergoing redraw and determine the fastest-growing buckling modes and corresponding growth rates in two sample sheets, one with uniform viscosity and one with stretching localized in a region of low viscosity. In §6.6 we consider a rectangular sheet segment under uniform tension along one axis and uniform compression along the other axis, and present a simple calculation of the number of wrinkles and growth rate, which we compare with our observations for the sheets considered in §§6.4–6.5. We compare the fastest-growing buckling modes with the deformations observed in redrawn glass sheets in §6.7, and outline some of the steps required to adapt the work so far to predict the buckling patterns observed in the final product. Finally, in §6.8 we discuss the implications of our findings.

6.2 Governing equations

We assume that the deformations in the sheet mid-surface are small, so that the glass sheet is almost planar. We use Cartesian coordinates $\boldsymbol{x} = (x, y, z)$, with the x-axis aligned with the direction of drawing, the y-axis spanning the sheet width as it enters the heater zone and z in the transverse direction as shown in figure 6.3. We consider the evolution in time t of a glass sheet of width $2b(x)$ and thickness $2h(x, y)$, with velocity $\boldsymbol{u} = (u, v, w)$ and mid-surface $H(x, y, t)$. Based on the analysis of buckling in a two-dimensional sheet in Chapter 5, we anticipate that the sheet buckles on a timescale shorter than that for stretching, and that the sheet width and thickness are fixed on this shorter timescale, while the mid-surface and velocity evolve. We neglect inertia, so the motion of the sheet is governed by the three-dimensional Stokes equations, and begin by considering a thin sheet whose length and width are comparable. In Chapter 3 we identified that the key dimensionless parameter relating surface tension and viscous stresses is $\delta/(\epsilon\,\mathrm{Ca}) \approx 0.5$. This suggests that surface tension may be significant, although numerical simulations show that it is not important in determining the thickness profile or necking in of the sheet (cf. figure 3.6). While surface tension may play a role in the exact stress distribution and hence buckling profile of the sheet, we neglect it here and focus on the fundamental fluid mechanics behind buckling of a viscous sheet undergoing redraw, and the dependence on the viscosity profile and the distance over which the sheet is drawn. We note, however, that Srinivasan et al. (2017) include surface tension in their analysis and find that it has a stabilising effect.

We non-dimensionalize the governing equations as in Chapter 3, except that we scale the out-of-plane velocity and time in line with the results of §5.2.3 for inertia-free buckling, i.e. we scale w to be a factor ϵ^{-2} larger than in the stretching problems considered in Chapters 2–4, and we introduce a short buckling timescale $\tau = \epsilon^2 t/(\delta b_{in}/U)$, where

$$\epsilon = \frac{\text{preform thickness}}{\text{preform width}} = \frac{2h_{in}}{2b_{in}} \ll 1, \tag{6.1a}$$

$$\delta = \frac{\text{length of drawing domain}}{\text{preform half-width}} = \frac{d}{b_{in}} = O(1). \tag{6.1b}$$

Note that δ is defined here using the distance over which the sheet is drawn rather than the distance over which it is heated and cooled; the reason for this distinction will become clear in §6.4.

For convenience, we also introduce special notation for in-plane variables, namely

$$\boldsymbol{X} = (\delta x, y), \quad \boldsymbol{\mathcal{U}} = (u, \delta v), \tag{6.2}$$

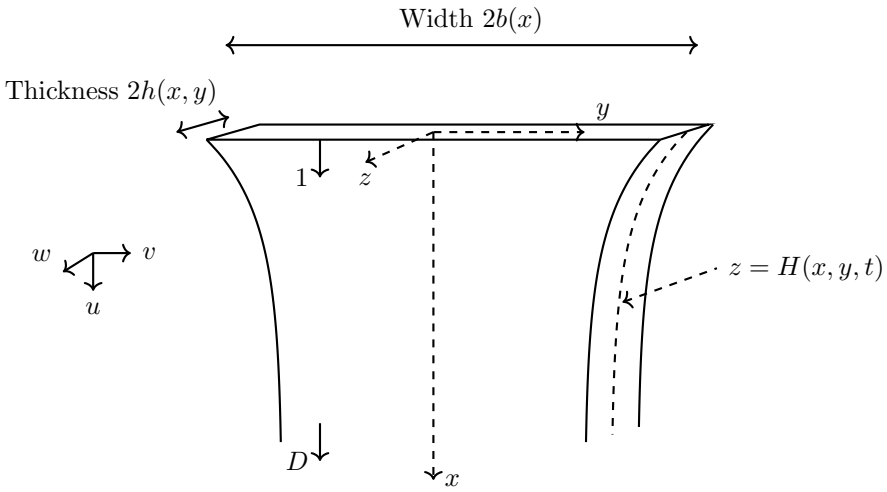

Figure 6.3: Three-dimensional glass sheet with width $2b(x)$ and thickness $2h(x,y)$ undergoing redraw in the x-direction. The sheet has mid-surface $z = H(x,y,t)$ and velocity $\boldsymbol{u} = (u,v,w)$.

for the in-plane position and velocity, an in-plane gradient vector

$$\tilde{\nabla} = \left(\delta^{-1}\frac{\partial}{\partial x}, \frac{\partial}{\partial y}\right), \tag{6.3}$$

and

$$\boldsymbol{\mathcal{S}} = -\delta^{-1}p\mathbb{I}^{2\times 2} + \mu\left(\tilde{\nabla}\boldsymbol{\mathcal{U}} + \tilde{\nabla}\boldsymbol{\mathcal{U}}^T\right), \tag{6.4a}$$

$$\bar{\boldsymbol{\sigma}} = \mu\left(\frac{\partial \boldsymbol{\mathcal{U}}}{\partial z} + \tilde{\nabla}w\right), \tag{6.4b}$$

for the in-plane stress tensor and out-of-plane stress components respectively, with p the pressure, μ the viscosity and $\mathbb{I}^{2\times 2}$ the identity matrix. For simplicity we allow μ to vary in x and y only (allowing variation in the z-direction gives rise to extra terms in the governing equations in the thin-sheet limit, see Pfingstag et al., 2011b, for details).

The dimensionless Stokes equations can be written

$$\tilde{\nabla}\cdot\boldsymbol{\mathcal{U}} + \epsilon^{-2}\frac{\partial w}{\partial z} = 0, \tag{6.5a}$$

$$\tilde{\nabla}\cdot\boldsymbol{\mathcal{S}} + \epsilon^{-2}\frac{\partial \bar{\boldsymbol{\sigma}}}{\partial z} = \mathbf{0}, \tag{6.5b}$$

$$\tilde{\nabla}\cdot\bar{\boldsymbol{\sigma}} + \frac{\partial}{\partial z}\left(-\delta^{-1}p + 2\epsilon^{-2}\mu\frac{\partial w}{\partial z}\right) = 0. \tag{6.5c}$$

On the sheet surfaces $z = z^{\pm} = H(\boldsymbol{X},\tau) \pm h(\boldsymbol{X},\tau)$, we impose no-flux and no-stress conditions

$$\delta\epsilon^{-2}\frac{\partial z^{\pm}}{\partial \tau} + \boldsymbol{\mathcal{U}}\cdot\tilde{\nabla}z^{\pm} = \epsilon^{-2}w, \tag{6.6a}$$

$$\boldsymbol{\mathcal{S}} \cdot \tilde{\nabla} z^{\pm} = \epsilon^{-2} \bar{\boldsymbol{\sigma}}, \tag{6.6b}$$

$$\bar{\boldsymbol{\sigma}} \cdot \tilde{\nabla} z^{\pm} = -p + 2\epsilon^{-2} \mu \frac{\partial w}{\partial z}. \tag{6.6c}$$

At the free edge $y = b(x, \tau)$ the no-flux and no-stress conditions are given by

$$\epsilon^{-2} \frac{\partial b}{\partial \tau} + \delta^{-2} u \frac{\partial b}{\partial x} = v, \tag{6.7a}$$

$$\boldsymbol{\mathcal{S}} \cdot \hat{\boldsymbol{n}} = \mathbf{0}, \tag{6.7b}$$

$$\bar{\boldsymbol{\sigma}} \cdot \hat{\boldsymbol{n}} = 0, \tag{6.7c}$$

where $\hat{\boldsymbol{n}}$ is the outward-pointing normal to the free edge. At the top of the drawing domain, $x = 0$, the sheet shape is known, its velocity $(1, 0, 0)$ is controlled by the rollers and it is simply-supported, so that

$$\boldsymbol{\mathcal{U}} = (1, 0), \quad w = 0, \tag{6.8a}$$

$$b = h = 1, \tag{6.8b}$$

$$H = \frac{\partial^3 H}{\partial x^2 \partial \tau} = 0. \tag{6.8c}$$

At the bottom of the drawing domain, $x = 1$, draw rollers impose an increased velocity $(D, 0, 0)$, and the sheet is again simply-supported, so the appropriate boundary conditions are

$$\boldsymbol{\mathcal{U}} = (D, 0), \quad w = 0, \tag{6.9a}$$

$$H = \frac{\partial^3 H}{\partial x^2 \partial \tau} = 0. \tag{6.9b}$$

We treat δ as an $O(1)$ constant and consider the thin-sheet limit $\epsilon \to 0$ to obtain a simplified system of equations in two spatial dimensions. The bulk equations have been derived previously (see, for example Howell, 1994), and the derivation is very similar to that carried out in the preceding chapters, so we give only a brief overview here. At leading order in ϵ, conservation of mass (6.5a) together with the no-flux condition (6.6a) on the free surface $z = \pm h$ yields

$$\frac{\partial h}{\partial \tau} = 0, \quad w = \delta \frac{\partial H}{\partial \tau}, \tag{6.10}$$

and the no-flux condition (6.7a) at the free edge $y = b$ yields

$$\frac{\partial b}{\partial \tau} = 0, \tag{6.11}$$

so the thickness and width of the sheet do not change on the buckling timescale, as expected. Carrying out the same process for the in-plane momentum (6.5b) and

corresponding no-stress condition (6.6b), the leading-order in-plane velocity may be written

$$\boldsymbol{\mathcal{U}} = \bar{\boldsymbol{\mathcal{U}}} - \delta(z-H)\tilde{\nabla}\left(\frac{\partial H}{\partial \tau}\right), \tag{6.12}$$

where

$$\bar{\boldsymbol{\mathcal{U}}} = \frac{1}{2h}\int_{z^-}^{z^+} \boldsymbol{\mathcal{U}}\, \mathrm{d}z \tag{6.13}$$

is the in-plane velocity averaged across the sheet thickness. We evaluate the transverse momentum equation (6.5c) at $O(1)$ and use the no-stress condition (6.6c) and mass conservation (6.5a) to obtain an expression for the leading-order pressure in terms of the in-plane velocity, namely

$$\delta^{-1}p = -2\mu\tilde{\nabla}\cdot\boldsymbol{\mathcal{U}}, \tag{6.14}$$

so, at leading order,

$$\boldsymbol{\mathcal{S}} = 2\mu\tilde{\nabla}\cdot\boldsymbol{\mathcal{U}}\mathbb{I}^{2\times 2} + \mu\left(\tilde{\nabla}\boldsymbol{\mathcal{U}} + \tilde{\nabla}\boldsymbol{\mathcal{U}}^T\right). \tag{6.15}$$

We then proceed to next order in the in-plane momentum equations, integrating across the sheet thickness and applying the boundary conditions (6.6b) to arrive at (to leading order)

$$\tilde{\nabla}\cdot\bar{\boldsymbol{\mathcal{S}}} = \mathbf{0}, \tag{6.16}$$

where

$$\bar{\mathcal{S}}_{xx} = 4\delta^{-1}\mu h\left(\frac{\partial \bar{u}}{\partial x} + \frac{\partial H}{\partial x}\frac{\partial^2 H}{\partial x \partial \tau}\right) + 2\delta\mu h\left(\frac{\partial \bar{v}}{\partial y} + \frac{\partial H}{\partial y}\frac{\partial^2 H}{\partial y \partial \tau}\right), \tag{6.17a}$$

$$\bar{\mathcal{S}}_{xy} = \bar{\mathcal{S}}_{yx} = \mu h\left(\frac{\partial \bar{u}}{\partial y} + \frac{\partial H}{\partial y}\frac{\partial^2 H}{\partial x \partial \tau} + \frac{\partial \bar{v}}{\partial x} + \frac{\partial H}{\partial x}\frac{\partial^2 H}{\partial y \partial \tau}\right), \tag{6.17b}$$

$$\bar{\mathcal{S}}_{yy} = 2\delta^{-1}\mu h\left(\frac{\partial \bar{u}}{\partial x} + \frac{\partial H}{\partial x}\frac{\partial^2 H}{\partial x \partial \tau}\right) + 4\delta\mu h\left(\frac{\partial \bar{v}}{\partial y} + \frac{\partial H}{\partial y}\frac{\partial^2 H}{\partial y \partial \tau}\right), \tag{6.17c}$$

with subscripts used to denote tensor components.

One additional equation is required to fully describe the system including the mid-surface H. This is obtained by multiplying the in-plane momentum equation (6.5b) with $(z-H)$, integrating across the sheet thickness and applying the no-stress condition (6.6b). Taking the divergence of the resulting equation and using the transverse momentum equation (6.5c) and corresponding no-stress condition (6.6c) yields

$$\delta\tilde{\nabla}\cdot\left(\tilde{\nabla}\cdot\boldsymbol{\mathcal{M}}\right) + \tilde{\nabla}\cdot\left(\tilde{\nabla}H\cdot\bar{\boldsymbol{\mathcal{S}}}\right) = 0, \tag{6.18}$$

where

$$\boldsymbol{\mathcal{M}} = -\mu\frac{h^3}{3}\begin{pmatrix} 4\delta^{-2}\dfrac{\partial^3 H}{\partial x^2\partial\tau} + 2\dfrac{\partial^3 H}{\partial y^2\partial\tau} & 2\delta^{-1}\dfrac{\partial^3 H}{\partial x\partial y\partial\tau} \\ 2\delta^{-1}\dfrac{\partial^3 H}{\partial x\partial y\partial\tau} & 2\delta^{-2}\dfrac{\partial^3 H}{\partial x^2\partial\tau} + 4\dfrac{\partial^3 H}{\partial y^2\partial\tau} \end{pmatrix}. \tag{6.19}$$

The governing equations (6.16)–(6.19) must be supplemented by appropriate boundary conditions. To determine the boundary conditions on the free surface $y = b(x)$, one might naively integrate the boundary conditions (6.7) multiplied by $(z-H)$ across the sheet thickness, as we did with the bulk equations (6.5) in deriving the governing equations (6.16)–(6.19). However, this gives rise to more boundary conditions than can be satisfied in general. There is a boundary layer near the sheet edge where the stresses adjust rapidly, and we must study the behaviour in this boundary layer to determine appropriate conditions for the bulk equations.

6.3 Free-boundary conditions

For a solid rectangular plate, Howell et al. (2009) show that the boundary conditions associated with the sheet mid-surface at a free edge $y =$ constant are

$$\mathcal{M}_{yy} = \frac{\partial \mathcal{M}_{xy}}{\partial x} + \int_{z^-}^{z^+} \tau_{yz}\,\mathrm{d}z = 0. \tag{6.20}$$

(We note that the notation used here and in recent viscous-sheet literature (Perdigou and Audoly, 2016; Srinivasan et al., 2017) is different from the notation used for solid plates in Howell et al., 2009.) In this section we systematically derive the boundary conditions at the free edge of a viscous sheet of arbitrary shape, using an analogous asymptotic analysis to the derivation of the conditions at the edges of a solid rectangular plate by Howell et al. (2009). We determine simple relations for the stresses and bending moments inside a boundary layer near the sheet edge, and from these infer conditions on the bulk stresses and moments at the edge. We expect our boundary conditions for the mid-surface to resemble (6.20), but to take into account the fact that, in the case of redraw of a thin glass sheet, the sheet edge is curved.

6.3.1 Boundary-layer governing equations

We first change from Cartesian coordinates to a coordinate system embedded in the sheet edge. We identify a tangent vector to the sheet edge $\hat{\boldsymbol{t}}$, and denote arclength

along the sheet edge by s as shown in figure 6.4. The position in the sheet is then given by

$$\boldsymbol{r}(s,n,z) = \int_0^s \hat{\boldsymbol{t}}(s')\,\mathrm{d}s' + n\hat{\boldsymbol{n}}(s) + z\hat{\boldsymbol{z}}, \tag{6.21}$$

where $\hat{\boldsymbol{z}}$ is a unit vector in the z direction. We note that $\partial\boldsymbol{r}/\partial s = (1-\kappa n)\hat{\boldsymbol{t}}$, where $\kappa = -\mathrm{d}\theta/\mathrm{d}s = -\nabla\cdot\hat{\boldsymbol{n}}$ is the curvature of the sheet edge, so that the gradient vector in this coordinate system is given by

$$\nabla = \hat{\boldsymbol{t}}\frac{1}{1-\kappa n}\frac{\partial}{\partial s} + \hat{\boldsymbol{n}}\frac{\partial}{\partial n} + \hat{\boldsymbol{z}}\frac{\partial}{\partial z}. \tag{6.22}$$

We scale into the boundary layer $n = \epsilon N$ at the sheet edge (using hats to denote variables inside this boundary layer), noting that n, $N < 0$ in the sheet. The three-

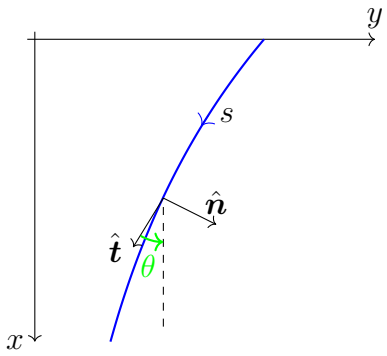

Figure 6.4: Curvilinear coordinates with unit vectors $\hat{\boldsymbol{n}}$ and $\hat{\boldsymbol{t}}$, and θ the angle between the tangent vector and the x-axis.

dimensional Stokes equations (6.5) are transformed to

$$\frac{\partial\hat{u}_s}{\partial s} + \epsilon^{-1}\frac{\partial}{\partial N}\left[(1-\epsilon\kappa N)\,\hat{u}_n\right] + \epsilon^{-2}\frac{\partial}{\partial z}\left[(1-\epsilon\kappa N)\,\hat{w}\right] = 0, \tag{6.23a}$$

$$\frac{\partial\hat{\tau}_{ss}}{\partial s} + \epsilon^{-1}\frac{\partial}{\partial N}\left[(1-\epsilon\kappa N)\,\hat{\tau}_{sn}\right] + \epsilon^{-1}\frac{\partial}{\partial z}\left[(1-\epsilon\kappa N)\,\hat{\tau}_{sz}\right] - \kappa\hat{\tau}_{sn} = 0, \tag{6.23b}$$

$$\frac{\partial\hat{\tau}_{sn}}{\partial s} + \epsilon^{-1}\frac{\partial}{\partial N}\left[(1-\epsilon\kappa N)\,\hat{\tau}_{nn}\right] + \epsilon^{-1}\frac{\partial}{\partial z}\left[(1-\epsilon\kappa N)\,\hat{\tau}_{nz}\right] + \kappa\hat{\tau}_{ss} = 0, \tag{6.23c}$$

$$\frac{\partial\hat{\tau}_{sz}}{\partial s} + \epsilon^{-1}\frac{\partial}{\partial N}\left[(1-\epsilon\kappa N)\,\hat{\tau}_{nz}\right] + \epsilon^{-1}\frac{\partial}{\partial z}\left[(1-\epsilon\kappa N)\,\hat{\tau}_{zz}\right] = 0, \tag{6.23d}$$

and the stress components in the new coordinate system are given by

$$\hat{\tau}_{ss} = -\hat{p} + \frac{2\mu}{1-\epsilon\kappa N}\left(\frac{\partial\hat{u}_s}{\partial s} - \kappa\hat{u}_n\right), \tag{6.24a}$$

$$\hat{\tau}_{nn} = -\hat{p} + 2\mu\epsilon^{-1}\frac{\partial\hat{u}_n}{\partial N}, \tag{6.24b}$$

$$\hat{\tau}_{ns} = \hat{\tau}_{sn} = \mu \left(\frac{\kappa}{1-\epsilon\kappa N} \hat{u}_s + \epsilon^{-1} \frac{\partial \hat{u}_s}{\partial N} + \frac{1}{1-\epsilon\kappa N} \frac{\partial \hat{u}_n}{\partial s} \right), \tag{6.24c}$$

$$\hat{\tau}_{zs} = \hat{\tau}_{sz} = \epsilon^{-1} \mu \left(\frac{\partial \hat{u}_s}{\partial z} + \frac{1}{1-\epsilon\kappa N} \frac{\partial \hat{w}}{\partial s} \right), \tag{6.24d}$$

$$\hat{\tau}_{zn} = \hat{\tau}_{nz} = \epsilon^{-1} \mu \left(\frac{\partial \hat{u}_n}{\partial z} + \epsilon^{-1} \frac{\partial \hat{w}}{\partial N} \right), \tag{6.24e}$$

$$\hat{\tau}_{zz} = -\hat{p} + 2\mu\epsilon^{-2} \frac{\partial \hat{w}}{\partial z}. \tag{6.24f}$$

We will assume that the viscosity μ is approximately uniform across the boundary layer. The no-flux and no-stress boundary conditions (6.6) on the free surface $z = \hat{z}^{\pm} = \hat{H} \pm \hat{h}$ are transformed to

$$\epsilon^{-2} \frac{\partial \hat{z}^{\pm}}{\partial \tau} + \hat{u}_s \frac{1}{1-\epsilon\kappa N} \frac{\partial \hat{z}^{\pm}}{\partial s} + \epsilon^{-1} \hat{u}_n \frac{\partial \hat{z}^{\pm}}{\partial N} = \epsilon^{-2} \hat{w}, \tag{6.25a}$$

$$\frac{1}{1-\epsilon\kappa N} \frac{\partial \hat{z}^{\pm}}{\partial s} \hat{\tau}_{ss} + \epsilon^{-1} \frac{\partial \hat{z}^{\pm}}{\partial N} \hat{\tau}_{sn} = \epsilon^{-1} \hat{\tau}_{sz}, \tag{6.25b}$$

$$\frac{1}{1-\epsilon\kappa N} \frac{\partial \hat{z}^{\pm}}{\partial s} \hat{\tau}_{ns} + \epsilon^{-1} \frac{\partial \hat{z}^{\pm}}{\partial N} \hat{\tau}_{nn} = \epsilon^{-1} \hat{\tau}_{nz}, \tag{6.25c}$$

$$\frac{1}{1-\epsilon\kappa N} \frac{\partial \hat{z}^{\pm}}{\partial s} \hat{\tau}_{zs} + \epsilon^{-1} \frac{\partial \hat{z}^{\pm}}{\partial N} \hat{\tau}_{zn} = \epsilon^{-1} \hat{\tau}_{zz}. \tag{6.25d}$$

On the free edge $N = 0$ the no-flux and no-stress boundary conditions (6.7) are simplified to

$$\hat{u}_n = 0, \tag{6.26a}$$

$$\hat{\tau}_{ns} = 0, \tag{6.26b}$$

$$\hat{\tau}_{nn} = 0, \tag{6.26c}$$

$$\hat{\tau}_{zn} = 0. \tag{6.26d}$$

6.3.2 Leading-order variables

Our procedure is now to expand variables in powers of the small aspect ratio of thickness to length, ϵ. We first consider the stress components (6.24), and determine how large they can be. This will allow us to determine which of the variables have N-dependence, i.e. which of the sheet properties vary across the boundary layer and which are uniform. The stress components $\hat{\tau}_{sn}$, $\hat{\tau}_{nn}$ and $\hat{\tau}_{zn}$ are all zero at the edge according to no-stress conditions (6.26), and increase to $O(1)$ as $N \to -\infty$ (by matching to the bulk), so we expect

$$\hat{\tau}_{sn}, \;\; \hat{\tau}_{nn}, \;\; \hat{\tau}_{zn} \;\; \sim O(1). \tag{6.27}$$

Comparing with definitions (6.24), we deduce

$$\hat{u}_{s0} = u_{s0}(s, 0, z, \tau), \tag{6.28a}$$

$$\hat{u}_{n0} = u_{n0}(s, 0, z, \tau), \tag{6.28b}$$

$$\hat{w}_0 = w_0(s, 0, \tau), \tag{6.28c}$$

so the leading-order velocity is uniform across the boundary layer, and

$$\frac{\partial \hat{u}_{n0}}{\partial z} + \frac{\partial \hat{w}_1}{\partial N} = 0. \tag{6.29}$$

Comparing the leading-order in-plane velocity (6.28a) and (6.28b) to the bulk (6.12), we can write the leading-order velocity inside the boundary layer in terms of bulk variables at the sheet edge, i.e.

$$\hat{u}_{s0} = \bar{u}_{s0} - (z - H_0)\frac{\partial w_0}{\partial s}, \tag{6.30a}$$

$$\hat{u}_{n0} = \bar{u}_{n0} - (z - H_0)\,\frac{\partial w_0}{\partial n}, \tag{6.30b}$$

where $\bar{u}_{s0}$ and $\bar{u}_{n0}$ are the bulk velocity components averaged across the sheet thickness according to (6.13), and all the terms on the right-hand side are evaluated at $n = 0$. Returning to the question of the size of the stress components, we balance terms in the momentum equations (6.23b) and (6.23d). Taking into account that $\hat{\tau}_{sn}$ and $\hat{\tau}_{zn}$ are $O(1)$ from (6.27), we deduce that

$$\hat{\tau}_{sz}, \;\; \hat{\tau}_{zz} \;\; \sim O(1). \tag{6.31}$$

Now that we have established the size of the terms in the governing equations (6.23)–(6.26), we proceed by evaluating at leading order in ϵ. Integrating the continuity equation (6.23a) across the sheet thickness and applying the kinematic boundary condition (6.25a) we find

$$\hat{w}_0 = \frac{\partial \hat{H}_0}{\partial \tau}, \quad \frac{\partial \hat{h}_0}{\partial \tau} = 0. \tag{6.32}$$

Integrating (6.32) with respect to τ we see that, since $\hat{w}_0$ is uniform across the boundary layer by (6.28c), it follows that the leading-order sheet centreline $\hat{H}_0$ and thickness $\hat{h}_0$ are uniform across the boundary layer if this is the case initially. The initial conditions are given by the steady-state solution on the stretching timescale t. Considering the no-flux condition (6.25a) on this longer stretching timescale (rescaling both time and out-of-plane velocity $\hat{w}$ for stretching) reveals $\partial \hat{z}_0^{\pm}/\partial N = 0$, so the sheet surfaces $\hat{z}_0^{\pm} = \hat{H}_0 \pm \hat{h}_0$ are uniform across the boundary layer on the stretching timescale, and so on the buckling timescale

$$\hat{z}_0^{\pm} = z_0^{\pm}(s, 0, \tau). \tag{6.33}$$

6.3.3 Stress conditions

To determine the variation of the stresses inside the boundary layer, we follow the same procedure we used in §6.2 to derive the bulk momentum equations (6.16)–(6.17). Integrating the momentum equations (6.23b)–(6.23d) and applying boundary conditions (6.25) yields

$$\frac{\partial}{\partial s}\int_{\hat{z}^-}^{\hat{z}^+} \hat{\tau}_{ss}\,\mathrm{d}z + \epsilon^{-1}\frac{\partial}{\partial N}\int_{\hat{z}^-}^{\hat{z}^+} (1-\epsilon\kappa N)\,\hat{\tau}_{sn}\,\mathrm{d}z - \kappa\int_{\hat{z}^-}^{\hat{z}^+} \hat{\tau}_{sn}\,\mathrm{d}z = 0, \tag{6.34a}$$

$$\frac{\partial}{\partial s}\int_{\hat{z}^-}^{\hat{z}^+} \hat{\tau}_{sn}\,\mathrm{d}z + \epsilon^{-1}\frac{\partial}{\partial N}\int_{\hat{z}^-}^{\hat{z}^+} (1-\epsilon\kappa N)\,\hat{\tau}_{nn}\,\mathrm{d}z + \kappa\int_{\hat{z}^-}^{\hat{z}^+} \hat{\tau}_{ss}\,\mathrm{d}z = 0, \tag{6.34b}$$

$$\frac{\partial}{\partial s}\int_{\hat{z}^-}^{\hat{z}^+} \hat{\tau}_{sz}\,\mathrm{d}z + \epsilon^{-1}\frac{\partial}{\partial N}\int_{\hat{z}^-}^{\hat{z}^+} (1-\epsilon\kappa N)\,\hat{\tau}_{nz}\,\mathrm{d}z = 0. \tag{6.34c}$$

Evaluating at leading order, integrating over $N \in (-\infty, 0]$ and applying edge conditions (6.26) on $N = 0$ gives

$$\int_{\hat{z}_0^-}^{\hat{z}_0^+} \hat{\tau}_{sn0}\,\mathrm{d}z = \int_{\hat{z}_0^-}^{\hat{z}_0^+} \hat{\tau}_{nn0}\,\mathrm{d}z = \int_{\hat{z}_0^-}^{\hat{z}_0^+} \hat{\tau}_{zn0}\,\mathrm{d}z = 0, \tag{6.35}$$

so the leading-order normal stress components, integrated across the sheet thickness, are uniform across the boundary layer and, since there are no stresses at the free edge, these averaged quantities are all uniformly equal to zero. Matching with the bulk, we obtain boundary conditions for the leading-order in-plane stress at the free edge, namely

$$\int_{\hat{z}_0^-}^{\hat{z}_0^+} \tau_{sn0}\,\mathrm{d}z = \int_{\hat{z}_0^-}^{\hat{z}_0^+} \tau_{nn0}\,\mathrm{d}z = \int_{\hat{z}_0^-}^{\hat{z}_0^+} \tau_{zn0}\,\mathrm{d}z = 0 \quad \text{on} \quad n = 0. \tag{6.36}$$

We note that the conditions on τ_{sn0} and τ_{nn0} are equivalent to the condition of no normal stress we have imposed at the sheet edge in Chapter 3.

6.3.4 Moment conditions

Since we are now also modelling out-of-plane deformations using the mid-surface equation (6.18), we require two further boundary conditions at the free edge. To determine the variation of the bending moments across the boundary layer, we follow the procedure used in §6.2 to derive the mid-surface equation (6.18) in the bulk. We multiply (6.23c) by $(z - \hat{H})$, integrate across the sheet thickness, and use boundary

condition (6.25c) to arrive at

$$\frac{\partial}{\partial s}\int_{\hat{z}^-}^{\hat{z}^+}(z-\hat{H})\hat{\tau}_{sn}\,\mathrm{d}z+\epsilon^{-1}\frac{\partial}{\partial N}\int_{\hat{z}^-}^{\hat{z}^+}(z-\hat{H})\,(1-\epsilon\kappa N)\,\hat{\tau}_{nn}\,\mathrm{d}z \\ +\frac{\partial\hat{H}}{\partial s}\int_{\hat{z}^-}^{\hat{z}^+}\hat{\tau}_{sn}\,\mathrm{d}z+\epsilon^{-1}\frac{\partial\hat{H}}{\partial N}\int_{\hat{z}^-}^{\hat{z}^+}(1-\epsilon\kappa N)\,\hat{\tau}_{nn}\,\mathrm{d}z \\ +\kappa\int_{\hat{z}^-}^{\hat{z}^+}(z-\hat{H})\hat{\tau}_{ss}\,\mathrm{d}z=\epsilon^{-1}\int_{\hat{z}^-}^{\hat{z}^+}(1-\epsilon\kappa N)\,\hat{\tau}_{nz}\,\mathrm{d}z. \quad (6.37)$$

Evaluating at leading order and using (6.33), (6.35) to eliminate terms, and then integrating over $N\in(-\infty,0]$ and using no-stress condition (6.26c) on $N=0$, gives

$$\int_{\hat{z}_0^-}^{\hat{z}_0^+}\left(z-\hat{H}_0\right)\hat{\tau}_{nn0}\,\mathrm{d}z=0, \quad (6.38)$$

so, to leading order, the nn-component of the bending moment is uniformly equal to zero across the boundary layer. Matching with the bulk we deduce that

$$\int_{z_0^-}^{z_0^+}(z-H_0)\,\tau_{nn0}\,\mathrm{d}z=0\quad\text{on}\quad n=0. \quad (6.39)$$

We now have two free-boundary conditions (6.36) for the in-plane stress components, together with one free-boundary moment condition (6.39), and we require another to close the problem. We evaluate the transverse momentum equation (6.34c) at $O(1)$ and use (6.35) to arrive at

$$\frac{\partial}{\partial s}\int_{\hat{z}_0^-}^{\hat{z}_0^+}\hat{\tau}_{sz0}\,\mathrm{d}z+\frac{\partial}{\partial N}\int_{\hat{z}_0^-}^{\hat{z}_0^+}\hat{\tau}_{zn1}\,\mathrm{d}z=0. \quad (6.40)$$

Integrating over $N\in(-\infty,0]$, applying no-stress condition (6.26d) on $N=0$ and matching with the bulk for $N\to-\infty$ gives

$$\int_{-\infty}^{0}\left(\frac{\partial}{\partial s}\int_{\hat{z}_0^-}^{\hat{z}_0^+}\hat{\tau}_{sz0}\,\mathrm{d}z\right)\,\mathrm{d}N=\int_{z_0^-}^{z_0^+}\tau_{zn1}\,\mathrm{d}z\quad\text{on}\quad n=0. \quad (6.41)$$

We are aiming to derive boundary conditions on the bulk variables, so we determine the boundary-layer stress component

$$\hat{\tau}_{sz0}=\mu\left(\frac{\partial\hat{u}_{s1}}{\partial z}+\frac{\partial\hat{w}_1}{\partial s}+\kappa N\frac{\partial\hat{w}_0}{\partial s}\right) \quad (6.42)$$

in terms of bulk quantities. This involves some easy but tedious calculations which we present in Appendix B. Inserting the result directly into (6.41) we arrive at

$$\int_{z_0^-}^{z_0^+}\tau_{zn1}\,\mathrm{d}z=-\frac{\partial}{\partial s}\left(\int_{z_0^-}^{z_0^+}(z-H_0)\tau_{sn0}\,\mathrm{d}z\right)\quad\text{on}\quad n=0. \quad (6.43)$$

This is the final boundary condition at the free edge.

6.3.5 Summary

Employing the tensor notation introduced in §6.2 for the bending moment $\boldsymbol{\mathcal{M}}$ and stress $\bar{\boldsymbol{\mathcal{S}}}$, the boundary conditions (6.36), (6.39) and (6.43) on the bulk variables at the free edge are thus

$$\bar{\mathcal{S}}_{sn} = \bar{\mathcal{S}}_{nn} = 0, \tag{6.44a}$$

$$\mathcal{M}_{nn} = 0, \tag{6.44b}$$

$$\int_{z_0^+}^{z_0^-} \tau_{zn1} \, \mathrm{d}z = -\frac{\partial \mathcal{M}_{sn}}{\partial s}. \tag{6.44c}$$

We can verify that these are the natural boundary conditions for the momentum (6.16) and centreline (6.18) equations by rewriting (6.16) and (6.18) in weak form and setting the boundary terms equal to zero, and that they are consistent with the conditions for a solid rectangular plate (Howell et al., 2009) by setting $\kappa = 0$, $s = x$ and $n = y$. This is also consistent with the boundary conditions derived heuristically by Srinivasan et al. (2017) by evaluating the work done on the edge and recognizing that it must be zero at a free edge.

We can write the final boundary condition (6.44c) in a more useful form for the problem at hand by considering the normal momentum equation in the bulk

$$\frac{\partial \tau_{sn}}{\partial s} + \frac{\partial}{\partial n}\left[(1-\kappa n)\tau_{nn}\right] + \epsilon^{-1}\frac{\partial}{\partial z}\left[(1-\kappa n)\tau_{nz}\right] + \kappa\tau_{ss} = 0. \tag{6.45}$$

Integrating with $(z-H)$ across the sheet thickness and applying no-stress conditions on the free surface gives

$$\begin{aligned}\frac{\partial}{\partial s}\int_{z^-}^{z^+}(z-H)\tau_{sn}\,\mathrm{d}z + \frac{\partial H}{\partial s}\int_{z^-}^{z^+}\tau_{sn}\,\mathrm{d}z \\ + \frac{\partial}{\partial n}\int_{z^-}^{z^+}(z-H)(1-\kappa n)\tau_{nn}\,\mathrm{d}z + \frac{\partial H}{\partial n}\int_{z^-}^{z^+}(1-\kappa n)\,\tau_{nn}\,\mathrm{d}z \\ + \kappa\int_{z^-}^{z^+}(z-H)\tau_{ss}\,\mathrm{d}z = \epsilon^{-1}\int_{z^-}^{z^+}(1-\kappa n)\tau_{nz}\,\mathrm{d}z.\end{aligned} \tag{6.46}$$

Evaluating at $O(1)$ allows us to rewrite the final boundary condition (6.43) on $n = 0$ as

$$2\frac{\partial \mathcal{M}_{sn}}{\partial s} + \frac{\partial \mathcal{M}_{nn}}{\partial n} + \kappa\mathcal{M}_{ss} = 0. \tag{6.47}$$

6.4 Compression zones

Studies by Filippov and Zheng (2010) and Srinivasan et al. (2017) note that the size and location of compression zones in glass sheets undergoing redraw depend strongly on the length of the heater zone. In both cases the authors consider thin sheets where the aspect ratio of the length of the drawing domain to the sheet half-width $\delta = O(1)$, and impose a temperature profile with a hot zone of some characteristic length. Their main qualitative observations regarding compression zones can be summarized as follows:

- when the heater zone length is comparable with sheet length considered, one compression zone is observed in the upper region of the heater zone,
- when the heater zone is short compared with the sheet length considered, two compression zones are observed, one in the upper region of the heater zone and one below (see figure 6.2).

We determine which parts of the sheet are under compression by calculating the principal stresses in the sheet (Filippov and Zheng, 2010), i.e. the eigenvalues of the stress tensor

$$\mathcal{P}^{\pm} = \frac{1}{2}\left(\bar{\mathcal{S}}_{xx} + \bar{\mathcal{S}}_{yy} \pm \sqrt{\left(\bar{\mathcal{S}}_{xx} - \bar{\mathcal{S}}_{yy}\right)^2 + 4\bar{\mathcal{S}}_{xy}^2}\right). \tag{6.48}$$

The principal stresses $\mathcal{P}^{\pm}$ together with their corresponding eigenvectors characterize the stress at a point in the sheet, and $\mathcal{P}^{+} > \mathcal{P}^{-}$. For redraw, we expect $P^{+} > 0$ everywhere, but P^{-} may change sign, depending on the sign of

$$\Delta = \bar{\mathcal{S}}_{xx}\bar{\mathcal{S}}_{yy} - \bar{\mathcal{S}}_{xy}^2. \tag{6.49}$$

In regions where $\mathcal{P}^{-} > 0$ ($\Delta > 0$), the sheet is under tension in every direction, but in regions where $\mathcal{P}^{-} < 0$ ($\Delta < 0$), the sheet experiences compression in the direction of the corresponding eigenvector. This compressive force may lead to buckling or wrinkling of the sheet, with the wrinkles aligned perpendicular to the axis of compression. We note that $\mathcal{P}^{-} = 0$ along the sheet edge by the no-stress conditions (6.44a).

6.4.1 Stresses in a planar sheet

We begin by calculating the steady-state solution, in which the mid-surface is flat so $H = 0$, and the stress profile

$$\bar{\boldsymbol{\mathcal{S}}}_0 := \bar{\boldsymbol{\mathcal{S}}}(H = 0) = \mu h\left[2\tilde{\nabla}\cdot\bar{\boldsymbol{u}}\mathbb{I} + \tilde{\nabla}\bar{\boldsymbol{u}} + \tilde{\nabla}\bar{\boldsymbol{u}}^T\right] \tag{6.50}$$

can be determined together with the sheet width b and thickness h by solving the governing equations

$$\tilde{\nabla} \cdot \left(h\bar{\boldsymbol{\mathcal{U}}}\right) = 0, \tag{6.51a}$$

$$\tilde{\nabla} \cdot \bar{\boldsymbol{\mathcal{S}}}_0 = \mathbf{0}, \tag{6.51b}$$

together with free-boundary conditions

$$\bar{\boldsymbol{\mathcal{U}}} \cdot \hat{\boldsymbol{n}} = 0, \tag{6.52a}$$

$$\bar{\boldsymbol{\mathcal{S}}}_0 \cdot \hat{\boldsymbol{n}} = 0 \tag{6.52b}$$

on $y = b(x)$, symmetry conditions

$$\frac{\partial \bar{u}}{\partial y} = \bar{v} = 0 \tag{6.53}$$

on $y = 0$, and feed and draw conditions

$$\bar{u} = h = b = 1, \quad \bar{v} = 0 \quad \text{on} \quad x = 0, \tag{6.54a}$$

$$\bar{u} = D, \quad \bar{v} = 0 \quad \text{on} \quad x = 1. \tag{6.54b}$$

We determine the steady-state solution shown in figure 6.6 numerically by mapping the equations (6.50)–(6.54) to a fixed domain $(x, y/b) \in [0,1] \times [0,1]$ and using the finite-element software FEniCS. We calculate the principal stresses $\mathcal{P}^{\pm}$ as well as the corresponding directions, which we will use later in the chapter. Our numerical method for determining the steady-state behaviour of the sheet is relatively straightforward compared with the ALE and deformed mesh methods used by Filippov and Zheng (2010) and Srinivasan et al. (2017) since, once the mapping is made, the governing equations are solved in a known rectangular domain. We use a 400×800 grid on the fixed square domain; for higher resolution plots of the principal stresses in figure 6.6 do not change visibly.

Motivated by our interest in wrinkling at the bottom of the heater zone (giving rise to buckling in the final product), we also investigate the occurrence of compression zones in a thin sheet in the asymptotic limit where the heater zone is short compared with the sheet width. We determine which parts of the sheet are under compression by calculating $\mathcal{P}^{-}$ using solutions to the short-heater-zone model outlined in §§3.2–3.3.

6.4.2 Results

We first examine the compression zones observed in the short-heater-zone limit. For a uniform viscosity profile, one compression zone is observed near the sheet edge in the upper part of the stretching domain (see figure 6.5a). A separate compression zone in the lower portion of the sheet is not observed. Despite the observations of Filippov and Zheng (2010) and Srinivasan et al. (2017), this is not very surprising since the compression zones observed in the lower portion of sheets with $O(1)$ aspect ratio but a short heater zone are actually located *below* the main stretching region (see figure 6.6b) where the sheet width is almost constant, and are therefore outside of the domain typically considered in the short-heater-zone approximation. In the short-heater-zone approximation, the compression regions change qualitatively when the heater profile is further localized within this zone (see figure 6.5b and c). In this case, two separate compression zones can be observed in the upper and lower parts of the sheet, and the lower region of compression is mostly located outside of what might sensibly be classified as the heater zone.

In our studies of stretching of thin glass sheets in Chapters 2–4, our main interest is in calculating the thickness and width of the sheet, and so we restrict our attention to the region in which the glass temperature is high and its viscosity is low, since most of the in-plane acceleration, thinning and lateral necking are confined to this region. This can be seen, for example, in figure 6.5(c), where the sheet width changes significantly for $x \in [0.15, 0.5]$, but is almost uniform outside of this interval, where the glass is more viscous and more resistant to stretching. In Chapters 2–4, this allows us to apply the draw conditions to the sheet at some fixed distance below the heater zone, once the sheet is viscous enough to resist further stretching, even if the draw rollers are actually further downstream. By contrast, returning our focus to out-of-plane buckling we observe that the sheet in figure 6.5(c) has a compression zone in $x > 0.5$, so for studies of buckling it is necessary to study the sheet behaviour in the region between the end of the heater zone and the draw rollers, where important sheet dynamics may occur. Furthermore, contrasting figures 6.5(b) and (c) we note that the distance between the end of the heater zone and the line $x =$ constant where the draw conditions are applied numerically has a significant effect on the size of the compression zone.

In the remainder of this chapter we will focus on sheets whose aspect ratio of length to half-width $\delta = O(1)$, with either uniform or localized heating. In figure 6.6 we plot the principal stresses $\mathcal{P}^{\pm}$ for the case $\delta = 1$ for (a) a sheet with uniform

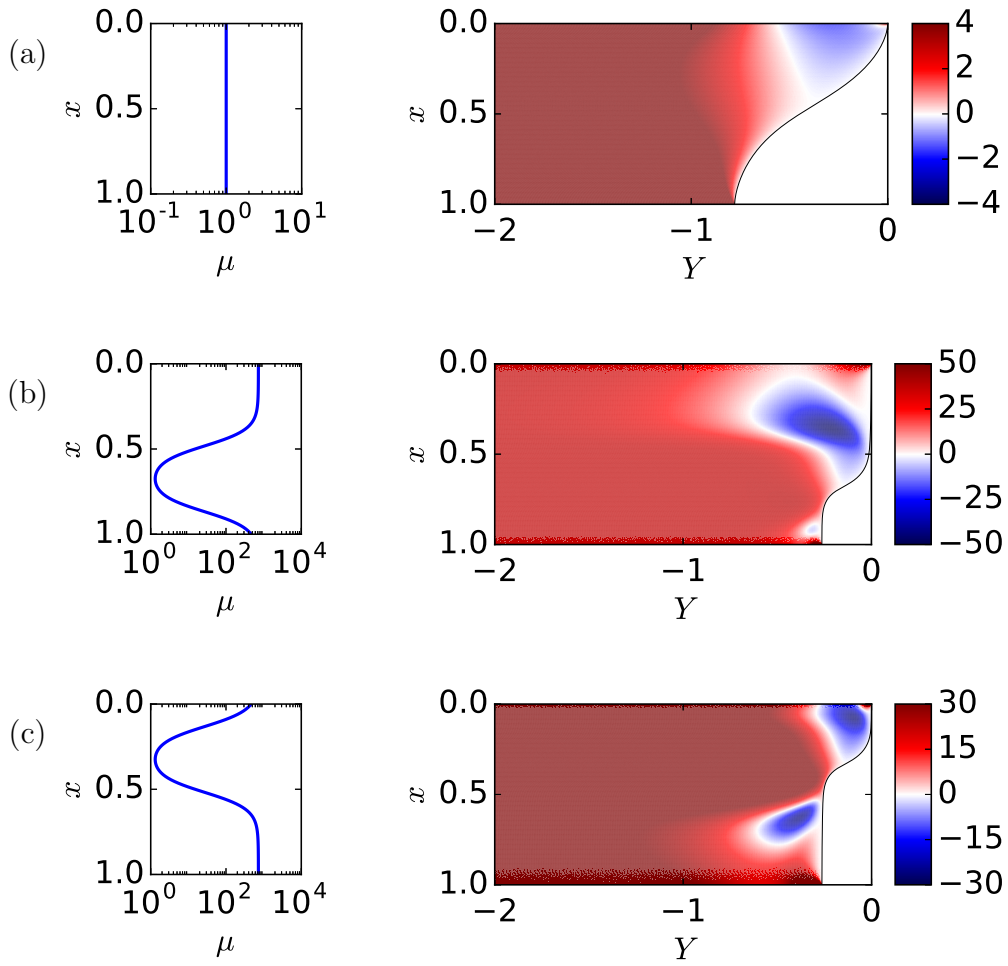

Figure 6.5: Principal stress $\mathcal{P}^-$ (6.48) in a thin sheet undergoing redraw with draw ratio $D = 20$ through a short heater zone for three different viscosity profiles (illustrated). Regions in which $\mathcal{P}^- > 0$ are coloured red, regions in which $\mathcal{P}^- < 0$ are coloured blue.

viscosity and (b) a sheet with localized heating

$$T(x) = \theta_0 + (1-\theta_0)\left(\frac{1}{1+\exp[-k(x-x_L)]} + \frac{1}{1+\exp[k(x-x_R)]} - 1\right), \quad (6.55)$$

for $\theta_0 = 0.8$, $k = 20$, $x_L = 0.25$ and $x_R = 0.75$, with viscosity

$$\mu = \exp\left[\frac{1}{\nu}\left(\frac{1}{T-T_c} - \frac{1}{1-T_c}\right)\right], \quad (6.56)$$

where $T_c = 0.34$ and $\nu = 0.1$. (We note that this is the profile supplied by Schott AG and used for comparison with experiment in the short-heater-zone limit in §3.5.) In the uniform viscosity case, $\mathcal{P}^- < 0$ near the sheet edge in the upper part of the sheet. In the localized heating case, $\mathcal{P}^- < 0$ in two separate regions, one in the upper part of the sheet and the other below the heater zone.

We also plot arrows indicating the axes along which the principal stresses are directed in figure 6.6. The tensile stress $\mathcal{P}^+$ is aligned primarily with the motion of the sheet, and is approximately parallel to the sheet edge. Meanwhile, $\mathcal{P}^-$ is aligned perpendicular to the motion of the sheet, and perpendicular to the sheet edge. We expect the wrinkles to form in the compression zones where $\mathcal{P}^- < 0$, and to be aligned perpendicular to $\mathcal{P}^-$, i.e. approximately parallel to the sheet edge.

We note that Srinivasan et al. (2017) also consider a viscosity profile of the form (6.55)–(6.56), with altered parameters $k = 40$, $x_L = 0.125$, $x_R = 0.625$ and $\nu = 0.15$, for a sheet with aspect ratio $\delta = 1.4$ undergoing redraw with draw ratio $D = 10$. For this profile, and others considered by Filippov and Zheng (2010) and Srinivasan et al. (2017), the compression zone in the lower region either stretches across the sheet width or is localized near the centre of the sheet, and the compression zone in the upper region may stretch across the sheet width or be localized near the sheet edge. We observe that the temperature and viscosity profiles (6.55)–(6.56) yield compressive zones that are localized near the sheet edge when the width of the preform is the same as the distance over which the sheet is drawn (see figure 6.6b), but extend towards the centre of the sheet as the aspect ratio of length to half-width δ is increased (see figure 6.7). This provides further evidence that the shape of the viscosity profile as well as both the length of the heater zone and the distance over which the sheet is drawn relative to the preform width are important for determining the compression zones and hence buckling profiles for a sheet undergoing redraw.

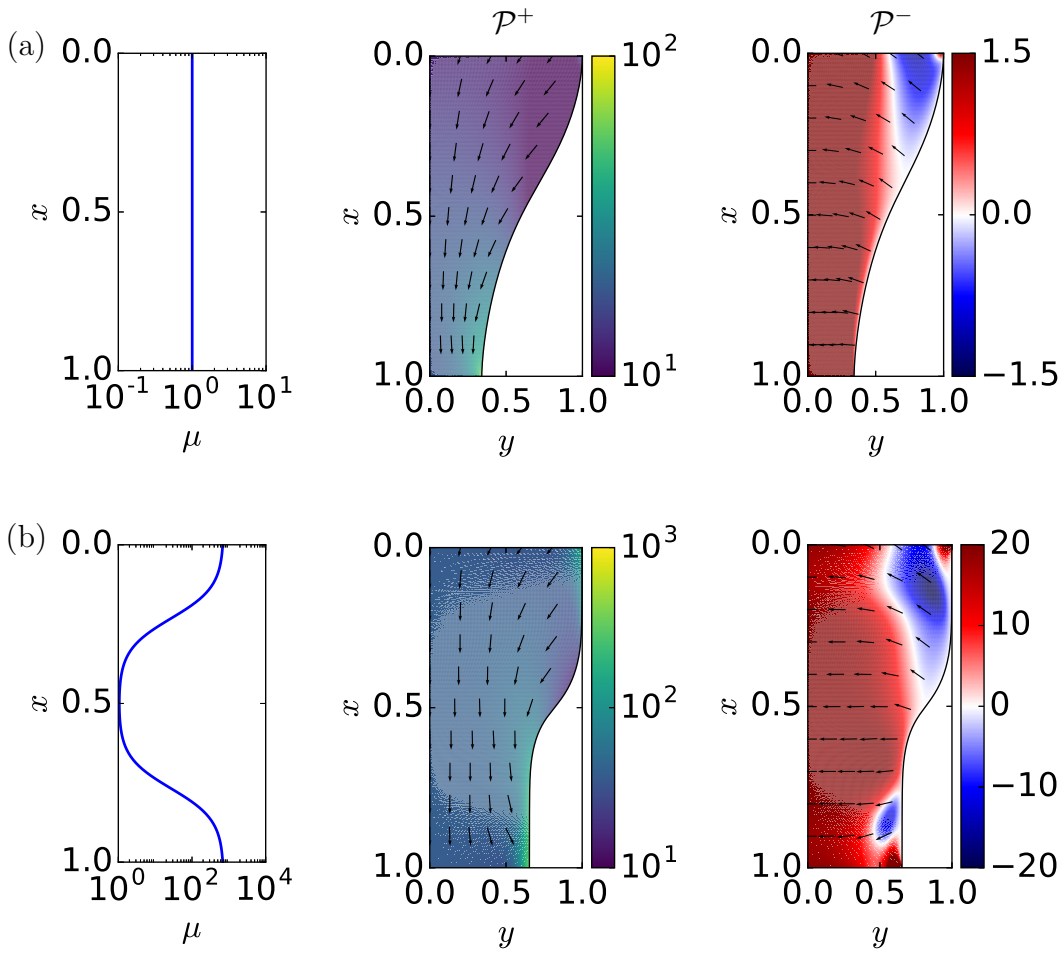

Figure 6.6: Principal stresses $\mathcal{P}^{\pm}$ (6.48) and corresponding eigenvectors in a thin sheet undergoing redraw with draw ratio $D = 20$, with aspect ratio drawing distance/half-width $= 1$, for two different viscosity profiles $\mu(x)$ (illustrated). Regions in which $\mathcal{P}^- > 0$ are coloured red, regions in which $\mathcal{P}^- < 0$ are coloured blue.

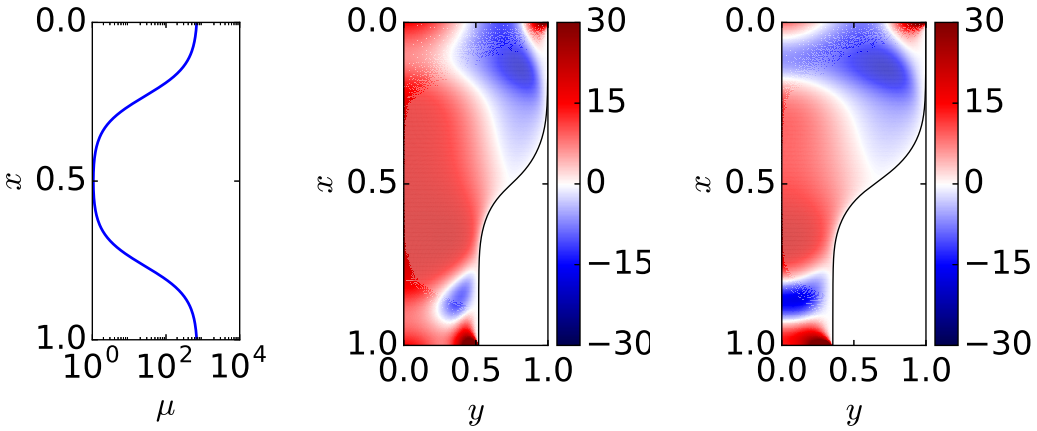

(a) (b) (c)

Figure 6.7: Principal stress $\mathcal{P}^-$ (6.48) in a thin sheet undergoing redraw with draw ratio $D = 20$ through a heater zone (6.55)–(6.56) (a), for a sheet whose aspect ratio of length to half-width δ is (b) 1.4 and (c) 2.0. Regions in which $\mathcal{P}^- > 0$ are coloured red, regions in which $\mathcal{P}^- < 0$ are coloured blue.

6.5 Buckling profiles

We investigate the stability of the sheet to out-of-plane deformations by considering an infinitesimal mid-surface deformation $|H| \ll 1$. Motivated by the observation of compression zones below the heater zone in sheets with aspect ratio $O(1)$ and localized heating in §6.4, we focus on a thin sheet whose aspect ratio of length to half-width $\delta = 1$, and investigate the effect of the viscosity profile on the buckling profile.

6.5.1 Linear-stability analysis

We linearize the governing equations (6.16)–(6.19) and boundary conditions (6.8)–(6.9) and (6.44) about the steady state solution. Linearizing the stress balance (6.16)–(6.17) for $H \ll 1$, we find that the stress is unchanged from the steady-state result $\boldsymbol{\mathcal{S}}_0$, and we only need to solve (6.18) for H. Linearizing the mid-surface equation (6.18), we consider a single mode $H = e^{\lambda t}\tilde{H}$, where λ is the growth rate and $\tilde{H}$ gives the spatial buckling profile. Substituting into (6.18), we find

$$\lambda \nabla \cdot \left(\nabla \cdot \tilde{\boldsymbol{\mathcal{M}}} \right) + \nabla \cdot \left(\nabla \tilde{H} \cdot \bar{\boldsymbol{\mathcal{S}}}_0 \right) = 0, \tag{6.57}$$

where $\bar{\boldsymbol{\mathcal{S}}}_0$ is the known steady-state stress profile (6.50) and

$$\tilde{\boldsymbol{\mathcal{M}}} = -\mu\frac{h^3}{3}\begin{pmatrix} 4\dfrac{\partial^2\tilde{H}}{\partial x^2} + 2\dfrac{\partial^2\tilde{H}}{\partial y^2} & 2\dfrac{\partial^2\tilde{H}}{\partial x\partial y} \\ 2\dfrac{\partial^2\tilde{H}}{\partial x\partial y} & 2\dfrac{\partial^2\tilde{H}}{\partial x^2} + 4\dfrac{\partial^2\tilde{H}}{\partial y^2} \end{pmatrix}. \tag{6.58}$$

On the boundaries, we integrate the conditions of simple-support at the rollers (6.8c) and (6.9b) and use the fact that the sheet is initially flat to arrive at

$$\tilde{H} = \frac{\partial^2\tilde{H}}{\partial x^2} = 0 \tag{6.59}$$

on $x = 0$ and $x = 1$, while the free-boundary conditions (6.44b) and (6.47) become

$$\tilde{\mathcal{M}}_{nn} = 2\frac{\partial\tilde{\mathcal{M}}_{sn}}{\partial s} + \frac{\partial\tilde{\mathcal{M}}_{nn}}{\partial n} + \kappa\tilde{\mathcal{M}}_{ss} = 0 \tag{6.60}$$

on $y = b(x)$. Finally, we impose symmetry conditions

$$\frac{\partial\tilde{H}}{\partial y} = \frac{\partial\tilde{\mathcal{M}}_{yy}}{\partial y} = 0 \tag{6.61}$$

along $y = 0$. We note that Srinivasan et al. (2017) use clamped boundary conditions in their computations rather than simple-support at the sheet ends. In reality neither boundary condition is correct; we discuss this further in §6.7.

In Chapters 3–4 and so far in this chapter we have used open-source finite-element software FEniCS to solve the two-dimensional steady-state equations governing the in-plane behaviour of a thin viscous sheet. In the case of the eigenvalue problem (6.57)–(6.61), numerical errors on the mesh scale were observed in FEniCS, and grid independence could not be achieved. Instead, we follow the example of Srinivasan et al. (2017) and use COMSOL, which suppresses these errors. We then solve the eigenvalue problem (6.57)–(6.61) on the fixed domain $(x, y/b) \in [0, 1] \times [0, 1]$, using quintic basis functions on an irregular mesh with elements whose size is below 0.02.

6.5.2 Results

In figure 6.8 we plot the fastest-growing buckling mode for (a) a sheet with uniform viscosity and (b) a sheet with localized heating (6.55)–(6.56). This is the eigenfunction $\tilde{H}$ associated with the largest value of real(λ) in the eigenvalue problem (6.57)–(6.61). The eigenfunctions are normalized so that $\max|\tilde{H}| = 1$. The level curve $\mathcal{P}^- = 0$ is also shown. In the case of a uniform heater zone we observe buckling in the upper portion of the sheet, near the sheet edge (see figure 6.8a). The deformation

is localized in the region under compression and for a sheet with viscosity $\mu \equiv 1$ undergoing redraw at draw ratio $D = 20$ the most unstable buckling mode has growth rate $\lambda = 2.5 \times 10^{-4}$. For a sheet with localized heating (6.55)–(6.56), we observe two compression zones in the sheet. The fastest-growing eigenmodes correspond to buckling in the lower compression region, below the heater zone (see figure 6.8b), and $\lambda = 1.3 \times 10^{-3} \pm \mathrm{i}\, 5.4 \times 10^{-7}$. For both the uniform viscosity case and the localized heating case, the wrinkles are aligned parallel to the sheet edge, and perpendicular to the compressive stress (cf. figure 6.6), as expected.

We note that the fastest-growing eigenmode and corresponding eigenvalue are complex in the short-heater-zone case. The eigenvalue has a very small imaginary part, which indicates that the buckling mode oscillates very slowly. In both cases the growth rate is small, which indicates that the wrinkles grow slowly. If real(λ) is sufficiently small that the actual timescale for wrinkle growth is comparable with the stretching timescale, it is possible that oscillations are swept out of the heater zone before they have time to grow significantly. We will give some explanation for the size of λ in §6.6.

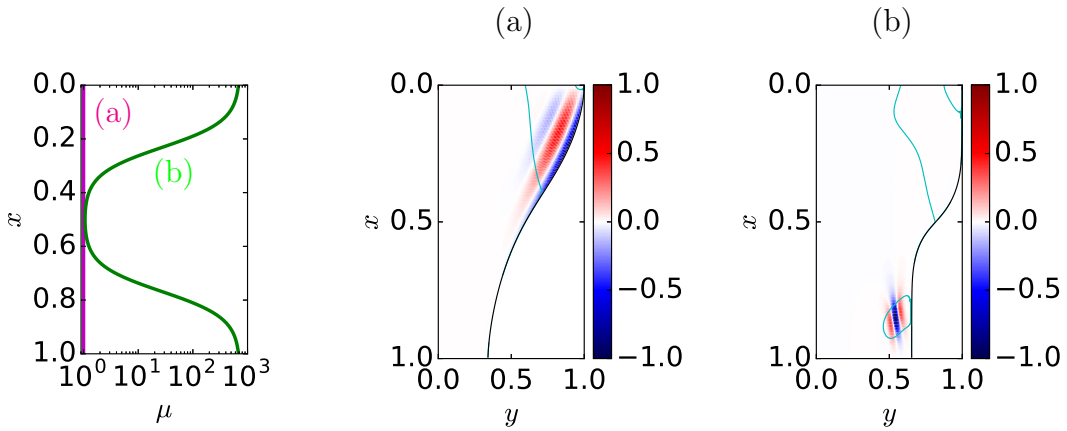

Figure 6.8: Fastest-growing buckling modes $\tilde{H}$ of the linear-stability problem (6.57)–(6.61) in a thin sheet undergoing redraw with draw ratio $D = 20$ through a domain of dimensionless length $\delta = 1$, with (a) uniform viscosity ($\lambda = 2.5 \times 10^{-4}$), and (b) a localized heater zone ($\lambda = 1.3 \times 10^{-3} \pm i\ 5.4 \times 10^{-7}$). In the case (b) the buckling mode is complex and the real part is plotted. Contours of $\mathcal{P}^- = 0$ are plotted in cyan for comparison.

6.6 Simple compression-zone problem

In §6.5, we determined the buckling profile and corresponding growth rate of buckling in the compression zone in a glass sheet undergoing redraw by solving numerically a fourth-order eigenvalue problem (6.57)–(6.61) in the whole sheet. In this section we focus our attention on the section of the sheet under compression, and estimate the expected growth rate and wavelength of buckling based on the bending stiffness $\mu h^3/3$ of the sheet, the size of the compression zone and the magnitude of the tension and compression forces inside this zone. We have seen that the compression zones in a sheet undergoing redraw are a range of shapes and sizes, and the stresses vary significantly across each compression zone (cf. figure 6.5 and 6.6). The properties of the compression zone in turn determine the buckling behaviour. We can gain insight into this complicated problem by considering a very simplified version in which a rectangular compression zone with uniform stresses and bending stiffness is embedded in a flat sheet under tension. We assume the principal stresses $\mathcal{P}^{\pm}$ are aligned along the edges of the rectangular compression zone.

We consider a sheet of length a and width b, under uniform tension $\mathcal{P}^{+} = \mathcal{T} > 0$ in the x_1 direction and compression $\mathcal{P}^{-} = -\mathcal{C} < 0$ in the x_2 direction as shown in figure 6.9. (In principle we could scale this rectangular sheet segment onto a unit square, but for direct comparison with real sheets it is more straightforward to use a rectangle of arbitrary size.) Comparing the fastest-growing buckling modes in

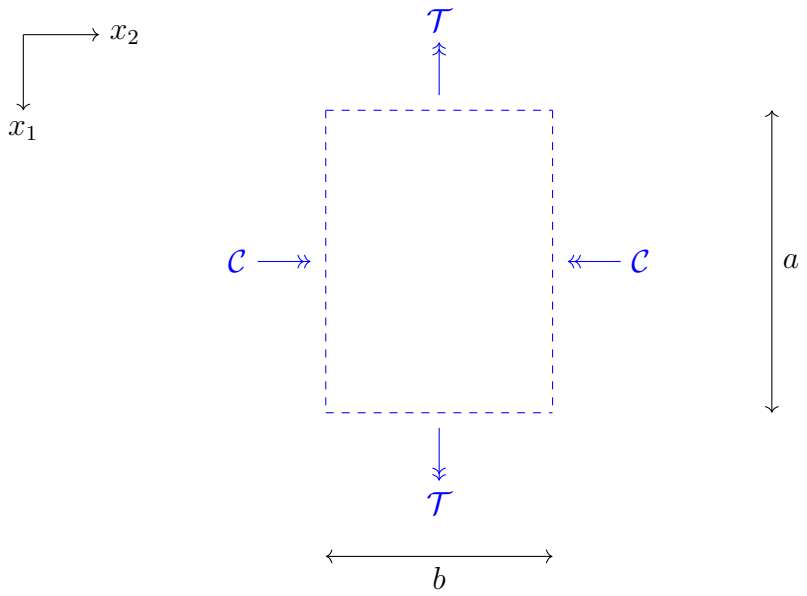

Figure 6.9: Rectangular sheet segment embedded in the coordinate system (x_1, x_2) experiencing tension along the x_1 axis and compression along the x_2 axis.

figure 6.8 with the principal stresses in figure 6.6, we observe that buckling is localized around the compression zones, and that the rest of the sheet is approximately flat. For simplicity, we assume here that the compression zone is simply-supported, so

$$H = \frac{\partial^3 H}{\partial x_1^2 \partial \tau} = 0 \quad \text{on} \quad x_1 = 0,\ a, \tag{6.62a}$$

$$H = \frac{\partial^3 H}{\partial x_2^2 \partial \tau} = 0 \quad \text{on} \quad x_2 = 0,\ b. \tag{6.62b}$$

We assume the thickness and viscosity are approximately uniform inside the rectangle, so that the centreline equation (6.57) can be simplified to

$$\frac{4\mu h^3}{3}\nabla^4 \frac{\partial H}{\partial \tau} = \mathcal{T}\frac{\partial^2 H}{\partial x_1^2} - \mathcal{C}\frac{\partial^2 H}{\partial x_2^2}. \tag{6.63}$$

This admits non-trivial solutions of the form

$$H = e^{\lambda \tau} \sin\left(\frac{n\pi x_1}{a}\right) \sin\left(\frac{m\pi x_2}{b}\right), \tag{6.64}$$

where n and m are positive integers, and the growth rate λ satisfies

$$\frac{4\mu h^3}{3}\lambda\pi^2 \left(\frac{n^2}{a^2} + \frac{m^2}{b^2}\right)^2 = \mathcal{C}\left(\frac{m^2}{b^2}\right) - \mathcal{T}\left(\frac{n^2}{a^2}\right). \tag{6.65}$$

We note that in this scenario λ is real, and that for any $\mathcal{C} > 0$ there exists $\lambda > 0$ for sufficiently large m, but that this positive growth rate may be very small. We seek the fastest-growing eigenmode by maximizing $\lambda > 0$ with respect to n and m. We observe that $\partial\lambda/\partial n < 0$ for all $n > 0$, so we choose $n = 1$, and λ is then maximized for

$$m = \frac{b}{a}\sqrt{1 + 2\frac{\mathcal{T}}{\mathcal{C}}}, \tag{6.66}$$

with growth rate

$$\lambda = \frac{3}{4\mu h^3}\frac{a^2}{4\pi^2}\frac{\mathcal{C}^2}{\mathcal{C} + \mathcal{T}}. \tag{6.67}$$

We note that the number of wrinkles m and growth rate λ depend not only on the size of the region under compression and the magnitude of the compressive force, but also on the viscosity, thickness and tension. Increasing the viscosity or thickness in the sheet suppresses the growth of out-of-plane deformations. Out-of-plane deformations are also penalized by the tensile force, so that increasing tension relative to compression increases the number of wrinkles m and also decreases the growth rate λ.

In a three-dimensional sheet undergoing redraw, the compression zones will not be rectangular and the principal stresses $P^{\pm}$ will vary over the compression zone, as will the viscosity μ and the thickness h. However, we can obtain rough estimates for the number of oscillations m and growth rate λ by approximating the average values across the compression region, using our numerical solution to the steady-state in-plane problem (6.51)–(6.54). Estimates for the average parameter values in the compression regions illustrated in figure 6.6 for (a) a uniform viscosity profile and (b) a sheet with a localized region of low viscosity are shown in table 6.1. Based on these approximations, the scaling law (6.66) predicts that there will be 3–4 wrinkles in the buckling region in the two sheets considered in §§6.4–6.5. This is comparable to the behaviour observed in the numerical solution to the linear-stability problem (6.57)–(6.61) illustrated in figure 6.8. Furthermore, the growth rates $\lambda = 2.5 \times 10^{-4}$ for a sheet with uniform viscosity and $\lambda = 1.3 \times 10^{-3} \pm \mathrm{i}\, 5.4 \times 10^{-7}$ for the profile (6.55)–(6.56) are comparable with the values $\lambda = 1.8 \times 10^{-4}$ and $\lambda = 1.3 \times 10^{-4}$ respectively suggested by the scaling law (6.67). In particular, we note that even though the growth rates computed in §6.5 may appear very small, they are in fact in line with the simple stability analysis performed here.

	Uniform viscosity	Localized heating
a	0.4	0.1
b	0.25	0.1
μ	1	300
h	0.75	0.2
$\mathcal{T}$	10	50
$\mathcal{C}$	0.5	10
n	1	1
m	4	3–4
λ	1.8×10^{-4}	1.3×10^{-4}

Table 6.1: Average parameters in compression zones for sheets with draw ratio D and either (a) uniform viscosity or (b) localized heating (6.55)–(6.56), estimated using the numerical solutions to the steady-state problem (6.51)–(6.54) shown in figure 6.6. These average parameters are used to calculate predictions for the number of wrinkles n and m and the growth rate λ using rectangle model (6.66)–(6.67).

6.7 Comparison with experimental observations

In experimental tests of the glass redraw process at Schott AG, the redrawn product is sometimes observed to have significant out-of-plane deformations (see figure 6.1). These deformations have a very regular shape, are typically localized near the sheet edge, and the wavelength and angle of the buckling pattern appear to be fixed during a given redraw cycle. In §6.5 we have calculated the fastest-growing buckling modes for the industrial furnace and viscosity profiles (6.55)–(6.56). We observe buckling localized near the sheet edge (see figure 6.8), which is consistent with the patterns observed in the final product. In principle we could apply the simple scaling analysis outlined in §6.6 or solve the linear-stability problem (6.57)–(6.61) numerically to estimate the buckling wavelength, and compare this with experimental observations, although we would require measurements of the drawing distance and the viscosity profile over the whole domain so that we could estimate the stresses in the sheet.

The analysis of a rectangular sheet segment under compression in §6.6 suggests that the growth rate of buckling may be decreased by changing the parameters in (6.67), for example by increasing the bending stiffness $\mu h^3/3$ or modifying the compression zone. We note that using (6.67) to control buckling is not straightforward in reality, since the aim is to produce sheets of some particular thickness, and since the dimensions a and b of the compression zone and the principal stresses $\mathcal{T}$ and $\mathcal{C}$ are determined by the nonlinear problem (6.51)–(6.54), and depend parametrically on the viscosity μ. However, one option is to introduce a second pair of rollers (Anderson et al., 2016) located near the lower compression zone and tilted to apply an outward force, in order to modify the stress profile and reduce or eliminate compression.

In the buckling solutions of the linear-stability problem calculated numerically in §6.5, the sheet mid-surface is always flat exiting the drawing region, i.e. there are no out-of-plane deformations in the final product. One reason for this is that the compression zones calculated in §6.4 (and those calculated by Filippov and Zheng, 2010 and Srinivasan et al., 2017 for other viscosity profiles and draw ratios) are always located just above the draw rollers (see, for example, figure 6.6b). The buckling modes predicted by the linear-stability analysis are based on the steady-state stress profile, and so will predict buckling profiles localized in the steady-state compression zones and away from the draw rollers. In Chapter 5 we saw that the stress profile in the sheet evolves as the sheet deforms, and that this in turn changes the buckling profile of the sheet (see, for example, figure 5.4). In the case of a three-dimensional

sheet, when out-of-plane deformations grow sufficiently large for the nonlinear terms in (6.16)–(6.19) to be important, the stress profile will evolve in response to the mid-surface deformation. In some parameter regimes, the compression zone may then stretch down as far as the draw rollers, so that the sheet experiences compression and can buckle there. However, further study of the full nonlinear problem (6.16)–(6.19) would be necessary to determine the cases for which this occurs. Furthermore, the boundary conditions in their current form would counteract the buckling in the sheet and smooth out any deformations as the sheet exits the drawing region. In our linear-stability analysis we assumed simple-support at each end of the sheet by imposing $H = H_{xx\tau} = 0$. However, the situations of real interest here are the ones in which the sheet exits the drawing domain with out-of-plane deformations that are "frozen in", so it is evident that the boundary condition $H = 0$ at the draw rollers is not appropriate when studying nonlinear buckling in redraw of a three-dimensional sheet. Before solving the nonlinear buckling problem it will be necessary to first reformulate the boundary conditions, taking into account the fact that the draw rollers may suppress the out-of-plane motion of the sheet but do not eliminate it.

6.8 Discussion

In this chapter we address out-of-plane deformation of a three-dimensional thin glass sheet undergoing redraw, motivated by the observation of out-of-plane ripples in the mid-surface of redrawn glass sheets at Schott AG. During the redraw process, the sheet is stretched by draw rollers to make it thin, but lateral contraction of the sheet edges can give rise to compression in some directions in parts of the sheet. We present a model to predict the buckling modes in the sheet, and derive the boundary conditions for the bending moment at the curved free edge of the sheet. These have an extra term compared with the conditions at a straight edge derived by Howell et al. (2009) for a solid rectangular plate, accounting for the curvature of the free edge.

We first calculate the principal stresses in the sheet in equilibrium, i.e. when it is planar, and determine the regions of the sheet that experience compression. We consider both the short-heater-zone limit and cases where the aspect ratio of drawing distance to sheet width is of $O(1)$, motivated by observations (Srinivasan et al., 2017) of one compression zone for long heater zones and two for short heater zones. In regimes where the heater zone is shorter than the sheet length considered, there is one compression zone in the upper part of the sheet and one in the lower part of

the sheet near the draw rollers, and we observe that the compression zone in the lower part of the sheet is actually located *below* the heater zone. This result implies that, when studying buckling behaviour in a sheet undergoing redraw through a short heater zone, it is not appropriate to apply the simplified model presented in Chapter 3 for the short-heater-zone limit, as buckle formation may occur outside of the solution domain if the draw rollers are located far below the heater zone in reality.

We present a linear-stability analysis for a sheet with $O(1)$ aspect ratio undergoing redraw, and calculate the fastest-growing eigenmodes and corresponding growth rates in two cases: (i) when the viscosity is uniform, and (ii) when the viscosity is varying, with a local minimum near the middle of the drawing domain and regions with very high viscosity near the ends of the drawing domain. When the viscosity is uniform, buckling is localized in the single compression zone in the upper part of the drawing domain. For the case of varying viscosity there are two compression zones, but the fastest-growing mode corresponds to buckling in the lower compression region. For the industrial temperature and viscosity profiles considered here, the buckling is localized near the sheet edge, and decays towards the centre of the sheet, in agreement with experimental observations.

We also present a simple model for buckling inside a compression zone by considering a rectangular sheet segment embedded in a tensile sheet, and derive scaling laws for the wavenumber and growth rate of out-of-plane deformations. We assume that the rectangle is under uniform tension along one axis and uniform compression along the other, and that the sheet is simply-supported at the rectangle boundaries. We thus write down the shape of each buckling mode, together with its growth rate. We then determine the maximum growth rate as a function of viscosity, sheet thickness, the size of the rectangle and the size of the tension and compression forces. In principle this growth rate may be decreased by adjusting the process to modify these parameters. However, in reality this is either difficult or counter-productive. For example, increasing the sheet thickness to increase the bending stiffness will slow down buckling, but this is not helpful in a process where the aim is to make very thin sheets. The size of the compression region and the magnitude of the compressive force are determined by a nonlinear system of equations, and changing the viscosity also changes these properties.

Finally, we compare our model with glass sheets redrawn at Schott AG, and consider the modifications necessary to predict the buckling observed in these sheets. Our linear-stability analysis predicts buckling modes localized near the sheet edge, and this agrees qualitatively with experimental observations. However, the buckling

modes predicted by linear-stability analysis are localized in the regions under compression in a planar, steady-state sheet during redraw. These regions are above the draw rollers, and the product exiting through the draw rollers is always flat. Numerical solution of the full nonlinear problem would be necessary to model the coupled evolution of the stress profiles and mid-surface, and the draw boundary conditions would need to be modified to reflect the fact that the draw rollers do not remove deformations from the sheet in reality.

Chapter 7

Conclusions

In this thesis we discuss mathematical modelling of thin viscous sheets in the context of the glass sheet redraw process, in particular focusing on the thickness profile and out-of-plane deformations of the sheet. In this chapter we summarize our results and suggest some further work that could be carried out in the future.

7.1 Summary of results

We treat molten glass as an incompressible, Newtonian fluid, with temperature-dependent viscosity and Reynolds number $\mathrm{Re} \ll 1$. We exploit the fact that sheets undergoing redraw are very thin compared with other lengthscales, and use asymptotic analysis to reduce the dimensionality of our mathematical models. We use these reduced models to investigate the thickness profile a of redrawn glass sheet and its dependence on process parameters, as well the development of out-of-plane deformations in a sheet undergoing redraw.

We present a model for heat and fluid flow in a thin two-dimensional glass sheet undergoing redraw in Chapter 2. By considering the thin-sheet limit, we determine that, in parameter regimes of interest, the temperature profile is independent of the thickness and velocity profiles of the glass sheet. Based on this finding, we supplement the equations governing fluid flow with a prescribed viscosity profile in the remainder of this thesis. We also investigate the stability of a redrawn sheet to draw resonance, in which perturbations to the thickness grow in amplitude above a critical draw ratio. We find that the critical draw ratio above which a sheet undergoing redraw becomes unstable is much larger than typical industrial draw ratios, which is consistent with the fact that draw resonance is not observed to be a problem in the redraw process in reality, and therefore it is not considered in the more complicated three-dimensional redraw processes analysed in later chapters.

A redrawn sheet is typically thicker at the edges than in the centre; this is a ubiquitous problem in the redraw of glass sheets and is observed for both long and short heater zones. In Chapter 3 we develop a mathematical model for redraw of a thin glass sheet through a very short heater zone. This study is motivated by experimental observations that, when the heater zone is short, the redrawn glass sheet has a uniform thickness profile except near the edges, where it is thicker. The thin-sheet approximation allows us to model the three-dimensional sheet using a two-dimensional model, and considering the asymptotic limit of a very short heater zone allows us to reduce the problem further to one spatial dimension in the bulk, with two-dimensional boundary layers at the edges where so-called "thick edges" form. Our analysis demonstrates that the extent of these thick edges depends linearly on the length of the heater zone through which the sheet is drawn, and this length may be scaled out of the problem. We compute numerical solutions to the two-dimensional boundary-layer problem, matching with an analytical solution in the one-dimensional bulk to give a complete picture of the thickness profile of the redrawn sheet. The predictions of this reduced model give excellent agreement with a numerical solution of the full three-dimensional Stokes problem, validating the various assumptions made in deriving the reduced model. The agreement with experimental data is also good, although a more accurate measurement of the furnace temperature profile might give further improvement. We observe that the ratio between the edge and bulk thicknesses scales with the square root of the draw ratio. This conforms with observations of film casting in the polymer industry. We show that this relationship is exact as a consequence of conservation of mass at the stress-free edge.

We also address the inverse problem: what shape preform will redraw to a final product with uniform thickness? In the short-heater-zone limit it is possible to reformulate this as a modified version of the forward problem, in which the sheet undergoes compression rather than stretching. We again compute numerical solutions of the two-dimensional boundary-layer problem and hence predict "optimal preform" profiles that will redraw to rectangular final products. We also investigate the option of linearly tapering the preform rather than using the exact optimal thickness profile, since this is more feasible in an industrial context. We find that the sharp corner in the preform gives rise to an unavoidable "kink" in the final product, which would need to be removed during post-production, but that the thickness at the edge can nonetheless be reduced significantly, so that the redrawn sheet can be rolled up without breakage.

In Chapter 4 we modify the mathematical model developed in Chapter 3 for the regime in which the heater zone through which the sheet is redrawn is much longer than the sheet width. We consider the asymptotic limit in which the ratio of sheet half-width to heater zone length is small, and determine analytical solutions for the leading-order behaviour. In doing so, we confirm that the preform shape is preserved in the absence of surface tension to leading order, and we quantify the effect of surface tension on the leading-order sheet shape. Previous work suggests that the next-order correction terms should scale with the square of the aspect ratio of sheet half-width to heater zone length. However, by matching between the one-dimensional bulk and two-dimensional boundary layers at the top and bottom of the heater zone we show that the first correction terms scale linearly with the aspect ratio, and this is in agreement with numerical solutions of the full three-dimensional problem calculated by Schott AG. We calculate the corrections to the bulk solution analytically, with unknown terms to be determined by matching with the leading-order solution in the aforementioned boundary layers. We calculate the solution in these two-dimensional boundary layers numerically. It is possible to rescale all process parameters out of the problem so that the two-dimensional equations need only be solved once. We observe excellent agreement between the two-term asymptotic solution for the thickness profile in the limit of a long heater zone and simulations performed by Schott AG in the absence of surface tension. When surface tension is included we again predict the final thickness profile to a very good approximation, except for in a small region near the edge of the sheet where surface tension smooths the sharp corners in the thickness profile, which is not resolved by our thin-sheet model.

We also address the inverse problem, which is simpler than in the short-heater-zone case because the thickness variations in the long-heater-zone case are at higher order in the small aspect ratio of width to length, and these correction terms are governed by a system of linear differential equations. The boundary layers at either end can be rescaled onto the canonical boundary-layer system from the forward problem, so that the preform required to redraw to a final product with uniform thickness may be calculated directly from the solution to the forward problem.

In Chapters 5 and 6 we address the problem of ripples or out-of-plane deformations appearing in the redrawn glass sheet in some processes. Inside the heater zone, the glass is stretched in the direction of drawing, but it is not necessarily the case that the sheet experiences tension in every direction. Indeed, there are regions in the sheet where the glass experiences tension in one direction and compression in another. The development of out-of-plane ripples in the sheet is linked to these compressive regions.

In Chapter 5 we develop a model for a two-dimensional glass sheet undergoing redraw in a gravitational field as a first step towards understanding the buckling behaviour of a sheet in which one region experiences tension and another compression. In the case of a two-dimensional sheet under the influence of gravity, the upper part of the sheet experiences tension due to the combined effect of gravity and the draw rollers, but if the effect of gravity is sufficiently large then the lower part of the sheet will experience compression because the glass accelerates beyond the draw speed and must subsequently decelerate. This compressive force renders the sheet unstable to out-of-plane buckling. We exploit the thin geometry of the sheet to reduce the model to one spatial dimension, and assume the sheet is nearly planar so the model can easily be expressed in Cartesian coordinates. We use a time-dependent model to capture the evolution of the out-of-plane deformation, and supplement the reduced mass and momentum equations with an equation for the centreline of the sheet. We compute numerically the fastest-growing eigenmodes of the linearized stability problem. We observe that the sheet typically buckles with one bump, but that far from the stability threshold it may oscillate in space, as both the magnitude of the compressive force and the size of the region under compression increase. We also compute numerical solutions to the nonlinear time-dependent governing equations. This allows us to investigate the feedback between the growth of the centreline and the velocity profile of the sheet and to model the evolution of the sheet shape as it grows. In particular, we note that inertia becomes less important as time proceeds, and that the sheet appears to adopt a self-similar shape near the bottom of the heater zone where the centreline deviation is maximized. We investigate the late-time behaviour of the system and determine that the buckling sheet is composed of a shrinking compressive boundary layer which drives the buckling, and a bulk region under tension where the amplitude is controlled by matching with the boundary layer. We find that the size of the compressive region decreases with $\text{time}^{-1/3}$ and determine asymptotic approximations to the sheet shape in the late-time limit.

In Chapter 6 we extend our model to buckling of a three-dimensional thin sheet undergoing redraw, and derive boundary conditions at the free curved edge of a thin viscous sheet. In this process, the sheet experiences tension in one direction due to the stretching effect of draw rollers, but may experience compression in the lateral direction as the sheet edges neck in. In "compression zones" where the sheet experiences compression in some direction, the sheet mid-surface is unstable to out-of-plane deformations, and localized buckling is observed. We investigate the occurrence of compression zones during redraw in the short-heater-zone limit as well as for sheets

where the length is comparable to half the preform width. In both regimes further sub-cases are considered in which the sheet has either uniform viscosity or a viscosity profile corresponding to localized heating of the sheet. Regardless of the sheet length, we observe one compressive zone in sheets with uniform viscosity and two compressive zones in sheets with localized heating. The second compressive zone is typically located in the region below the heater zone, which is discarded in the short-heater-zone limit in studies of stretching planar sheets since the viscosity is very large and the sheet shape does not change significantly.

We perform a linear-stability analysis and calculate the fastest growing eigenmodes and corresponding growth rates for the cases of uniform viscosity and localized heating. In a sheet with uniform viscosity, buckling is localized in the single compressive zone, while in a sheet with localized heating the fastest-growing eigenmode corresponds to buckling in the lower compressive region, below the heater zone and close to the draw rollers. This is consistent with a similar linear-stability analysis carried out by Srinivasan et al. (2017). In our particular case, the buckling modes predicted with the viscosity profile of Schott AG are located near the sheet edge, and this is consistent with ripples observed in sheets drawn at Schott AG. We also consider a very idealized model for the compressive zone in a sheet during redraw, in which a uniform rectangular sheet segment under compression in one direction is embedded in a sheet under tension. By determining the fastest-growing mode in such a rectangular sheet segment, as a function of the size of the zone, the stress inside the zone and the viscosity and thickness of the sheet, we predict approximate scaling laws for the dominant wavenumber and growth rate of buckling during redraw. Finally, we present a discussion of the further steps required to relate our analysis thus far to experimental observations.

7.2 Future work

We have made a number of simplifying assumptions about the role of temperature and heat flow in the redraw process; one could extend the work in this thesis by relaxing these assumptions:

- The thickness profiles plotted in Chapter 4 are all for the case of uniform viscosity. For comparison with experiment it will be necessary to use a profile that better reflects the reality inside the furnace, as in Chapter 3.

- In §3.5, we noted a discrepancy between the thickness profile predicted by both full numerical simulation and reduced models and thickness profiles observed experimentally. Although the good agreement between the full simulation and the reduced model indicates that neglecting both surface tension and coupled heat flow is valid, there is evidence to suggest that the supposed *furnace* profile used for both models, and therefore the temperature and viscosity profiles used to predict the fluid flow in the sheets, is not fully accurate. Re-measuring the furnace profile and then redoing the calculation should improve the agreement between predictions and observations.

- In Chapter 2 we model heat flow in a two-dimensional thin sheet, and determine that heat flow is decoupled from fluid flow to leading order in the redraw process. This allows us to impose a prescribed temperature (and hence viscosity) profile when solving the equations of motion for the sheet. Although this seems to be valid for the redraw processes studied in this thesis, it may not always be the case. We discuss possible approaches to relaxing this assumption in §2.3, and doing so could broaden the applicability of this work.

In addition, the following areas could benefit from further attention:

- In Chapter 4 we note that our two-dimensional thin-sheet model cannot predict the rounding of the sheet edges due to surface tension, which was observed in full numerical simulations of the three-dimensional system. This is true whenever surface tension is present; the sheet thickness is modified by the smoothing effect of surface tension in a region near the sheet edge whose size is comparable to the sheet thickness. One can resolve this behaviour by scaling into the boundary layer and re-introducing previously neglected terms. It is then possible, in principle, to numerically solve a Stokes problem to determine the shape of each two-dimensional slice at the sheet edges.

- In Chapter 5 we note that our nearly-planar assumption prevents the model from predicting "tipping over" or slumping of the sheet at very late times. This could be captured by matching the existing model in Cartesian coordinates with an arclength formulation of the problem in which large centreline deformations are permitted.

Finally, in Chapter 6 we present a preliminary analysis of buckling in a three-dimensional thin glass sheet during redraw. This should be extended in the following ways:

- Our linear-stability analysis predicts buckling modes which are localized in the regions under compression in steady state, and these regions are located above the draw rollers. By studying the full nonlinear problem we could predict the evolution of the stresses in the sheet and determine the process parameters for which the out-of-plane deformations reach the draw rollers.

- So far we have assumed that the centreline is flat at the draw rollers. This is unrealistic, since ripples are observed in redrawn sheets. It will be necessary to develop more appropriate draw-roller boundary conditions which reflect the fact that the draw rollers only touch the sheet at two points near the edges, and that deformed sheets may in principle pass through the rollers.

7.3 Closing remarks

The subject of this thesis arose from a real-life industrial process. The mathematical consideration of glass drawing is a well-studied area, but open problems in the glass redraw process motivate further development and study of models tailored specifically for redraw. These open problems relate to three-dimensional behaviour of thin viscous sheets, and each give rise to interesting free-boundary fluid dynamics problems. Industrially relevant assumptions about the thinness of the sheet and the length of the heater zone compared with its width result in natural small parameters, motivating the use of perturbation methods to analyse models for the redraw process. A significant amount of insight is gained from asymptotic analysis, supplemented with numerical methods where appropriate.

This work gives key insight into the thickness profile of a glass sheet produced using the redraw process, and the results should allow for design optimization that can minimize costs and improve efficiency within the glass industry. As noted in the previous section, our model for buckling of glass sheets during redraw is far from complete. However, it is our hope that it may provide a foundation for the development of a comprehensive theory of buckling in thin viscous sheets with non-uniform stress profiles.

Appendix A

Length and timescales for buckling

We seek a lengthscale ϵ^θ and timescale ϵ^β for which inertia, bending and tension are balanced in the centreline equation (5.18),

$$\begin{aligned}
&\epsilon^\phi \bar{\mathrm{Re}} \left(\epsilon^{-\theta}\frac{\partial}{\partial \xi}+\frac{\partial}{\partial x}\right)\int_{z^-}^{z^+}\left(\epsilon^{-\beta}u_\tau+u_t\right)(z-H)\,\mathrm{d}z \\
&\quad+\epsilon^\phi \bar{\mathrm{Re}} \left(\epsilon^{-\theta}\frac{\partial}{\partial \xi}+\frac{\partial}{\partial x}\right)\int_{z^-}^{z^+}\left(\epsilon^{-\theta}uu_\xi+uu_x+\epsilon^{-\beta}wu_z\right)(z-H)\,\mathrm{d}z = \\
&\qquad\left(\epsilon^{-\theta}\frac{\partial}{\partial \xi}+\frac{\partial}{\partial x}\right)^2\int_{z^-}^{z^+}(z-H)\left(-p+2\epsilon^{-\theta}u_\xi+2u_x\right)\mathrm{d}z \\
&\quad+\left(\epsilon^{-\theta}\frac{\partial}{\partial \xi}+\frac{\partial}{\partial x}\right)\left[\left(\epsilon^{-\theta}H_\xi+H_x\right)\int_{z^-}^{z^+}\left(-p+2\epsilon^{-\theta}u_\xi+2u_x\right)\mathrm{d}z\right] \\
&\qquad-\epsilon^{\phi-\beta}\overline{\mathrm{Re}}\int_{z^-}^{z^+}\left(\epsilon^{-\beta}w_\tau+w_t+\epsilon^{-\theta}uw_\xi+uw_x+\epsilon^{-\beta}ww_z\right)\mathrm{d}z. \quad \text{(A.1)}
\end{aligned}$$

The left-hand-side of (A.1) corresponds to inertial effects, while on the right-hand-side the first term is a bending term, the second term tension and the third term inertia. We determine the size of each of these terms by performing an asymptotic analysis in the thin-sheet limit $\epsilon \to 0$, with θ and β unknowns to be determined by ensuring the three effects are the same size, assuming ϕ, θ, $\beta > 0$. We follow the procedure used in Chapters 2–4 to derive the leading-order governing equations, noting conditions that must hold for this procedure to be valid. Since θ and β are still to be determined, we propose general expansions

$$u = u^{(0)} + \epsilon^\kappa u^{(1)} + \epsilon^{2\kappa} u^{(2)} + \cdots, \quad \text{(A.2a)}$$

$$w = w^{(0)} + \epsilon^\kappa w^{(1)} + \epsilon^{2\kappa} w^{(2)} + \cdots, \quad \text{(A.2b)}$$

$$h = h^{(0)} + \epsilon^\kappa h^{(1)} + \epsilon^{2\kappa} h^{(2)} + \cdots, \quad \text{(A.2c)}$$

$$H = H^{(0)} + \epsilon^{\kappa} H^{(1)} + \epsilon^{2\kappa} H^{(2)} + \cdots, \tag{A.2d}$$

$$p = p^{(0)} + \epsilon^{\kappa} p^{(1)} + \epsilon^{2\kappa} p^{(2)} + \cdots, \tag{A.2e}$$

where $\kappa \in \mathbb{R}$ is chosen so that powers of ϵ^{θ}, ϵ^{β}, ϵ^{ϕ} and ϵ^2 are all encompassed in the expansion. We use bracketed superscripts for indices to avoid confusion between ordering and differentiation, and we take the largest possible choice of κ to avoid the appearance of extraneous terms. We define integers

$$m = \frac{\beta}{\kappa}, \quad n = \frac{\theta}{\kappa}, \quad q = \frac{\phi}{\kappa}, \quad j = \frac{2}{\kappa} \tag{A.3}$$

to act as indices in our expansion so, for example, the scaling for the buckling timescale $\epsilon^{\beta} = \epsilon^{m\kappa}$.

The largest contribution from the inertia terms in the centreline equation (A.1) is $O\left(\max\left(\epsilon^{\phi-2\theta}, \epsilon^{\phi-2\beta}\right)\right)$, depending on whether θ or β is larger. We determine the size of the bending and tension terms by performing an asymptotic analysis of the governing equations (5.12) and boundary conditions (5.15)–(5.17). Letting k be a dummy index, we follow the usual procedure used in deriving the motion of thin viscous sheets (see, for example, Chapter 2). We first consider the transverse momentum equation (5.12c). Based on the derivation of the leading-order velocity and thickness in a two-dimensional flat sheet in §2.2, we expect σ_{zz} to enter the transverse momentum equation before the other terms, and determine this (and hence the leading-order pressure) by integrating across the sheet thickness and applying no-stress condition (5.17c). We can then substitute for the transverse velocity w using conservation of mass (5.12a). Systematically evaluating (5.12c) at successive orders, subject to the condition that all terms other than σ_{zz} vanish at that order, we find at each order $\epsilon^{k\kappa}$

$$-p^{(k-m)} = -2w_z^{(k)} = 2u_{\xi}^{(k+n-m)} + 2u_x^{(k-m)}, \tag{A.4a}$$

with subscripts denoting differentiation as before, while the condition that the other terms do not enter at that order may be written

$$k + m - q - j < 0, \tag{A.4b}$$

$$k + n - q - j < 0, \tag{A.4c}$$

$$u_z^{(k+n-m)} + w_{\xi}^{(k+2n-j)} + w_x^{(k+n-j)} = 0, \tag{A.4d}$$

$$u_z^{(k-m)} + w_{\xi}^{(k+n-j)} + w_x^{(k-j)} = 0. \tag{A.4e}$$

We emphasize that this step is simply an evaluation of the stress component $\sigma_{zz} = -p + 2w_z$, which will later be used to determine the leading-order pressure in terms of the velocity. The inequalities (A.4b)–(A.4c) are used to check whether the inertial terms on the left-hand side of (5.12c) play a role at $O(\epsilon^{k\kappa})$, while (A.4d)–(A.4e) are necessary to ensure the two σ_{xz} terms on the right-hand side of (5.12c) vanish. We can better quantify the conditions (A.4d) and (A.4e) by evaluating the in-plane momentum equation (5.12b) at $O(\epsilon^{k\kappa+\theta-\beta-2}) = O(\epsilon^{(k+n-m-j)\kappa})$ and $O(\epsilon^{k\kappa-\beta-2}) = O(\epsilon^{(k-m-j)\kappa})$ respectively. This time, we expect to integrate across the sheet and use the no-stress boundary condition (5.17b) to evaluate terms in the expansion of σ_{xz}, and in order for a term to be zero we require the contributions to the momentum balance (5.12b) from inertia and the σ_{xx} stress component to be sufficiently small. The smallness of the inertial term is guaranteed by conditions (A.4b)–(A.4c) provided $n \leq m$ (i.e. $\theta \leq \beta$), and there is no contribution from σ_{xx} on the right-hand side of (5.12b) provided

$$u_\xi^{(k+3n-m-j)} = 0, \tag{A.5a}$$

$$k - m + 2n - j < 0. \tag{A.5b}$$

We may obtain two results of significance from our expression (A.4)–(A.5) for the σ_{zz} stress component by considering the cases $k - m < 0$ and $k - m = 0$. In the first scenario we find that the transverse velocity is uniform across the sheet width up to $O(\epsilon^{\beta}) = O(\epsilon^{m\kappa})$, i.e.

$$w_z^{(k)} = 0 \quad \text{if} \quad \begin{cases} k < m, \\ u_\xi^{(k+3n-m-j)} = 0, \\ k - m + 2n - j < 0, \\ k + n - q - j < 0, \\ k + m - q - j < 0. \end{cases} \tag{A.6}$$

Setting $k - m = 0$ in (A.4)–(A.5), we can solve for the leading-order pressure

$$-p^{(0)} = 2u_\xi^{(n)} + 2u_x^{(0)} \ \text{ if } \ u_\xi^{(3n-j)} = 0, \quad \theta < 1, \quad 2m - q - j < 0, \tag{A.7}$$

using the fact that (A.5b) reduces to $2n < j$ (i.e. $\theta < 1$) and that $n \leq m$.

The results (A.6)–(A.7) are complicated by validity conditions involving the spatial variation of the in-plane velocity u with the buckling distance ξ. We determine this dependence by analysing the conservation-of-mass equation (5.12a) and noting that $u_\xi^{(k)} = 0$ provided either k is sufficiently large that no other terms are present at that order, or if the terms present can be evaluated to zero. Inserting our result for the transverse velocity (A.6) into the conservation-of-mass equation (5.12a), and

updating the conditions associated with (A.6), we find that the spatial variation of the in-plane velocity is simplified according to

$$u_\xi^{(k)} = 0 \quad \text{if} \quad \begin{cases} k < n, \\ u_\xi^{(k+2n-j)} = 0, \\ k + n - j < 0, \\ k + 2m - n - q - j < 0. \end{cases} \tag{A.8}$$

In particular, evaluating for $k = 0$ we uncover two scenarios regarding the exponent n in the buckling lengthscale $\epsilon^\theta = \epsilon^{n\kappa}$: either $n = 0$ so that there is only one lengthscale, or $0 < \theta < 1$ and

$$u_\xi^{(0)} = 0 \text{ if } \quad 2m - n < q + j, \tag{A.9}$$

so that the leading-order velocity does not change over the short (buckling) lengthscale. From this result we deduce that the tension

$$\mathcal{T} = \int_{z^-}^{z^+} \left(-p + 2\epsilon^{-\theta} u_\xi + 2u_x\right) \mathrm{d}z \tag{A.10}$$

is $O(1)$, so that the tension and inertia terms in (A.1) balance provided

$$q - 2m = -2n, \quad n < m, \tag{A.11}$$

that is (using definition (A.3))

$$\phi - 2\beta = -2\theta, \quad \theta < \beta. \tag{A.12}$$

Combining (A.4d), (A.5), (A.6) and (A.8) and integrating for u we find

$$u^{(k)} = \bar{u}^{(k)}(x) - (z - H^{(0)}) \left(w_\xi^{(m+n+k-j)} + w_x^{(k+m-j)}\right), \tag{A.13}$$

where

$$\bar{u}^{(k)} = \frac{1}{2h^{(0)}} \int_{z^{-(0)}}^{z^{+(0)}} u^{(k)} \, \mathrm{d}z. \tag{A.14}$$

We define the bending moment

$$\mathcal{M} = \int_{z^-}^{z^+} (z - H) \left(-p + 2\epsilon^{-\theta} u_\xi + 2u_x\right) \mathrm{d}z, \tag{A.15}$$

and note that inertia, tension and bending in the centreline equation (5.18) are only balanced if this bending moment is $O(1)$. Inserting (A.5) and (A.13) into definition (A.15) we see this is only achieved if

$$\beta + 2\theta - 2 = 0. \tag{A.16}$$

Combining the two balance conditions (A.12) and (A.16), we find

$$\theta = \frac{2}{3} - \frac{\phi}{6}, \quad \beta = \frac{2}{3} + \frac{\phi}{3} \tag{A.17}$$

provided $\phi \leq 4$, so the lengthscale and timescale associated with buckling for a given Reynolds number are

$$\text{lengthscale} \sim \epsilon^{2/3}\,\mathrm{Re}^{-1/6}, \quad \text{timescale} \sim \epsilon^{2/3}\,\mathrm{Re}^{1/3}\,. \tag{A.18}$$

Appendix B

Calculation of $\hat{\tau}_{sz0}$

B.1 Introduction

In Chapter 6 we derive the boundary conditions for the stress and bending moment at a curved free edge. In §6.3.4 we derive the condition

$$\int_{-\infty}^{0} \left(\frac{\partial}{\partial s} \int_{\hat{z}_0^-}^{\hat{z}_0^+} \hat{\tau}_{sz0} \, \mathrm{d}z \right) \, \mathrm{d}N = \int_{z_0^-}^{z_0^+} \tau_{zn1} \, \mathrm{d}z \quad \text{on} \quad n = 0. \tag{B.1}$$

In this appendix we determine the boundary-layer stress component

$$\hat{\tau}_{sz0} = \mu \left(\frac{\partial \hat{u}_{s1}}{\partial z} + \frac{\partial \hat{w}_1}{\partial s} + \kappa N \frac{\partial \hat{w}_0}{\partial s} \right) \tag{B.2}$$

in terms of bulk quantities. We use (6.28c) to substitute for $\hat{w}_0$. Integrating (6.29) and using (6.30b) gives the out-of-plane velocity correction

$$\hat{w}_1 = \frac{\partial w_0}{\partial n}(n = 0)N + c(s, \tau). \tag{B.3}$$

The unknown function $c(s, \tau)$ arises from the integration, and we shall see later that it is not necessary to determine it, although we will use the fact that it is independent of z (comparing definition (6.24f) with (6.31)). We can use expressions (6.28c) and (B.3) for the out-of-plane velocity to rewrite the stress component as

$$\hat{\tau}_{sz0} = \mu \left[\frac{\partial \hat{u}_{s1}}{\partial z} + \frac{\partial^2 w_0}{\partial s \partial n}(s, 0, \tau)N + \frac{\partial c}{\partial s} + \kappa N \frac{\partial w_0}{\partial s}(s, 0, \tau) \right]. \tag{B.4}$$

It now remains to determine the velocity component $\hat{u}_{s1}$ in terms of bulk quantities.

B.2 Governing equations for $\hat{u}_{s1}$

We return to the momentum equation (6.23b) and use the fact that the leading-order in-plane velocity and the viscosity are both uniform across the boundary layer to

arrive at

$$\frac{\partial^2 \hat{u}_{s1}}{\partial N^2} + \frac{\partial^2 \hat{u}_{s1}}{\partial z^2} = 0. \tag{B.5}$$

Now that we have a governing equation for $\hat{u}_{s1}$, we require boundary conditions to determine the solution. Evaluating the no-stress condition (6.26b) at $O(1)$ and simplifying with the in-plane velocity solutions (6.30) yields

$$\frac{\partial \hat{u}_{s1}}{\partial N}(s, N=0) = -\kappa \left[\bar{u}_{s0} - (z - H_0) \frac{\partial w_0}{\partial s} \right] - \frac{\partial}{\partial s} \left[\bar{u}_{n0} - (z - H_0) \frac{\partial w_0}{\partial n} \right], \tag{B.6}$$

where all the bulk terms on the right-hand-side are evaluated at $n = 0$ here and throughout the remainder of this section and §B.3. Evaluating the no-stress condition (6.25b) at $O(1)$ and substituting for the out-of-plane velocity using (6.28c) and (B.3) yields

$$\frac{\partial \hat{u}_{s1}}{\partial z} = -N \frac{\partial^2 w_0}{\partial s \partial n}(s, 0, \tau) - \frac{\partial c}{\partial s} - \kappa N \frac{\partial w_0}{\partial s}(s, 0, \tau) \quad \text{on} \quad z = z_0^{\pm}. \tag{B.7}$$

In the bulk, we note that the leading-order stress component evaluated at the sheet edge

$$\tau_{sn0}(s, 0, z, \tau) = \mu \left(\frac{\partial u_{n0}}{\partial s} + \kappa u_{s0} + \frac{\partial u_{s0}}{\partial n} \right) \tag{B.8}$$

is linear in z, and so may be written in the form

$$\tau_{sn0}(s, 0, z, \tau) = \frac{1}{2h_0} \int_{z_0^-}^{z_0^+} \tau_{sn0} \, \mathrm{d}z + \frac{12}{(2h_0)^3} (z - H_0) \int_{z_0^-}^{z_0^+} (z - H_0) \tau_{sn0} \, \mathrm{d}z. \tag{B.9}$$

Enforcing matching between the inner and outer regions and using definitions (6.30) for the leading-order in-plane velocity components yields

$$\begin{aligned} \lim_{N \to -\infty} \mu \frac{\partial \hat{u}_{s1}}{\partial N} = \mu \left(-\kappa \bar{u}_{s0} - \frac{\partial \bar{u}_{n0}}{\partial s} - \frac{\partial H_0}{\partial s} \frac{\partial w_0}{\partial n} \right) + \frac{1}{2h_0} \int_{z_0^-}^{z_0^+} \tau_{sn0} \, \mathrm{d}z \\ + (z - H_0) \left[\mu \left(\frac{\partial^2 w_0}{\partial n \partial s} + \kappa \frac{\partial w_0}{\partial s} \right) + \frac{12}{(2h_0)^3} \int_{z_0^-}^{z_0^+} (z - H_0) \tau_{sn0} \, \mathrm{d}z \right]. \end{aligned} \tag{B.10}$$

Cross-differentiating (B.7) and (B.10) we derive a compatibility condition

$$\mu - \left(\frac{\partial^2 w_0}{\partial s \partial n} + \kappa \frac{\partial w_0}{\partial s} \right) = \frac{6}{(2h_0)^3} \int_{z_0^-}^{z_0^+} (z - H_0) \tau_{sn0} \, \mathrm{d}z. \tag{B.11}$$

B.3 Change of variables

We introduce a new variable Φ defined by

$$\mu\hat{u}_{s1} = \left[\mu\left(-\kappa\bar{u}_{s0} - \frac{\partial\bar{u}_{n0}}{\partial s} - \frac{\partial H_0}{\partial s}\frac{\partial w_0}{\partial n}\right) + \frac{1}{2h_0}\int_{z_0^-}^{z_0^+}\tau_{sn0}\,\mathrm{d}z\right]N + N(z-H_0)\frac{6}{(2h_0)^3}\left(\int_{z_0^-}^{z_0^+}(z-H_0)\tau_{sn0}\,\mathrm{d}z\right) - \mu z\frac{\partial c}{\partial s} + \Phi. \quad \text{(B.12)}$$

By construction, $\partial\Phi/\partial N \to 0$ as $N \to -\infty$, while the differential equation for $\hat{u}_{1s}$, (B.5), becomes

$$\frac{\partial^2\Phi}{\partial N^2} + \frac{\partial^2\Phi}{\partial z^2} = 0. \quad \text{(B.13)}$$

The free-surface condition (B.7) tells us that

$$\frac{\partial\Phi}{\partial z} = 0 \quad \text{on} \quad z = z_0^{\pm}, \quad \text{(B.14)}$$

and the edge condition (B.6) becomes

$$\frac{\partial\Phi}{\partial N} = \frac{-1}{2h_0}\int_{z_0^-}^{z_0^+}\tau_{sn0}\,\mathrm{d}z - \frac{12}{(2h_0)^3}(z-H_0)\int_{z_0^-}^{z_0^+}(z-H_0)\tau_{sn0}\,\mathrm{d}z \quad \text{(B.15)}$$

on $N = 0$.

B.4 Solution

We solve for Φ using separation of variables. In order to satisfy the far-field condition as $N \to -\infty$ and free-surface condition (B.14), solutions to (B.13) must be of the form

$$\Phi = \sum_{k=1}^{\infty}\alpha_k \mathrm{e}^{k\pi N/2h_0}\cos\left(k\pi\frac{z-z_0^-}{2h_0}\right) + \text{constant}, \quad \text{(B.16)}$$

where the Fourier coefficients α_k are determined using the edge condition (B.15) and are given by

$$\alpha_k = \frac{12}{h_0}\frac{1}{k^3\pi^3}\left[1-(-1)^k\right]\int_{z_0^-}^{z_0^+}(z-H_0)\tau_{sn0}\,\mathrm{d}z. \quad \text{(B.17)}$$

Returning to the quantity of interest $\hat{\tau}_{sz0}$, we note that (B.2) is transformed to

$$\hat{\tau}_{sz0} = \frac{\partial\Phi}{\partial z}, \quad \text{(B.18)}$$

so we use (B.16)–(B.17) to rewrite our final boundary condition (B.1) as

$$\int_{z_0^-}^{z_0^+} \tau_{zn1}\ \mathrm{d}z = -\frac{\partial}{\partial s}\left(\int_{z_0^-}^{z_0^+} (z - H_0)\tau_{sn0}\ \mathrm{d}z\right) \quad \text{on} \quad n = 0, \tag{B.19}$$

where we have used the identity

$$\sum_{k=1}^{\infty} \frac{\left[1 - (-1)^k\right]}{k^4\pi^4} = \frac{1}{48}. \tag{B.20}$$

Bibliography

Anderson, J. G., Klingensmith, L. K., Peris, J. P., and Ulrich, D. J. (2016). Active edge roll control in a glass drawing process. US Patent 9,394,193.

Ansys Inc. Polyflow (2013). Release 15.0.

Batty, C., Uribe, A., Audoly, B., and Grinspun, E. (2012). Discrete viscous sheets. *ACM T. Graphic.*, 31(4):113.

Beaulne, M. and Mitsoulis, E. (1999). Numerical simulation of the film casting process. *Int. Polym. Proc.*, 14(3):261–275.

Benjamin, T. B. and Mullin, T. (1988). Buckling instabilities in layers of viscous liquid subjected to shearing. *J. Fluid Mech.*, 195:523–540.

Boyd, J. P. (1999). The devil's invention: asymptotic, superasymptotic and hyperasymptotic series. *Acta Appl. Math.*, 56(1):1–98.

Buckmaster, J. D., Nachman, A., and Ting, L. (1975). The buckling and stretching of a viscida. *J. Fluid Mech.*, 69(01):1–20.

Buellesfeld, F., Lange, U., Biertuempfel, R., Pudlo, L., and Jung, H. (2014). Method for production of glass components. US Patent 20,140,342,120.

Burke, S. (2016, (accessed 22 March 2016)). This glass can bend in half without shattering (online video clip). `http://edition.cnn.com/videos/cnnmoney/2016/03/18/bendable-glass-schott-burke-pkg.cnn-money/video/playlists/technology/`. CNN Money.

Chiu-Webster, S. and Lister, J. R. (2006). The fall of a viscous thread onto a moving surface: a fluid-mechanical sewing machine. *J. Fluid Mech.*, 569:89–111.

Cruickshank, J. O. (1988). Low-Reynolds-number instabilities in stagnating jet flows. *J. Fluid Mech.*, 193:111–127.

Cruickshank, J. O. and Munson, B. R. (1981). Viscous fluid buckling of plane and axisymmetric jets. *J. Fluid Mech.*, 113:221–239.

Debbaut, B., Marchal, J. M., and Crochet, M. J. (1995). Viscoelastic effects in film casting. In *Theoretical, Experimental, and Numerical Contributions to the Mechanics of Fluids and Solids*, pages 679–698. Springer.

Dewynne, J., Ockendon, J. R., and Wilmott, P. (1989). On a mathematical model for fiber tapering. *SIAM J. Appl. Math.*, 49(4):983–990.

d'Halewyu, S., Agassant, J. F., and Demay, Y. (1990). Numerical simulation of the cast film process. *Polym. Eng. Sci.*, 30(6):335–340.

Dobroth, T. and Erwin, L. (1986). Causes of edge beads in cast films. *Polym. Eng. Sci.*, 26(7):462–467.

Driscoll, T. A., Hale, N., and Trefethen, L. N. (2014). *Chebfun Guide*. Pafnuty Publications.

Filippov, A. and Zheng, Z. (2010). Dynamics and shape instability of thin viscous sheets. *Phys. Fluids*, 22(2):023601.

Fortin, M. (1981). Old and new finite elements for incompressible flows. *Int. J. Numer. Meth. Fl.*, 1(4):347–364.

Griffiths, I. M. and Howell, P. D. (2008). Mathematical modelling of non-axisymmetric capillary tube drawing. *J. Fluid Mech.*, 605:181–206.

Horvatitsch, T. (2016). Ultra-thin glass. *Schott Solutions 1/2016*, pages 6–11.

Howell, P. D. (1994). *Extensional thin layer flows*. PhD thesis, University of Oxford.

Howell, P. D. (1996). Models for thin viscous sheets. *Eur. J. Appl. Math.*, 7(04):321–343.

Howell, P. D., Kozyreff, G., and Ockendon, J. R. (2009). *Applied Solid Mechanics, Chapter 6*. Cambridge University Press.

Hyun, J. C. (1999). Draw resonance in polymer processing: a short chronology and a new approach. *Korea–Aust. Rheol. J.*, 11(4):279–285.

Kropinski, M. C. A., Ward, M. J., and Keller, J. B. (1995). A hybrid asymptotic-numerical method for low Reynolds number flows past a cylindrical body. *SIAM J. Appl. Math.*, 55(6):1484–1510.

Lange, U. (2013). Internal Schott AG report, 5 pages.

Lange, U. (2014). Private communications.

Lange, U. (2016). Internal Schott AG report, 8 pages.

Le Merrer, M., Quéré, D., and Clanet, C. (2012). Buckling of viscous filaments of a fluid under compression stresses. *Phys. Rev. Lett.*, 109(6):064502.

Logg, A. and Wells, G. N. (2010). DOLFIN: Automated finite element computing. *ACM T. Math. Software*, 37(2).

Logg, A., Wells, G. N., and Hake, J. (2012). DOLFIN: A C++/Python finite element library. In *Automated Solution of Differential Equations by the Finite Element Method*, pages 173–225. Springer.

Mahadevan, L., Ryu, W. S., and Samuel, A. D. T. (1998). Fluid 'rope trick' investigated. *Nature*, 392(6672):140–140.

Matovich, M. A. and Pearson, J. R. A. (1969). Spinning a molten threadline. Steady-state isothermal viscous flows. *Ind. Eng. Chem. Fund.*, 8(3):512–520.

Modest, M. F. (2013). *Radiative heat transfer, Chapter 3.* Academic Press.

Morris, S. W., Dawes, J. H. P., Ribe, N. M., and Lister, J. R. (2008). Meandering instability of a viscous thread. *Phys. Rev. E*, 77(6):066218.

Myers, M. R. (1989). A model for unsteady analysis of preform drawing. *AIChE Journal*, 35(4):592–602.

O'Kiely, D., Breward, C. J. W., Griffiths, I. M., Howell, P. D., and Lange, U. (2015). Edge behaviour in the glass sheet redraw process. *J. Fluid Mech.*, 785:248–269.

Paek, U. and Runk, R. (1978). Physical behavior of the neck-down region during furnace drawing of silica fibers. *Journal of Applied Physics*, 49(8):4417–4422.

Pearson, J. R. A. and Matovich, M. A. (1969). Spinning a molten threadline. Stability. *Ind. Eng. Chem. Fund.*, 8(4):605–609.

Perdigou, C. (2015). *Stability of viscous sheets in open flow*. PhD thesis, Université Pierre et Marie Curie-Paris VI.

Perdigou, C. and Audoly, B. (2016). The viscous curtain: General formulation and finite-element solution for the stability of flowing viscous sheets. *J. Mech. Phys. Solids*, 96:291–311.

Petrie, C. J. S. and Denn, M. M. (1976). Instabilities in polymer processing. *AIChE Journal*, 22(2):209–236.

Pfingstag, G., Audoly, B., and Boudaoud, A. (2011a). Linear and nonlinear stability of floating viscous sheets. *J. Fluid Mech.*, 683:112–148.

Pfingstag, G., Audoly, B., and Boudaoud, A. (2011b). Thin viscous sheets with inhomogeneous viscosity. *Phys. Fluids*, 23(6):063103.

Renardy, M. (2006). Draw resonance revisited. *SIAM J. Appl. Math.*, 66(4):1261–1269.

Ribe, N. M. (2001). Bending and stretching of thin viscous sheets. *J. Fluid Mech.*, 433:135–160.

Scheid, B., Quiligotti, S., Tran, B., Gy, R., and Stone, H. A. (2009). On the (de)stabilization of draw resonance due to cooling. *J. Fluid Mech.*, 636:155–176.

Schultz, W. W. and Davis, S. H. (1982). One-dimensional liquid fibers. *J. Rheol.*, 26(4):331–345.

Shah, Y. T. and Pearson, J. R. A. (1972). On the stability of nonisothermal fiber spinning. *Ind. Eng. Chem. Fund.*, 11(2):145–149.

Silagy, D., Demay, Y., and Agassant, J. F. (1999). Numerical simulation of the film casting process. *Int. J. Num. Meth. Fl.*, 30(1):1–18.

Skorobogatiy, M. and Mahadevan, L. (2000). Folding of viscous sheets and filaments. *Europhys. Lett.*, 52(5):532.

Slim, A. C., Teichman, J., and Mahadevan, L. (2012). Buckling of a thin-layer Couette flow. *J. Fluid Mech.*, 694:5–28.

Smith, S. and Stolle, D. (2000). Nonisothermal two-dimensional film casting of a viscous polymer. *Polym. Eng. Sci.*, 40(8):1870–1877.

Srinivasan, S., Zhiyan, W., and Mahadevan, L. (2017). Wrinkling instability of an inhomogenously stretched viscous sheet. *In preparation for submission to Phys. Rev. Fluids.*

Taroni, M., Breward, C. J. W., Cummings, L. J., and Griffiths, I. M. (2012). Asymptotic solutions of glass temperature profiles during steady optical fibre drawing. *J. Eng. Math.*, 80:1–20.

Taylor, G. I. (1969). Instability of jets, threads, and sheets of viscous fluid. In *Applied Mechanics*, pages 382–388. Springer.

Tchavdarov, B., Yarin, A. L., and Radev, S. (1993). Buckling of thin liquid jets. *J. Fluid Mech.*, 253:593–615.

Trouton, F. T. (1906). On the coefficient of viscous traction and its relation to that of viscosity. *P. Roy. Soc. Lond. A Mat.*, 77(519):426–440.

Wang, D., Li, K., and Teo, W. K. (1996). Polyethersulfone hollow fiber gas separation membranes prepared from NMP/alcohol solvent systems. *J. Membrane Sci.*, 115(1):85–108.

Ward, M. J., Heshaw, W. D., and Keller, J. B. (1993). Summing logarithmic expansions for singularly perturbed eigenvalue problems. *SIAM J. Appl. Math.*, 53(3):799–828.